



catalysts

Catalytic Applications of Clay Minerals and Hydrotalcites

Edited by

Juan Cecilia and Carmen Pilar Jiménez Gómez

Printed Edition of the Special Issue Published in *Catalysts*

Catalytic Applications of Clay Minerals and Hydrotalcites

Catalytic Applications of Clay Minerals and Hydrotalcites

Editors

Juan Cecilia

Carmen Pilar Jiménez Gómez

MDPI • Basel • Beijing • Wuhan • Barcelona • Belgrade • Manchester • Tokyo • Cluj • Tianjin



Editors

Juan Cecilia	Carmen Pilar Jiménez Gómez
Department of Inorganic Chemistry, Crystallography and Mineralogy	Department of Inorganic Chemistry, Crystallography and Mineralogy
Málaga	Málaga
Málaga	Málaga
Spain	Spain

Editorial Office

MDPI
St. Alban-Anlage 66
4052 Basel, Switzerland

This is a reprint of articles from the Special Issue published online in the open access journal *Catalysts* (ISSN 2073-4344) (available at: www.mdpi.com/journal/catalysts/special_issues/Clay_Minerals_Hydrotalcites).

For citation purposes, cite each article independently as indicated on the article page online and as indicated below:

LastName, A.A.; LastName, B.B.; LastName, C.C. Article Title. <i>Journal Name</i> Year , Volume Number, Page Range.
--

ISBN 978-3-0365-3552-4 (Hbk)

ISBN 978-3-0365-3551-7 (PDF)

© 2022 by the authors. Articles in this book are Open Access and distributed under the Creative Commons Attribution (CC BY) license, which allows users to download, copy and build upon published articles, as long as the author and publisher are properly credited, which ensures maximum dissemination and a wider impact of our publications.

The book as a whole is distributed by MDPI under the terms and conditions of the Creative Commons license CC BY-NC-ND.

Contents

About the Editors	vii
Preface to "Catalytic Applications of Clay Minerals and Hydrotalcites"	ix
Juan Antonio Cecilia and Carmen Pilar Jiménez-Gómez Catalytic Applications of Clay Minerals and Hydrotalcites Reprinted from: <i>Catalysts</i> 2021 , <i>11</i> , 68, doi:10.3390/catal11010068	1
Alex de Nazaré de Oliveira, Irlon Maciel Ferreira, David Esteban Quintero Jimenez, Fernando Batista Neves, Linéia Soares da Silva and Ana Alice Farias da Costa et al. An Efficient Catalyst Prepared from Residual Kaolin for the Esterification of Distillate from the Deodorization of Palm Oil Reprinted from: <i>Catalysts</i> 2021 , <i>11</i> , 604, doi:10.3390/catal11050604	5
Zhen Song, Jiameng Wang, Fanji Liu, Xiqing Zhang, Énio Matusse and Lihong Zhang MgF ₂ -Modified Hydrotalcite-Derived Composites Supported Pt-In Catalysts for Isobutane Direct Dehydrogenation Reprinted from: <i>Catalysts</i> 2021 , <i>11</i> , 478, doi:10.3390/catal11040478	17
Xiaopeng Yu, Fubao Zhang, Yi Wang and Dejun Cheng Easily Recycled CuMgFe Catalysts Derived from Layered Double Hydroxides for Hydrogenolysis of Glycerol Reprinted from: <i>Catalysts</i> 2021 , <i>11</i> , 232, doi:10.3390/catal11020232	29
Ming Zhang, Zhen Song, Mengquan Guo, Xiangxiang Li, Yanjun Lin and Lihong Zhang Effect of Reduction Atmosphere on Structure and Catalytic Performance of PtIn/Mg(Al)O/ZnO for Propane Dehydrogenation Reprinted from: <i>Catalysts</i> 2020 , <i>10</i> , 485, doi:10.3390/catal10050485	41
Guillermo R. Bertolini, Carmen P. Jiménez-Gómez, Juan Antonio Cecilia and Pedro Maireles-Torres Gas-Phase Hydrogenation of Furfural to Furfuryl Alcohol over Cu-ZnO-Al ₂ O ₃ Catalysts Prepared from Layered Double Hydroxides Reprinted from: <i>Catalysts</i> 2020 , <i>10</i> , 486, doi:10.3390/catal10050486	57
Jiaxin Li, Ming Zhang, Zhen Song, Shuo Liu, Jiameng Wang and Lihong Zhang Hierarchical PtIn/Mg(Al)O Derived from Reconstructed PtIn-hydrotalcite-like Compounds for Highly Efficient Propane Dehydrogenation Reprinted from: <i>Catalysts</i> 2019 , <i>9</i> , 767, doi:10.3390/catal9090767	79

About the Editors

Juan Cecilia

Juan Antonio Cecilia has a degree in Chemistry (2005) and is a Doctor in Inorganic Chemistry (2011) and an Associated Professor (2020) for the University of Malaga (Spain).

His main research line is the synthesis of adsorbents and catalysts for environmental applications, such as hydrotreating reactions, dehydration reactions, hydrogenating reactions, oxidation reactions, the valorization of biomass in valuable products, H₂ purification processes, CO₂ capture and the storage or the adsorption of biomolecules, dyes, pesticides or olefins between them. He has published 135 articles in scientific journals with a high impact factor (JCR) in the fields of materials, catalysis and adsorption (h-index: 32; citations: 3410). He is a reviewer for 60 journals and he has been an editor and guest editor of Special Issues.

Carmen Pilar Jiménez Gómez

Carmen Pilar Jiménez Gómez has a degree in Chemical Engineering (2014) and is a Doctor of Inorganic Chemistry (2018) for the University of Malaga (Spain). She has carried out several studies at the Queen Mary University of London as well as the Universities of Ancona and Bologna (Italy).

Her main research line is the design synthesis of catalysts for the valorization of biomass of sugar, mainly regarding the synthesis of chemicals coming from furfural through hydrogenation and oxidations reactions.

She has published 26 articles in scientific journals with a high impact factor (JCR) in the fields of materials, catalysis and adsorption (h-index: 11; citations: 528). She is a reviewer for 10 journals and she has been the editor and guest editor of two Special Issues.

Preface to “Catalytic Applications of Clay Minerals and Hydrotalcites”

Clay minerals are inexpensive and available materials with a wide range of applications (adsorbent, ion exchanger, support, catalyst, paper coating, ceramic, and pharmaceutical applications, among others). Clay minerals can be easily modified through acid/basic treatments, the insertion of bulky ions or pillars into the interlayer spacing, and acid treatment, improving their physicochemical properties.

Considering their low cost and high availability, clay minerals display a relatively high specific surface area in such a way that they have a great potential to be used as catalytic supports, since they can disperse expensive active phases as noble metals on the porous structures of their surfaces. In addition, the low cost of these supports allows their implementation on an industrial scale more easily than other supports, which are only feasible at the laboratory scale. Hydrotalcites (considered as anionic or basic clays) are also inexpensive materials with a great potential to be used as catalysts, since their textural properties could also be modified easily through the insertion of anions in their interlayer spacing. In the same way, these hydrotalcites, formed by layered double hydroxides, can lead to their respective mixed oxides after thermal treatment. These mixed oxides are considered basic catalysts with a high surface area, so they can also be used as catalytic supports.

Juan Cecilia and Carmen Pilar Jiménez Gómez

Editors

Editorial

Catalytic Applications of Clay Minerals and Hydrotalcites

Juan Antonio Cecilia *  and Carmen Pilar Jiménez-Gómez

Departamento de Química, Inorgánica, Cristalografía y Mineralogía, Facultad de Ciencias, Campus de Teatinos, Universidad de Málaga, 29071 Málaga, Spain; carmenpjg@uma.es

* Correspondence: jacecilia@uma.es

1. Introduction

Clay minerals are the most abundant minerals on the surface of Earth. These minerals are well-known from the paleolithic period where the primitive person used clay minerals to produce ceramics or pottery. The number of uses and applications has been increasing as life has evolved. Nowadays, clay minerals are employed in a wide range of applications. Between them, their use is highlighted in the ceramic field as potteries, refractories, and porcelain, in rubber industry as fillers, in paper industry as fillers or coatings in the pharmaceutical field. Other interesting applications are as adsorbent and filter, drilling fluids of deodorizing agent, catalyst, catalytic support among others. In an elemental classification, the clay minerals can be grouped as cationic clays, which are very common in nature, and anionic clays, which are rare in nature although the cost for their synthesis is relatively low [1,2]. Considering the structural and morphological composition of cationic and anionic clays, this editorial is focused on the use of these clay minerals for catalytic applications, highlighting the possible modifications of its structure to improve its catalytic behavior.

2. Cationic Clays

Among clay minerals, phyllosilicates are the minerals that have received the most attention due to their chemical composition and textural properties. Phyllosilicates are lamellar silicates which are composed by tetrahedral sheets $[\text{MO}_4]^{4-}$, where M can be Si^{4+} , Al^{3+} or Fe^{3+} , and octahedral sheets which are connected through sharing edges. The partial substitution of Si^{4+} by Al^{3+} in the tetrahedral sheets and the partial substitution of Al^{3+} or Fe^{3+} by Mg^{2+} in the octahedral sheets generate a deficiency of positive charge, which is counterbalanced by the incorporation of alkaline or alkaline-earth cations in the interlayer spacing between adjacent sheets [3]. These phyllosilicates display both Lewis and Brønsted acid sites on the edge of these sheets. Thus, Brønsted acid sites are attributed to the external hydroxyl groups while Lewis acid sites are ascribed to the partial substitution of Si^{4+} by Al^{3+} . The acidity on the surface decreases according to water adsorbed on the clay increases [4]. Besides acid sites, the presence of Fe^{3+} ions in the edges of the sheets can also provide electron-accepting or oxidizing sites [5]. In the same way, the redox behavior of the clay minerals can be modified by the substitution of the alkaline or alkaline-earth cations located in the interlayer spacing by other cations such as Ag^+ , Cu^{2+} or Fe^{3+} [6]. However, in many cases, the amount of available active sites is very limited. It has been reported in the literature that the interlayer spacing is between 7 Å and 14 Å in such a way that most of the molecules cannot access all active sites, so the only active centers available are those located on the outer surface [7].

It has been reported in the literature that the specific surface area determined by the BET equation is ranged between 10–150 m^2g^{-1} [8]. In most cases, N_2 molecules cannot access the interlayer spacing, so the specific surface area is mainly ascribed to the interparticular voids [7]. In any case, the surface area is remarkable so that these phyllosilicates can also be used as catalytic supports to disperse a wide variety of active phases.

Citation: Cecilia, J.A.; Jiménez-Gómez, C.P. Catalytic Applications of Clay Minerals and Hydrotalcites. *Catalysts* **2021**, *11*, 68. <https://doi.org/10.3390/catal11010068>

Received: 21 December 2020

Accepted: 3 January 2021

Published: 6 January 2021

Publisher's Note: MDPI stays neutral with regard to jurisdictional claims in published maps and institutional affiliations.



Copyright: © 2021 by the authors. Licensee MDPI, Basel, Switzerland. This article is an open access article distributed under the terms and conditions of the Creative Commons Attribution (CC BY) license (<https://creativecommons.org/licenses/by/4.0/>).

In this sense, the acid treatment of the phyllosilicates can increase the surface area because of a partial solution of the octahedral sheet [9]. This partial digestion is more pronounced in the case of Mg-rich phyllosilicates as saponites or sepiolite [10]. The acid treatment also produces a higher amount of acid sites due to the generation of partially coordinated Al^{3+} -species, forming Brønsted acid sites as well as the cationic exchange of the alkaline or alkaline-earth cations by H^+ -species in the interlayer spacing [11].

The ability to change ions located in the interlaminar spacing by other bulkier ions provide some phyllosilicates as smectites great potential in the field of catalysis as pillared structures may be formed with a specific surface area much higher than the starting materials. In this sense, the substitution of Na^+ by oligomeric (hydr)oxy aluminum cations provokes an increase of the interlayer spacing. In the next step, a thermal treatment favors the condensation between the silanol groups of the smectites sheets and the -OH groups of the oligomeric cations, leading to pillared clays (PILCs) [12]. Besides Al_2O_3 pillars, a wide variety of pillars have been synthesized from their respective polyoxocations. Between them, it can be highlighted the formation of Zr, Cr, Ti, Fe, Al/Ce, Al/Fe or Al/Co. The formation of these pillars can provide Lewis or Brønsted acid sites [13]. In addition, the increase of the surface area can allow for the use of these pillared clays as support, leading to bi-functional catalysts in many cases [13].

The synthesis of porous clay heterostructures (PCHs) is another alternative to obtain materials with high specific surface area [14]. The synthesis of PCHs consists in the substitution of the cations of the interlayer space by a bulky organic cation, which enhances the interlayer spacing. Then, silicon precursor in the form of alkoxide is polymerized around the organic cation, forming a silica structure between adjacent layers. Finally, the organic matter is removed under thermal treatment [15]. Through this synthetic strategy, it is possible to modulate the pore diameter according to the specific conditions of the catalytic reactions [15]. From this methodology, it is also possible to incorporate some heteroatoms in the pillars such as Al, Zr or Ti [16,17]. In these structures, Brønsted acid sites are observed in the sheets of smectite while Lewis acid sites are ascribed to the existence of Si-O-M bridges in the pillared structure. In addition, the increase of the specific surface area, modulated pore diameter and narrow pore diameter distribution allows its use of catalytic support [17].

Future perspectives for cationic clays could be based on the increase of the availability of sheets through a controlled delamination, the combination of organic–inorganic interactions, the deposition of nanoparticles, and the design of hierarchical structures, among others.

3. Anionic Clays

The number of natural anionic clays is fewer than that observed for natural cationic clays. However, these anionic clays also named hydrotalcites or layered double hydroxides can be easily and quickly synthesized in the laboratory [1]. This family of clays have also attracted the scientific community due to its wide range of applications in many fields such as medicine, biochemistry, electrochemistry, photochemistry, and polymers as additives. In addition, this material can also be used as an ion exchanger, an adsorbent, and a catalytic support or catalyst [18].

The most studied and best-known anionic clay are those composed by Mg^{2+} and Al^{3+} species. Its elemental base is composed of octahedrons, which are shared through their edges in such a way that each octahedron consists of one Mg^{2+} in the center of the octahedron and six OH^- on their vertexes. The partial substitution of Mg^{2+} by Al^{3+} causes a charge deficiency on the brucite sheet, which must be counterbalanced by the inclusion on anions, mainly CO_3^{2-} in the interlayer spacing [18].

The structure of the anionic clays is not limited to Mg^{2+} and Al^{3+} species. Thus, Mg^{2+} cations can be partially or totally replaced by Cu^{2+} , Zn^{2+} or Ni^{2+} , while Al^{3+} cations can be partially or totally replaced by Cr^{3+} or Fe^{3+} [18]. Traditionally, anionic clays have been synthesized by co-precipitation method, although alternative methods such as mechanochemi-

cal, tribochemistry, microwave or sonication methods have been reported to obtain anionic clays with different crystallinity in the last years.

From a catalytic point view, anionic clays display poor catalytic behavior as a consequence to its basicity is very low, which is probably due to H₂O blocking the basic sites [19]. However, a thermal treatment causes dehydroxylation in the brucite sheets as well as the removal of CO₃²⁻ located in the interlayer spacing causes a collapse of its structure leading to their respective mixed oxides. The properties of the obtained oxides depend on M²⁺/M³⁺ molar ratio and the chemical composition. Thus, the presence of MgO can provide basic sites while Al₂O₃ can provide acid sites. On the other hand, other oxides such as CuO or NiO are reducible in their respective metallic species. Considering the great variety of M²⁺ and M³⁺ species, it is possible to synthesize many polyfunctional catalysts from anionic clays [18].

The thermal treatment leads to the formation of small particles. This fact generates high porosity ascribed to the voids between particles, achieving a surface area between 100–300 m²g⁻¹ in such a way that the obtained oxide can also be employed as catalytic support.

The lamellar structure of the anionic clays can also form pillared structures due to the substitution of the CO₃²⁻ by a bulkier anion such as isopolyanions, heteropolyanions or ferro/ferricyanides. However, the formation of these pillars are not easy, as the anionic exchange capacity is more complex than that observed in cationic clays since the hydrolysis between the -OH groups and the anion can also collapse the layered structure or the low stability of the anionic clays [19]. Considering these disadvantages, the pillared anionic clays may be prepared by different methods such as the exchange of inorganic/organic anions, and the structure reconstruction or direct coprecipitation. In any case, the design of pillared anionic clays is less common than cationic clays [19].

The future perspectives related to the use of anionic clays in the catalysis field are focused on the design of an efficient method to incorporate active metal anions in the interlayer spacing with high regioselectivity. Another parameter that can be developed is the controlled exfoliation of the sheets to obtain materials with high surface area. The incorporation of metal complexes or metal nanoparticles to form functionalized hydrotalcites and to carry out one-pot catalytic reactions is another important point to be addressed.

Funding: The authors thanks to RTI2018-099668-BC22 and RTI2018-094918-B-C44 of Ministerio de Ciencia, Innovación y Universidades, and project UMA18-FEDERJA-126 of Junta de Andalucía and FEDER funds for the financial support.

Institutional Review Board Statement: Not applicable.

Informed Consent Statement: Not Applicable.

Data Availability Statement: Data sharing not applicable.

Conflicts of Interest: The authors declare no conflict of interest.

References

1. Vaccari, A. Preparation and catalytic properties of cationic and anionic clays. *Catal. Today* **1998**, *41*, 53–71. [CrossRef]
2. Vaccari, A. Clays and catalysis: A promising future. *Appl. Clay Sci.* **1999**, *14*, 161–198. [CrossRef]
3. Brigatti, M.F.; Galan, E.; Theng, B.K.G. *Structures and Mineralogy of Clay Minerals*; Elsevier: Amsterdam, The Netherlands, 2006; pp. 19–86.
4. Hensen, E.J.M.; Poduval, D.G.; Lighthart, D.A.J.; van Veen, J.A.R.; Rigutto, M.S. Quantification of strong Brønsted acid sites in aluminosilicates. *J. Phys. Chem. C* **2010**, *114*, 8363–8374. [CrossRef]
5. Sanchís, R.; Cecilia, J.A.; Soriano, M.D.; Vázquez, M.I.; Dejoz, A.; López-Nieto, J.M.; Rodríguez-Castellón, E.; Solsona, B. Porous clays heterostructures as supports of iron oxide for environmental catalysis. *Chem. Eng. J.* **2018**, *334*, 1159–1168. [CrossRef]
6. Soma, Y.; Soma, M.; Harada, I. The reaction of aromatic molecules in the interlayer of transition-metal ion-exchanged montmorillonite studied by resonance Raman spectroscopy. *J. Phys. Chem.* **1984**, *88*, 3034–3038. [CrossRef]
7. Thommes, M.; Kaneko, K.; Neimark, A.; Olivier, J.; Rodríguez-Reinoso, F.; Rouquerol, J.; Sing, K. Physisorption of gases, with special reference to the evaluation of surface area and pore size distribution (IUPAC Technical Report). *Pure Appl. Chem.* **2015**, *87*, 1051–1069. [CrossRef]

8. Michot, L.J. Determination of surface areas and textural properties of clay minerals. *Develop. Clay Sci.* **2018**, *9*, 23–47.
9. Osthaus, B.B. Chemical determination of tetrahedral ions in nontronite and montmorillonite. *Clays Clay Miner.* **1953**, *2*, 404–417. [CrossRef]
10. Cecilia, J.A.; Pardo, L.; Pozo, M.; Bellido, E.; Franco, F. Microwave-assisted acid activation of clays composed of 2:1 clay minerals: A comparative study. *Minerals* **2018**, *8*, 376. [CrossRef]
11. Varna, R.S. Clay and clay-supported reagents in organic synthesis. *Tetrahedron* **2002**, *58*, 1235–1255. [CrossRef]
12. Abeysinghe, S.; Unruh, D.K.; Forbes, T.Z. Crystallization of Keggin-type polyaluminum species by supramolecular interactions with disulfonate anions. *Cryst. Growth Des.* **2012**, *12*, 2044–2051. [CrossRef]
13. Gil, A.; Gandía, L.M.; Vicente, M.A. Recent advances in the synthesis and catalytic applications of pillared clays. *Catal Rev.* **2000**, *42*, 145–212. [CrossRef]
14. Galarneau, A.; Barodawalla, A.; Pinnavaia, T. Porous clay heterostructures formed by gallery-templated synthesis. *Nature* **1995**, *374*, 529–531. [CrossRef]
15. Cecilia, J.A.; García-Sancho, C.; Vilarrasa-García, E.; Jiménez-Jiménez, J.; Rodríguez-Castellón, E. Synthesis, characterization, uses and applications of porous clays heterostructures: A review. *Chem. Rec.* **2018**, *18*, 1–21.
16. Chmielarz, L.; Piwowarska, Z.; Kustrowski, P.; Wegrzyn, A.; Gil, B.; Kowalczyk, A.; Dudek, B.; Dziembaj, R.; Michalik, M. Comparison study of titania pillared interlayered clays and porous clay heterostructures modified with copper and iron as catalysts of the DeNO_x process. *Appl. Clay Sci.* **2011**, *53*, 164–173. [CrossRef]
17. Cecilia, J.A.; García-Sancho, C.; Franco, F. Montmorillonite based porous clay heterostructures: Influence of Zr in the structure and acidic properties. *Micropor. Mesopor. Mater.* **2013**, *176*, 95–102. [CrossRef]
18. Xu, Z.P.; Zhang, J.; Adebajo, M.O.; Zhang, H.; Zhou, C. Catalytic applications of layered double hydroxides and derivatives. *Appl. Clay Sci.* **2011**, *53*, 139–150. [CrossRef]
19. Cavani, F.; Trofiró, F.; Vaccari, A. Hydrotalcite-type anionic clays: Preparation, properties and applications. *Catal. Today* **1991**, *11*, 173–301. [CrossRef]

Communication

An Efficient Catalyst Prepared from Residual Kaolin for the Esterification of Distillate from the Deodorization of Palm Oil

Alex de Nazaré de Oliveira ^{1,2,3,*}, Irlon Maciel Ferreira ³ , David Esteban Quintero Jimenez ³,
Fernando Batista Neves ³, Linéia Soares da Silva ⁴, Ana Alice Farias da Costa ^{1,2}, Erika Tallyta Leite Lima ^{1,2},
Luíza Helena de Oliveira Pires ⁵, Carlos Emmerson Ferreira da Costa ^{1,2}, Geraldo Narciso da Rocha Filho ^{1,2} 
and Luís Adriano Santos do Nascimento ^{1,2,*} 

- ¹ Graduation Program in Chemistry, Federal University of Pará, Augusto Corrêa Street, Guamá, Belém 66075-110, PA, Brazil; analilice@hotmail.com (A.A.F.d.C.); erikatallyta@hotmail.com (E.T.L.L.); emmerson@ufpa.br (C.E.F.d.C.); geraldonrf@gmail.com (G.N.d.R.F.)
- ² Laboratory of Oils of the Amazon, Federal University of Pará, Belém 66075-750, PA, Brazil
- ³ Laboratory of Biocatalysts and Applied Organic Synthesis, Chemistry Course, Federal University of Amapá, Campus University Marco Zero of Equador, Rodovia Juscelino Kubitschek de Oliveira Km 02, Zerão, Macapá 68902-280, AP, Brazil; irlon.ferreira@gmail.com (I.M.F.); derteriom@gmail.com (D.E.Q.J.); fertista3798@gmail.com (F.B.N.)
- ⁴ Federal Institute of Education, Science and Technology of Amapá, Macapá 68909-398, AP, Brazil; dasilvalineia@gmail.com
- ⁵ High School of Application, University of Pará, Belém, Pará 66095-780, CEP, Brazil; lulenapires@hotmail.com
- * Correspondence: alexoliveiraquimica@hotmail.com (A.d.N.d.O.); adrui1@yahoo.com.br (L.A.S.d.N.); Tel.: +55-91-98171-4947 (A.d.N.d.O.)

Citation: de Nazaré de Oliveira, A.; Ferreira, I.M.; Jimenez, D.E.Q.; Neves, F.B.; Soares da Silva, L.; Farias da Costa, A.A.; Lima, E.T.L.; de Oliveira Pires, L.H.; Ferreira da Costa, C.E.; Narciso da Rocha Filho, G.; et al. An Efficient Catalyst Prepared from Residual Kaolin for the Esterification of Distillate from the Deodorization of Palm Oil. *Catalysts* **2021**, *11*, 604. <https://doi.org/10.3390/catal11050604>

Academic Editor: Juan Antonio Cecilia

Received: 15 April 2021
Accepted: 3 May 2021
Published: 7 May 2021

Publisher's Note: MDPI stays neutral with regard to jurisdictional claims in published maps and institutional affiliations.



Copyright: © 2021 by the authors. Licensee MDPI, Basel, Switzerland. This article is an open access article distributed under the terms and conditions of the Creative Commons Attribution (CC BY) license (<https://creativecommons.org/licenses/by/4.0/>).

Abstract: The distillate from the deodorization of palm oil (DDPO) is an agro-industrial residue, approximately 84% of which consists of free fatty acids (FFAs), which can be used for the production of fatty acid ethyl esters (FAEE). A catalyst (10HPMo/AlSiM) obtained from a waste material, Amazon *flint* kaolin, was applied in the esterification of the DDPO, reaching a conversion index of 94%, capable of maintaining satisfactory activity (>75%) after four consecutive cycles. *Flint* kaolin is therefore proven to be an efficient option in the search for new heterogeneous low-cost catalysts obtained from industrial by-products, contributing to the reduction of environmental impact and adding value to widely available wastes that would otherwise be discarded directly into the environment. Based on the catalytic results, esterification of DDPO using 10HPMo/AlSiM can be a cheaper alternative for the production of sustainable fuels.

Keywords: kaolin; mesoporous; heterogeneous catalyst; esterification; waste valorization

1. Introduction

Since the discovery of the family of mesoporous molecular sieves known as M41S in 1992 [1,2], MCM-41 (*Mobil Composition of Matter No. 41*) has been the most widely studied, due to its widerange of potential applications either as a catalyst [3] or catalytic support [4]. This is due to its combination of elevated surface areas and a well-defined pore size, which can be controlled and stabilized, while it is also easy to obtain [5,6]. The preparation of MCM-41 commonly involves sodium or ammonium hydroxide, hexadecyltrimethylammonium bromide (CTABr) as a driver and silica gel or tetraethylorthosilicate (TEOS) as a source of silica [2,6–8]. However, the use of TEOS for obtaining MCM-41 has toxic effect, and the materials involved in the process are expensive [7,9–11]. For economic and environmental reasons, efforts to find new sources of inorganic silicates containing high levels of silica at a low cost are increasing [12–14].

To circumvent such challenges, the use of alternative sources of silica, such as kaolin, to replace commercial options, applied in the synthesis of mesoporous materials, reduces the toxicity of the process and reduces costs, as they represent a natural raw material,

that is both inexpensive and widely available [4,15–18]. The preparation of mesoporous aluminosilicates from natural clay minerals has been investigated, due to the high silicon and aluminum content used in the synthesis of these mesoporous materials [15,19,20].

In the Amazon, the production of kaolin generates significant amounts of tailings, among which *flint* kaolin, FK, is deposited in the mine after the exploitation of soft kaolin, generating major environmental impacts, as it mainly comprises clay mineral kaolin, and contains high levels of silicon, aluminum, titanium and iron [21–23]. These low-quality kaolinitic tailings have been used as a raw material in various chemical processes, including as a catalyst [18,22,24–26], catalytic support [4,27], in zeolite synthesis [21,28,29] and as mesopore [15–17].

New heterogeneous catalysts and catalytic supports have been developed for application in the esterification of FFAs, including mesoporous silica [4,15–17,30], clay minerals [4,18,22,24–26,31] and several catalytic supports with heteropoly acids (HPAs) [4,15,30–35]. The HPAs are notable due to their high Brønsted acidity and redox properties [36,37], which favor the protonation of the carbonyl of FFAs during alcoholic esterification [4,15,30,31,34]. Supporting an HPA in a suitable matrix is known to control the strength and distribution of its active sites [36–38], and it can be applied in a wide range of heterogeneous reactions, including the esterification of low-cost raw materials with high FFA levels for the clean and efficient synthesis of mono alkyl esters (biodiesel), and with water as a by-product [4,30,31,33,34,39–44].

Several previous studies have investigated the possibility of using low-cost raw materials [4,16,26,31,45–48] which can potentially be applied in the synthesis of monoalkyl esters [4,30,31,33,34,39–44]. Notable among these is a by-product from the refining of vegetable oil, a distillate from the deodorization of palm oil (DDPO), around 84% of which is made up of FFAs [4,16,26,31]. The use of these FFAs to generate coproducts with a higher added value is a viable option for the mitigation of possible environmental impacts due to the disposal of such waste [49]. In this case, heterogeneous acid catalysts can esterify the FFAs into esters [4,16,26,31,50,51], and offer advantages such as separation and recovery at the end of the process, as well as subsequent reuse capacity, while avoiding the generation of secondary products and toxic effluents [4,30,31,34,40,43,52].

The use of 12-molybdophosphoric acid ($H_3PMo_{12}O_{40}$, HPMo) functionalized on silica (alternative source, FK) with a well-ordered hexagonal arrangement as an efficient acid catalyst for the esterification of eugenol, was recently reported by our group [15]. This study focused on the synthesis, characterization and application of a catalytic material as a contribution to Green Chemistry, since this catalyst comes from residues which are abundant in the Amazon region [15]. Therefore, the present work aimed to apply this mesoporous material, with an ordered hexagonal phase, in addition to describing a purpose for FK, to produce a low cost catalyst, anchored with HPMo in its mesopores [15], in the DDPO ethanolic esterification reaction. The raw materials used were chosen due to their low-cost and wide availability as waste in the Amazon region. Ethanol was used as it is produced from renewable sources, unlike methanol, which is generally derived from fossil sources [4,31,53]. The reaction between ethanol and DDPO (as a source of FFAs) was chosen as both reagents have greener properties and are widely available for the production of renewable FAEE.

2. Results and Discussion

2.1. Influence of Time on the Esterification Reaction of DDPO

The duration of the reaction process strongly influences the consumption of reagents and the formation of products of interest. As expected, for the esterification reaction, the initial conversion of 62% obtained 30 min after the start of the reaction gradually increased over time (Figure 1a). The reaction conversion percentage was higher in the 30 to 120 min intervals, with conversions varying from 62 to 94%, respectively. However, from 120 to 150 min, the conversion remained practically unchanged. The results obtained herein after 2 h of reaction were better than those obtained by Pires et al. [4] using 12-tungstophosphoric

acid supported on metakaolin waste (25%HPW/MK700) to catalyze DDPO, where after 2 h an 83% conversion to FAEE was obtained. Although Aranda et al. [54] achieved a 90% conversion of DDPO in 1 h of reaction using H_2SO_4 as a catalyst, the disadvantages of the homogeneous sulfuric acid catalyst are well known, such as its non-reusability and corrosion of equipment characteristics. The results achieved in this study still provided a better reaction time (≤ 2 h) than other previously published studies [26,34,52,53,55,56].

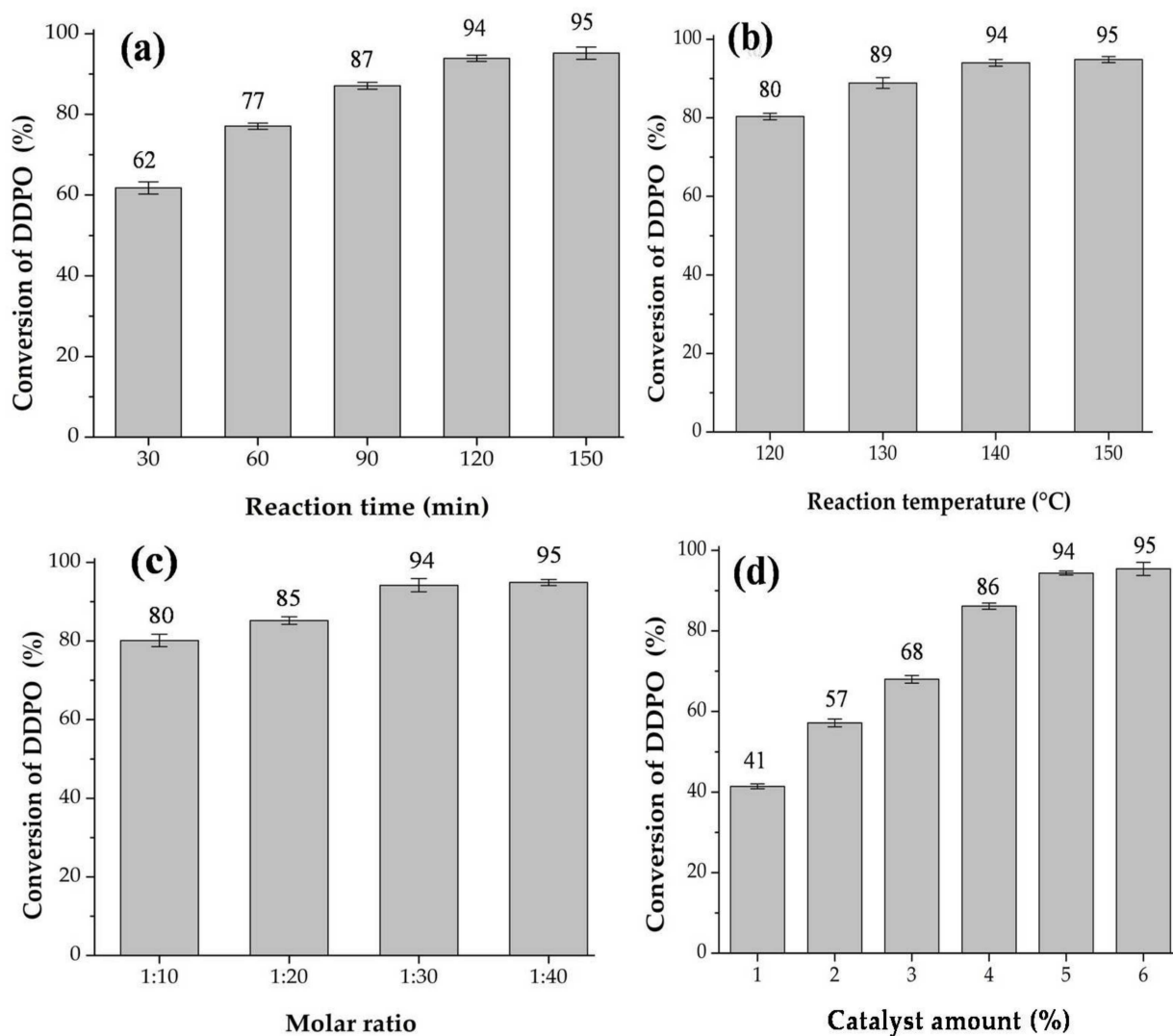


Figure 1. Influence of reaction parameters on esterification: (a) reaction time, (b) reaction temperature, (c) molar ratio DDPO: EtOH, (d) Catalyst amount. Reaction conditions: 1:30 molar ratio (DDPO: EtOH), reaction temperature 140 °C, reaction time 2 h and 5% catalyst.

2.2. Influence of Temperature on DDPO Esterification Reaction

The effect of the reaction temperature was investigated, and the results are shown in Figure 1b. The reaction was studied by varying the temperature from 120 to 150 °C without altering the other experimental conditions. An 80% increase in conversion was observed at 120 °C. At higher temperatures, the reaction attained equilibrium, with a conversion of 94% at 140 °C. These results show that higher temperatures increase the kinetic energy of the molecules, which accelerates the reaction, facilitating the mass transfer between the reactants and the catalyst surface [57]. Therefore, the ideal reaction temperature was determined to be 140 °C, lower than that required for other catalysts (150 to 210 °C) in similar reactions [4,26,31,33,34,44,52,53,56,58].

2.3. Influence of the Molar Ratio of DDPO and Ethanol in the Esterification Reaction

Theoretically, the esterification reaction occurs at a stoichiometric ratio of 1 mol of FFA to 1 mol of alcohol, generating 1 mol of ester and 1 mol of water. As the esterification reaction is reversible (hydrolysis), an excess of alcohol is required to drive the reaction towards ester formation and avoid hydrolysis [4,22,24,26,31,51].

To study the influence of the substrate molar ratio, the reaction was carried out by varying the DDPO: EtOH molar ratio from 1:10 to 1:40. According to Figure 1c, the conversion of DDPO increased with the molar ratio, reaching a maximum value of 94% with the DDPO: EtOH molar ratio of 1:30. As the molar ratio increased, however, an appreciable increase in conversion was not observed, which can be attributed to the occurrence of the reverse hydrolysis reaction of part of the esters produced in the presence of excess ethanol [4,30,31]. Thus, the 1:30 molar ratio was determined to be ideal for the esterification reaction, achieving maximum DDPO conversion. It should be stated that lower proportions, such as 1:10 and 1:20, were also used, attaining 80 and 85% conversion, respectively, showing that the 10HPMo/AlSiM catalyst maintained a strong catalytic performance. This can reduce the production costs of the process on a nonlaboratory scale, as less ethanol would be needed to promote the reaction. Even so, studies have shown that a high molar ratio of 1:30, 1:40 or 1:90 is necessary to shift the reaction balance to a direct basis, in order to achieve maximum conversion [27,31,33,34,37,38,40].

2.4. Influence of Amount of Catalyst on DDPO Esterification

Control experiments with AlSiM and HPMo were also carried out under optimized conditions. At first, the esterification reaction of DDPO with EtOH without a catalyst exhibited a conversion close to 20%, while the esterification reaction in the presence of AlSiM did not reach 23%. Therefore, AlSiM alone is unable to promote a high conversion during the esterification of DDPO, indicating that the catalytic activity is mainly due to the HPMo present in AlSiM, which makes 10HPMo/AlSiM highly active. The same reaction was carried out with the active amount of HPMo (64 mg) which converted 90% of DDPO in homogeneous esterification.

Figure 1d shows the variation in the conversion of DDPO based on the amount of catalyst during ethanolic esterification. The effect of the amount of the 10HPMo/AlSiM catalyst was investigated by the variation in the dosage, which varied from 1 to 6% by mass, based on DDPO mass. It was observed that the DDPO conversion increased from 41 to 94% as the catalyst dosage increased from 1 to 5%. A 4% load can be used without drastically reducing the conversion of DDPO (86%), which shows the efficiency of the catalyst. An additional increase in the amount of catalyst resulted in not significant changes in the conversion of DDPO, indicating that 5% is the catalyst dosage that ensures the appropriate number of active acid sites for the esterification of DDPO.

2.5. Comparison with Data from Literature

A comparison with other types of heterogeneous and homogeneous catalysts used in the esterification of FFAs described in literature was performed (Table 1). The results obtained in this study indicate that the catalyst has a strong potential for use in the esterification reaction of DDPO, a low-quality organic matter (see Table 1). The 94% observed value for the conversion to esters during the esterification of DDPO with EtOH using the 10HPMo/AlSiM catalyst is close to the values of 62% [59], 90% [54] and 99.9% [45] achieved by sulfuric acid as a catalyst, a substance which has well-known disadvantages. Similar results were obtained using solid acid catalysts such as CsHPW/MCM (92%) [60], MF9S4 (<93%) [26], BLMW (<94%) [31], with even better results than those reported for MP-S-16 (15) (<82%) [30], 25% HPW/MK700 (83%) [4] and CrWO₂ and CrWTiO₂ (<86%) [52,56]. However, the use of chromium is not environmentally friendly in comparison with the aforementioned HPMo material. H₃PMo/Al₂O₃ (97%) [33], AM41-2H-O (98%) [16], HPMo/Nb₂O₅ (99.9%) [34] were better than the results achieved in the present study. Although all of the catalysts mentioned are reasonably efficient in the esterification

reactions of FFA residues, with high conversion to esters, in most cases, higher temperatures (≥ 140 °C) and longer reaction times (≥ 2 h) than those of the present study were necessary. In addition, the cost of the preparation of our material modified with HPMo was low, since it used kaolinitic residue as a precursor to aluminosilicate, and we still believe that it is more environmentally friendly.

Table 1. Comparison of the catalytic activity of 10HPMo/AlSiM with other catalysts for the esterification of different free fatty acids.

Catalyst	FFAs	Alcohol	M: R ^a	(°C) ^b	(h) ^c	(%) ^d	Ref.
Al-MCM-41Si/Al = 8	Palmitic	MeOH	1:60	130	2	79	[3]
25%HPW/MK700	DDPO	EtOH	1:10	200	2	83	[4]
AM41-2H-O	DDPO	MeOH	1:30	130	2	98	[16]
MF9S4	Oleic	MeOH	1:60	160	4	98.9	[22]
MF8S4M4W15	Oleic	MeOH	1:60	115	2/3	96.5	[25]
MF9S4	DDPO	MeOH	1:60	160	4	92.8	[26]
MP-S-16 (15)	CKO	MeOH	1:8	140	5	82	[30]
BLMW	DDPO	EtOH	1:30	160	2	93.3	[31]
H ₂ SO ₄	Soapstock	MeOH	1:18	50	14	99.9	[45]
CrWO ₂	PFAD	MeOH	1:2	170	3	86	[52]
CrWTiO ₂	PFAD	MeOH	1:2	170	3	80	[56]
H ₂ SO ₄	PFAD	MeOH	1:3	60	3	62	[59]
H ₂ SO ₄	DDPO	MeOH	1:3	130	1	90	[54]
CsHPW/MCM	PFAD	MeOH	1:15	85	4	92	[60]
10HPMo/AlSiM	DDPO	EtOH	1:30	140	2.5	94	Present work

^a Molar ratio; ^b Temperature; ^c Time; ^d Conversion of FFA, Methanol = MeOH.

Therefore, the reaction of esterification of DDPO with EtOH is accelerated by HPMo as an active species (Brønsted acid sites) in the structure of AlSiM, making the catalyst reasonably effective. The results obtained using 10HPMo/AlSiM as a catalyst for the esterification of DDPO with EtOH are largely satisfactory, as the results are similar or superior to those presented in literature using different reagents and catalysts (Table 1).

Finally, it must be noted that the costs of production of the catalyst from Amazonian FK are encouraging. The use of this waste as a raw material for a low-cost silica source for the production of catalytic supports proved to be quite feasible [15–17]. While in the reaction EtOH was also used as a solvent and DDPO by-product as FFAs, all are raw materials that have greener properties for sustainable FAEEs production [31]. Thus, the use of industrial by-products, such as FK and DDPO, in the synthesis of new mesoporous material and FAEEs makes production sustainable, reduces the environmental liabilities caused by its disposal and adds economic value to waste.

2.6. Catalyst Deactivation and Recyclability

Recovery, stability and reuse are important aspects of heterogeneous catalysts [30,34,37]. The reuse of 10HPMo/AlSiM in the esterification reaction was analyzed for four successive catalytic cycles under the optimal reaction conditions established in this study. The results in relation to the repeated use of the catalyst are shown in Table 2.

Table 2 also shows the results obtained for DDPO conversion using the recycled catalyst. A gradual reduction in DDPO conversion, from 94 to 74.6% in the fourth cycle, was observed, results which are still superior to those of the autocatalysis (20%), indicating that the material can be reused for several cycles and retain the potential to protonate FFAs. The TOF values followed the same trend. This reduction in catalytic activity can be attributed to factors such as loss of mass or even the blockage or destruction of pores by remaining impurities, even after the purification stage (filtration, washing and drying), in addition to the leaching of the active species of the support shown in Table 2 (as no amounts of HPMo were added to the catalyst) [15,30,31,34]. The leaching of the active species (Mo) from the reused catalyst was monitored by the XRF and UV–vis techniques [4,15,27,31,61].

Table 2. Properties of acidity, leaching of active species and catalyst conversion during recycling.

Cycles	(g) ^a	(mmol H ⁺ g ⁻¹) ^b	%MoO ₃ ^c	(mg) ^d	(μg) ^e	(%) ^f	(%) ^g	(min ⁻¹) ^h
10HPMo/AlSiM	-	5.84	7.40	20.8	0.60	2.88	94	244
10HPMo/AlSiM R1	2.34	5.41	7.37	20.2	0.55	2.72	90	221
10HPMo/AlSiM R2	2.17	5.21	7.36	19.7	0.58	2.95	84	217
10HPMo/AlSiM R3	1.93	5.05	7.36	19.1	0.58	3.01	79	216
10HPMo/AlSiM R4	1.88	4.58	6.93	18.5	0.70	3.08	75	216

^a Dry mass of the catalyst recovered after each reuse cycle for 2 h at 140 °C (the reagents were always recalculated to maintain the same conditions: DDPO: EtOH = 1: 30 and 5% catalyst); ^b surface acidity calculated by titration; ^c XRF of the catalysts after tests; ^d mass of HPMo anchored in AlSiM measured by UV–vis; ^e mass of leached HPMo detected by UV–vis; ^f percentage of leaching in the reaction medium; ^g conversion of DDPO; ^h TOF (turnover frequency) = ((Conversion% × moles of DDPO fed) / (No. of mol of Mo species) × (reaction time)); No. of moles of Mo species = (mass of HPMo / 1825.25) × (95.95 / 1825.25) [15,30,31], according to the results of the UV–vis analysis; R: refers to the reused catalyst.

The results of XRF analysis of the reused catalysts showed that the percentage content of MoO₃ in the new and reused catalysts was practically the same, until the third reuse cycle (see Supplementary Materials). Analysis of the reaction mixtures by UV–vis confirmed there was leaching of active species (Mo) of close to 3% in all the reuse cycles. This can be attributed to the loss of active sites during friction in the reactor during the reaction, and also during the recovery process [15,30,31,34]. These observations ensure that HPMo leaching from AlSiM support is within acceptable limits (3%) [15,27,31]. The acidity values of the reused catalyst measured by titration revealed a decline after each run, in comparison with the new catalyst, which was consistent with the declining values of the DDPO conversion (Table 2).

To verify the integrity of the catalyst after successive esterification reactions, it was analyzed by the XRD, DRS and FTIR techniques after a fourth reuse cycle (Figure 2a–c). Figure 2a shows the XRD of the 10HPMo/AlSiM and 10HPMo/AlSiM R4 catalysts. There was a clear reduction in peak intensity corresponding to reflection (100), followed by the absence of reflection (110, 200 and 210), a strong indication that the hexagonal mesostructure had become disordered, [4,15,62], but was still preserved [4,62]. This was expected, since the reactions were conducted under aggressive mechanical agitation and temperature conditions [15,30,37,62].

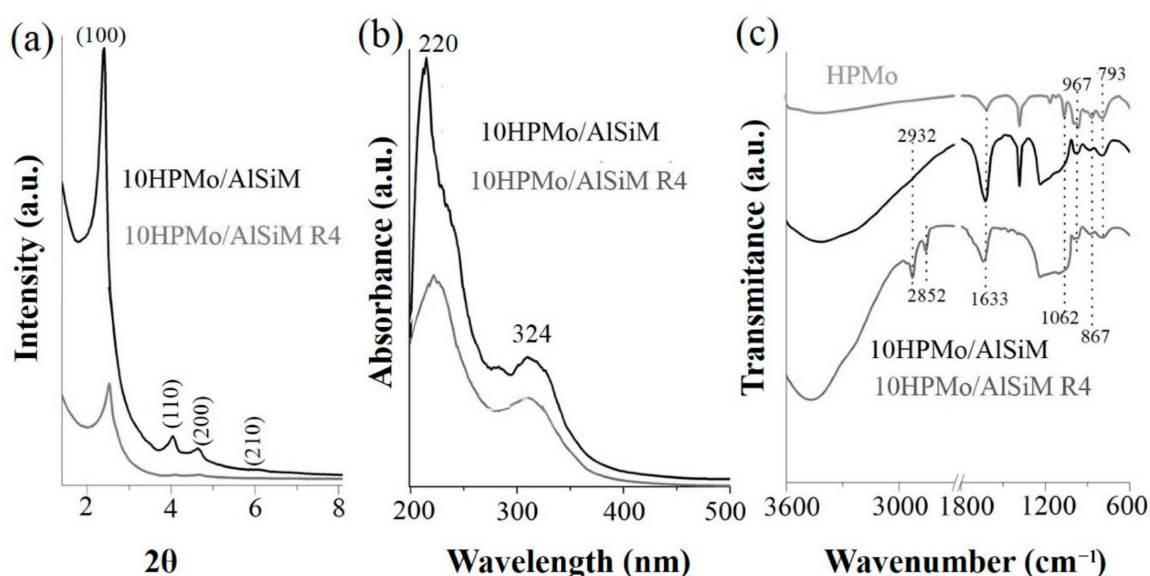


Figure 2. (a) Comparison of XRD standards, (b) DRS spectra, (c) FTIR spectra of the new catalyst and after the fourth reuse cycle. R: refers to the reused catalyst.

In the DRS absorption spectrum of 10HPMo/AlSiM-R4 shown in Figure 2b, broad and less intense bands appeared at 220 and 324 nm, indicating the presence of HPMo and the stability of the catalyst after the four reaction cycles [15,62–65]. Analyzing the FTIR spectra of 10HPMo/AlSiM-R4 in Figure 2c, there was a marked presence of bands in the 800 to 1100 cm^{-1} range, characteristic of HPMo with a Keggin structure, which was maintained after the fourth catalytic cycle. Some new prominent adsorption bands, such as at 2932 and 2852 cm^{-1} , were attributed to the symmetrical stretching of the CH_3 bonds, while a very discrete band, at 1465 cm^{-1} , was attributed to the asymmetric CH_3 deformation. The adsorption of organic molecules in the reused catalyst can be clearly seen, and may involve impurities such as triglycerides and unsaponifiable matter present in around 16% of the DDPO [4,16,26,31]. The adsorption of these molecules on the catalyst surface contributed to the reduction of catalytic activity [31,66,67]. This is in line with studies that demonstrated that catalysts with PAHs or other anchored solid acids could be recycled and have been found to have effective recycling capacity [4,15,30,34,38].

Finally, through the use of FRX, UV-vis, DRX, DRS and FTIR techniques, it was observed that active species were still present in the material, and it was concluded that the hexagonal structure of the mesopore was preserved after the recyclability tests. From previously published works [15,19,20] and the results achieved here with 10HPMo/AlSiM, it is possible to predict the use of AlSiM, synthesized at low cost, as a catalytic support to be applied in other types of organic transformation reactions, operating in a predominantly heterogeneous phase.

3. Experimental Section

3.1. Materials

All chemical reagents and solvents were analytical grade and used without further purification. DDPO is a residue (viscosity at 60 $^{\circ}\text{C}$ = 12.296 $\text{mm}^2 \text{s}^{-1}$; density at 60 $^{\circ}\text{C}$ = 0.862 g mL^{-1} ; water content < 0.5%; oxidative stability > 150 h; acidity index = 177.15 mg KOH g^{-1}) consists of 84.0-wt% free fatty acid (FFA) (42% palmitic, 41% oleic, 10% linoleic, 5% stearic, 2% lauric and 1.5% myristic), 12-wt% triglycerides, diglycerides and monoglycerides and 4-wt% unsaponifiable matter [4,16,26,31], kindly donated by Companhia Refinadora da Amazônia, Agropalma S/A (Brazil). *Flint* kaolin of the Capim River Region (Pará, Brazil) was used as Si and Al source and was kindly supplied by the Institute of Geology-UFGPA, ethanol (EtOH, 98%, synthetic grade, Nuclear, São Paulo, SP–Brazil), hydrochloric acid (HCl, 37%, Fmaia, Belo Horizonte, MG–Brazil) and sodium hydroxide (NaOH, VETEC, Rio de Janeiro, RJ–Brazil). The preparation and characterization of the 10HPMo/AlSiM were described in a previous work [15].

3.2. Characterization of Fresh and Reused Catalyst

The chemical compositions of the samples were obtained with Shimadzu EDX-700 energy dispersive X-ray spectrometer (EDX; EDX-700, SHIMADZU, Kyoto, Japan), with a rhodium X-ray source tube (40 kV, SHIMADZU, Kyoto, Japan). For each analysis, approximately 500 mg (powder) of each sample was deposited in a lower sample holder made of polyethylene film in order to determine the MoO_3 content present in the fresh and reused catalyst.

X-ray diffraction analysis were performed on a Bruker D8 Advance diffractometer (Bruker D8Advance; Bruker Corp, Billerica, MA, USA), using powder method, at a $1^{\circ} < 2\theta > 10^{\circ}$ interval. $\text{Cu K}\alpha$ ($\lambda = 1.5406 \text{ \AA}$, 40 kV e 40 mA) radiation was used.

Diffuse ultraviolet–visible reflectance spectroscopy (DRS) readings were recorded, in the range of 200–500 nm, on a Shimadzu UV–vis model ISR-2600 Plus spectrophotometer (EDX; EDX-700, SHIMADZU, Kyoto, Japan).

Fourier transform infrared spectroscopy (FTIR) spectra were obtained from a spectrophotometer of Shimadzu (Kyoto, Japan) model IRP Prestige-21A with a resolution of 32 and 100 scans and analyzed by Thermo Electron Corporation, IR 100 model with a resolution of 4 and 32 scans. For the analysis of all materials KBr pellets were used and the spectra were obtained in the region 4000–400 cm^{-1} .

The leaching of the HPMo catalysts was performed in UV–vis equipment of Thermo Scientific (Waltham, MA, USA), model Evolution array UV–vis spectrophotometer, with 200 to 600 nm scan and 30 scan resolution. The liquids were placed in a quartz tube. The quantification of the HPMo leached in the reaction medium was made using the analytical curve constructed from the postreaction solution (1 to 5 mg L^{-1} of HPMo), which was diluted with 0.1 mol L^{-1} HCl to avoid any hydrolysis anion $[\text{PMo}_{12}\text{O}_{40}]^{3-}$, with an absorbance equation ($y = 0.0999 + 0.0025x$) of $\lambda_{\text{max}} = 310 \text{ nm}$ and an excellent correlation coefficient ($R^2 = 0.9999$) based on our previous studies [15,31].

3.3. Catalytic Activity

Prior to the experiments, the catalysts were activated at 130 °C for 2 h. Tests of the catalysts were conducted in one run on a PARR 4871 multi-reactor (Parr Instrument Company, Moline, IL, USA). In a typical experiment, the DDPO was mixed with alcohol at a molar ratio of 1:10, 1:20, 1:30 and 1:40 (DDPO: EtOH) and 1, 2, 3, 4, 5 and 6% *w/w* of the solid acid catalyst (as compared to the mass of DDPO). The reaction mixture was stirred (500 rpm) and heated from room temperature to 120, 130, 140 and 150 °C. Once the desired temperature was reached, the system was maintained for 30, 60, 90, 120 and 150 min, considered to be the kinetic contact time. At the end of the reaction, the catalyst was separated from the reaction medium by vacuum filtration, and the excess methanol and water produced were removed by evaporation at 120 °C. The percentage conversion of DDPO to the corresponding ester was estimated by acid measurement of the product by titration with 0.1 mol L^{-1} hydroxide, according to the methods described in the literature. [4,16,26,31]. Reaction parameters such as time, molar ratio, temperature, and catalyst loading were optimized and evaluated. In addition, the recyclability of the catalyst was assessed in the DDPO esterification reaction under the same conditions listed above. At the end of each reaction cycle, the catalyst was filtered under vacuum, washed with 50 mL of ethanol to remove residues and dried at 150 °C for 12 h. The catalyst was reused in four reaction cycles.

4. Conclusions

Experimental investigations revealed that the 10HPMo/AlSiM catalyst exhibited excellent catalytic activity during the esterification reaction of DDPO with ethanol, reaching a conversion of 94%. The XRF, XRD, DRS and FTIR characterization results for this material confirmed the preservation of HPMo after the fourth cycle of reuse in the reaction, where it exhibited a conversion rate of over 75%. The use of two industrial by-products—*Flint* kaolin for the synthesis of mesoporous material and DDPO for the production of ethyl esters—enables sustainable production, reducing possible environmental impacts arising from their provision, in addition to adding economic value to such residues. The results obtained were comparable with previously published results on the use of this reaction and the availability of FK makes this material a promising alternative to those already used. Thus, the results obtained in the present study encourage the search for varied applications for both the 10HPMo/AlSiM catalyst and AlSiM support in oxidation reactions and heavy metal removal, among others.

Supplementary Materials: The following are available online at <https://www.mdpi.com/article/10.3390/catal11050604/s1>, Elemental analysis by XRF of Table 2.

Author Contributions: Conceptualization, L.A.S.d.N.; methodology, C.E.F.d.C. and G.N.d.R.F.; formal analysis, A.d.N.d.O., L.H.d.O.P., F.B.N., D.E.Q.J., L.S.d.S., A.A.F.d.C., and E.T.L.L.; investigation, A.d.N.d.O., E.T.L.L. and L.H.d.O.P.; resources, I.M.F., D.E.Q.J. and C.E.F.d.C.; data curation, L.A.S.d.N.; writing—original draft preparation, A.d.N.d.O., L.H.d.O.P., I.M.F., and E.T.L.L.; writing—review and editing, A.d.N.d.O., L.H.d.O.P., F.B.N., D.E.Q.J., L.S.d.S., A.A.F.d.C. and L.A.S.d.N.; visualization, G.N.d.R.F. and L.A.S.d.N.; supervision, C.E.F.d.C., G.N.d.R.F. and L.A.S.d.N.; project administration, L.A.S.d.N.; funding acquisition, G.N.d.R.F. and L.A.S.d.N. All authors have read and agreed to the published version of the manuscript.

Funding: This research was funded by Banco da Amazônia grant number 2018/212 and CNPQ, grant number 432221/2018-2.

Data Availability Statement: Not applicable.

Acknowledgments: The authors would like to thank the laboratories that supported this work: Laboratory of Research and Analysis of Fuels (LAPAC/UFPA), Laboratory of Catalysis and Oil Chemistry (LCO/UFPA) and LABNANO-AMAZON/UFPA. CAPES/UNIFAP, BIORG/UNIFAP and PROPESP/UFPA for the financial support.

Conflicts of Interest: The authors declare no conflict of interest.

References

- Kresge, C.T.; Roth, W.J. The Discovery of Mesoporous Molecular Sieves from the Twenty Year Perspective. *Chem. Soc. Rev.* **2013**, *42*, 3663–3670. [CrossRef] [PubMed]
- Beck, J.S.; Vartuli, J.C.; Roth, W.J.; Leonowicz, M.E.; Kresge, C.T.; Schmitt, K.D.; Chu, C.T.-W.; Olson, D.H.; Sheppard, E.W.; McCullen, S.B.; et al. A New Family of Mesoporous Molecular Sieves Prepared with Liquid Crystal Templates. *J. Am. Chem. Soc.* **1992**, *27*, 10834–10843. [CrossRef]
- Carmo, A.C.; de Souza, L.K.C.; da Costa, C.E.F.; Longo, E.; Zamian, J.R.; da Rocha Filho, G.N. Production of Biodiesel by Esterification of Palmitic Acid over Mesoporous Aluminosilicate Al-MCM-41. *Fuel* **2009**, *88*, 461–468. [CrossRef]
- Pires, L.H.O.; Oliveira, A.N.; Monteiro Junior, O.V.; Angélica, R.S.; Costa, C.E.F.; Zamian, J.R.; Nascimento, L.A.S.; Rocha Filho, G.N. Esterification of a Waste Produced from the Palm Oil Industry over 12-Tungstophosphoric Acid Supported on Kaolin Waste and Mesoporous Materials. *Appl. Catal. B Environ.* **2014**, *160–161*, 122–128. [CrossRef]
- Sayari, A. Catalysis by Crystalline Mesoporous Molecular Sieves. *Chem. Mater.* **1996**, *8*, 1840–1852. [CrossRef]
- Fontes, M.S.B.; Melo, D.M.A.; Costa, C.C.; Braga, R.M.; Melo, M.A.F.; Alves, J.A.B.L.R.; Silva, M.L.P. Effect of Different Silica Sources on Textural Parameters of Molecular Sieve MCM-41. *Cerâmica* **2016**, *62*, 85–90. [CrossRef]
- Da Lacerda Júnior, O.S.; Cavalcanti, R.M.; de Matos, T.M.; Venâncio, J.D.B. Synthesis of MCM-41 Mesoporous Material Using Freshwater Sponge as a Source of Silica. *Química Nova* **2013**, *36*, 1348–1353. [CrossRef]
- Ciesla, U.; Schüth, F. Ordered Mesoporous Materials. *Microporous Mesoporous Mater.* **1999**, *27*, 131–149. [CrossRef]
- Du, C.; Yang, H. Investigation of the Physicochemical Aspects from Natural Kaolin to Al-MCM-41 Mesoporous Materials. *J. Colloid Interface Sci.* **2012**, *369*, 216–222. [CrossRef]
- Kumar, P.; Mal, N.; Oumi, Y.; Yamana, K.; Sano, T. Mesoporous Materials Prepared Using Coal Fly Ash as the Silicon and Aluminium Source. *J. Mater. Chem.* **2001**, *11*, 3285–3290. [CrossRef]
- Yang, H.; Deng, Y.; Du, C.; Jin, S. Novel Synthesis of Ordered Mesoporous Materials Al-MCM-41 from Bentonite. *Appl. Clay Sci.* **2010**, *47*, 351–355. [CrossRef]
- Kang, F.; Wang, Q.; Xiang, S. Synthesis of Mesoporous Al-MCM-41 Materials Using Metakaolin as Aluminum Source. *Mater. Lett.* **2005**, *59*, 1426–1429. [CrossRef]
- Madhusoodana, C.D.; Kameshima, Y.; Nakajima, A.; Okada, K.; Kogure, T.; MacKenzie, K.J.D. Synthesis of High Surface Area Al-Containing Mesoporous Silica from Calcined and Acid Leached Kaolinites as the Precursors. *J. Colloid Interface Sci.* **2006**, *297*, 724–731. [CrossRef]
- Wang, G.; Wang, Y.; Liu, Y.; Liu, Z.; Guo, Y.; Liu, G.; Yang, Z.; Xu, M.; Wang, L. Synthesis of Highly Regular Mesoporous Al-MCM-41 from Metakaolin. *Appl. Clay Sci.* **2009**, *44*, 185–188. [CrossRef]
- De Oliveira, A.N.; Lima, E.T.L.; Oliveira, D.T.; Andrade, E.H.A.; Angélica, R.S.; Costa, C.E.F.; Rocha Filho, G.N.; Costa, F.F.; Luque, R.; Nascimento, L.A.S. Acetylation of Eugenol over 12-Molybdophosphoric Acid Anchored in Mesoporous Silicate Support Synthesized from Flint Kaolin. *Materials* **2019**, *12*, 2995. [CrossRef]
- Lima, E.T.L.; Queiroz, L.S.; de Pires, L.H.O.; Angélica, R.S.; Costa, C.E.F.; Zamian, J.R.; Rocha Filho, G.N.; Luque, R.; Nascimento, L.A.S. Valorization of Mining Waste in the Synthesis of Organofunctionalized Aluminosilicates for the Esterification of Waste from Palm Oil Deodorization. *ACS Sustain. Chem. Eng.* **2019**, *7*, 7543–7551. [CrossRef]
- De Oliveira, A.N.; Lima, E.T.L.; de Andrade, E.H.A.; Zamian, J.R.; da Rocha Filho, G.N.; da Costa, E.F.; de Pires, L.H.O.; Luque, R.; do Nascimento, L.A.S. Acetylation of Eugenol on Functionalized Mesoporous Aluminosilicates Synthesized from Amazonian Flint Kaolin. *Catalysts* **2020**, *10*, 478. [CrossRef]

18. De Oliveira, A.N.; de Oliveira, D.T.; Angélica, R.S.; de Andrade, E.H.A.; do Silva, J.K.R.; da Roca Filho, G.N.; Coral, N.; de Pires, L.H.O.; Luque, R.; do Nascimento, L.A.S. Efficient Esterification of Eugenol Using a Microwave-Activated Waste Kaolin. *React. Kinet. Mech. Catal.* **2020**, *130*, 633–653. [CrossRef]
19. Sun, C.; Zhang, F.; Wang, X.; Cheng, F. Facile Preparation of Ammonium Molybdophosphate/Al-MCM-41 Composite Material from Natural Clay and Its Use in Cesium Ion Adsorption. *Eur. J. Inorg. Chem.* **2015**, *2015*, 2125–2131. [CrossRef]
20. Sun, C.; Zhang, F.; Li, S.; Cheng, F. Synthesis of SBA-15 Encapsulated Ammonium Molybdophosphate Using Qaidam Natural Clay and Its Use in Cesium Ion Adsorption. *RSC Adv.* **2015**, *5*, 35453–35460. [CrossRef]
21. Rocha Junior, C.A.F.; Angélica, R.S.; Neves, R.F. Synthesis of Faujasite-type Zeolite: Comparison between Processed and *Flint* Kaolin. *Cerâmica* **2015**, *61*, 259–268. [CrossRef]
22. Nascimento, L.A.S.; Tito, L.M.Z.; Angélica, R.S.; Costa, C.E.F.; Zamian, J.R.; Rocha Filho, G.N. Esterification of Oleic Acid over Solid Acid Catalysts Prepared from Amazon *Flint* Kaolin. *Appl. Catal. B Environ.* **2011**, *101*, 495–503. [CrossRef]
23. Carneiro, B.S.; Angélica, R.S.; Scheller, T.; de Castro, E.A.S.; de Neves, R.F. Mineralogical and Geochemical Characterization of the Hard Kaolin from the Capim Region, Pará, Northern Brazil. *Cerâmica* **2003**, *49*, 237–244. [CrossRef]
24. Nascimento, L.A.S.; Angélica, R.S.; Costa, C.E.F.; Zamian, J.R.; Rocha Filho, G.N. Comparative Study between Catalysts for Esterification Prepared from Kaolins. *Appl. Clay Sci.* **2011**, *51*, 267–273. [CrossRef]
25. Oliveira, A.N.; da Costa, L.R.S.; Pires, L.H.O.; Nascimento, L.A.S.; Angélica, R.S.; da Costa, C.E.F.; Zamian, J.R.; da Rocha Filho, G.N. Microwave-Assisted Preparation of a New Esterification Catalyst from Wasted *Flint* Kaolin. *Fuel* **2013**, *103*, 626–631. [CrossRef]
26. Nascimento, L.A.S.; Angélica, R.S.; Costa, C.E.F.; Zamian, J.R.; Rocha Filho, G.N. Conversion of Waste Produced by the Deodorization of Palm Oil as Feedstock for the Production of Biodiesel Using a Catalyst Prepared from Waste Material. *Bioresour. Technol.* **2011**, *102*, 8314–8317. [CrossRef]
27. Lacerda Júnior, O.S.; Cavalcanti, R.M.; de Matos, T.M.; Angélica, R.S.; da Rocha Filho, G.N.; Barros, I.D.C.L. Esterification of Oleic Acid Using 12-Tungstophosphoric Supported in *Flint* Kaolin of the Amazonia. *Fuel* **2013**, *108*, 604–611. [CrossRef]
28. Maia, A.A.B.; Saldanha, E.; Angélica, R.S.; Souza, C.A.G.; Neves, R.F. The Use of Kaolin Wastes from the Amazon Region on the Synthesis of Zeolite A. *Cerâmica* **2007**, *53*, 319–324. [CrossRef]
29. Moraes, C.G.; Rodrigues, E.C.; Neves, R.F. Analcime Zeolite Production from Amazon Kaolin. *Cerâmica* **2013**, *59*, 563–569. [CrossRef]
30. Khayoon, M.S.; Hameed, B.H. Single-Step Esterification of Crude Karanj (*Pongamia Pinnata*) Oil to Fatty Acid Methyl Esters over Mesostructured SBA-16 Supported 12-Molybdophosphoric Acid Catalyst. *Fuel Process. Technol.* **2013**, *114*, 12–20. [CrossRef]
31. Oliveira, A.N.; Lima, M.A.B.; Pires, L.H.O.; Silva, M.R.; Luz, P.T.S.; Angélica, R.S.; Rocha Filho, G.N.; Costa, C.E.F.; Luque, R.; Nascimento, L.A.S. Bentonites Modified with Phosphomolybdic Heteropolyacid (HPMo) for Biowaste to Biofuel Production. *Materials* **2019**, *12*, 1431. [CrossRef] [PubMed]
32. Wang, H.; Liu, L.; Gong, S. Esterification of Oleic Acid to Biodiesel over a 12-Phosphotungstic Acid-Based Solid Catalyst. *J. Fuel Chem. Technol.* **2017**, *45*, 303–310. [CrossRef]
33. Carvalho, A.K.F.; Conceição, L.R.V.; Silva, J.P.V.; Perez, V.H.; de Castro, H.F. Biodiesel Production from *Mucor Circinelloides* Using Ethanol and Heteropolyacid in One and Two-step Transesterification. *Fuel* **2017**, *202*, 503–511. [CrossRef]
34. Conceição, L.R.V.; Carneiro, L.M.; Giordani, D.S.; de Castro, H.F. Synthesis of Biodiesel from Macaw Palm Oil Using Mesoporous Solid Catalyst Comprising 12-Molybdophosphoric Acid and Niobia. *Renew. Energy* **2017**, *113*, 119–128. [CrossRef]
35. Brahmkhatri, V.; Patel, A. An Efficient Green Catalyst Comprising 12-Tungstophosphoric Acid and MCM-41: Synthesis Characterization and Diesterification of Succinic Acid, a Potential Bio-platform Molecule. *Green Chem. Lett. Rev.* **2012**, *5*, 161–171. [CrossRef]
36. Clemente, M.C.H.; Martins, G.A.V.; de Freitas, E.F.; Dias, J.A.; Dias, S.C.L. Ethylene Production via Catalytic Ethanol Dehydration by 12-Tungstophosphoric Acid@ceria-Zirconia. *Fuel* **2019**, *239*, 491–501. [CrossRef]
37. Patel, A.; Brahmkhatri, V. Kinetic Study of Oleic Acid Esterification over 12-Tungstophosphoric Acid Catalyst Anchored to Different Mesoporous Silica Supports. *Fuel Process. Technol.* **2013**, *113*, 141–149. [CrossRef]
38. Brahmkhatri, V.; Patel, A. 12-Tungstophosphoric Acid Anchored to SBA-15: An Efficient, Environmentally Benign Reusable Catalysts for Biodiesel Production by Esterification of Free Fatty Acids. *Appl. Catal. A Gen.* **2011**, *403*, 161–172. [CrossRef]
39. Mongkolbovornkij, P.; Champreda, V.; Sutthisripok, W.; Laosiripojana, N. Esterification of Industrial-Grade Palm Fatty Acid Distillate over Modified ZrO₂ (with WO₃-, SO₄- and TiO₂-): Effects of Co-solvent Adding and Water Removal. *Fuel Process. Technol.* **2010**, *91*, 1510–1516. [CrossRef]
40. Da Conceição, R.L.V.; Carneiro, L.M.; Rivaldi, J.D.; de Castro, H.F. Solid Acid as Catalyst for Biodiesel Production via Simultaneous Esterification and Transesterification of Macaw Palm Oil. *Ind. Crop. Prod.* **2016**, *89*, 416–424. [CrossRef]
41. Akinfalabi, S.I.; Rashid, U.; Yunus, R.; Taufiq-Yap, Y.H. Synthesis of Biodiesel from Palm Fatty Acid Distillate Using Sulfonated Palm Seed Cake Catalyst. *Renew. Energy* **2017**, *111*, 611–619. [CrossRef]
42. Lokman, I.M.; Rashid, U.; Taufiq-Yap, Y.H. Production of Biodiesel from Palm Fatty Acid Distillate Using Sulfonated-Glucose Solid Acid Catalyst: Characterization and Optimization. *Chin. J. Chem. Eng.* **2015**, *23*, 1857–1864. [CrossRef]
43. Soltani, S.; Rashid, U.; Yunus, R.; Taufiq-Yap, Y.H. Biodiesel Production in the Presence of Sulfonated Mesoporous ZnAl₂O₄ Catalyst via Esterification of Palm Fatty Acid Distillate (PFAD). *Fuel* **2016**, *178*, 253–262. [CrossRef]

44. Embong, N.H.; Maniam, G.P.; Mohd, M.H.; Lee, K.T.; Huisingh, D. Utilization of Palm Fatty Acid Distillate in Methyl Esters Preparation Using $\text{SO}_4^{2-}/\text{TiO}_2\text{-SiO}_2$ as a Solid Acid Catalyst. *J. Clean. Prod.* **2016**, *116*, 244–248. [CrossRef]
45. Pantoja, S.S.; de Mescouto, V.A.; da Costa, C.E.F.; Zamian, J.R.; Zamian, J.R.; da Rocha Filho, G.N.; do Nascimento, L.A.S. High-Quality Biodiesel Production from Buriti (*Mauritia Flexuosa*) Oil Soapstock. *Molecules* **2019**, *24*, 94. [CrossRef]
46. Lima, R.P.; da Luz, P.T.S.; Braga, M.; dos Batista, P.R.S.; da Costa, C.E.F.; Zamian, J.R.; do Nascimento, L.A.S.; da Rocha Filho, G.N. Murumuru (*Astrocaryum Murumuru Mart.*) Butter and Oils of Buriti (*Mauritia Flexuosa Mart.*) and Pracaxi (*Pentaclethra Maculoba (Willd.) Kuntze*) can be Used for Biodiesel Production: Physico-Chemical Properties and Thermal and Kinetic Studies. *Ind. Crop. Prod.* **2017**, *97*, 536–544. [CrossRef]
47. Aboim, J.B.; de Oliveira, D.T.; Ferreira, J.E.; Siqueira, A.S.; Dall’Agnol, L.T.; da Rocha, G.N.; Gonçalves, E.C.; Nascimento, L.A.S. Determination of Biodiesel Properties Based on a Fatty Acid Profile of Eight Amazon Cyanobacterial Strains Grown in Two Different Culture Media. *RSC Adv.* **2016**, *6*, 109751–109758. [CrossRef]
48. De Oliveira, D.T.; Vasconcelos, C.; Feitosa, A.M.T.; Aboim, J.B.; de Oliveira, A.N.; Xavier, L.P.; Santos, A.S.; Gonçalves, E.C.; da Rocha Filho, G.N.; do Nascimento, L.A.S. Lipid Profile Analysis of Three New Amazonian Cyanobacteria as Potential Sources of Biodiesel. *Fuel* **2018**, *234*, 785–788. [CrossRef]
49. Aguiéiras, E.C.G.; Souza, S.L.; Langone, M.A.P. Study of Immobilized Lipase Lipozyme RM IM in Esterification Reactions for Biodiesel Synthesis. *Quim. Nova* **2013**, *36*, 646–650. [CrossRef]
50. Bastos, R.R.C.; da Luz Corrêa, A.P.; da Luz, P.T.S.; da Rocha Filho, G.N.; Zamian, J.R.; da Conceição, L.R.V. Optimization of Biodiesel Production Using Sulfonated Carbon-Based Catalyst from an Amazon Agro-Industrial Waste. *Energy Convers. Manag.* **2020**, *205*, 112457. [CrossRef]
51. Da Corrêa, A.P.L.; Bastos, R.R.C.; da Rocha Filho, G.N.; Zamian, J.R.; da Conceição, L.R.V. Preparation of Sulfonated Carbon-Based Catalysts from Murumuru Kernel Shell and Their Performance in the Esterification Reaction. *RSC Adv.* **2020**, *10*, 20245–20256. [CrossRef]
52. Wan, Z.; Lim, J.K.; Hameed, B.H. Chromium-Tungsten Heterogeneous Catalyst for Esterification of Palm Fatty Acid Distillate to Fatty Acid Methyl Ester. *J. Taiwan Inst. Chem. Eng.* **2015**, *54*, 64–70. [CrossRef]
53. Da Conceição, L.R.V.; Reis, C.E.R.; de Lima, R.; Cortez, D.V.; de Castro, H.F. Keggin-Structure Heteropolyacid Supported on Alumina to be Used in Trans/Esterification of High-Acid Feedstocks. *RSC Adv.* **2019**, *9*, 23450–23458. [CrossRef]
54. Aranda, D.A.G.; Santos, R.T.P.; Tapanes, N.C.O.; Ramos, A.L.D.; Antunes, O.A.C. Acid-Catalyzed Homogeneous Esterification Reaction for Biodiesel Production from Palm Fatty Acids. *Catal. Lett.* **2008**, *122*, 20–25. [CrossRef]
55. Peruzzolo, T.M.; Stival, J.F.; Baika, L.M.; Ramos, L.P.; Grassi, M.T.; Rocco, M.L.M.; Nakagaki, S. Efficient Esterification Reaction of Palmitic Acid Catalyzed by WO_3-x /Mesoporous Silica. *Biofuels* **2020**, 1–11. [CrossRef]
56. Wan, Z.; Hameed, B.H. Chromium-Tungsten-Titanium Mixed Oxides Solid Catalyst for Fatty Acid Methyl Ester Synthesis from Palm Fatty Acid Distillate. *Energy Convers. Manag.* **2014**, *88*, 669–676. [CrossRef]
57. Araujo, R.O.; da Char, J.S.; Queiroz, L.S.; da Rocha Filho, G.N.; da Costa, C.E.F.; da Silva, G.C.T.; Landers, R.; Costa, M.J.F.; Gonçalves, A.A.S.; de Souza, L.K.C. Low Temperature Sulfonation of Acai Stone Biomass Derived Carbons as Acid Catalysts for Esterification Reactions. *Energy Convers. Manag.* **2019**, *196*, 821–830. [CrossRef]
58. Olutoye, M.A.; Wong, C.P.; Chin, L.H.; Hameed, B.H. Synthesis of FAME from the Methanolysis of Palm Fatty Acid Distillate Using Highly Active Solid Oxide Acid Catalyst. *Fuel Process. Technol.* **2014**, *124*, 54–60. [CrossRef]
59. Chabukswar, D.D.; Heer, P.K.K.S.; Gaikar, V.G. Esterification of Palm Fatty Acid Distillate Using Heterogeneous Sulfonated Microcrystalline Cellulose Catalyst and Its Comparison with H_2SO_4 Catalyzed Reaction. *Eng. Chem. Res.* **2013**, *52*, 7316–7326. [CrossRef]
60. Wimonrat, T. Supported Cesium Polyoxotungstates as Catalysts for the Esterification of Palm Fatty Acid Distillate. *Mendeleev Commun.* **2013**, *23*, 46–48. [CrossRef]
61. Oliveira, C.F.; Dezaneti, L.M.; Garcia, F.A.C.; de Macedo, J.L.; Dias, J.A.; Dias, S.C.L.; Alvim, K.S.P. Esterification of Oleic Acid with Ethanol by 12-Tungstophosphoric Acid Supported on Zirconia. *Appl. Catal. A Gen.* **2010**, *372*, 153–161. [CrossRef]
62. Méndez, F.J.; Llanos, A.; Echeverría, M.; Jáuregui, R.; Villasana, Y.; Díaz, Y.; Liendo-Polanco, G.; Ramos-García, M.A.; Zoltan, T.; Brito, J.L. Mesoporous Catalysts Based on Keggin-Type Heteropolyacids Supported on MCM-41 and Their Application in Thiophene Hydrodesulfurization. *Fuel* **2013**, *110*, 249–258. [CrossRef]
63. Morey, M.S.; Bryan, J.D.; Schwarz, S.; Stucky, G.D. Pore Surface Functionalization of MCM-48 Mesoporous Silica with Tungsten and Molybdenum Metal Centers: Perspectives on Catalytic Peroxide Activation. *Chem. Mater.* **2000**, *12*, 3435–3444. [CrossRef]
64. Pacula, A.; Pamin, K.; Krysiak-Czerwenka, J.; Olejniczak, Z.; Gil, B.; Bielanska, E.; Dula, R.; Serwicka, E.M.; Drelinkiewicz, A. Physicochemical and Catalytic Properties of Hybrid Catalysts Derived from 12-Molybdophosphoric Acid and Montmorillonites. *Appl. Catal. A Gen.* **2015**, *498*, 192–204. [CrossRef]
65. Vazquez, P.G.; Blanco, M.N.; Caceres, C.V. Catalysts Based on Supported 12-Molybdophosphoric Acid. *Catal. Lett.* **1999**, *60*, 205–215. [CrossRef]
66. Melero, J.A.; Bautista, L.F.; Morales, G.; Iglesias, J.; Sánchez-Vázquez, R. Biodiesel Production from Crude Palm Oil Using Sulfonic Acid-Modified Mesostructured Catalysts. *Chem. Eng. J.* **2010**, *161*, 323–331. [CrossRef]
67. Melero, J.A.; Bautista, L.F.; Iglesias, J.; Morales, G.; Sánchez-Vázquez, R.; Wilson, K.; Lee, A.F. New Insights in the Deactivation of Sulfonic Modified SBA-15 Catalysts for Biodiesel Production from Low-Grade Oleaginous Feedstock. *Appl. Catal. A Gen.* **2014**, *488*, 111–118. [CrossRef]

Article

MgF₂-Modified Hydrotalcite-Derived Composites Supported Pt-In Catalysts for Isobutane Direct Dehydrogenation

Zhen Song, Jiameng Wang, Fanji Liu, Xiqing Zhang, Énio Matusse and Lihong Zhang *

Department of Catalysis Science and Technology and Tianjin Key Laboratory of Applied Catalysis Science & Technology, School of Chemical Engineering and Technology, Tianjin University, Tianjin 300350, China; songzhens12345@163.com (Z.S.); wangjiameng0216@163.com (J.W.); lfj19961018@163.com (F.L.); zhangxiqing1997@163.com (X.Z.); enio_matusse@outlook.com (É.M.)

* Correspondence: zlh_224@tju.edu.cn; Tel.: +86-150-2225-5828

Abstract: Here, a simple method was developed to prepare an MgF₂-modified hydrotalcite-derived composite, which was used as support for the Pt-In catalyst for isobutane direct dehydrogenation. The catalysts, composites, and their precursors were characterized by numerous characterization techniques. The results provided evidence for the MgF₂ promoter effect on the physical–chemical properties and dehydrogenation performance of the supported Pt-In catalysts. The catalyst with MgF₂ shows exceptional isobutene selectivity that can be stabilized at 95%, and the conversion increases from 50% to 58% during the reaction process. Moreover, the existence of MgF₂ plays an important role in the resistance to coke formation and Pt sintering by improving the Pt dispersion, inhibiting the reduction of the In³⁺ species, and adjusting the acidity of the catalyst.

Citation: Song, Z.; Wang, J.; Liu, F.; Zhang, X.; Matusse, É.; Zhang, L. MgF₂-Modified Hydrotalcite-Derived Composites Supported Pt-In Catalysts for Isobutane Direct Dehydrogenation. *Catalysts* **2021**, *11*, 478. <https://doi.org/10.3390/catal11040478>

Academic Editors: Juan Antonio Cecilia and Carmen Pilar Jiménez Gómez

Received: 16 March 2021
Accepted: 6 April 2021
Published: 8 April 2021

Publisher's Note: MDPI stays neutral with regard to jurisdictional claims in published maps and institutional affiliations.



Copyright: © 2021 by the authors. Licensee MDPI, Basel, Switzerland. This article is an open access article distributed under the terms and conditions of the Creative Commons Attribution (CC BY) license (<https://creativecommons.org/licenses/by/4.0/>).

Keywords: isobutane dehydrogenation; MgF₂ promoter; hydrotalcite-derived composites; supported Pt-In catalysts

1. Introduction

In recent years, the sharp increase in the global demand for olefins is driven by the rapid growth in the demand for downstream products in the world [1]. Additionally, isobutene, as a raw material of butyl rubber [2], polyisobutene, and other downstream products, has attracted a lot of attention. At present, the direct dehydrogenation of isobutane represents an environmentally friendly and cost-effective preparation method [3,4].

It is well known that Pt is the most effective active metal for dehydrogenation of light alkanes, but it is easy to sinter and has relatively poor stability [5,6]. Some metallic promoters, such as Sn [7–9], In [10–13], Cu [14], Zn [15,16], Ga [17,18], K [19,20], or Ge [21,22], are usually used to enhance the interaction with Pt from the electronic and geometric aspects so as to resist coke deposition, suppress Pt sintering, and improve the catalytic performance. In addition, the non-metallic promoters, involving element B [23], F [24,25], Cl [26], and P [27], are usually applied to adjust the acid sites and promote the dispersion of active sites on the surface of catalysts. In general, these promoters can not only modify the surrounding environment of the Pt active sites of catalyst, but also adjust some properties of the supports.

The support materials can also influence the catalytic performance, and a lot of studies have been conducted on the support materials, such as Al₂O₃ [9,28,29], MgO [30], SiO₂ [27,31], ZrO₂ [15,23,32], and spinel ZnAl₂O₄ [7,33,34], for isobutane dehydrogenation catalysts. Now, the focus has been switched to calcined hydrotalcite or hydrotalcite-like (HT) composites, which have been used in direct dehydrogenation of propane and have good performance compared to other supports [10–12]. Calcined hydrotalcite or hydrotalcite-like (HT) materials are the typical composite metal oxides [35–37]. These have suitable surface acidic characteristics and high specific surface area, which is conducive to

the adsorption of alkanes and the desorption of alkenes and enhances Pt particle dispersion. Among recent studies, some have reported that PtIn catalysts with calcined MgAl hydrotalcite-like as supports compared to spinel as supports exhibited high activity and better selectivity in propane dehydrogenation reaction processes [12]; others reported that Pt-based catalysts substituting Al with In cation on calcined hydrotalcite-like supports also displayed excellent performance of alkanes dehydrogenation [38]. In particular, as far as we know, no report discusses the catalytic performance of Pt-In catalysts supported on MgF₂-modified calcined hydrotalcite-like carriers in isobutane direct dehydrogenation.

In our work, we successfully synthesized the MgF₂-modified HT-derived composite supported Pt-In catalyst, which exhibited great catalytic performance. The synthesis process includes hydrothermal, alkali-etching, calcination, and impregnation of Pt and In precursors, together with calcination and reduction pretreatment. To discuss the relationships of the isobutane dehydrogenation performance of catalysts with the physicochemical properties, numerous characterization techniques were employed for the as-prepared and spent catalysts.

2. Results and Discussion

2.1. Characterization of Composite Supports and Catalysts

2.1.1. The X-Ray Diffraction (XRD)

Figure 1A,B shows the X-ray diffraction (XRD) patterns of the support composites and corresponding supported Pt-In catalysts with calcining and reducing treatment. The characteristic peaks of HT phase (JCPDS file No. 51-1525) are observed in the composites (Figure 1A). Obviously, the HT phase is the only crystalline phase for the reference HT composite. At the same time, an additional MgF₂ phase (JCPDS file No. 41-1443) can be detected in the HT-MgF₂ composite, followed by the decrease in HT diffraction peak intensity. After calcination and reduction (see Figure 1B), the diffraction peaks of the periclase MgO phase (JCPDS file No. 45-0946) appear. However, the diffraction peaks of the Pt and In species cannot be found. This arises from their small particle size and/or low concentration below XRD detection limit, indicating that Pt and In particles are well dispersed on the supports.

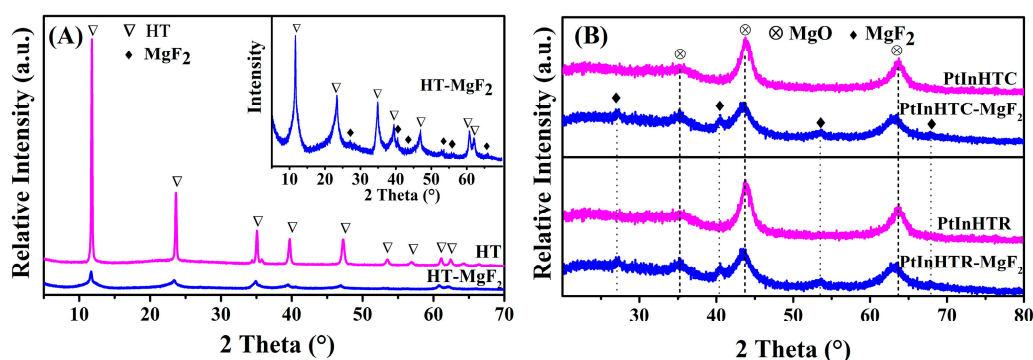


Figure 1. X-ray diffraction (XRD) patterns of (A) the support composites and (B) the calcined and reduced catalysts.

2.1.2. N₂-Adsorption–Desorption Isotherms

The textural properties of the catalysts were characterized by a low-temperature N₂ adsorption–desorption technique, and the results are depicted in Figure 2A,B. As shown in Figure 2A, the isotherms exhibit the type IV curves with the H2 hysteresis loops indicating the characteristics of the hierarchical mesoporous structure. The corresponding pore size distributions are broad and mainly concentrated in the range of 3–30 nm, further confirming the hierarchical mesoporous feature. Compared with the textural properties of PtInHTC, PtInHTC-MgF₂ exhibits an increase in S_{BET} of 216 m²·g^{−1}, D_p of 4.9 and 12.3 nm and V_p. Additionally, the S_{BET} of PtInHTC-MgF₂ is higher than that of the previous

dehydrogenation catalysts [13,38,39]. This means that the pore channel of PtInHTC-MgF₂ can provide more surface and space for adsorption and reaction of isobutane.

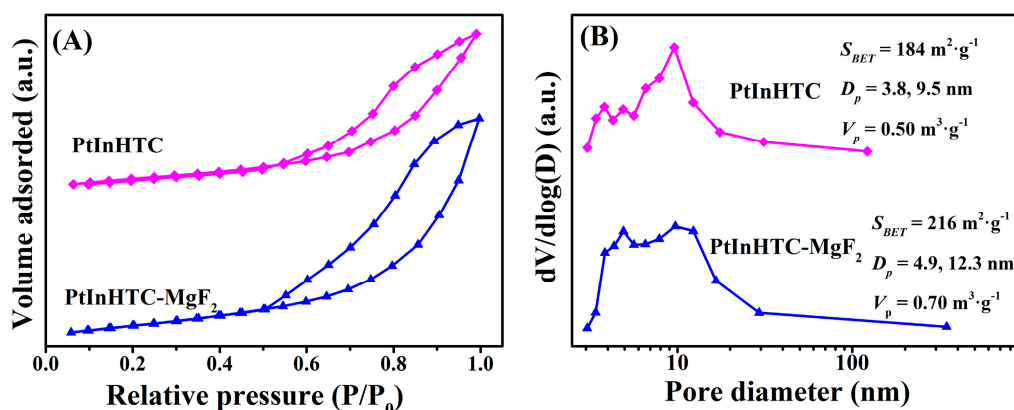


Figure 2. (A) Low temperature N₂ adsorption–desorption isotherms, (B) pore size distributions curves, and textural data of the calcined catalysts, involving BET special surface area (S_{BET}), the most probable pore size determined by the BJH method (D_p), and total pore volume (V_p).

2.1.3. The Scanning Electron Microscopy (SEM) and the Transmission Electron Microscopy (TEM)

The morphologies of calcined catalysts are described by SEM images in Figure 3. Overall, the typical mesoporous morphology can be found for these composites. The calcined sample PtInHTC without MgF₂ mainly presents the large block mass particles [11]. The catalyst PtInHTC-MgF₂ shows that the abundant well-defined triangular pore channels are constructed by intersecting nanosheets. This means that the MgF₂ plays a key role in tuning the morphology and pore structure of catalysts. The main reason is that the presence of F⁻ anions can activate the substrates to liberate more metal ions for nucleation and growth to obtain interconnected nanosheets in the synthesis process [40]. Figure 3C–F gives TEM images and particle size distribution (PSD) of the reduced catalysts. Their PSD are narrow, and the Pt (111) plan from Pt particles can be found on the reduced catalysts according to the lattice spacing of 0.226 nm, although there is no peak of metal Pt in the XRD phase (Figure 1B). These indicate the metal particles are well dispersed on these catalysts. It is important to point out that the average particle size decreases from 1.3 nm of PtInHTR to 1.2 nm of PtInHTR-MgF₂, with a simultaneous narrowing of PSD. This can be attributed to the additional dispersion effect of MgF₂ on active metals. The small size of active metals is more favorable for the dehydrogenation reaction because the small active metals are less active for cracking reaction and deep dehydrogenation [41].

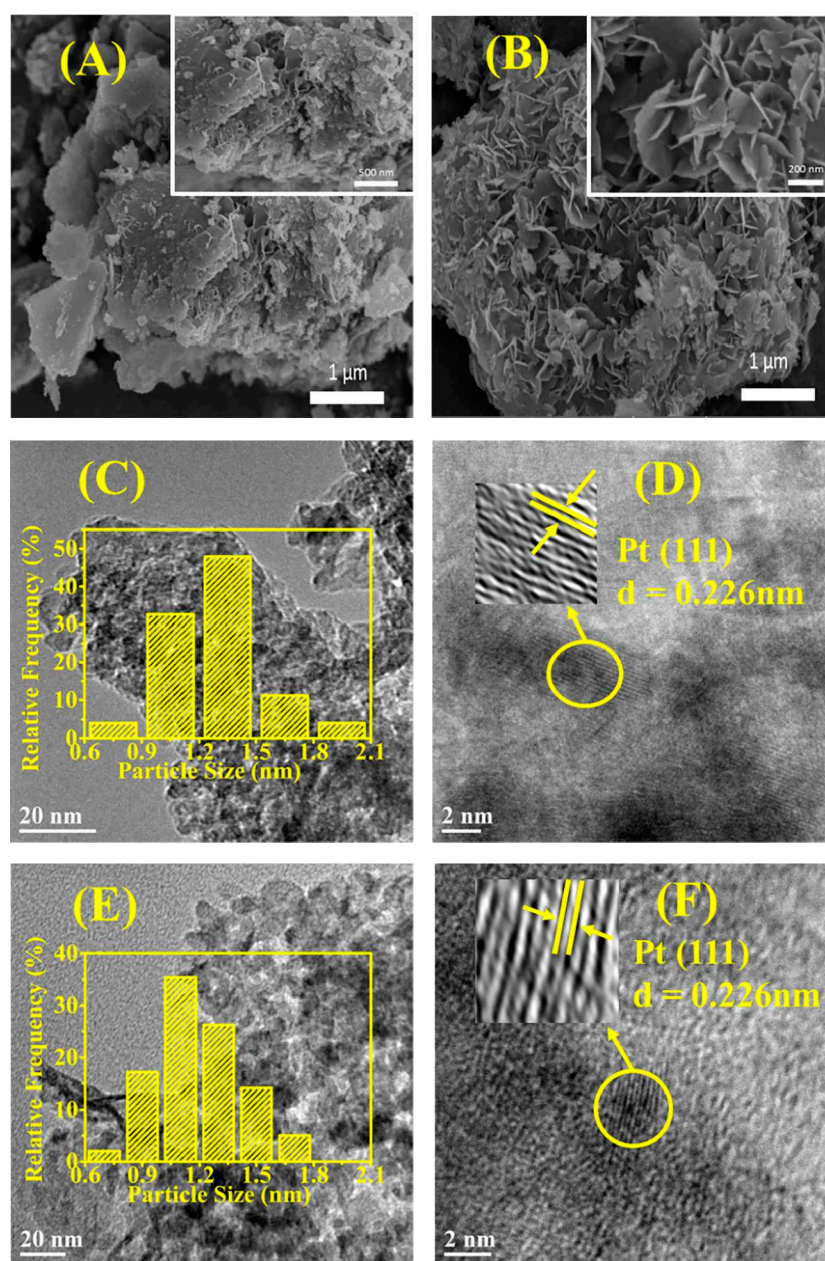


Figure 3. SEM images of PtInHTC (A) and PtInHTC-MgF₂ (B), TEM micrographs of catalysts PtInHTC (C,D), and PtInHTC-MgF₂ (E,F).

2.1.4. The Temperature-Programmed Reduction (H₂-TPR)

The H₂-TPR results in Figure 4 show the reducibility of catalysts PtInHTC and PtInHTC-MgF₂. It can be clearly seen that the catalyst PtInHTC exhibits a wide reduction peak with the maximum value at 466 °C (peak I) and shoulder peak at 560 °C (peak II), while the three relative separated peaks are mainly at 460 °C (peak I), 550 °C (peak II), and 634 °C (peak III) for catalyst PtInHTC-MgF₂. According to the previous literature [12,42,43], peak I is attributed to the reduction of PtO₂, and peak II can be related to the co-reduction of the Pt and In species. The formation of the peak III may be due to the removal of a small amount of surface hydroxyl. In addition, it can be found that the lower reduction temperature of peak I and peak II can be obtained for the catalyst PtInHTC-MgF₂. This indicates that the formation of MgF₂ can reduce the reduction temperature of the Pt species to a certain extent. In other words, the weaker interaction between the Pt species and

supports can be achieved when the MgF_2 species modified the supports. Additionally, it can be seen that the Pt species can be reduced before $600\text{ }^\circ\text{C}$ for two catalysts.

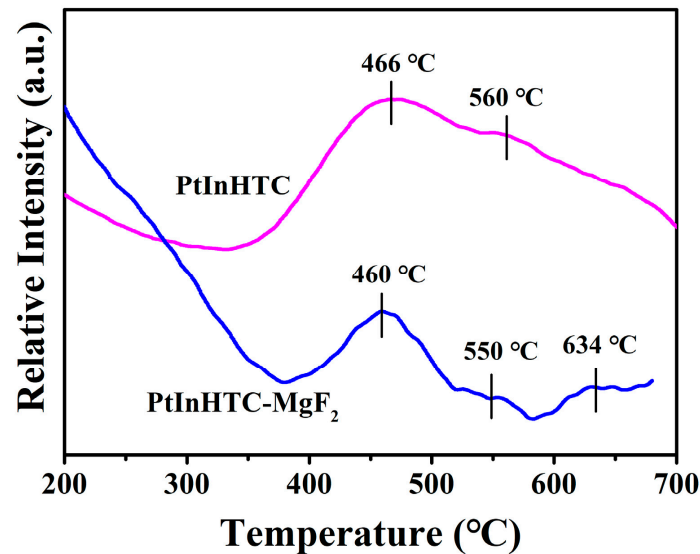


Figure 4. H_2 -TPR profiles of the catalysts.

2.1.5. X-Ray Photoelectron Spectroscopy (XPS)

The surface elemental compositions and chemical states of In, Mg, and F elements on the reduced catalysts were analyzed using X-ray photoelectron spectroscopy (XPS), and the XPS spectra of whole survey, In 3d, Mg 1s, and F 1s regions are shown in Figure 5, with a summary of the binding energy (BE) and ratio of $\text{In}^{3+}/\text{In}^0$ for the samples in Table 1.

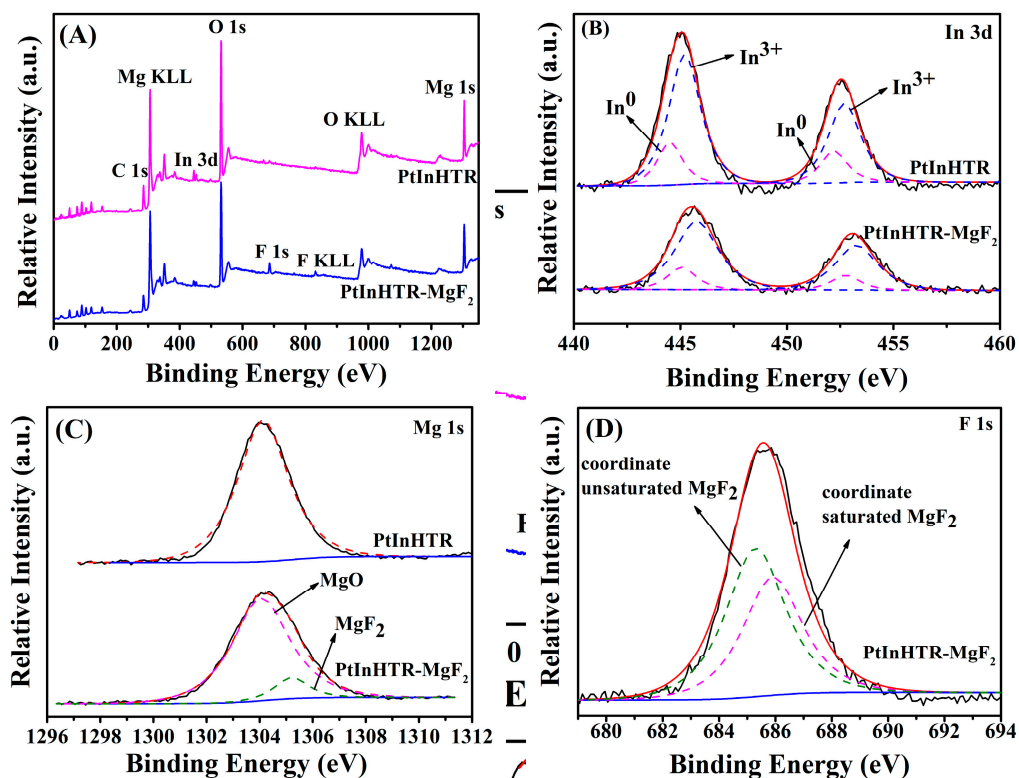


Figure 5. X-ray photoelectron spectroscopy (XPS) spectrum of (A) the whole survey, (B) In 3d, (C) Mg 1s, and (D) F 1s for the reduced catalysts.

Table 1. XPS results of the In 3d regions for the reduced catalysts.

Samples	Binding Energy (eV)				In ³⁺ /In ⁰ ^a
	In 3d _{5/2}		In 3d _{3/2}		
	In ⁰	In ³⁺	In ⁰	In ³⁺	
PtInHTR	444.5	445.2	452.2	452.7	3.5
PtInHTR-MgF ₂	444.5	445.2	452.2	452.7	4.2

^a Calculated from the corresponding fitting peak area.

In Figure 5A, it can be seen that the F element is exactly detectable in PtInHTR-MgF₂, compared with the sample PtInHTR. According to the results of XRD above, this further demonstrates the existence of MgF₂ on PtInHTR-MgF₂. To explore the metal-support interaction in depth, the XPS spectra are mainly focused on the In 3d regions instead of the Pt 4f regions owing to the overlapping of the Pt 4f and Al 2p region peaks [44]. As shown in Figure 5B, the broad In 3d peak in the range of 440–460 eV can be deconvoluted into four peaks, which refer to two In species on the surface of PtInHTR-MgF₂. The low BE value is attributed to the zero-valent In (In⁰), and the high BE is ascribed to the oxidation state of the surface In species (In³⁺). As listed in Table 1, the ratio of In³⁺/In⁰ of PtInHTR-MgF₂ is higher than that of PtInHTR, indicating that the presence of MgF₂ can inhibit the reduction of In³⁺ ions on the surface to avoid the formation of a PtIn alloy. Compared with PtInHTR and PtInHTR-MgF₂, the same BE values for the different In species indicate that there is no electron transfer between the In species and MgF₂. Accordingly, it can be deduced that the smaller amount of In⁰ species should be due to the coverage of MgF₂ resulting in the difficult reduction of In³⁺ species. Usually, it is proposed that the In³⁺ species are favorable to dehydrogenation reaction, in view of the blockage of the active Pt sites by the In⁰ species [10,13,45].

Then, Figure 5C illustrates the Mg 1s XPS spectra of the samples, and it can be observed that Mg species present in two chemical states. The peaks appearing at BE of 1304.1 eV and 1305.2 eV can be attributed to MgO and MgF₂ species in the reduced catalysts, respectively [46]. Moreover, according to the deconvolution of the spectra of F 1s (in Figure 5D), we can see two relevant fitted peaks, representing two different coordination states of the F species. The peak of F 1s at 686.0 eV comes from the saturated MgF₂, and the peak with BE of 685.4 eV is attributed to F bound to under-coordinated Mg, namely, four- and five-fold coordinated, which is responsible for the Lewis acid sites [47]. Usually, the small MgF₂ particles are deemed to be the reason of the formation of the under-coordinated Mg and even weak acid sites [47]. However, the weak acid sites are favorable for coking-resistance in the dehydrogenation reaction. Therefore, it is reasonable to conclude that the formation of MgF₂, especially the under-coordinated Mg species in MgF₂, significantly affects the acidity and stability of catalysts and facilitates the resistance to coking and sintering.

2.2. Catalytic Dehydrogenation Performance of Catalysts

Figure 6 depicts the isobutane conversion, isobutene yield, and selectivity of isobutene and by-product methane over the reduced catalysts in the isobutane dehydrogenation reaction for 9 h. As can be seen from Figure 6A, the catalysts PtInHTR and PtInHTR-MgF₂ exhibit a rapid loss in conversion during the first 30 min and then attain a period of stable conversion throughout the dehydrogenation test. In detail, the catalyst PtInHTR gives the lowest conversion, while the conversion of PtInHTR-MgF₂ increases from 50% to 58% within 9 h. That is to say, the formation of MgF₂ really enhances the activity of the catalysts. It can be assigned to the special pore channels and surface features. From Figure 6B, it can be found that the isobutene selectivity of the catalyst PtInHTR-MgF₂ can be stabilized at 95% during the reaction process. Correspondingly, the catalyst PtInHTR exhibits declining isobutene selectivity. In addition, the selectivity of by-product methane is less than 5% and much lower than the corresponding isobutene selectivity. In particular, for catalyst PtInHTR-MgF₂ the by-product methane is almost completely inhibited during the reaction.

This indicates that the MgF_2 -modification can inhibit the cracking reaction and improve the selectivity and stability of catalysts. Additionally, it is clear that the isobutene yield of PtInHTR- MgF_2 is no less than 55% and is much higher than that of PtInHTR. The excellent catalytic dehydrogenation performance is closely related to the properties of the active species, promoters, and supports. The small size of Pt particles [48], stable In_2O_3 state [10,45], and suitable acidic properties of the supports [49] on catalysts can greatly improve the activity and selectivity of the catalyst. According to the TEM and XPS analysis above, PtInHTR- MgF_2 has a small active metal particle size, a stable chemical state of the In^{3+} species, and abundant weak acid sites, which are responsible for resistance to coking and sintering. Therefore, PtInHTR- MgF_2 exhibited high activity and stable selectivity.

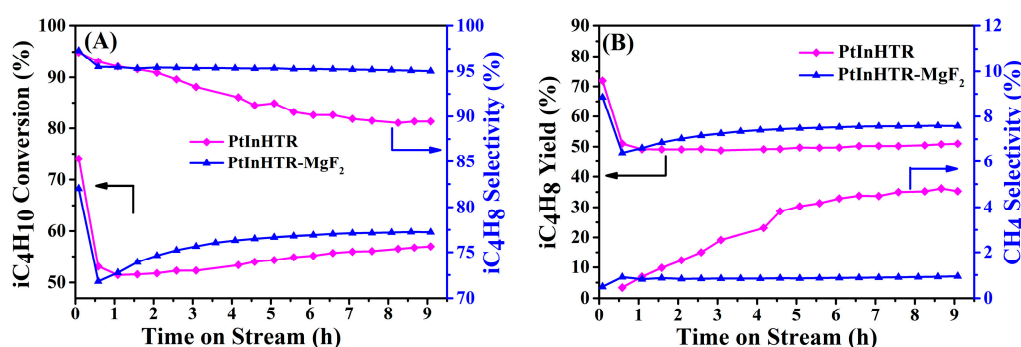


Figure 6. (A) Isobutane conversion and isobutene selectivity, (B) isobutene yield and by-product methane selectivity as functions of time. (Reaction conditions: 600 °C, 1 atm, $\text{H}_2:i\text{C}_4\text{H}_{10} = 1:1$ (molar ratio), $\text{WHSV} (i\text{C}_4\text{H}_{10}) = 3 \text{ h}^{-1}$, $m_{\text{cat}} = 0.5 \text{ g}$).

In view of the superior dehydrogenation performance of PtInHTR- MgF_2 , the detailed information compared with previously reported catalysts is collected in Table 2. In terms of conversion and selectivity, it demonstrates that the investigation of the catalyst PtInHTR- MgF_2 is meaningful.

Table 2. Comparison of catalytic performance of various catalysts in isobutane dehydrogenation ^a.

Catalysts	Pt Contents (wt%)	WHSV (h^{-1})	Isobutane Conversion (%) ^b	Isobutene Selectivity (%) ^b	References
PtInHTR- MgF_2	0.5	3	50–58	96–95	Present work
InPtSn/ ZnAl_2O_4	0.4	4	54–38	94–96	[33]
PtNi/ $\text{LaFeO}_3/\text{SiO}_2$	0.3	3	39–39	84–91	[39]
PtSnKMg/ Al_2O_3	0.5	2	34–29	80–95	[50]
PtSnKZn/ Al_2O_3	0.5	2	36–32	96–96	[51]
PtSnNa/ZSM-5	0.5	2.5	52–52	84–84	[52]

^a From the considered articles, only the best catalytic performance is indexed. ^b Two data are recorded from the initial and the end stage, respectively.

2.3. Characterization of the Spent Catalysts

2.3.1. Thermogravimetric Analysis (TG-DTA) and the X-ray Diffraction (XRD)

According to the TG curves in Figure 7A, the total mass losses of PtInHTU and PtInHTU- MgF_2 are 60% and 17%, respectively. As expected, the coke deposition can be suppressed by forming MgF_2 micro-crystals. The positive anti-coking ability is mainly related to the small active metals particles and weak acid sites supplied by MgF_2 nanoparticles over PtInHTR- MgF_2 . From the differential thermal analysis(DTA) peaks of the spent PtInHTU, it can be determined that there are two successive coke combustion regions, representing two different coke deposits. The small DTA peak at the low temperature range is assigned to the amorphous coke, while the big peak at a high temperature of 570 °C corresponds to the formation of serious graphitized coke [53]. Interestingly, only a small DTA peak, resulting from the combustion of amorphous coke, can be detected

for PtInHTU-MgF₂. This suggests that it is more difficult for the active metal sites on PtInHTU-MgF₂ to be fully covered by the coke deposits and easier to be regenerated than those on PtInHTU. Additionally, from the XRD patterns shown in Figure 7B, the diffraction peaks of carbon at 2θ of 26° can be detected for the PtInHTU catalyst, but it is not detected on the PtInHTU-MgF₂ catalyst. This explains that there is a large amount of carbon on the catalyst PtInHTU catalyst, which is also consistent with the TG results.

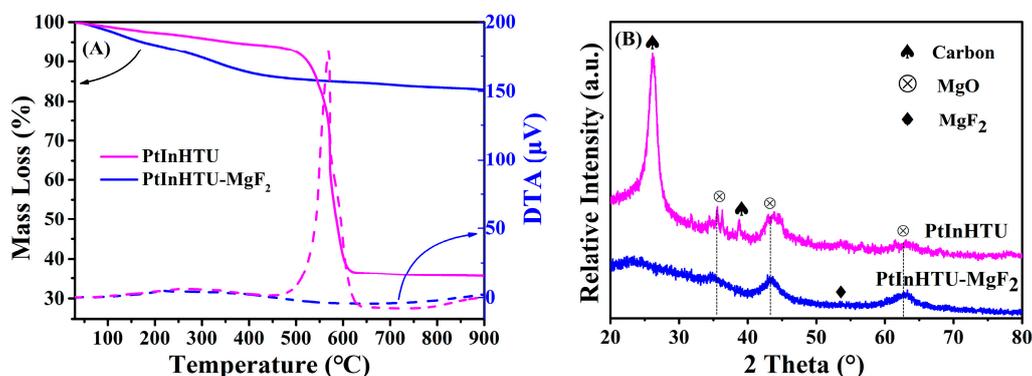


Figure 7. Thermogravimetric Analysis (TG-DTA) curves (A) and XRD patterns (B) of the spent catalysts.

2.3.2. SEM and TEM

The formation of coke deposits also can be confirmed by the SEM and TEM images of the spent catalysts (see Figure 8). Firstly, typical flake mesoporous materials can be kept for each spent catalyst, suggesting that there is no significant texture change for these catalysts after reaction. Additionally, more graphitized coke can be seen on the surface of PtInHTU. As expected, only the granular amorphous coke deposits can be seen on PtInHTU-MgF₂, which is consistent with the TG results. By analyzing the particle size distribution of the spent catalysts, it can be found that the average diameters of PtInHTU and PtInHTU-MgF₂ has a slight increase from 1.3 to 2.7 nm and 1.2 to 2.1 nm, respectively. This demonstrates that the anti-sintering ability can be enhanced by introducing the MgF₂ species.

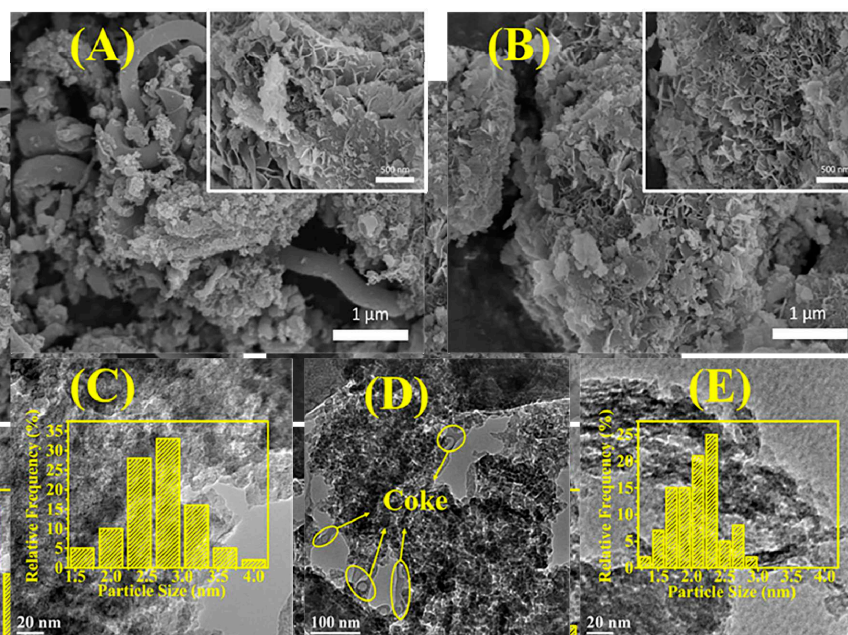


Figure 8. SEM images of spent catalysts: (A) PtInHTU, (B) PtInHTU-MgF₂; TEM micrographs of spent catalysts (C,D) PtInHTU, (E) PtInHTU-MgF₂.

3. Materials and Methods

3.1. Materials Used

Mg(NO₃)₂·6H₂O (Analytical grade chemicals, Fuchen Chemical Regents Factory, Tianjin, China), Al(NO₃)₃·9H₂O (Analytical grade chemicals, Fuchen Chemical Regents Factory, Tianjin, China), urea (Analytical grade chemicals, Fuchen Chemical Regents Factory, Tianjin, China), SiO₂ (>98%, TANSAIL Advanced Materials Co. Ltd., Nanjing, China), KF (Analytical grade chemicals, Aladdin Industrial Corporation, Shanghai, China), H₂PtCl₆·6H₂O (Analytical grade chemicals, Mascot Chemical Co. Ltd., Tianjin, China), In(NO₃)₃·xH₂O (Analytical grade chemicals, Aladdin Industrial Corporation, Shanghai, China).

3.2. Synthesis of Composites and Precursors

The HT-MgF₂ precursors were prepared by using the hydrothermal and alkali-etching method. Firstly, 0.2 g SiO₂, 0.02 mol KF, 2.31 g Mg(NO₃)₂·6H₂O, 1.69 g Al(NO₃)₃·9H₂O, and 2.7 g urea were dissolved into 65 mL deionized water and stirred vigorously for 30 min. Then, the mixed solution was poured in a 100 mL Teflon autoclave and maintained at 100 °C for 20 h. The as-prepared product was filtered, washed with deionized water to neutrality, and dried in air at 100 °C overnight. Finally, 1 g the dried sample was put into 50 mL NaOH solution (1 mol·L⁻¹) and stirred for 10 h. The resulting suspension was washed with deionized water to pH = 7, and the solid product was dried overnight at 100 °C. The obtained precursor was labeled as HT-MgF₂.

The HT samples were prepared under same conditions, except without adding 0.02 mol KF into the initial solution. The corresponding precursor was named as HT.

3.3. Synthesis of Catalysts

The calcined products were acquired by calcining at 600 °C for 4 h with a heating rate of 2 °C·min⁻¹. The corresponding PtInHTC-MgF₂ catalyst was obtained via the stepwise incipient wetness impregnation method. Firstly, the In-based precursor was obtained by impregnating calcined HT-MgF₂ with In(NO₃)₃·xH₂O aqueous solution at room temperature for 6 h and dried at 120 °C for 12 h. After that, the solid was calcined at 550 °C for 4 h. At the same time, the same procedure as In impregnation was conducted to introduce the Pt species using H₂PtCl₆·H₂O as a precursor, except for an impregnation time of 2 h. The loading amount of Pt and In was 0.5 wt% and 1.4 wt%, respectively. After drying and calcination, the resulting solids were defined as PtInHTC-MgF₂. PtInHTC was prepared in a same manner.

The calcined catalysts were reduced by 5 vol% H₂/N₂ at a flow rate of 30 mL·min⁻¹ and 600 °C for 2 h with a heating rate of 5 °C·min⁻¹ to obtain the corresponding reduced catalysts, which were labeled as PtInHTR and PtInHTR-MgF₂.

After the reaction of isobutane dehydrogenation to isobutene, the spent catalysts were marked as PtInHTU and PtInHTU-MgF₂.

3.4. Precursors, Composites and Catalysts Characterization

The XRD patterns of samples were collected on a Bruker D8-Focus X-ray diffractometer (Germany) equipped with a Cu K α radiation ($\lambda = 0.15418$ nm).

Low-temperature N₂ adsorption–desorption tests were carried on a TriStar 3000 micromeritics apparatus (Micromeritics, Norcross, GA, USA).

The scanning electron microscopy (SEM) images were obtained using a MAIA3 TESAN.

The transmission electron microscopy (TEM) morphologies were observed on a JEM-2100F field-emission transmission electron microscope.

The temperature-programmed reduction (H₂-TPR) was carried out by automatic multi-purpose adsorption apparatus (tp 5080 XQINSTRUMENT CO., Tianjin, China).

The X-ray photoelectron spectra (XPS) of catalysts were tested on a Thermo ESCALAB 250Xi (US) using Al K α radiation.

Thermogravimetric analysis (TG-DTA) was carried out on a DTG-50/50H (PerkinElmer, Waltham, MA, USA).

3.5. Catalytic Dehydrogenation Performance Test

The isobutane dehydrogenation to isobutene reactions were performed in a fixed-bed continuous-flow reactor at 600 °C under atmospheric pressure. The calcined catalyst (0.5 g, 40–60 mesh) was placed into the reactor and reduced at 600 °C for 2 h with a heating rate of 5 °C·min⁻¹ in 5 vol% H₂/N₂. After reduction, the isobutane and hydrogen (the molar ratio of iC₄H₁₀:H₂ = 1:1) were introduced into the reactor, in which the weight hourly space velocity (WHSV) of isobutane was 3 h⁻¹. The reactions were performed at 600 °C, and an online gas chromatograph (GC) equipped with a flame ionization detector (Al₂O₃ packed column) was employed to analyze the gaseous products.

4. Conclusions

In summary, the MgF₂-modified hydrotalcite-derived composites supported Pt-In catalyst PtInHTR-MgF₂ can be synthesized by a combination of the hydrothermal method, alkali-etching, and impregnation strategy. The formation of MgF₂ can not only construct the special texture and morphology of catalyst, but also disperse the active metals, inhibit the reduction of the In³⁺ species, and adjust the acidity of the catalyst. These features can improve the activity and selectivity of isobutane direct dehydrogenation and make the catalyst obtain a high durability and excellent resistance to coking and sintering.

Author Contributions: Conceptualization, Z.S. and J.W.; methodology and experiments, Z.S. and J.W.; Statistics and data validation, Z.S. and É.M.; writing—original draft preparation, Z.S.; writing—review and editing, F.L. and X.Z.; research ideas, analyzed data, revised the manuscript and funding acquisition, L.Z. All authors have read and agreed to the published version of the manuscript.

Funding: This research was funded by the National Natural Science Foundation of China (21776214).

Institutional Review Board Statement: Not applicable.

Informed Consent Statement: Not applicable.

Data Availability Statement: Data is contained within the article.

Conflicts of Interest: The authors declare no conflict of interest.

References

- Zhu, G.; Li, P.; Zhao, F.; Song, H.; Xia, C. Selective aromatization of biomass derived diisobutylene to p-xylene over supported non-noble metal catalysts. *Catal. Today* **2016**, *276*, 105–111. [CrossRef]
- Sharma, R.K.; Mohanty, S.; Gupta, V. Advances in butyl rubber synthesis via cationic polymerization: An overview. *Polym. Int.* **2021**. [CrossRef]
- Chen, C.; Zhang, S.M.; Wang, Z.; Yuan, Z.Y. Ultrasmall Co confined in the silanols of dealuminated beta zeolite: A highly active and selective catalyst for direct dehydrogenation of propane to propylene. *J. Catal.* **2020**, *383*, 77–87. [CrossRef]
- Chen, C.; Sun, M.L.; Hu, Z.P.; Ren, J.T.; Zhang, S.M.; Yuan, Z.Y. New insight into the enhanced catalytic performance of ZnPt/HZSM-5 catalysts for direct dehydrogenation of propane to propylene. *Catal. Sci. Technol.* **2019**, *9*, 1979–1988. [CrossRef]
- Hill, J.M.; Cortright, R.D.; Dumesic, J.A. Silica- and L-zeolite-supported Pt, Pt/Sn and Pt/Sn/K catalysts for isobutane dehydrogenation. *Appl. Catal. A* **1998**, *168*, 9–21. [CrossRef]
- Ohta, M.; Ikeda, Y.; Igarashi, A. Additive effect on properties of Pt/ZnO catalyst for dehydrogenation of isobutane at low temperatures. *J. Jpn. Petrol. Inst.* **2002**, *45*, 150–155. [CrossRef]
- Miura, H.; Itoh, T. Selective deposition of Sn on the Pt surface of Pt/ZnAl₂O₄ catalyst and addition effect on isobutane dehydrogenation. *React. Kinet. Catal. Lett.* **1999**, *66*, 189–194. [CrossRef]
- Rashidi, M.; Nikazar, M.; Rahmani, M.; Mohamadghasemi, Z. Kinetic modeling of simultaneous dehydrogenation of propane and isobutane on Pt-Sn-K/Al₂O₃ catalyst. *Chem. Eng. Res. Des.* **2015**, *95*, 239–247. [CrossRef]
- Zangeneh, F.T.; Sahebdehfar, S.; Bahmani, M. Propane Dehydrogenation over a Commercial Pt-Sn/Al₂O₃ Catalyst for Isobutane Dehydrogenation: Optimization of Reaction Conditions. *Chin. J. Chem. Eng.* **2013**, *21*, 730–735. [CrossRef]
- Tolek, W.; Suriye, K.; Prasertdam, P.; Panpranot, J. Enhanced stability and propene yield in propane dehydrogenation on PtIn/Mg(Al)O catalysts with various In loadings. *Top. Catal.* **2018**, *61*, 1624–1632. [CrossRef]
- Li, J.; Zhang, M.; Song, Z.; Liu, S.; Wang, J.; Zhang, L. Hierarchical PtIn/Mg(Al)O derived from reconstructed PtIn-hydrotalcite-like compounds for highly efficient propane dehydrogenation. *Catalysts* **2019**, *9*, 767. [CrossRef]
- Xia, K.; Lang, W.; Li, P.; Long, L.; Yan, X.; Guo, Y. The influences of Mg/Al molar ratio on the properties of PtIn/Mg(Al)O-x catalysts for propane dehydrogenation reaction. *Chem. Eng. J.* **2016**, *284*, 1068–1079. [CrossRef]

13. Xia, K.; Lang, W.; Li, P.; Yan, X.; Guo, Y. The properties and catalytic performance of PtIn/Mg(Al)O catalysts for the propane dehydrogenation reaction: Effects of pH value in preparing Mg(Al)O supports by the co-precipitation method. *J. Catal.* **2016**, *338*, 104–114. [CrossRef]
14. Ma, Z.; Wu, Z.; Miller, J.T. Effect of Cu content on the bimetallic Pt-Cu catalysts for propane dehydrogenation. *Catal. Struct. React.* **2017**, *3*, 43–53. [CrossRef]
15. Liu, Y.; Xia, C.; Wang, Q.; Zhang, L.; Huang, A.; Ke, M.; Song, Z. Direct dehydrogenation of isobutane to isobutene over Zn-doped ZrO₂ metal oxide heterogeneous catalysts. *Catal. Sci. Technol.* **2018**, *8*, 4916–4924. [CrossRef]
16. Silvestre-Albero, J.; Sanchez-Castillo, M.A.; He, R.; Sepulveda-Escribano, A.; Rodriguez-Reinoso, F.; Dumesic, J.A. Microcalorimetric, reaction kinetics and DFT studies of Pt-Zn/X-zeolite for isobutane dehydrogenation. *Catal. Lett.* **2001**, *74*, 17–25. [CrossRef]
17. Siddiqi, G.; Sun, P.; Galvita, V.; Bell, A.T. Catalyst performance of novel Pt/Mg(Ga)(Al)O catalysts for alkane dehydrogenation. *J. Catal.* **2010**, *274*, 200–206. [CrossRef]
18. Wang, T.; Jiang, F.; Liu, G.; Zeng, L.; Zhao, Z.J.; Gong, J.L. Effects of Ga doping on Pt/CeO₂-Al₂O₃ catalysts for propane dehydrogenation. *AIChE J.* **2016**, *62*, 4365–4376. [CrossRef]
19. Yang, K.; Yin, Y.; Lai, S.; Zhu, L.; Zhang, J.; Lai, W.; Lian, Y.; Fang, W. Aromatization of n-Butane and i-Butane over PtSnK/ZSM-5 Catalysts: Influence of SiO₂/Al₂O₃ Ratio. *Catal. Lett.* **2018**, *148*, 3570–3582. [CrossRef]
20. Li, Q.; Yang, G.B.; Wang, K.; Wang, X.T. Preparation of carbon-doped alumina beads and their application as the supports of Pt-Sn-K catalysts for the dehydrogenation of propane. *React. Kinet. Mech. Catal.* **2020**, *129*, 805–817. [CrossRef]
21. Ballarini, A.D.; de Miguel, S.R.; Castro, A.A.; Scelza, O.A. n-Decane dehydrogenation on Pt, PtSn and PtGe supported on spinels prepared by different methods of synthesis. *Appl. Catal. A* **2013**, *467*, 235–245. [CrossRef]
22. Rimaz, S.; Chen, L.W.; Kawi, S.; Borgna, A. Promoting effect of Ge on Pt-based catalysts for dehydrogenation of propane to propylene. *Appl. Catal. A* **2019**, *588*, 117266. [CrossRef]
23. Ji, Z.H.; Miao, D.Y.; Gao, L.J.; Pan, X.L.; Bao, X.H. Effect of pH on the catalytic performance of PtSn/B-ZrO₂ in propane dehydrogenation. *Chin. J. Catal.* **2020**, *41*, 719–729. [CrossRef]
24. Wu, G.; Wang, X.; Wei, W.; Sun, Y. Fluorine-modified Mg-Al mixed oxides: A solid base with variable basic sites and tunable basicity. *Appl. Catal. A* **2010**, *377*, 107–113. [CrossRef]
25. Wu, G.; Wang, X.; Chen, B.; Li, J.; Zhao, N.; Wei, W.; Sun, Y. Fluorine-modified mesoporous Mg-Al mixed oxides: Mild and stable base catalysts for O-methylation of phenol with dimethyl carbonate. *Appl. Catal. A* **2007**, *329*, 106–111. [CrossRef]
26. Liu, J.; Liu, C.; Ma, A.; Rong, J.; Da, Z.; Zheng, A.; Qin, L. Effects of Al₂O₃ phase and Cl component on dehydrogenation of propane. *Appl. Surf. Sci.* **2016**, *368*, 233–240. [CrossRef]
27. Zhu, Q.; Zhang, H.; Zhang, S.; Wang, G.; Zhu, X.; Li, C. Dehydrogenation of isobutane over a Ni-P/SiO₂ catalyst: Effect of P addition. *Ind. Eng. Chem. Res.* **2019**, *58*, 7834–7843. [CrossRef]
28. Matveyeva, A.N.; Wärnå, J.; Pakhomov, N.A.; Murzin, D.Y. Kinetic modeling of isobutane dehydrogenation over Ga₂O₃/Al₂O₃ catalyst. *Chem. Eng. J.* **2020**, *381*, 122741. [CrossRef]
29. Dong, A.H.; Wang, K.; Zhu, S.Z.; Yang, G.B.; Wang, X.T. Facile preparation of PtSn-La/Al₂O₃ catalyst with large pore size and its improved catalytic performance for isobutane dehydrogenation. *Fuel Process. Technol.* **2017**, *158*, 218–225. [CrossRef]
30. Sun, G.; Huang, Q.; Li, H.; Liu, H.; Zhang, Z.; Wang, X.; Wang, Q.; Wang, J. Different supports-supported Cr-based catalysts for oxidative dehydrogenation of isobutane with CO₂. *Chin. J. Catal.* **2014**, *32*, 1424–1429. [CrossRef]
31. Deng, L.D.; Zhou, Z.J.; Shishido, T. Behavior of active species on Pt-Sn/SiO₂ catalyst during the dehydrogenation of propane and regeneration. *Appl. Catal. A* **2020**, *606*, 117826. [CrossRef]
32. Otroshchenko, T.P.; Kondratenko, V.A.; Rodemerck, U.; Linke, D.; Kondratenko, E.V. Non-oxidative dehydrogenation of propane, n-butane, and isobutane over bulk ZrO₂-based catalysts: Effect of dopant on the active site and pathways of product formation. *Catal. Sci. Technol.* **2017**, *7*, 4499–4510. [CrossRef]
33. Liu, J.; Zhou, W.; Jiang, D.; Wu, W.; Miao, C.; Wang, Y.; Ma, X. Isobutane dehydrogenation over InPtSn/ZnAl₂O₄ catalysts: Effect of indium promoter. *Ind. Eng. Chem. Res.* **2018**, *57*, 11265–11270. [CrossRef]
34. Vu, B.K.; Song, M.B.; Ahn, I.Y.; Suh, Y.W.; Suh, D.J.; Kim, W.I.; Koh, H.L.; Choi, Y.G.; Shin, E.W. Pt-Sn alloy phases and coke mobility over Pt-Sn/Al₂O₃ and Pt-Sn/ZnAl₂O₄ catalysts for propane dehydrogenation. *Appl. Catal. A* **2011**, *400*, 25–33. [CrossRef]
35. Zhang, M.; Song, Z.; Guo, M.Q.; Li, X.X.; Lin, Y.J.; Zhang, L.H. Effect of reduction atmosphere on structure and catalytic performance of PtIn/Mg(Al)O/ZnO for propane dehydrogenation. *Catalysts* **2020**, *10*, 485. [CrossRef]
36. Wu, P.; Xia, L.; Liu, Y.; Wu, J.S.; Chen, Q.Y.; Song, S.X. Simultaneous sorption of arsenate and fluoride on calcined Mg-Fe-La hydrotalcite-like compound from water. *ACS Sustain. Chem. Eng.* **2018**, *6*, 16287–16297. [CrossRef]
37. Mimura, N.; Takahara, I.; Saito, M.; Sasaki, Y.; Murata, K. Dehydrogenation of ethylbenzene to styrene in the presence of CO₂ over calcined hydrotalcite-like compounds as catalysts. *Catal. Lett.* **2002**, *78*, 125–128. [CrossRef]
38. Sun, P.; Siddiqi, G.; Vining, W.C.; Chi, M.; Bell, A.T. Novel Pt/Mg(In)(Al)O catalysts for ethane and propane dehydrogenation. *J. Catal.* **2011**, *282*, 165–174. [CrossRef]
39. Yang, X.; Liu, G.; Li, Y.; Zhang, L.; Wang, X.; Liu, Y. Novel Pt-Ni bimetallic catalysts Pt(Ni)-LaFeO₃/SiO₂ via lattice atomic-confined reduction for highly efficient isobutane dehydrogenation. *Trans. Tianjin Univ.* **2018**, *25*, 245–257. [CrossRef]
40. Wang, Q.; Wang, X.; Xu, J.; Ouyang, X.; Hou, X.; Chen, D.; Wang, R.; Shen, G. Flexible coaxial-type fiber supercapacitor based on NiCo₂O₄ nanosheets electrodes. *Nano Energy* **2014**, *8*, 44–51. [CrossRef]

41. Liu, Y.; Li, Y.; Ge, M.; Chen, X.; Guo, M.; Zhang, L. Perovskite-derived Pt-Ni/Zn(Ni)TiO₃/SiO₂ catalyst for propane dehydrogenation to propene. *Catal. Lett.* **2019**, *149*, 2552–2562. [CrossRef]
42. Passos, F.B.; Aranda, D.A.G.; Schmal, M. Characterization and catalytic activity of bimetallic Pt-In/Al₂O₃ and Pt-Sn/Al₂O₃ catalysts. *J. Catal.* **1998**, *178*, 478–488. [CrossRef]
43. Marchesini, F.A.; Gutierrez, L.B.; Querini, C.A.; Miro, E.E. Pt, In and Pd, In catalysts for the hydrogenation of nitrates and nitrites in water. FTIR characterization and reaction studies. *Chem. Eng. J.* **2010**, *159*, 203–211. [CrossRef]
44. Im, J.; Choi, M. Physicochemical stabilization of Pt against sintering for a dehydrogenation catalyst with high activity, selectivity, and durability. *ACS Catal.* **2016**, *6*, 2819–2826. [CrossRef]
45. Xia, K.; Lang, W.; Li, P.; Yan, X.; Guo, Y. Analysis of the catalytic activity induction and deactivation of PtIn/Mg(Al)O catalysts for propane dehydrogenation reaction. *RSC Adv.* **2015**, *5*, 64689–64695. [CrossRef]
46. Chen, H.; Jie, Y.; Chang, L.; Chen, X. Reaction behavior of MgF₂ powder in hexafluoropropylene/air atmospheres at high temperatures. *Solid State Ion.* **2019**, *340*, 115016. [CrossRef]
47. Han, W.; Zhang, C.; Wang, H.; Zhou, S.; Tang, H.; Yang, L.; Wang, Z. Sub-nano MgF₂ embedded in carbon nanofibers and electrospun MgF₂ nanofibers by one-step electrospinning as highly efficient catalysts for 1,1,1-trifluoroethane dehydrofluorination. *Catal. Sci. Technol.* **2017**, *7*, 6000–6012. [CrossRef]
48. Chen, X.; Ge, M.; Li, Y.; Liu, Y.; Wang, J.; Zhang, L. Fabrication of highly dispersed Pt-based catalysts on γ -Al₂O₃ supported perovskite Nano islands: High durability and tolerance to coke deposition in propane dehydrogenation. *Appl. Surf. Sci.* **2019**, *490*, 611–621. [CrossRef]
49. Zhao, S.Y.; Xu, B.L.; Yu, L.; Fan, Y.N. Catalytic dehydrogenation of propane to propylene over highly active PtSnNa/ γ -Al₂O₃ catalyst. *Chin. Chem. Lett.* **2018**, *29*, 475–478. [CrossRef]
50. Zhang, Y.; Zhou, Y.; Wan, L.; Xue, M.; Duan, Y.; Liu, X. Effect of magnesium addition on catalytic performance of PtSnK/ γ -Al₂O₃ catalyst for isobutane dehydrogenation. *Fuel Process. Technol.* **2011**, *92*, 1632–1638. [CrossRef]
51. Zhang, Y.; Zhou, Y.; Shi, J.; Sheng, X.; Duan, Y.; Zhou, S.; Zhang, Z. Effect of zinc addition on catalytic properties of PtSnK/ γ -Al₂O₃ catalyst for isobutane dehydrogenation. *Fuel Process. Technol.* **2012**, *96*, 220–227. [CrossRef]
52. Vaezifar, S.; Faghihian, H.; Kamali, M. Dehydrogenation of isobutane over Sn/Pt/Na-ZSM-5 catalysts: The effect of SiO₂/Al₂O₃ ratio, amount and distribution of Pt nanoparticles on the catalytic behavior. *Korean J. Chem. Eng.* **2010**, *28*, 370–377. [CrossRef]
53. Li, B.; Xu, Z.; Jing, F.; Luo, S.; Chu, W. Facile one-pot synthesized ordered mesoporous Mg-SBA-15 supported PtSn catalysts for propane dehydrogenation. *Appl. Catal. A* **2017**, *533*, 17–27. [CrossRef]

Article

Easily Recycled CuMgFe Catalysts Derived from Layered Double Hydroxides for Hydrogenolysis of Glycerol

Xiaopeng Yu ^{1,*}, Fubao Zhang ², Yi Wang ¹ and Dejun Cheng ¹

¹ Department of Chemical Engineering, Sichuan University of Science and Engineering, Zigong 643000, China; yiwanghg@suse.edu.cn (Y.W.); sunshine80131515@suse.edu.cn (D.C.)

² Zhonghao Chenguang Research Institute of Chemical Industry Co. Ltd., Zigong 643201, China; zhangfubao@haohua.chemchina.com

* Correspondence: xiaopengyu@suse.edu.cn; Tel.: +86-813-5506-521

Abstract: A series of CuMgFe catalysts with different (Cu + Mg)/Fe molar ratios derived from hydrotalcites were prepared by coprecipitation for the hydrogenolysis of glycerol to 1,2-propanediol (1,2-PDO). X-ray diffraction (XRD), scanning electron microscopy (SEM), transmission electron microscopy (TEM), X-ray photoelectron spectra (XPS), vibrating sample magnetometer (VSM), hydrogen temperature-programmed reduction (H₂-TPR), CO₂-TPD, and H₂-TPD (temperature-programmed desorption of CO₂ and H₂) were used to investigate the physicochemical properties of the catalysts. The CuMgFe-layered double oxides (CuMgFe-4LDO) catalyst with (Cu + Mg)/Fe molar ratio of 4 exhibited superior activity and stability. The high glycerol conversion and 1,2-propanediol selectivity over CuMgFe-4LDO catalyst were attributed to its strong basicity, excellent H₂ activation ability, and an increase in the surface Cu content. The CuMgFe catalysts could be easily recycled with the assistance of an external magnetic field due to their magnetism.

Citation: Yu, X.; Zhang, F.; Wang, Y.; Cheng, D. Easily Recycled CuMgFe Catalysts Derived from Layered Double Hydroxides for Hydrogenolysis of Glycerol. *Catalysts* **2021**, *11*, 232. <https://doi.org/10.3390/catal11020232>

Academic Editors: Juan Antonio Cecilia and Carmen Pilar Jiménez Gómez
Received: 20 January 2021
Accepted: 7 February 2021
Published: 9 February 2021

Publisher's Note: MDPI stays neutral with regard to jurisdictional claims in published maps and institutional affiliations.



Copyright: © 2021 by the authors. Licensee MDPI, Basel, Switzerland. This article is an open access article distributed under the terms and conditions of the Creative Commons Attribution (CC BY) license (<https://creativecommons.org/licenses/by/4.0/>).

Keywords: CuMgFe; layered double hydroxides; hydrogenolysis of glycerol; 1,2-propanediol; recycled

1. Introduction

Biodiesel is considered as a possible new pattern of renewable energy. Large-scale biodiesel production has brought about a surplus by-product of glycerol. Undoubtedly, the conversion of excess glycerol into higher-value chemicals can increase the economic value of the biodiesel industry. Different processes such as oxidation, dehydration, and hydrogenolysis have been proposed for the conversion of glycerol [1–5]. One of the attractive ways is hydrogenolysis to 1,2-propanediols (1,2-PDOs) because 1,2-PDO is widely used as a monomer for antifreeze agent, polyester resins, paints additive, liquid detergent, food, etc. Some results have been reported in selective catalytic hydrogenolysis of glycerol to 1,2-PDO [6–24].

Noble metals such as Rh, Ru and Pt are extensively used in the hydrogenolysis of glycerol owing to their high reactivity [9–15]. Nevertheless, these catalysts usually facilitate excessive C–C cleavage, resulting in a poor selectivity to 1,2-PDO. Cu-based catalysts exhibit high selectivity to 1,2-PDO in the hydrogenolysis of glycerol due to poor activity for C–C bond cleavage and high efficiency for C–O bond hydro-dehydrogenation. Cu–Cr [16], Cu/ZnO [17,18], Cu/Al₂O₃ [17,19], Cu/SiO₂ [20,21], Cu/MgO [22,23] catalysts have been reported by several groups. It has been demonstrated that the activity of Cu-based catalysts for hydrogenolysis of glycerol depends strongly on the dispersion and/or the surface area of exposed Cu [8,20,21]. Additionally, the acidity/basicity of Cu-based catalysts also plays an important role in the hydrogenolysis reaction of glycerol [22,24].

Layered double hydroxides (LDHs), also known as hydrotalcite-like compounds, are a class of anionic clay materials that allow the uniform mixing of different bivalent and trivalent cations. Thermal decomposition of LDHs leads to the formation of mixed oxides with small crystal size, basicity, high dispersion, and large specific surface area.

It has been reported that Cu-based catalysts derived from hydrotalcites are of basicity and dispersed copper particles [8,24–27], which could improve the catalytic performance in the hydrogenolysis of glycerol. Geng et al. [28] disclosed that the Cu–Ca–Al catalyst derived from hydrotalcite is more active and selective for the formation of propanediols. Nonetheless, these catalysts suffer from serious difficulties in the recovery and reuse from the perspective of ecological and economical sustainability. Magnetic catalysts can be easily separated by an external magnetic field, reducing the consumption of auxiliary substances, saving energy and time in separation, and bringing significant economic and environmental benefits. However, to the best of our knowledge, there is no detailed understanding of magnetic Cu-based catalysts derived from hydrotalcites in the hydrogenolysis of glycerol.

The aim of the present work is to develop easily recycled Cu-containing catalysts in the hydrogenolysis of glycerol. Magnetic CuMgFe mixed-oxide catalysts derived from hydrotalcites were prepared by coprecipitation, and the effect of (Cu + Mg)/Fe molar ratio on the activity of the catalysts was discussed in detail.

2. Results and Discussion

2.1. Characterization Results

2.1.1. Structure and Morphology of CuMgFe-xLDH and CuMgFe-xLDO

The XRD patterns of CuMgFe-xLDH are shown in Figure 1a. CuMgFe-2LDH, CuMgFe-3LDH, CuMgFe-4LDH, and CuMgFe-5LDH exhibited the characteristic reflections of hydrotalcite. Compared with CuMgFe-2LDH, the sharp diffraction peaks of CuMgFe-3LDH evidenced a better crystallization of the phase of hydrotalcite. Oppositely, CuMgFe-4LDH and CuMgFe-5LDH exhibited a lower crystallization with the increase of (Cu + Mg)/Fe molar ratio. Increasing (Cu + Mg)/Fe molar ratio might lead to the structural distortion and the orderliness decline of hydrotalcite.

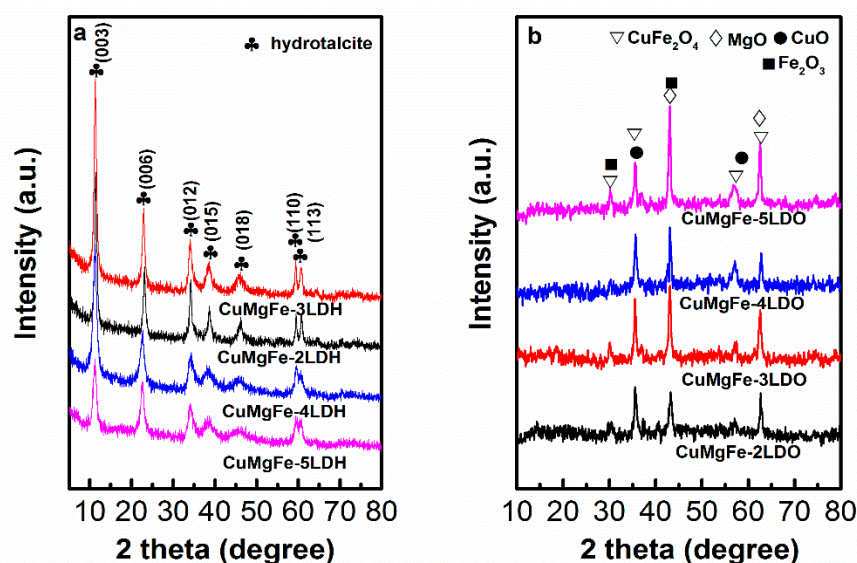


Figure 1. XRD patterns of (a) CuMgFe-xLDH and (b) CuMgFe-xLDO.

The XRD patterns of CuMgFe-xLDO catalysts with different (Cu + Mg)/Fe molar ratios are shown in Figure 1b. After calcination at 600 °C, all LDHs were transformed to mixed oxides and spinel phase. For all the CuMgFe-xLDO samples, the diffraction peaks at around 30.2°, 35.5°, 57.1°, and 62.7° corresponded to the (220), (311), (511), and (440) planes of CuFe₂O₄ spinel phase (JCPDS card no. 77-0010), respectively. Meanwhile, the CuO phase (at around 35.5° (002) and 58.3° (202)) also might be present, but its diffraction peaks were partially overlapped with those of CuFe₂O₄. Consequently, it was difficult to distinguish in the XRD results. The diffraction peaks at 30.3° and 43.3° could correspond to the (220) and (400) planes of the Fe₂O₃ phase (JCPDS card no. 39-1346), respectively.

Additionally, the diffraction peaks at 42.9° and 62.3° were also observed, which could be associated with the (200) and (220) planes of the MgO phase (JCPDS card no. 04-0829).

The morphology of CuMgFe-3LDH and CuMgFe-4LDH revealed by SEM is shown in Figure 2. CuMgFe-3LDH displayed a layered structure of solid lamellar (Figure 2A), whereas some solid lamellar structures accumulated obviously in CuMgFe-4LDH (Figure 2B). Figure 2C,D shows the images of CuMgFe-3LDO and CuMgFe-4LDO after calcination, which maintained the plate-like morphology of the original precursor. High resolution transmission electron microscope (HRTEM) was also used to reveal the structure of CuMgFe-4LDO sample. A typical HRTEM image of CuMgFe-4LDO showed two identified reflection patterns with interplanar distances of 0.253 nm and 0.205 nm (Figure 2E), corresponding to the (002) plane of CuO phase and (220) plane of CuFe_2O_4 phase [29,30], respectively, which was in line with the XRD results.

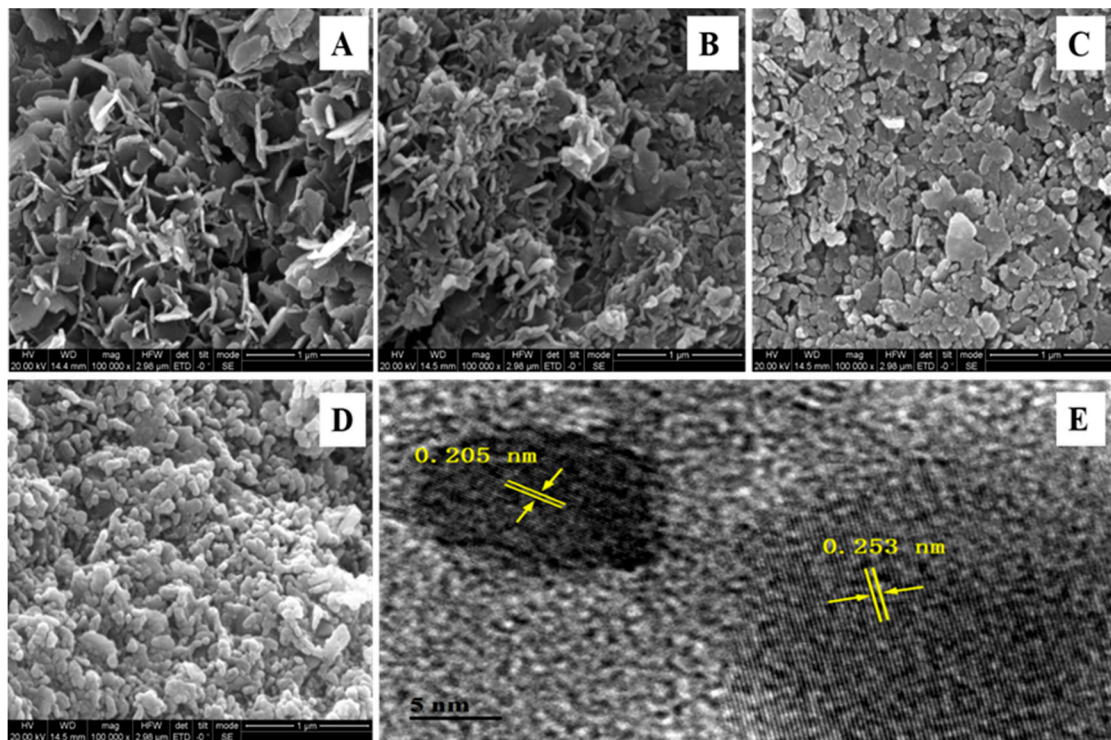


Figure 2. SEM images of the (A) CuMgFe-3LDH, (B) CuMgFe-4LDH, (C) CuMgFe-3LDO, and (D) CuMgFe-4LDO. HRTEM image of (E) CuMgFe-4LDO.

2.1.2. Magnetic Behavior of CuMgFe-xLDO Catalysts

The magnetic behavior of the catalysts was analyzed using VSM. All catalysts showed narrow S-shape type loops in Figure 3, indicating that all catalysts were ferromagnetic. Magnetic saturation (M_s), remanence (M_r), and coercivity (H_c) calculated from magnetically recorded data are listed in Table 1. The lower saturation magnetization and coercivity values might be due to the presence of CuO and MgO in the catalysts. The ratio of the remanence to the saturation magnetization (M_r/M_s) decreased in the following order: CuMgFe-5LDO > CuMgFe-3LDO > CuMgFe-2LDO > CuMgFe-4LDO, which was related to the inter- and intragrain exchange interactions, sub-lattice magnetization, magnetic anisotropy, and morphology of the tested sample [31]. The lower ratio corroborated its significant superparamagnetic behavior [32].

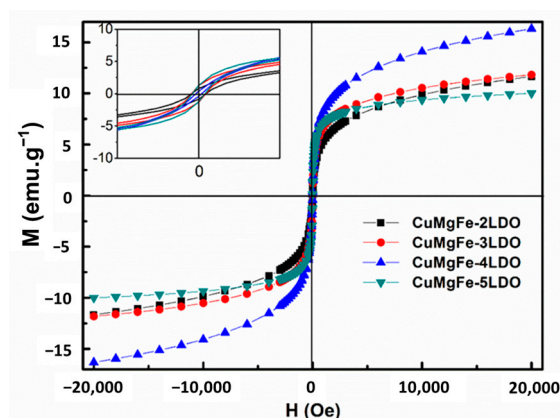


Figure 3. Magnetic hysteresis curves for the CuMgFe-xLDO catalysts.

Table 1. The magnetic properties of CuMgFe-xLDO catalysts.

Sample	M_s (emu.g ⁻¹)	M_r (emu.g ⁻¹)	M_r/M_s	H_c (Oe)
CuMgFe-2LDO	11.70	0.91	0.08	26.71
CuMgFe-3LDO	11.82	1.41	0.12	27.86
CuMgFe-4LDO	16.30	0.41	0.03	13.45
CuMgFe-5LDO	10.00	1.38	0.14	26.20

2.1.3. H₂-TPR of CuMgFe-xLDO Catalysts

The reducibility of catalysts was investigated by hydrogen temperature-programmed reduction (H₂-TPR). As shown in Figure 4, the first shoulder peak (at 205 °C, 209 °C, 191 °C, and 210 °C) in the low-temperature range for all the samples was ascribed to the reduction of CuO to Cu. The subsequent peak (at 235 °C, 242 °C, 225 °C, and 246 °C) was attributed to the reduction of CuFe₂O₄ to metallic Cu and Fe₂O₃ [33,34]. The third peak in the range of 300–550 °C might correspond to the transformation of Fe₂O₃ to Fe₃O₄ [35]. The peak in the high-temperature range of 550–900 °C for all the samples could be attributed to the continuous reduction of Fe₃O₄ to metallic Fe via FeO [33,36]. It should be noted that the reduction temperature of CuO in the CuMgFe-xLDO samples shifted to lower temperature compared with that of pristine CuO (around 290 °C) [33], and the reduction peak of CuFe₂O₄ in the CuMgFe-xLDO samples decreased significantly in comparison with that of pristine CuFe₂O₄ (around 340 °C) [33]. The findings indicated that the strong synergistic effect between copper and iron occurred in the CuMgFe-xLDO samples. Furthermore, the reduction peaks of CuO and CuFe₂O₄ in the CuMgFe-4LDO catalyst were lower than those of other catalysts, suggesting that the stronger interaction between copper and iron might occur in the CuMgFe-4LDO catalyst. Cu species could be well dispersed on the CuMgFe-4LDO catalyst surface.

2.1.4. XPS Analysis of CuMgFe-xLDO Catalysts

Cu 2p and Fe 2p spectra of CuMgFe-xLDO catalysts are shown in Figure 5a,b. A Cu 2p_{3/2} main peak at 933.5–933.9 eV was accompanied by a satellite peak at 942.2–942.8 eV, which was related to CuFe₂O₄. Additionally, all catalysts exhibited a Cu 2p_{3/2} peak at 931.8–931.9 eV together with a satellite peak at 940.0–940.2 eV, which could be associated with the presence of CuO. A Cu 2p_{1/2} main peak at 952.2–952.8 eV along with a satellite peak at 961.6–962.0 eV was also observed, in accordance with those of Cu²⁺ [37,38]. All Fe 2p spectra in Figure 5b showed two main peaks at 710.9–711.1 eV and 724.2–724.5 eV, which belonged to Fe 2p_{3/2} and Fe 2p_{1/2}, respectively. Two accompanying satellite peaks at the binding energies of 718.5–718.8 eV and 732.3–732.8 eV were characteristics of Fe³⁺ cations [38–40]. Mg 1s spectra of CuMgFe-xLDO catalysts are also presented in Figure 5c. All catalysts showed a peak at 1303.5–1304.1 eV, which could be due to the presence of MgO [41].

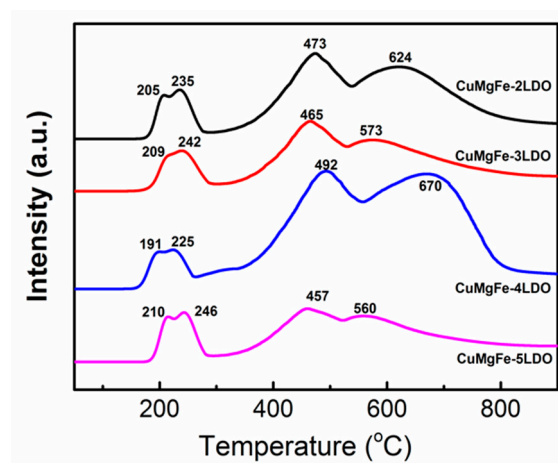


Figure 4. Hydrogen temperature-programmed reduction (H_2 -TPR) profiles of CuMgFe-xLDO catalysts.

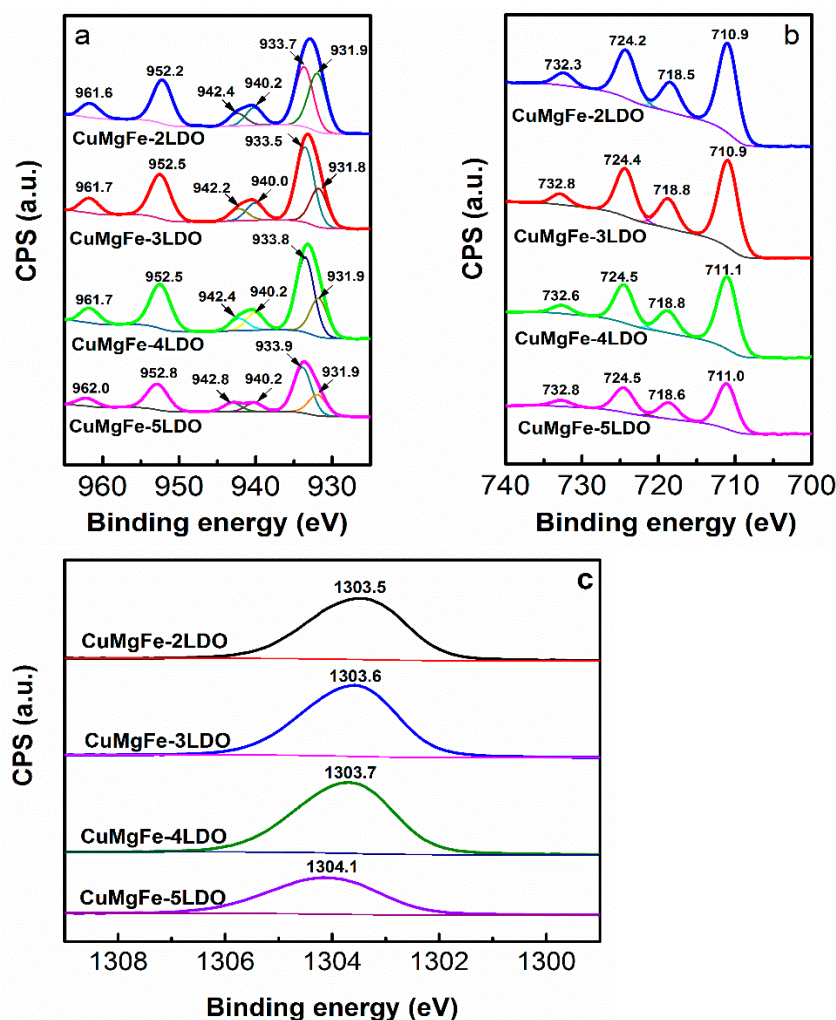


Figure 5. XPS spectra of (a) Cu 2p, (b) Fe 2p, and (c) Mg 1s of the CuMgFe-xLDO catalysts.

The surface element composition of CuMgFe-xLDO catalysts is summarized in Table 2. The surface Cu content and surface Cu/(Mg + Fe) atomic ratio of the CuMgFe-4LDO catalyst were slightly higher than those of the other catalysts, suggesting that Cu species could be well dispersed on the CuMgFe-4LDO catalyst. This was in line with the H_2 -TPR results.

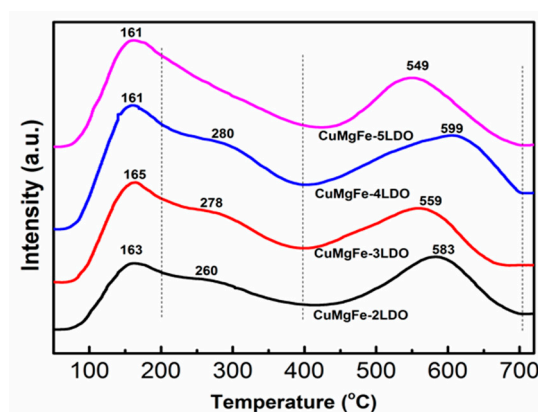
Table 2. The surface element composition and the base sites amounts of CuMgFe-xLDO catalysts.

Catalyst	Cu (mol%) ^a	Cu/(Mg + Fe) Atomic Ratio ^a	Base Sites Amounts		
			W ^b + M ^b (μmol/g)	S ^b (μmol/g)	Total Amount (μmol/g)
CuMgFe-2LDO	5.08	0.289	60.1	53.6	113.7
CuMgFe-3LDO	5.01	0.290	84.2	61.4	145.6
CuMgFe-4LDO	5.26	0.325	109.0	90.5	199.5
CuMgFe-5LDO	4.92	0.278	83.9	45.6	129.5

^a The values were calculated from XPS; ^b W: T < 200 °C; M: 200 °C < T < 400 °C; S: T > 400 °C.

2.1.5. Basicity of Reduced Catalysts

The base properties of the CuMgFe-LDO catalysts were evaluated by the adsorption of CO₂ on the basic sites. The CO₂-TPD profiles of CuMgFe-LDO catalysts are presented in Figure 6. There were two obvious desorption domains occurring at 50–400 °C and 400–700 °C for all the catalysts. The stronger the basic sites of a catalyst were, the higher the desorption temperature of CO₂ was [42]. The low-temperature peaks below 200 °C could be attributed to the desorption of CO₂ on weak basic sites, while the desorption peaks in the range of 200–400 °C could be ascribed to the desorption of CO₂ on medium basic sites. The peaks at 549–599 °C were associated with the desorption of CO₂ on strong basic sites. The weak and medium basic sites corresponded to surface OH[−] and Lewis acid-base pairings, respectively, and the strong basic sites were related to the contribution of low-coordination surface O^{2−} [43–45]. Notably, the desorption temperature on strong basic sites of the CuMgFe-4LDO catalyst was significantly higher than those of the other catalysts. It has been reported that dehydrogenation of glycerol leads to glyceraldehyde and it subsequently dehydrates to hydroxyacrolein on basic sites of the catalyst [46]. The strongest basic sites on the CuMgFe-4LDO catalyst might enhance its catalytic performance. As shown in Table 2, the total amount of basic sites decreased in the following order: CuMgFe-4LDO > CuMgFe-3LDO > CuMgFe-5LDO > CuMgFe-2LDO, indicating that the total amount of basic sites of the catalyst increased with the moderate increase of (Cu + Mg)/Fe molar ratio. Conversely, excessive (Cu + Mg)/Fe molar ratio decreased significantly the contribution of medium and strong basic sites, and thereby reducing the total amount of basic sites of the CuMgFe-5LDO catalyst. This could be associated with the morphology, crystal plane, and crystal size of MgO in the CuMgFe-5LDO catalyst. Li et al. found that MgO (100) surface primarily ended with alternant Mg²⁺/O^{2−} ions providing medium basic sites, while MgO (111) surface primarily ended with O^{2−} ions providing strong basic sites [47]. It was reported by Marianou et al. that the basicity of MgOs was strongly affected by the morphology, texture, and chemical composition of the materials [48]. Samples with smaller crystal size and higher surface area exhibited a higher total number of basic sites [48].

**Figure 6.** CO₂-TPD patterns of the reduced CuMgFe-xLDO catalysts.

2.1.6. H₂-TPD of Reduced Catalysts

H₂-TPD profiles of the CuMgFe-xLDO catalysts are shown in Figure 7. In the range of 50–700 °C, the desorption of H₂ might be assigned to three different H species. The desorption peak at low temperature (50–350 °C, H_α) might be attributed to hydrogen desorption from Cu sites. The desorption peak at high temperature (350–700 °C, H_β, H_γ) could correspond to the hydrogen desorption from two different Fe sites. Apparently, the CuMgFe-4LDO catalyst exhibited the highest H_α desorption peak temperature, indicating that a stronger metal-hydrogen interaction occurred on the surface of the CuMgFe-4LDO catalyst. This could be due to the high Cu dispersion in the CuMgFe-4LDO catalyst, which afforded more unsaturated coordination centers for the hydrogen adsorption [33]. It has been reported that enhanced H₂ activation ability could improve the activity for glycerol hydrogenolysis [24].

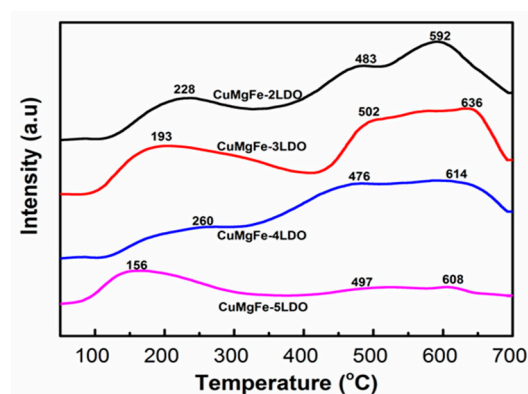


Figure 7. H₂-TPD profiles of the CuMgFe-xLDO catalysts.

2.2. Hydrogenolysis of Glycerol

2.2.1. Effect of (Cu + Mg)/Fe Molar Ratio on Catalytic Performance of Reduced CuMgFe-xLDO Catalysts

The conversions of glycerol over CuMgFe-xLDO catalysts for the hydrogenolysis of glycerol are summarized in Table 3. With the increase in (Cu + Mg)/Fe molar ratios from 2 to 4, the conversion of glycerol increased from 38.0% to 47.8%. On the contrary, the conversion of glycerol over the CuMgFe-5LDO catalyst decreased. The CuMgFe-4LDO catalyst exhibited the highest glycerol conversion and 1,2-PDO selectivity among all the catalysts.

Table 3. Hydrogenolysis of glycerol on reduced CuMgFe-xLDO catalysts ^a.

Catalyst	Conversion (%)	Selectivity	
		1,2-PDO (%)	Others (%) ^b
CuMgFe-2LDO	38.0	96.9	3.1
CuMgFe-3LDO	41.3	97.0	3.0
CuMgFe-4LDO	47.8	97.5	2.5
CuMgFe-5LDO	37.5	96.2	3.4

^a Reaction conditions: 8.0 g 75% glycerol solution, 2.0 MPa H₂, 180 °C, 10 h, 0.60 g reduced catalyst. ^b Ethylene glycol, methanol, ethanol, and 1-propanol.

According to the reaction mechanism from glycerol to 1,2-PDO proposed by Montassier [49], first, dehydrogenation of glycerol on copper would form glyceraldehyde in equilibrium with its enolic tautomer. Then, a nucleophilic reaction of water or adsorbed OH species led to a dehydroxylation reaction. Subsequently, 1,2-PDO was formed by hydrogenation of the intermediate unsaturated aldehyde (2-hydroxy acrolein). Therefore, it can be concluded that the hydrogenolysis of glycerol to 1,2-PDO needs both metal sites for activation of hydrogen and base sites for dehydration. The higher hydrogenolysis activity

over CuMgFe-4LDO catalyst might be due to the following factors. Primarily, the increase in the surface Cu content might be a factor in improving the hydrogenolysis activity of glycerol (Table 2). Furthermore, compared with the other catalysts, the stronger basic sites and the higher amount of basicity (Figure 6 and Table 2) on the CuMgFe-4LDO catalyst favored dehydration reaction of glyceraldehyde and its enolic tautomer. Consequently, the intermediate unsaturated aldehyde (2-hydroxy acrolein) was formed. Finally, on the basis of the H₂-TPD results (Figure 7), enhancing H₂ activation on Cu metal sites accelerated hydrogenation of intermediate unsaturated aldehyde (2-hydroxy acrolein), thereby improving the selectivity to 1,2-PDO.

2.2.2. Hydrogenolysis of Glycerol on Reduced CuMgFe-4LDO Catalyst at Different Temperatures

The activity of CuMgFe-4LDO catalyst for hydrogenolysis of glycerol at different temperatures is summarized in Table 4. The conversion of glycerol increased significantly from 47.8% (at 180 °C) to 75.3% (at 200 °C), suggesting that glycerol hydrogenolysis accelerated with increasing reaction temperature. Nevertheless, the selectivity to 1,2-PDO declined slightly from 97.5% (at 180 °C) to 96.5% (at 200 °C), indicating that no obvious cleavage of C–C bonds over CuMgFe-4LDO catalyst occurred even at higher temperatures.

Table 4. Hydrogenolysis of glycerol on reduced CuMgFe-4LDO catalyst at different temperatures ^a.

Temperature (°C)	Conversion (%)	Selectivity	
		1, 2-PDO (%)	Others (%) ^b
180	47.8	97.5	2.5
190	60.5	97.2	2.8
200	75.3	96.5	3.5

^a Reaction conditions: 8.0 g 75% glycerol solution, 2.0 MPa H₂, 10 h, 0.60 g reduced catalyst. ^b Ethylene glycol, methanol, ethanol, and 1-propanol.

2.2.3. Recycled Usage of Reduced CuMgFe-4LDO Catalyst

The recycling procedure of the CuMgFe-4LDO catalyst was performed for examining the stability of the catalyst. The spent catalysts were separated by an external magnetic field. Due to the magnetism for CuMgFe-4LDO catalysts, the catalysts could be easily recycled, as shown in Figure 8. The activity of recycled CuMgFe-4LDO catalyst is summarized in Table 5. The conversion of glycerol decreased slightly from 47.8% (of the fresh catalyst) to 46.9% (in the second recycle), and then it remained stable (in the third and the fourth recycles). After five times of recycling, the conversion of glycerol over the CuMgFe-4LDO catalyst decreased by 3.5%. No apparent weight loss of catalysts was observed after five times recycles.

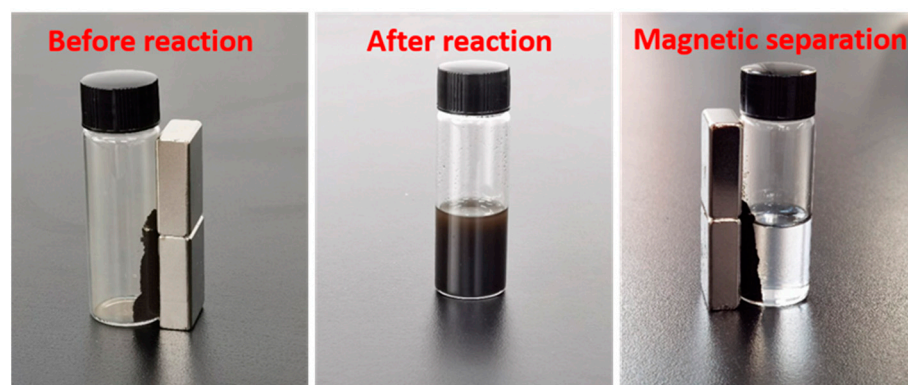


Figure 8. Images of magnetic characteristics and magnetic separation for reduced CuMgFe-4LDO catalyst.

Table 5. Hydrogenolysis of glycerol and composition on recycled CuMgFe-4LDO ^a.

Recycles	Conversion (%)	Selectivity		Composition ^c		
		1, 2-PDO (%)	Others ^b (%)	Cu (mol %)	Mg (mol %)	Fe (mol %)
1	47.8	97.5	2.5	7.23	72.98	19.79
2	46.9	97.4	2.6	–	–	–
3	46.6	97.3	2.7	–	–	–
4	46.1	97.4	2.6	–	–	–
5	44.3	97.2	2.8	7.15	73.85	19.00

^a Reaction conditions: 8.0 g 75% glycerol solution, 2.0 MPa H₂, 180 °C, 10 h, 0.60 g catalyst. ^b Ethylene glycol, methanol, ethanol, and 1-propanol. ^c the values were determined by induced coupled plasma-optical emission spectroscopy (ICP-OES).

To explore the reasons for activity loss, the compositions of the reduced catalyst and five-times-recycled catalyst were determined by induced coupled plasma-optical emission spectroscopy (ICP-OES). No obvious leaching Cu was observed after five recycles (Table 5). Meanwhile, to confirm further no Cu leaching, the catalyst was filtered off after 5 h reaction (halfway through the reaction) in the fifth recycle. At this moment, glycerol conversion and the selectivity to 1,2-propanediol were 28.5% and 97.0%, respectively. Then, the filtrate was transferred to a 100 mL stainless steel autoclave. Moreover, hydrogenolysis of glycerol was still performed under no catalyst conditions. Once more, after 5 h reaction, glycerol conversion and the selectivity to 1,2-propanediol did not further increase, indicating that no Cu leached into the filtrate. Furthermore, the XRD results of the reduced catalyst and five-times-recycled catalyst were also analyzed (Figure S1), Cu metal sizes were calculated from the diffraction peaks (220) according to the Scherrer equation. Cu metal size increased from 9.2 nm to 10.8 nm after five recycles, suggesting that the decreased activity of CuMgFe-4LDO catalyst could be due to slight sintering of copper metal.

3. Materials and Methods

3.1. Preparation of CuMgFe-Mixed Oxides Catalysts

Four CuMgFe-LDH precursors with different (Cu²⁺ + Mg²⁺)/Fe³⁺ molar ratios were prepared by coprecipitation. The A solution was a 0.2 M aqueous solution containing the nitrates of Cu²⁺, Mg²⁺, and Fe³⁺. The B solution was an aqueous solution of NaOH and Na₂CO₃ with a concentration of 0.25 M and 0.8 M, respectively. Solution A and B were added drop-wise into the deionized water with vigorous stirring. During the coprecipitation, the slurry was kept at pH 10.0 ± 0.1 by adjusting dropping rates. The resulting suspension was aged at 60 °C for 18 h. The final precipitate was filtered, washed, and dried at 110 °C for 12 h. Layered double hydroxides were gained, and they are denoted as CuMgFe-*x*LDH (*x* = 2, 3, 4 or 5 according to the (Cu²⁺ + Mg²⁺)/Fe³⁺ molar ratios of 2, 3, 4, or 5). Subsequently, the hydrotalcites were calcined at 600 °C for 5 h in air, and the products are designated as CuMgFe-*x*LDO (*x* = 2, 3, 4, or 5). The nominal Cu content is 9 wt% in the CuMgFe-*x*LDO samples.

3.2. Characterization of Precursors and Catalysts

The X-ray diffraction patterns were detected on a Philips X'pert-PRO diffractometer using Cu K α radiation (45 kV, 50 mA) (PANalytical, Etten-Leur, Netherlands).

The morphology of the CuFeMg-LDH was investigated using a Quanta 400 FEG scanning electron microscope (FEI, Hillsboro, Oregon, OR, USA) with an accelerating voltage of 20 kV.

Transmission electron microscopy (TEM) images were obtained using a Tecnai G² F20 transmission electron microscope (FEI, Hillsboro, Oregon, OR, USA). The samples were ultrasonically dispersed in ethanol.

The reducibility of the catalysts was studied by hydrogen temperature-programmed reduction (H₂-TPR) using a fixed-bed reactor. The catalysts were reduced under a 10% H₂/Ar mixed gas (30 mL/min) from 50 °C to 900 °C at a rate of 10 °C/min. The hydro-

gen consumption was analyzed on-line using an SC-200 gas chromatograph (Chuanyi, Chongqing, China) equipped with a thermal conductivity detector (TCD).

The X-ray photoelectron spectra (XPS) were obtained using an XSAM800 spectrometer (Kratos, Manchester, UK) with an Al K α ($h\nu = 1486.6$ eV) X-ray source, and the binding energies were corrected using C (1 s) at 284.6 eV.

The basicity and the H₂-activation ability of the reduced catalysts were determined by temperature-programmed desorption of CO₂ and H₂ (CO₂-TPD and H₂-TPD). The catalysts were reduced at 400 °C in 10% H₂/Ar for 2 h and then cooled to 50 °C in a He flow. Subsequently, CO₂ was fed into the reactor for 0.5 h. Then the catalysts were purged at 50 °C with He for 3 h. Finally, the samples were heated linearly to 750 °C at a rate of 10 °C/min in a He flow. While the desorbed CO₂ was recorded continuously by a TCD detector. H₂-TPD was carried out by the same procedure. Only CO₂ was supplanted by the 10% H₂/Ar.

The magnetization was characterized by a superconducting quantum interference SQUID magnetometer (Quantum Design, San Diego, CA, USA) with a maximum field of 20 kOe at room temperature. The saturation magnetization (M_s), coercive force (H_c), and residual magnetization (M_r) were measured.

Chemical composition was analyzed by using an induced coupled plasma-optical emission spectroscopy (ICP-OES) analyzer (Spectro Arcos, SPECTRO Analytical Instruments GmbH, Kleve, Germany).

3.3. Catalytic Experiments

Hydrogenolysis of glycerol was performed in a 100 mL stainless steel autoclave with a mechanical stirrer and an electric temperature controller, operated under H₂ pressure of 2.0 MPa. Prior to reaction, the catalysts were reduced by 10% H₂/Ar stream at 400 °C for 2 h in a fixed-bed flowed reactor. A total of 8.0 g aqueous solution of 75 wt% glycerol and 10 wt% (based on glycerol) of the catalysts were charged into the autoclave. The liquid products were analyzed by using a Scion 456C GC gas chromatograph (Techcomp, Shanghai, China) equipped with a flame ionization detector (PEG-20M column: 30 m × 0.25 mm × 0.5 μm). The gas products were analyzed by using a Scion 456C GC gas chromatograph equipped with a thermal conductivity detector (TDX-01 column: 3 m × 3 mm).

4. Conclusions

The CuMgFe-*x*LDO catalysts derived from different (Cu + Mg)/Fe metal ratios were prepared by coprecipitation. The activity of the CuMgFe-4LDO catalyst was higher than those of other CuMgFe-*x*LDO catalysts, and the conversion of glycerol and the selectivity to 1,2-PDO reached 47.8% and 97.5% at 180 °C, respectively. The superior catalytic performance of CuMgFe-4LDO was associated with its strong basicity, excellent H₂ activation ability, and an increase in the surface Cu content. The CuMgFe-4LDO catalyst also exhibited good stability. Furthermore, the CuMgFe-*x*LDO catalysts could be easily recycled with the assistance of an external magnetic field due to their magnetism.

Supplementary Materials: The following are available online at <https://www.mdpi.com/2073-4344/11/2/232/s1>, Figure S1: XRD patterns of the reduced and spent CuMgFe-4LDO catalysts.

Author Contributions: Conceptualization, X.Y.; methodology, X.Y. and F.Z.; software, X.Y.; validation, X.Y.; formal analysis, X.Y.; investigation, X.Y. and F.Z.; resources, X.Y. and Y.W.; data curation, X.Y.; writing—original draft preparation, X.Y.; writing—review and editing, X.Y., F.Z., and Y.W.; supervision, X.Y.; project administration, Y.W. and D.C.; funding acquisition, X.Y. All authors have read and agreed to the published version of the manuscript.

Funding: This research was funded by the National Natural Science Foundation of China (Grant No. 21706168).

Data Availability Statement: Data presented in this study are available on request from the corresponding author.

Conflicts of Interest: The authors declare no conflict of interest.

References

- Zope, B.N.; Hibbitts, D.D.; Neurock, M.; Davis, R.J. Reactivity of the gold/water interface during selective oxidation catalysis. *Science* **2010**, *330*, 74–78. [CrossRef]
- Dalil, M.; Edake, M.; Sudeau, C.; Dubois, J.L.; Patience, G.S. Coke promoters improve acrolein selectivity in the gas-phase dehydration of glycerol to acrolein. *Appl. Catal. A Gen.* **2016**, *522*, 80–89. [CrossRef]
- Yun, D.; Yun, Y.S.; Kim, T.Y.; Park, H.; Lee, J.M.; Han, J.W.; Yi, J. Mechanistic study of glycerol dehydration on Brønsted acidic amorphous aluminosilicate. *J. Catal.* **2016**, *341*, 33–43. [CrossRef]
- Sun, D.; Yamada, Y.; Sato, S.; Ueda, W. Glycerol hydrogenolysis into useful C3 chemicals. *Appl. Catal. B Environ.* **2016**, *193*, 75–92. [CrossRef]
- Wang, C.; Jiang, H.; Chen, C.; Chen, R.; Xing, W. Solvent effect on hydrogenolysis of glycerol to 1,2-propanediol over Cu–ZnO catalyst. *Chem. Eng. J.* **2015**, *264*, 344–350. [CrossRef]
- Dam, J.T.; Hanefeld, U. Renewable chemicals: Dehydroxylation of glycerol and polyols. *ChemSusChem* **2011**, *4*, 1017–1034.
- Wang, Y.; Zhou, J.; Guo, X. Catalytic hydrogenolysis of glycerol to propanediols: A review. *RSC Adv.* **2015**, *5*, 74611–74628. [CrossRef]
- Yuan, Z.; Wang, L.; Wang, J.; Xia, S.; Chen, P.; Hou, Z.; Zheng, X. Hydrogenolysis of glycerol over homogeneously dispersed copper on solid base catalysts. *Appl. Catal. B Environ.* **2011**, *101*, 431–440. [CrossRef]
- Mane, R.; Patil, S.; Shirai, M.; Rayalu, S.; Rode, C. Influence of carbon based supports on selectivity behavior of diols and propanol in Ru catalyzed glycerol hydrogenolysis. *Appl. Catal. B Environ.* **2017**, *204*, 134–146. [CrossRef]
- Balaraju, M.; Rekha, V.; Prabhavathi Devi, B.L.A.; Prasad, R.B.N.; Sai Prasad, P.S.; Lingaiah, N. Surface and structural properties of titania-supported Ru catalysts for hydrogenolysis of glycerol. *Appl. Catal. A Gen.* **2010**, *384*, 107–114. [CrossRef]
- Zhou, W.; Zhao, Y.; Wang, S.; Ma, X. The effect of metal properties on the reaction routes of glycerol hydrogenolysis over platinum and ruthenium catalysts. *Catal. Today* **2017**, *298*, 2–8. [CrossRef]
- Furikado, I.; Miyazawa, T.; Koso, S.; Shimao, A.; Kunimori, K.; Tomishige, K. Catalytic performance of Rh/SiO₂ in glycerol reaction under hydrogen. *Green Chem.* **2007**, *9*, 582–588. [CrossRef]
- Shinmi, Y.; Koso, S.; Kubota, T.; Nakagawa, Y.; Tomishige, K. Modification of Rh/SiO₂ catalyst for the hydrogenolysis of glycerol in water. *Appl. Catal. B Environ.* **2010**, *94*, 318–326. [CrossRef]
- Rodrigues, R.; Isoda, N.; Gonçalves, M.; Figueiredo, F.C.A.; Mandelli, D.; Carvalho, W.A. Effect of niobia and alumina as support for Pt catalysts in the hydrogenolysis of glycerol. *Chem. Eng. J.* **2012**, *198–199*, 457–467. [CrossRef]
- Zhou, W.; Zhao, Y.; Wang, Y.; Wang, S.; Ma, X. Glycerol hydrogenolysis to 1,3-propanediol on tungstate/zirconia-supported platinum: Hydrogen spillover facilitated by Pt(111) Formation. *ChemCatChem* **2016**, *8*, 3663–3671. [CrossRef]
- Xiao, Z.; Wang, X.; Xiu, J.; Wang, Y.; Williams, C.T.; Liang, C. Synergetic effect between Cu⁰ and Cu⁺ in the Cu–Cr catalysts for hydrogenolysis of glycerol. *Catal. Today* **2014**, *234*, 200–207. [CrossRef]
- Feng, Y.; Yin, H.; Wang, A.; Shen, L.; Yu, L.; Jiang, T. Gas phase hydrogenolysis of glycerol catalyzed by Cu/ZnO/MO_x (MO_x = Al₂O₃, TiO₂, and ZrO₂) catalysts. *Chem. Eng. J.* **2011**, *168*, 403–412. [CrossRef]
- Hou, M.; Jiang, H.; Liu, Y.; Chen, R. Role of initial water content in glycerol hydrogenolysis to 1,2-propanediol over Cu–ZnO catalyst. *Reac. Kinet. Mech. Cat.* **2017**, *122*, 1129–1143. [CrossRef]
- Vila, F.; López Granados, M.; Ojeda, M.; Fierro, J.L.G.; Mariscal, R. Glycerol hydrogenolysis to 1,2-propanediol with Cu/γ-Al₂O₃: Effect of the activation process. *Catal. Today* **2012**, *187*, 122–128. [CrossRef]
- Huang, Z.; Liu, H.; Cui, F.; Zuo, J.; Chen, J.; Xia, C. Effects of the precipitation agents and rare earth additives on the structure and catalytic performance in glycerol hydrogenolysis of Cu/SiO₂ catalysts prepared by precipitation-gel method. *Catal. Today* **2014**, *234*, 223–232. [CrossRef]
- Zhu, S.; Gao, X.; Zhu, Y.; Zhu, Y.; Zheng, H.; Li, Y. Promoting effect of boron oxide on Cu/SiO₂ catalyst for glycerol hydrogenolysis to 1,2-propanediol. *J. Catal.* **2013**, *303*, 70–79. [CrossRef]
- Yuan, Z.; Wang, J.; Wang, L.; Xie, W.; Chen, P.; Hou, Z.; Zheng, X. Biodiesel derived glycerol hydrogenolysis to 1,2-propanediol on Cu/MgO catalysts. *Bioresour. Technol.* **2010**, *101*, 7088–7092. [CrossRef] [PubMed]
- Pandhare, N.N.; Pudi, S.M.; Biswas, P.; Sinha, S. Selective hydrogenolysis of glycerol to 1,2-propanediol over highly active and stable Cu/MgO catalyst in the vapor phase. *Org. Process Res. Dev.* **2016**, *20*, 1059–1067. [CrossRef]
- Xia, S.; Nie, R.; Lu, X.; Wang, L.; Chen, P.; Hou, Z. Hydrogenolysis of glycerol over Cu_{0.4}/Zn_{5.6–x}Mg_xAl₂O_{8.6} catalysts: The role of basicity and hydrogen spillover. *J. Catal.* **2012**, *296*, 1–11. [CrossRef]
- Xia, S.; Zheng, L.; Nie, R.; Chen, P.; Lou, H.; Hou, Z. Trivalent metal ions M³⁺ in M_{0.02}Cu_{0.4}Mg_{5.6}Al_{1.98}(OH)₁₆CO₃ layered double hydroxide as catalyst precursors for the hydrogenolysis of glycerol. *Chin. J. Catal.* **2013**, *34*, 986–992. [CrossRef]
- Xia, S.; Yuan, Z.; Wang, L.; Chen, P.; Hou, Z. Hydrogenolysis of glycerol on bimetallic Pd–Cu/solid-base catalysts prepared via layered double hydroxides precursors. *Appl. Catal. A Gen.* **2011**, *403*, 173–182. [CrossRef]
- Mondal, S.; Janardhan, R.; Lal Meena, M.; Biswas, P. Highly active Cu–Zn–Mg–Al–O catalyst derived from layered double hydroxides (LDHs) precursor for selective hydrogenolysis of glycerol to 1,2-propanediol. *J. Environ. Chem. Eng.* **2017**, *5*, 5695–5706. [CrossRef]

28. Geng, G.; Wei, R.; Liang, T.; Zhou, M.; Xiao, G. Hydrogenolysis of glycerol to propanediols on Cu–Ca–Al hydrotalcites derived catalysts. *Reac. Kinet. Mech. Catal.* **2016**, *117*, 239–251. [CrossRef]
29. Fan, G.; Li, F. Effect of sodium borohydride on growth process of controlled flower-like nanostructured Cu₂O/CuO films and their hydrophobic property. *Chem. Eng. J.* **2011**, *167*, 388–396. [CrossRef]
30. Peng, S.; Li, L.; Srinivasan, M. Electrospun CuFe₂O₄ nanotubes as anodes for high-performance lithium-ion batteries. *J. Energy Chem.* **2014**, *23*, 301–307. [CrossRef]
31. Shafi, K.V.P.M.; Gedanken, A.; Prozorov, R.; Balogh, J. Sonochemical preparation and size-dependent properties of nanostructured CoFe₂O₄ particles. *Chem. Mater.* **1998**, *10*, 3445–3450. [CrossRef]
32. Xiao, Z.; Jin, S.; Wang, X.; Li, W.; Wang, J.; Liang, C. Preparation, structure and catalytic properties of magnetically separable Cu-Fe catalysts for glycerol hydrogenolysis. *J. Mater. Chem.* **2012**, *22*, 16598–16605. [CrossRef]
33. Gao, W.; Zhao, Y.; Liu, J.; Huang, Q.; He, S.; Li, C.; Zhao, J.; Wei, M. Catalytic conversion of syngas to mixed alcohols over CuFe-based catalysts derived from layered double hydroxides. *Catal. Sci. Technol.* **2013**, *3*, 1324–1332. [CrossRef]
34. Oar-Arteta, L.; Remiro, A.; Vicente, J.; Aguayo, A.T.; Bilbao, J.; Gayubo, A.G. Stability of CuZnOAl₂O₃/HZSM-5 and CuFe₂O₄/HZSM-5 catalysts in dimethyl ether steam reforming operating in reaction–regeneration cycles. *Fuel Process. Technol.* **2014**, *126*, 145–154. [CrossRef]
35. Lin, X.; Zhang, Y.; Yin, L. Effect of various precipitants on activity and thermal stability of CuFe₂O₄ water-gas shift catalysts. *J. Fuel Chem. Technol.* **2014**, *42*, 1087–1092. [CrossRef]
36. Sun, Y.; Tao, L.; You, T.; Li, C.; Shan, H. Effect of sulfation on the performance of Fe₂O₃/Al₂O₃ catalyst in catalytic dehydrogenation of propane to propylene. *Chem. Eng. J.* **2014**, *244*, 145–151. [CrossRef]
37. Zhang, Q.; Wang, H.; Ning, P.; Song, Z.; Liu, X.; Duan, Y. In situ DRIFTS studies on CuO-Fe₂O₃ catalysts for low temperature selective catalytic oxidation of ammonia to nitrogen. *Appl. Surf. Sci.* **2017**, *419*, 733–743. [CrossRef]
38. Shi, X.; Chu, B.; Wang, F.; Wei, X.; Teng, L.; Fan, M.; Li, B.; Dong, L.; Dong, L. Mn-modified CuO, CuFe₂O₄ and γ -Fe₂O₃ three-phase strong synergistic coexistence catalyst system for NO reduction by CO with wider active window. *ACS Appl. Mater. Interfaces* **2018**, *10*, 40509–40522. [CrossRef]
39. Faheem, M.; Jiang, X.; Wang, L.; Shen, J. Synthesis of Cu₂O–CuFe₂O₄ microparticles from Fenton sludge and its application in the Fenton process: The key role of Cu₂O in the catalytic degradation of phenol. *RSC Adv.* **2018**, *8*, 5740–5748. [CrossRef]
40. Karim, K.M.R.; Tarek, M.; Ong, H.R.; Abdullah, H.; Yousuf, A.; Cheng, C.K.; Khan, M.M.R. Photoelectrocatalytic reduction of carbon dioxide to methanol using CuFe₂O₄ modified with graphene oxide under visible light irradiation. *Ind. Eng. Chem. Res.* **2019**, *58*, 563–572. [CrossRef]
41. Dubecký, F.; Kindl, D.; Hubík, P.; Mičušík, M.; Dubecký, M.; Boháček, P.; Vanko, G.; Gombia, E.; Nečas, V.; Mudroň, J. A comparative study of Mg and Pt contacts on semi-insulating GaAs: Electrical and XPS characterization. *Appl. Surf. Sci.* **2017**, *395*, 131–135. [CrossRef]
42. Li, W.H.; Sun, Y.H. Surface properties and CO adsorption on zirconia polymorphs. *J. Mol. Catal. A Chem.* **2005**, *227*, 119–124.
43. Coleman, L.J.I.; Epling, W.; Hudgins, P.R.; Croiset, E. Ni/Mg–Al mixed oxide catalyst for the steam reforming of ethanol. *Appl. Catal. A Gen.* **2009**, *363*, 52–63. [CrossRef]
44. Yu, X.; Wang, N.; Chu, W.; Liu, M. Carbon dioxide reforming of methane for syngas production over La-promoted NiMgAl catalysts derived from hydrotalcites. *Chem. Eng. J.* **2012**, *209*, 623–632. [CrossRef]
45. Wang, Y.; Li, H.; Li, X.; Chen, D.; Xiao, W. An effective iron catalyst supported on mixed MgO–Al₂O₃ for Fischer-Tropsch synthesis to olefins. *Ind. Eng. Chem. Res.* **2020**, *59*, 11462–11474. [CrossRef]
46. Balaraju, M.; Jagadeeswaraiyah, K.; Sai Prasad, P.S.; Lingaiah, N. Catalytic hydrogenolysis of biodiesel derived glycerol to 1,2-propanediol over Cu–MgO catalysts. *Catal. Sci. Technol.* **2012**, *2*, 1967–1976. [CrossRef]
47. Li, S.; Lv, S.; Zhang, Y.; Li, J.; Liu, Z.; Wang, L. Syngas-derived olefins over iron-based catalysts: Effects of basic properties of MgO nanocrystals. *J. Fuel Chem. Technol.* **2018**, *46*, 1342–1351. [CrossRef]
48. Marianou, A.A.; Michailof, C.M.; Ipsakis, D.K.; Karakoulia, S.A.; Kalogiannis, K.G.; Yiannoulakis, H.; Triantafyllidis, K.S.; Lappas, A.A. Isomerization of glucose into fructose over natural and synthetic MgO catalysts. *ACS Sustain. Chem. Eng.* **2018**, *6*, 16459–16470. [CrossRef]
49. Montassier, C.; Giraud, D.; Barbier, J. Polyol conversion by liquid phase heterogeneous catalysis over metals. *Stud. Sur. Sci. Catal.* **1988**, *41*, 165–170.

Article

Effect of Reduction Atmosphere on Structure and Catalytic Performance of PtIn/Mg(Al)O/ZnO for Propane Dehydrogenation

Ming Zhang ¹, Zhen Song ¹, Mengquan Guo ¹, Xiangxiang Li ¹, Yanjun Lin ^{2,*} and Lihong Zhang ^{1,*} 

¹ Department of Catalysis Science and Technology and Tianjin Key Laboratory of Applied Catalysis Science Technology, School of Chemical Engineering and Technology, Tianjin University, Tianjin 300350, China; minne_zhang@hotmail.com (M.Z.); songzhens12345@163.com (Z.S.); Guo_mengquan@163.com (M.G.); lixx_37@tju.edu.cn (X.L.)

² State Key Laboratory of Chemical Resource Engineering, Beijing University of Chemical Technology, Beijing 100029, China

* Correspondence: linyj@mail.buct.edu.cn (Y.L.); zlh_224@163.com (L.Z.); Tel.: +86-136-4138-6787 (Y.L.); +86-150-2225-5828 (L.Z.)

Received: 17 March 2020; Accepted: 24 April 2020; Published: 29 April 2020

Abstract: The effect of reduction atmospheres, H₂/N₂, C₃H₈/H₂/N₂, C₃H₈ and CO, on the structure and propane direct dehydrogenation performance of PtIn/Mg(Al)O/ZnO catalyst derived from ZnO-supported PtIn-hydrotalcite was studied. The physicochemical properties of the as-prepared and used catalytic system were characterized by various characterization methods. The results show that the dehydrogenation performance, especially the stability of the PtIn/Mg(Al)O/ZnO catalyst, was significantly improved along with the change in reduction atmosphere. The highest catalytic activity (51% of propane conversion and 97% propylene selectivity), resistance toward coke deposition, and stability for more than 30 h were achieved with the H₂/N-reduced catalyst. The optimal dehydrogenation performance and coke resistance are mainly related to the high Pt dispersion and In⁰/In³⁺ molar ratio, strong Pt–In interaction and small metal particle size, depending on the nature of the reduction atmospheres. The reconstruction of meixnerite favors the stability and coke resistance to some extent.

Keywords: propane dehydrogenation; reduction atmosphere; coke deposition; meixnerite; PtIn/Mg(Al)O/ZnO

1. Introduction

In recent years, the dehydrogenation of low alkanes to the corresponding alkenes has drawn great attention from the world, due to their extensive utilization as raw materials and a versatile class of intermediates in the polymer industry. In this context, it is particularly important to dehydrogenate propane to propylene (PDH) because of the rapidly growing demand for propylene in the production of propylene oxide, acrylonitrile and polypropylene [1–3]. The preparation and structure studies of catalysts with high efficiency propylene yield become the key point of PDH.

At present, Al-Cu catalysts, Co/SiO₂ catalysts, Ce-based catalysts, etc., are mainly novel catalysts developed by researchers [4–6]. However, Pt-based catalysts are still regarded as the most effective catalysts for PDH process, especially when working with a promoter, such as In, Sn, Ga or Zn, which can further improve propylene selectivity [1,7–10].

The support materials, Al₂O₃ [11], SiO₂ [6], ZrO₂ [12,13] and zeolite [3,14], can also affect catalytic performance on account of the significant differences in textural properties. Especially, the Mg(Al)O

oxides obtained by calcining hydrotalcite compounds (HT) have been studied extensively during the past years, owing to their suitable acid–base properties, high thermal stability, large surface area and memory effect [15–23]. Simultaneously, the stability of support plays an important role in reactions. Many works have been tried to stabilize the HT-based catalysts by combining with graphene networks [17,24], growing on metal (Al, Ni) or alloy substrates [25,26] and loading on oxide materials (γ -Al₂O₃, ZnO, SnO₂) [27–29].

It is well known that the activity of PDH is susceptible to many factors. Some researchers have studied the preparation conditions of Mg(Al)O support, such as Mg/Al molar ratio, pH value, and calcination temperature of the HT precursor [19,21,30,31]. Others have discussed the effect of loading methods and precursors of Pt on PDH [32,33]. Still others investigated the dehydrogenation reaction conditions (temperature, co-feed gas), In/Pt molar ratio and formation of PtIn alloy [15,34,35]. Most of the factors have been studied in detail. However, this does not seem to be the case for the reduction atmosphere of Mg(Al)O-supported Pt-based catalysts. Thus, the relationships between reduction atmosphere and catalysts' performance deserve to be studied.

In this paper, the influence of reduction atmospheres on the structural properties and catalytic performance of the PtIn/Mg(Al)O/ZnO (PtIn/MAZ) catalytic system was studied. ZnO was employed as the support for PtIn/Mg(Al)O catalytic system on account of its good stability. On this basis, ZnO-supported HT was prepared by the hydrothermal method, then In and Pt elements were introduced into the HT layer by sequential impregnation-induced reconstruction. H₂/N₂, C₃H₈/H₂/N₂, C₃H₈ and CO were selected as the reduction atmospheres, which are commonly used or produced in the reaction and likely to affect the catalytic performance. The precursors, calcined samples and reduced catalytic system were characterized by X-ray diffraction (XRD), transmission electron microscopy (TEM), X-ray photoelectron spectroscopy (XPS), Thermogravimetric (TG) and CO chemisorption. The PDH reaction was performed at 600 °C and atmospheric pressure with the gas mixture of C₃H₈, H₂ and N₂.

2. Results and Discussion

2.1. Catalytic Activity

A series of PtIn/MAZ reduced with different atmospheres (H₂/N₂, C₃H₈/H₂/N₂, C₃H₈ and CO) at 600 °C for 2.5 h were evaluated in PDH reaction, and their propane conversions and propylene and by-product selectivities as a function of time on stream are shown in Figure 1. During the 17 h on stream, propane conversion and propylene selectivity showed an obvious improvement with the reduction atmosphere changing from CO to C₃H₈ and to C₃H₈/H₂/N₂. This should arise from the different surface chemical states of the active metal species. An “induction period” appeared for all samples, especially the activity of the CO-reduced sample, which had a long induction period. This can be explained by the in-situ creation of the active metal species [11]. Additionally, it was found that there nearly no cracking products were formed on the samples reduced with C₃H₈ and C₃H₈/H₂/N₂ during the period of ~ 17 h. However, the CO-reduced sample had more cracking products at the initial stage and presented a decreasing tendency with time on stream, together with ascending propylene selectivity. This agrees with the phenomenon that CO pre-reduction can result in violent cracking at the initial stage [36,37]. Furthermore, the replacement of C₃H₈/H₂/N₂ by H₂/N₂ slightly decreased the conversion but enhanced the initial activity and catalytic stability. Nevertheless, there were no obvious difference between their propylene and by-product selectivities during the reaction lasting for 17 h.

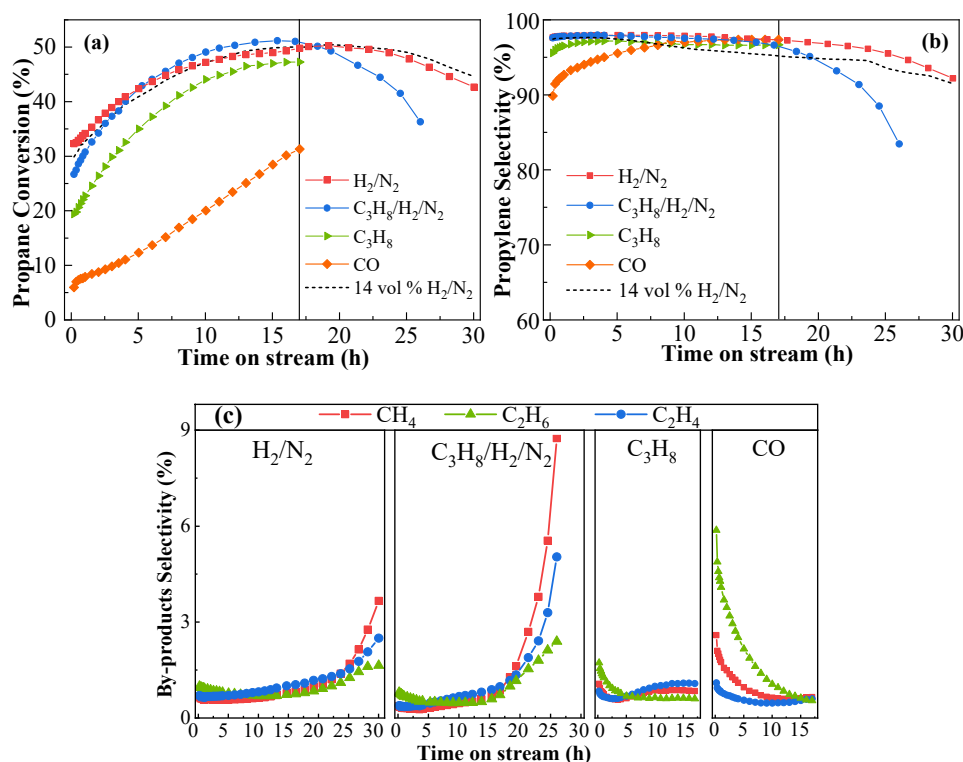


Figure 1. Catalytic performances of PtIn/MAZ catalytic system reduced with different atmospheres: (a) propane conversion; (b) propylene selectivity; (c) by-product selectivity (reduction conditions: T = 600 °C, t = 2.5 h; reaction conditions: T = 600 °C, weight hourly space velocity (WSHV) = 3 h⁻¹, atmospheric pressure in the gas mixture of C₃H₈:H₂:N₂ molar ratio = 8:7:35; reaction time: 30 h for H₂/N₂ and 14 vol % H₂/N₂ reduced catalyst, 26 h for C₃H₈/H₂/N₂-reduced catalyst, 17 h for C₃H₈ and CO-reduced catalyst).

Since the activities of C₃H₈/H₂/N₂- and H₂/N₂-reduced catalytic systems were much higher than those of the others, the reaction time was extended to 30 h to compare the stability of the C₃H₈/H₂/N₂- and H₂/N₂-reduced catalytic systems. When the reaction time was prolonged, some distinct and significant differences could be found between them. With a reaction of 30 h, the propane conversion and propylene selectivity of H₂/N₂-reduced samples were maintained at more than 45% and 92% and the by-product selectivity was less than 4%, respectively. However, the C₃H₈/H₂/N₂-reduced catalyst showed a rapid decrease of propane conversion and propylene selectivity after 18 h along with the increase of cracking products. In order to evaluate the effect of H₂ content, the 14 vol% H₂/N₂ with the same H₂ content as C₃H₈/H₂/N₂ was also adopted for the comparison. It is noticeable that the propane conversion and propylene selectivity of the 14 vol% H₂/N₂-reduced sample was similar to that of the H₂/N₂-reduced one. This indicates that the reducibility of H₂/N₂ is quite similar to that of 14 vol% H₂/N₂ under this reduction temperature. Therefore, the different performance between H₂/N₂ and C₃H₈/H₂/N₂ is arising from the presence of C₃H₈ in C₃H₈/H₂/N₂, which makes the C₃H₈/H₂/N₂-reduced sample rapidly deactivate along with the increase of cracking products. Meanwhile, the H₂/N₂-reduced sample had effective catalytic stability and crack resistance.

2.2. Texture and Structure of Reduced Catalytic Systems

2.2.1. XRD

According to the XRD patterns of precursors and calcined samples obtained with different preparation processes in Figure S1, it could be confirmed that the HT phase can be formed on the ZnO precursor (hydrozincite phase, JCPDS file No. 19-1458); even the ZnO-supported PtIn-HT can be acquired by impregnation-induced reconstruction. After calcination, only MgO phases (JCPDS file

No. 87-0651) could be indexed on ZnO (JCPDS file No. 75-0576). The Al_2O_3 diffraction peaks could not be found, as it is retained and located in interstitial sites in the MgO framework after calcination [38]. There were no diffraction peaks of Pt-(In-)-based compounds, as a result of their low concentration or uniform distribution [38].

In order to evaluate the crystalline phase of the reduced PtIn/MAZ catalytic system, XRD characterization was conducted, and the results are shown in Figure 2. It can be noted that the XRD patterns of all samples show the same crystalline diffraction peaks. The main crystalline phases were ZnO and MgO and the peaks were same with those of calcined ones (Figure S1B). This means the change in reduction atmosphere did not cause the obvious change of crystal phases. The diffraction peaks of Pt(In)-species still could not be recognized for the reduced PtIn/MAZ catalytic system. This is owing to the small and uniform distribution of Pt(In) species on the support or the low concentration [19].

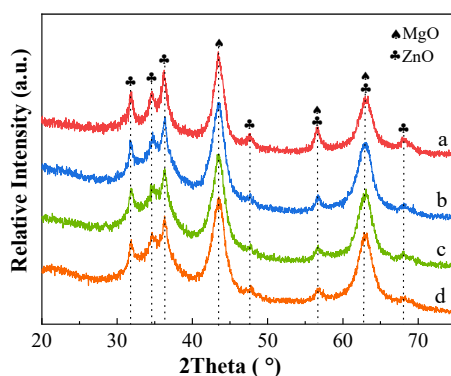


Figure 2. XRD patterns of PtIn/MAZ catalytic systems reduced with different atmospheres: (a) H_2/N_2 ; (b) $\text{C}_3\text{H}_8/\text{H}_2/\text{N}_2$; (c) C_3H_8 ; (d) CO (reduction conditions: $T = 600\text{ }^\circ\text{C}$, $t = 2.5\text{ h}$).

2.2.2. TEM

The morphology, phase composition and particle size distribution (PSD) of the reduced catalytic system are given in Figure 3. Although it is difficult to distinguish the diffraction of metallic phases from the XRD patterns in Figure 1, the metallic Pt (111) nanoparticles (NPs) can be recognized in the HR-TEM depending on the lattice spacing of 0.226 nm. Meanwhile, PtIn alloy ($d = 0.208\text{ nm}$) can be detected on the H_2/N_2 -reduced sample. From the PSD of all samples, the average particle size of metals was in the range from 0.85–1.20 nm. The small metal NPs can be related to the PtIn-HT reconstruction, as described in Figure S1. Moreover, the average metal particle sizes of H_2/N_2 - and $\text{C}_3\text{H}_8/\text{H}_2/\text{N}_2$ -reduced samples are smaller than that of C_3H_8 - and CO-reduced ones. This indicates that the H_2 -containing reduction gas is more efficient to obtain smaller metallic particles. The smaller metal particles are more active for propane dehydrogenation performance and beneficial to resist the coke deposition [39].

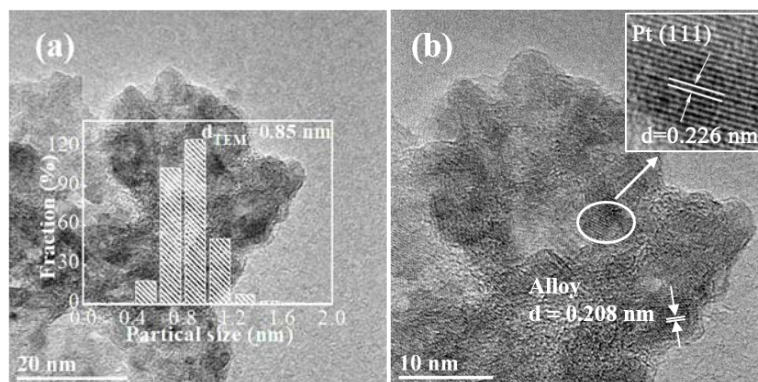


Figure 3. Cont.

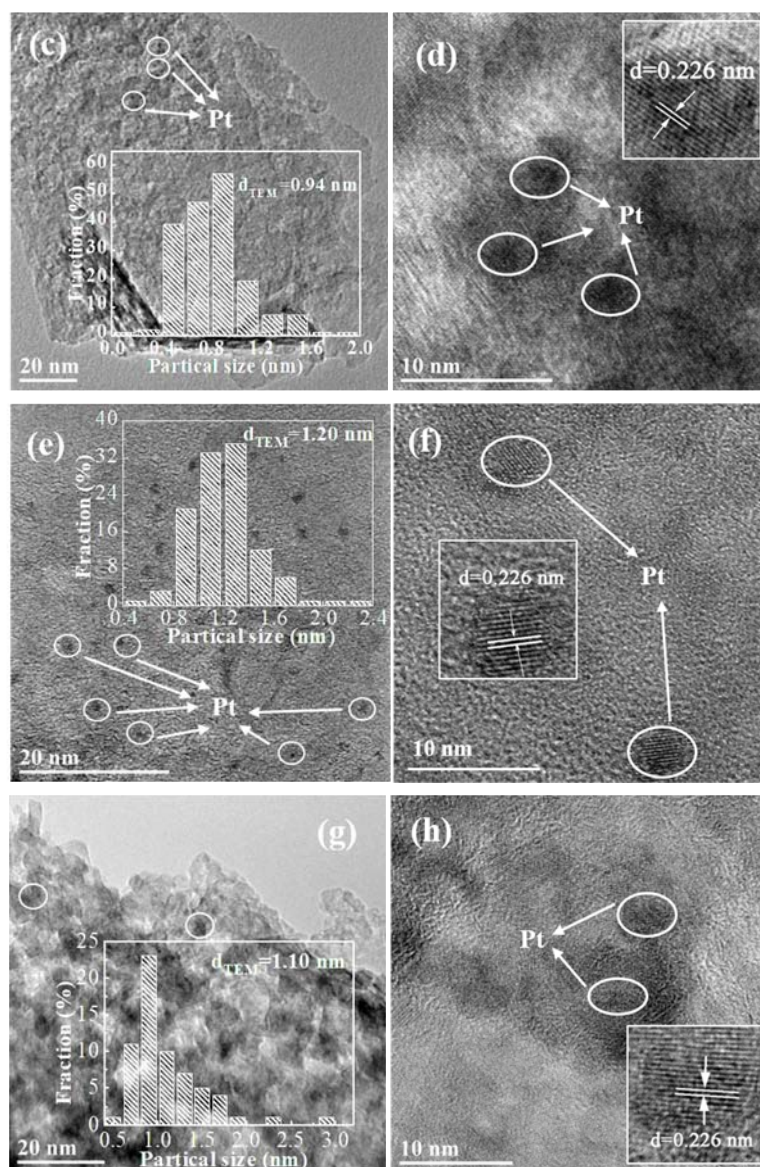


Figure 3. TEM images, HR-TEM and the statistics of PSD in the insets of PtIn/MAZ catalytic system reduced with different atmospheres: (a,b) H_2/N_2 ; (c,d) $\text{C}_3\text{H}_8/\text{H}_2/\text{N}_2$; (e,f) C_3H_8 ; (g,h) CO (reduction conditions: $T = 600\text{ }^\circ\text{C}$, $t = 2.5\text{ h}$).

2.2.3. XPS

The chemical states of In species over the reduced catalytic system were determined by XPS measurements. The Pt 4f spectra is not shown here due to the difficulty of distinguishing it from the Al 2p peak [40]. The XPS spectra of the $\text{In}3d_{5/2}$ region are shown in Figure 4, and the semi-quantitative results of the corresponding spectra are summarized in Table 1. The $\text{In}3d_{5/2}$ level can be split into two peaks at $\sim 444.1\text{ eV}$ and $\sim 445.2\text{ eV}$, which represent In^0 (metallic In or PtIn alloy) and In^{3+} , respectively. As shown in Table 1, the $\text{In}^0/\text{In}^{3+}$ molar ratios for H_2/N_2 -, $\text{C}_3\text{H}_8/\text{H}_2/\text{N}_2$ -, C_3H_8 - and CO-reduced samples were 2.50, 1.22, 0.59 and 0.78, respectively. According to the downward trend of the $\text{In}^0/\text{In}^{3+}$ molar ratio from H_2/N_2 to $\text{C}_3\text{H}_8/\text{H}_2/\text{N}_2$ and to C_3H_8 , it is assumed that the presence of C_3H_8 can impede the formation of zero-valence In. The deduction is based on the similar reducibility between H_2/N_2 and 14 vol % H_2/N_2 , which has been proved by the corresponding catalytic performance in Figure 1. In view of this, the $\text{In}^0/\text{In}^{3+}$ molar ratio in the $\text{C}_3\text{H}_8/\text{H}_2/\text{N}_2$ -reduced sample should be equal to or higher than that of the H_2/N_2 -reduced one, due to the co-existence of H_2 and C_3H_8 . The opposite

results indicate that the C_3H_8 must impede the reduction of In^{3+} ions. In this way, it is not difficult to understand why the In^0/In^{3+} molar ratio of CO-reduced sample was higher than C_3H_8 -reduced one. The In^0/In^{3+} molar ratio of the CO-reduced sample was lower than that of H_2 -containing reduced sample, indicating that the reduction ability of CO to In^{3+} was weaker than that of H_2 . The In^0 has been proved to promote the transfer of coke from the active site to the support and the stabilization of the active metal species [40,41]. Meanwhile, the presence of C_3H_8 leads to a decrease of In^0 , thus the propylene selectivity of the H_2/N_2 -, $C_3H_8/H_2/N_2$ - and C_3H_8 -reduced catalytic systems decreases accordingly (see Figure 1).

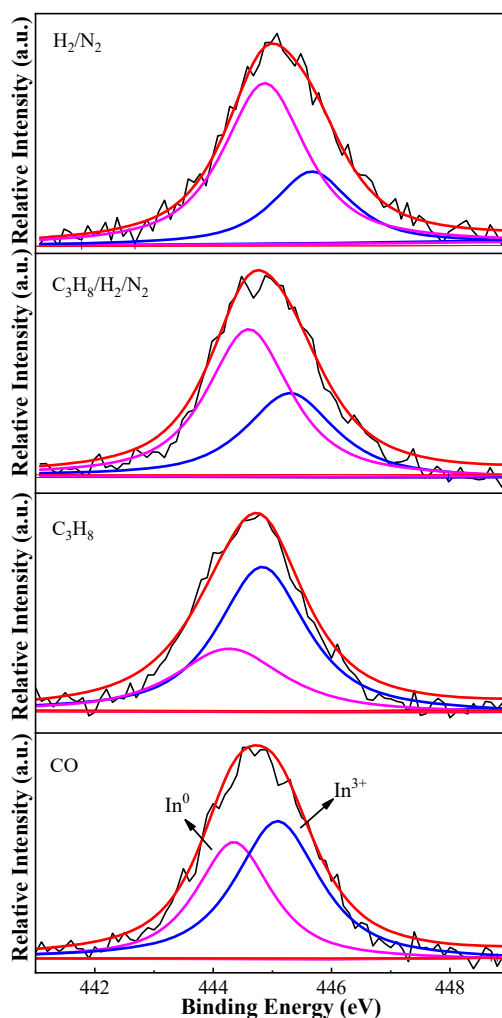


Figure 4. $In3d_{5/2}$ XPS spectra of a PtIn/MAZ catalytic system reduced with different atmospheres (reduction conditions: $T = 600\text{ }^{\circ}C$, $t = 2.5\text{ h}$).

Table 1. XPS results and Pt dispersion of a PtIn/MAZ catalytic system reduced with different atmospheres ^a (reduction conditions: $T = 600\text{ }^{\circ}C$, $t = 2.5\text{ h}$).

Reduction Atmosphere	Binding Energy (eV)		In^0/In^{3+} Molar Ratio ^b	Pt Dispersion ^c
	In^0	In^{3+}		
H_2/N_2	444.9	445.7	2.50	48%
$C_3H_8/H_2/N_2$	444.5	445.2	1.22	34%
C_3H_8	444.3	444.8	0.59	—
CO	444.4	445.1	0.78	—

^a All samples were protected with Ar from oxidation prior to test. ^b Calculated from the fitting peak area results of $In3d_{5/2}$ XPS spectra. ^c Computed from the CO chemisorption results.

The binding energy (BE) value of In^0 presented a slightly decreasing trend in accordance with the order of H_2/N_2 -, $\text{C}_3\text{H}_8/\text{H}_2/\text{N}_2$ -, CO- and C_3H_8 -reduced samples, signifying the weakening Pt–In interaction and transfer of electrons from metallic In to Pt species [22]. The electron-rich Pt sites are beneficial to hindering the adsorption of alkenes on active sites, consequently decreasing the likelihood of hydrogenolysis and coking [42].

The Pt dispersion of H_2/N_2 - and $\text{C}_3\text{H}_8/\text{H}_2/\text{N}_2$ -reduced samples was evaluated by CO chemisorption due to their far better propane dehydrogenation performance than the other two samples. According to the results in Table 1, the 48% dispersion of H_2/N_2 reduced sample is obviously higher than the 34% dispersion of the $\text{C}_3\text{H}_8/\text{H}_2/\text{N}_2$ -reduced one. This indicates that the H_2/N_2 -reduced catalyst had a higher utilization of Pt. Combined with the high $\text{In}^0/\text{In}^{3+}$ molar ratio and the formation of PtIn alloy in the H_2/N_2 -reduced sample, it can be deduced that the Pt–In synergistic effect, high Pt dispersion and large In^0 content result in good activity and high stability to some degree.

2.3. Analysis of The Used Catalytic System

2.3.1. XRD

Figure 5 shows the XRD patterns of the used catalytic system. Compared with the reduced catalytic system, the characteristic diffraction peaks of graphite (JCPDS file No. 75-1621) appear at 2θ of ca. 26° and 44° . The peak intensity at 2θ of 26° cuts down progressively following the order of the catalyst reduced with C_3H_8 , $\text{C}_3\text{H}_8/\text{H}_2/\text{N}_2$, CO and H_2/N_2 , which is correlated with the crystallinity of graphite. It can be declared that the heavily condensed coke species are more difficult to form on the H_2/N_2 -reduced catalyst than others. At the same time, this also means that the H_2/N_2 -reduced catalyst is easy to regenerate via oxidation in air [43]. In addition, the Pt and In species still cannot be distinguished, indicating that the metal species are quite stable and highly dispersed on the surface of PtIn/MAZ.

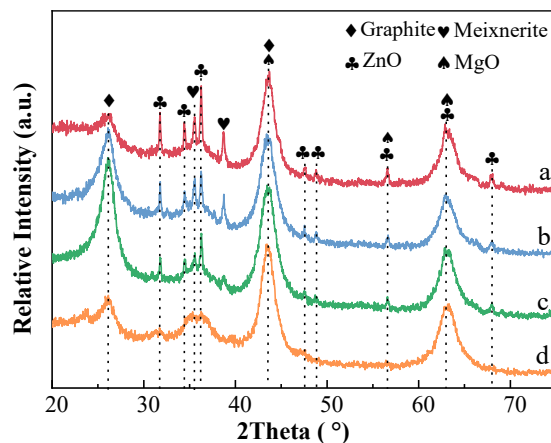


Figure 5. XRD patterns of the used PtIn/MAZ catalytic system reduced with different atmospheres: (a) H_2/N_2 ; (b) $\text{C}_3\text{H}_8/\text{H}_2/\text{N}_2$; (c) C_3H_8 ; (d) CO (reduction conditions: $T = 600^\circ\text{C}$, $t = 2.5\text{ h}$; reaction conditions: $T = 600^\circ\text{C}$, $\text{WSHV} = 3\text{ h}^{-1}$, atmospheric pressure in the gas mixture of $\text{C}_3\text{H}_8:\text{H}_2:\text{N}_2$ molar ratio = 8:7:35 for 17 h).

It is interesting to notice that the diffraction peaks of meixnerite (JCPDS file No. 38-0478) appeared at 2θ of 35° and 39° in the used catalytic system, instead of the reduced ones reported in [43]. This arises from the high dispersion or low content of meixnerite. On the other hand, the intensity of the corresponding diffraction peaks decreased gradually with the order of H_2/N_2 , $\text{C}_3\text{H}_8/\text{H}_2/\text{N}_2$, C_3H_8 and CO-reduced sample, and even completely disappeared for PtIn/MAZ reduced with CO.

The formation of meixnerite can be explained by the reconstruction of the calcined HT under the humidified conditions [41,44–46]. As we all know, the calcination can cause H_2O and $-\text{OH}$ removal from the structure [47,48]. However some highly temperature-stable $\text{M}-\text{OH}_2$ can be formed on the

surface of PtIn/MAZ after reduction with H-containing gas, due to the strong water affinity of calcined HT structure [45]. It is just that the PDH reaction further provides the sufficient -OH_2 concentration level and exposure time on the surface of calcined HT, which makes the calcined HT reconstruct into meixnerite. Therefore, the differences of meixnerite peak intensity among the H_2/N_2 -, $\text{C}_3\text{H}_8/\text{H}_2/\text{N}_2$ - and C_3H_8 -reduced samples can arise from the different levels of -OH_2 , depending on the reducibility of these atmospheres. As a result, the strong diffraction peaks of meixnerite can be obtained by the H_2/N_2 -reduced sample. The complete disappearance of meixnerite for the CO-reduced sample may have been induced by the formation of bicarbonate species, together with the consumption of oxygen, resulting in no conditions for the formation of meixnerite [36]. As a kind of HT with an interlayer -OH anion, the high crystallinity meixnerite may be helpful to keep the high dispersion and uniform distribution of surface metal active sites during reaction. As a result, the good stability of the H_2/N_2 -reduced sample can arise from the formation of meixnerite to a certain extent [17].

Additionally, it has been proved that the meixnerite has Brønsted basicity [49], which is different from the Lewis basicity of calcined HT. Thus, the formation of meixnerite can adjust the acid–base properties of the catalyst and improve its coke resistance [50,51]. However, it is difficult to evaluate the acid–base properties by conventional methods because of the influence of deposited coke on the formed meixnerite [50,51]. As compared with the diffraction strength of meixnerite, the only direct evidence is that the diffraction strength of graphite and the amount of deposited coke (see TG analysis below) show an opposite trend in accordance with the order from H_2/N_2 - to $\text{C}_3\text{H}_8/\text{H}_2/\text{N}_2$ - and C_3H_8 -reduced catalysts.

2.3.2. TEM

After a reaction of 17 h, the TEM images and the PSD statistics of the used catalytic system reduced with different atmospheres are shown in Figure 6. It was found that the range of PSD became wider, but the average metal particle size only showed a slight increase compared with the corresponding reduced catalytic system. The slight aggregation of metal particles agrees with the fact that the reaction is not in the deactivation stage (Figure 1). It is worth noting that the metal sintering degree of the $\text{C}_3\text{H}_8/\text{H}_2/\text{N}_2$ -reduced sample was higher than that of the H_2/N_2 -reduced one, although they had similar catalytic performance during a reaction of 17 h. Therefore, this can be used to explain the stable catalytic performance of the H_2/N_2 -reduced catalyst and the rapid decline in reactivity of the $\text{C}_3\text{H}_8/\text{H}_2/\text{N}_2$ -reduced sample after a reaction of 17 h. This is attributable to the initial smaller metal particles and high Pt dispersion of the H_2/N_2 -reduced catalyst. Meanwhile, it indicates strong Pt–In or Pt–support interaction, which results in the superior stability of Pt during the PDH reaction [40]. Coke deposits can be found on the support surface of the used catalytic system instead of the active site, which means that the formed coke should be shifted to the surface of support before a reaction of 17 h [40].

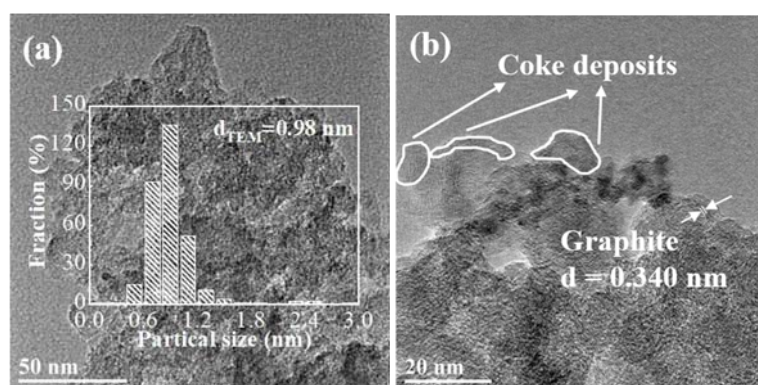


Figure 6. Cont.

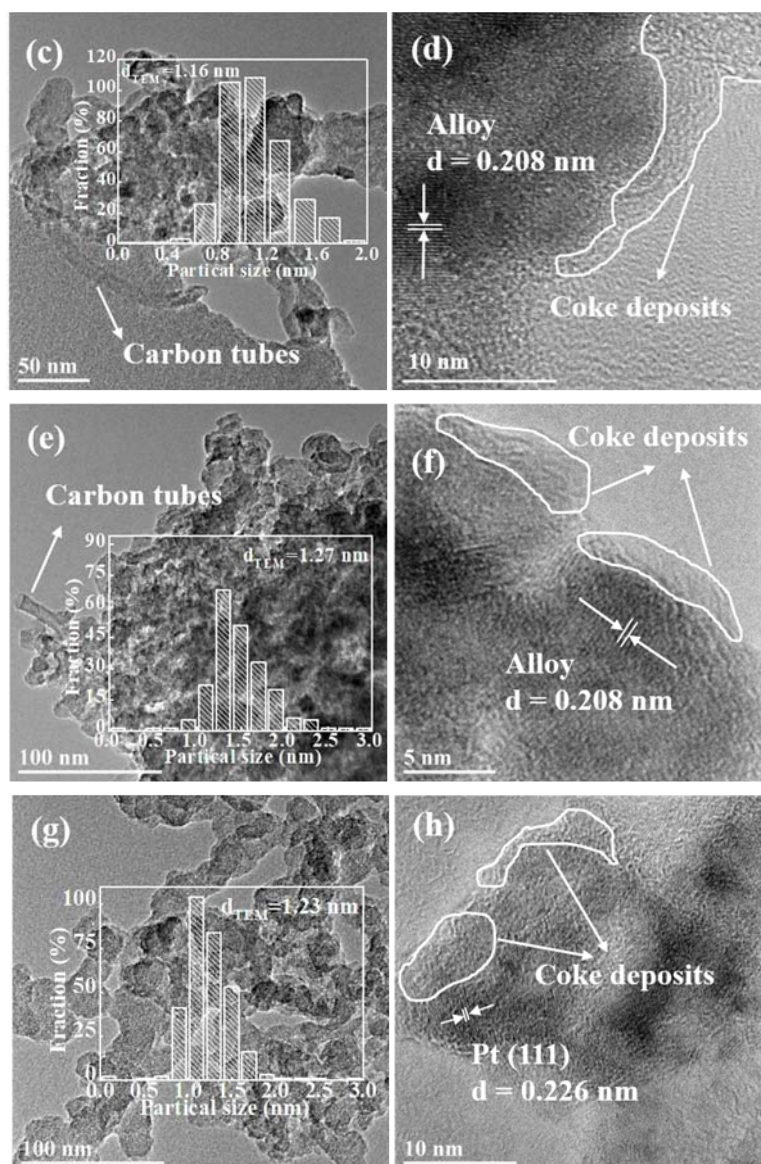


Figure 6. TEM images and the statistics of PSD in the insets of the used PtIn/MAZ catalytic system reduced with different atmospheres: (a,b) H_2/N_2 ; (c,d) $\text{C}_3\text{H}_8/\text{H}_2/\text{N}_2$; (e,f) C_3H_8 ; (g,h) CO (reduction conditions: $T = 600\text{ }^\circ\text{C}$, $t = 2.5\text{ h}$; reaction conditions: $T = 600\text{ }^\circ\text{C}$, $\text{WSHV} = 3\text{ h}^{-1}$, atmospheric pressure in the gas mixture of $\text{C}_3\text{H}_8:\text{H}_2:\text{N}_2$ molar ratio = 8:7:35 for 17 h).

2.3.3. TG

In order to evaluate the amounts of deposited coke on the used catalytic system, the TG test was adopted, and the results are shown in Figure 7. The total deposited coke content of the catalyst pre-reduced with H_2/N_2 was only 27 wt %, and lower than the others, which coincided with its high propylene selectivity (see Figure 1). The lowest coke formation on H_2/N_2 -reduced catalyst should be related to the small metal particle size, strong Pt–In interaction and suitable acid–base properties caused by the formation of meixnerite. Meanwhile, the more In^0 species also can promote the transfer of coke deposition from the active sites to the support, maintaining the stability of active metal species, ensuring the selectivity of propylene and reducing the occurrence of cracking. The pre-reduction with $\text{C}_3\text{H}_8/\text{H}_2/\text{N}_2$ and C_3H_8 made the deposited coke content increase to ca. 50 wt %. The severe coke deposition has been proposed to explain the fast loss of activity of the $\text{C}_3\text{H}_8/\text{H}_2/\text{N}_2$ -reduced sample [47]. This is thought to be related to their wide PSD [47]. The mass loss of CO-reduced catalyst is lower than the $\text{C}_3\text{H}_8/\text{H}_2/\text{N}_2$ and C_3H_8 -reduced one is, because it is far below propane conversion than them.

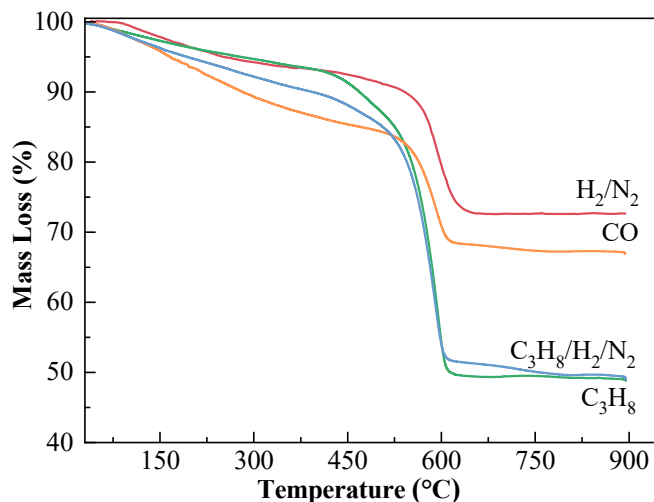


Figure 7. TG curves of the used PtIn/MAZ catalytic system reduced with different atmospheres (reduction conditions: $T = 600\text{ }^{\circ}\text{C}$, $t = 2.5\text{ h}$; reaction conditions: $T = 600\text{ }^{\circ}\text{C}$, $\text{WSHV} = 3\text{ h}^{-1}$, atmospheric pressure in the gas mixture of $\text{C}_3\text{H}_8:\text{H}_2:\text{N}_2$ molar ratio = 8:7:35 for 17 h).

In comparison with the state-of-the-art Pt-based catalysts in the literature (Table S1), the PtIn/MAZ catalytic system obtained in this work possesses much higher catalytic performance and attractive stability.

3. Materials and Methods

3.1. Materials

The reagents for the preparation of catalyst were analytical grade chemicals. $\text{Zn}(\text{NO}_3)_2 \cdot 6\text{H}_2\text{O}$, $\text{Mg}(\text{NO}_3)_2 \cdot 6\text{H}_2\text{O}$, $\text{Al}(\text{NO}_3)_3 \cdot 9\text{H}_2\text{O}$ and urea were purchased from Tianjin Fuchen Chemical Regents Factory (Tianjin, China). $\text{H}_2\text{PtCl}_6 \cdot 6\text{H}_2\text{O}$ was purchased from Tianjin Mascot Chemical Co. Ltd (Tianjin, China). $\text{InNO}_3 \cdot x\text{H}_2\text{O}$ was purchased from Aladdin Industrial corporation (Shanghai, China).

3.2. Preparation of ZnO Precursor

The ZnO precursor was prepared by the hydrothermal method. Briefly, 0.004 mol of $\text{Zn}(\text{NO}_3)_2 \cdot 6\text{H}_2\text{O}$ and 0.083 mol of urea was fully dissolved in 65 mL deionized water, then moved to a Teflon-lined stainless steel autoclave at $100\text{ }^{\circ}\text{C}$ for 20 h. After cooling to room temperature, the products were filtrated and washed with deionized water till neutrality, then dried at $100\text{ }^{\circ}\text{C}$ overnight to obtain the ZnO precursor.

3.3. Preparation of MAZ Support

The Mg(Al)O/ZnO (MAZ) precursor was prepared by the hydrothermal method. The molar ratio of Mg/Al is 2. Firstly, 0.1 g of ZnO precursor was introduced in 65 ml of a mixed solution, including 0.003 mol of $\text{Mg}(\text{NO}_3)_2 \cdot 6\text{H}_2\text{O}$, 0.0015 mol of $\text{Al}(\text{NO}_3)_3 \cdot 9\text{H}_2\text{O}$ and 0.1 mol of urea under vigorous stirring. After hydrothermal treatment in a Teflon-lined stainless-steel autoclave at $100\text{ }^{\circ}\text{C}$ for 20 h, the mixture was cooled to room temperature. Next, the slurry was filtrated and washed with deionized water till to neutrality, then dried at $100\text{ }^{\circ}\text{C}$ overnight. Finally, the corresponding MAZ support was obtained by calcining the precursor at $600\text{ }^{\circ}\text{C}$ for 4 h in a muffle furnace with a heating rate of $5\text{ }^{\circ}\text{C min}^{-1}$.

3.4. Preparation and Reduction of PtIn/MAZ

The PtIn/MAZ precursor was synthesized via successive incipient wetness impregnation method. Firstly, the MAZ support was impregnated with an $\text{InNO}_3 \cdot x\text{H}_2\text{O}$ aqueous solution at room temperature

for 6 h and dried at 120 °C for 12 h to acquire the In/MAZ precursor. After calcination at 550 °C for 4 h, the In-based calcined product was obtained and labelled as In/MAZ. Next, the same processes were performed on In/MAZ by impregnating with an $\text{H}_2\text{PtCl}_6 \cdot 6\text{H}_2\text{O}$ aqueous solution to acquire the PtIn/MAZ precursor.

The calcined product PtIn/MAZ was obtained by calcining the corresponding precursor at 550 °C for 4 h with a heating rate of 5 °C min^{-1} [19,41]. To be consistent with previous research [22], the loading amounts of Pt and In were 0.5 wt % and 1.4 wt %, respectively.

Before the PDH reaction, PtIn/MAZ was reduced with different atmospheres. The reduction atmospheres of H_2/N_2 (5 vol % H_2), $\text{C}_3\text{H}_8/\text{H}_2/\text{N}_2$ (16 vol % C_3H_8 and 14 vol % H_2), C_3H_8 and CO were used to reduce PtIn/MAZ at 600 °C for 2.5 h respectively. In order to compare with H_2/N_2 (5 vol % H_2) and $\text{C}_3\text{H}_8/\text{H}_2/\text{N}_2$ (16 vol % C_3H_8 and 14 vol % H_2), the reduction gas of 14 vol % H_2/N_2 was also evaluated in the PDH reaction.

3.5. Catalyst Characterizations

The X-ray diffraction (XRD) patterns were recorded on a Bruker D8-Focus X-ray diffractometer (BRUKER AXS GMBH, Karlsruhe, Germany) equipped with $\text{Cu K}\alpha$ radiation ($\lambda = 0.15418$ nm). The samples were scanned from the 2θ value of 20°–75°, with a scanning speed of 8° \cdot min^{-1} . The X-ray tube was manipulated at 40 kV and 40 mA.

The transmission electron microscopy (TEM) images were taken with a JEM-2100F field-emission transmission electron microscope (JEOL, Tokyo, Japan) operated at 200 kV. The as-synthesized samples were dispersed, sonicated in ethanol, and dropped on carbon-film coated copper grids.

X-ray photoelectron spectroscopy (XPS) was carried out on a Perkin-Elmer PHI 5000C ESCA (PerkinElmer, Waltham, MA, USA) using $\text{Al K}\alpha$ radiation. Prior to the analysis, the samples were reduced under different atmospheres (30 mL min^{-1}) at 600 °C for 2.5 h, and the binding energies were calibrated using the $\text{C}1\text{s}$ peak at 284.8 eV as an internal standard. The whole process from reduction to test was strictly protected with Ar, which can avoid the re-oxidation of In^0 .

Thermogravimetric (TG) analysis was carried out with a DTG-50/50H thermal analyzer (PerkinElmer, Waltham, MA, USA) to determine the quantity of coke on the used catalyst, and the TG curves were recorded from room temperature to 900 °C at an increasing rate of 10 °C min^{-1} .

Dispersion of metals was determined by CO chemisorption, CO chemisorption was conducted on AutoChem II 2920 analyzer (Micromeritics, Norcross, GA, USA). For a fresh catalyst, 100 mg of sample was pre-reduced with different atmospheres at 600 °C for 2.5 h and then purged with Ar flow at 300 °C for 0.5 h. CO chemisorption was carried out at 30 °C by injecting 50 μL CO every 3 min until the peak area became stable. The adsorption capacity of CO is calculated by the following Equation.

$$\text{CO uptakes } (\mu\text{mol g}^{-1}_{\text{cat}}) = n \times (A - B) \times 50 \times 10 / A \times 22.4 \quad (1)$$

where n stands for the number of chemical adsorption peaks, A represents the average value of the peak area when the peak area remains constant, and B stands for the total area of the chemical adsorption peaks.

3.6. Catalytic Measurements

The PDH reactions were carried out in a fixed-bed quartz reactor with an 8-mm inner diameter. A quantity of 0.4 g of fresh catalyst (particle size of 40 to 60 meshes) was placed into the center of quartz tube reactor and reduced with different reduction atmospheres, as described in Section 2.3. Afterwards, the mixed gas, including C_3H_8 , H_2 and N_2 ($\text{C}_3\text{H}_8:\text{H}_2:\text{N}_2$ molar ratio = 8:7:35), was fed at a rate of 62 mL min^{-1} into the reactor. The PDH reactions were performed at atmospheric pressure, 600 °C and a weight hourly space velocity (WHSV) of 3 h^{-1} , which was generally used in relevant studies [21,52,53]. A gas chromatograph equipped with an FID detector and Al_2O_3 column was

employed to analyze the gas compositions. The propane conversion and propylene selectivity were calculated by the following Equations:

$$\text{Conversion}(\%) = \frac{\text{propane, in} - \text{propane, out}}{\text{propane, in}} \times 100 \quad (2)$$

$$\text{Selectivity}(\%) = \frac{\text{propylene, out}}{\text{propane, in} - \text{propane, out}} \times 100 \quad (3)$$

4. Conclusions

A catalyst, PtIn/Mg(Al)O/ZnO, can be obtained by calcination and reduction of ZnO-supported PtIn-HT. The reduction atmosphere has a profound influence on the physicochemical nature and catalytic performance of the PtIn/Mg(Al)O/ZnO catalyst. The propane conversion and propylene selectivity of the catalyst reduced with H₂/N₂ can reach 51% and 97%, respectively, and even stabilize at 45% and 92% after running for 30 h. This is mainly attributable to its high Pt dispersion and In⁰/In³⁺ molar ratio, strong Pt–In interaction and small metal particle size, which also result in a low content of coke deposits on the surface of the H₂/N₂-reduced catalyst. In addition, meixnerite can be formed after the reaction, and the crystallinity is influenced by the reduction atmosphere. At the same time, the formation of the high-crystallinity meixnerite can re-disperse the metal active sites and adjust the acid–base properties of the catalyst, thus improving the stability and coke resistance to some extent.

Supplementary Materials: The following are available online at <http://www.mdpi.com/2073-4344/10/5/485/s1>, Figure S1: XRD patterns of precursors (A) and the corresponding calcined samples (B): (a) ZnO; (b) MAZ; (c) In/MAZ; (d) PtIn/MAZ. Table S1. Comparison of the catalytic performance of some state-of-the-art catalysts used in propane dehydrogenation.

Author Contributions: M.Z. wrote the manuscript, performed the experiments and analyzed data; M.Z., Z.S. and M.G. collected references and characterized the physic-chemical properties of materials; X.L. collected and checked data; Y.L. analyzed data and checked the manuscript; L.Z. provided research ideas, analyzed data and revised the manuscript. All authors have read and agreed to the published version of the manuscript.

Funding: This research was funded by National Natural Science Foundation of China (21776214, 21776018).

Conflicts of Interest: The authors declare no conflict of interest.

References

1. Sun, P.; Siddiqi, G.; Chi, M.; Bell, A.T. Synthesis and characterization of a new catalyst Pt/Mg(Ga)(Al)O for alkane dehydrogenation. *J. Catal.* **2010**, *274*, 192–199. [CrossRef]
2. Sahebdelfar, S.; Bijani, P.M.; Saeedizad, M.; Zangeneh, F.T.; Ganji, K. Modeling of adiabatic moving-bed reactor for dehydrogenation of isobutane to isobutene. *Appl. Catal. A* **2011**, *395*, 107–113. [CrossRef]
3. Caeiro, G.; Carvalho, R.H.; Wang, X.; Lemos, M.A.N.D.; Lemos, F.; Guisnet, M.; Ramôa Ribeiro, F. Activation of C2-C4 alkanes over acid and bifunctional zeolite catalysts. *J. Mol. Catal. A Chem.* **2006**, *255*, 131–158. [CrossRef]
4. Schäferhans, J.; Gómez-Quero, S.; Aneeva, D.V.; Rothenberg, G. Novel and effective copper-aluminum propane dehydrogenation catalysts. *Chem.-Eur. J.* **2011**, *17*, 12254–12256. [CrossRef] [PubMed]
5. Beckers, J.; Rothenberg, G. Sustainable selective oxidations using ceria-based materials. *Green Chem.* **2010**, *12*, 939–948. [CrossRef]
6. Hu, B.; Bean Getsoian, A.; Schweitzer, N.M.; Das, U.; Kim, H.; Niklas, J.; Poluektov, O.; Curtiss, L.A.; Stair, P.C.; Miller, J.T.; et al. Selective propane dehydrogenation with single-site CoII on SiO₂ by a non-redox mechanism. *J. Catal.* **2015**, *322*, 24–37. [CrossRef]
7. Pakhomov, N.A. Reversible and Irreversible Deactivation of Supported Bimetallic Catalysts for the Dehydrogenation of Lower Paraffins. *Kinet. Catal.* **2001**, *42*, 334–343. [CrossRef]
8. De Miguel, S.; Castro, A.; Scelza, O.; Fierro, J.L.G.; Soria, J. FTIR and XPS study of supported PtSn catalysts used for light paraffins dehydrogenation. *Catal. Lett.* **1996**, *36*, 201–206. [CrossRef]

9. Jablonski, E.L.; Castro, A.A.; Scelza, O.A.; de Miguel, S.R. Effect of Ga addition to Pt/Al₂O₃ on the activity, selectivity and deactivation in the propane dehydrogenation. *Appl. Catal. A* **1999**, *183*, 189–198. [CrossRef]
10. Homs, N.; Llorca, J.; Riera, M.; Jolis, J.; Fierro, J.G.; Sales, J.; de la Piscina, P.R. Silica-supported PtSn alloy doped with Ga, In or, Tl: Characterization and catalytic behavior in n-hexane dehydrogenation. *J. Mol. Catal. A Chem.* **2003**, *200*, 251–259. [CrossRef]
11. Chen, M.; Xu, J.; Cao, Y.; He, H.; Fan, K.; Zhuang, J. Dehydrogenation of propane over In₂O₃-Al₂O₃ mixed oxide in the presence of carbon dioxide. *J. Catal.* **2010**, *272*, 101–108. [CrossRef]
12. Hoang, D.L.; Farrage, S.A.F.; Radnik, J.; Pohl, M.M.; Schneider, M.; Lieske, H.; Martin, A. A comparative study of zirconia and alumina supported Pt and Pt–Sn catalysts used for dehydrocyclization of n-octane. *Appl. Catal. A* **2007**, *333*, 67–77. [CrossRef]
13. Liu, Y.; Xia, C.; Wang, Q.; Zhang, L.; Huang, A.; Ke, M.; Song, Z. Direct dehydrogenation of isobutane to isobutene over Zn-doped ZrO₂ metal oxide heterogeneous catalysts. *Catal. Sci. Technol.* **2018**, *8*, 4916–4924. [CrossRef]
14. Azzam, K.G.; Jacobs, G.; Shafer, W.D.; Davis, B.H. Dehydrogenation of propane over Pt/KL catalyst: Investigating the role of L-zeolite structure on catalyst performance using isotope labeling. *Appl. Catal. A* **2010**, *390*, 264–270. [CrossRef]
15. Sun, P.; Siddiqi, G.; Vining, W.C.; Chi, M.; Bell, A.T. Novel Pt/Mg(In)(Al)O catalysts for ethane and propane dehydrogenation. *J. Catal.* **2011**, *282*, 165–174. [CrossRef]
16. Li, Y.; Li, J.; Yang, X.; Wang, X.; Xu, Y.; Zhang, L. Preparation of CeO₂-Modified Mg(Al)O-Supported Pt–Cu Alloy Catalysts Derived from Hydrotalcite-Like Precursors and Their Catalytic Behavior for Direct Dehydrogenation of Propane. *Trans. Tianjin Univ.* **2019**, *25*, 169–184. [CrossRef]
17. Zhu, Y.; An, Z.; Song, H.; Xiang, X.; Yan, W.; He, J. Lattice-Confined Sn (IV/II) Stabilizing Raft-Like Pt Clusters: High Selectivity and Durability in Propane Dehydrogenation. *Acs Catal.* **2017**, *7*, 6973–6978. [CrossRef]
18. Gao, S.; Lu, T.; Li, S.; Zhong, H. The mechanism on the pH value influencing the property of glutamic acid/layered double hydroxide compounds. *Colloids Surf. A* **2009**, *351*, 26–29. [CrossRef]
19. Xia, K.; Lang, W.; Li, P.; Long, L.; Yan, X.; Guo, Y. The influences of MgAl molar ratio on the properties of PtInMg(Al)O-x catalysts for propane dehydrogenation reaction. *Chem. Eng. J.* **2016**, *284*, 1068–1079. [CrossRef]
20. Mascolo, G.; Mascolo, M.C. On the synthesis of layered double hydroxides (LDHs) by reconstruction method based on the “memory effect”. *Micropor. Mesopor. Mater.* **2015**, *214*, 246–248. [CrossRef]
21. Xia, K.; Lang, W.; Li, P.; Yan, X.; Guo, Y. The properties and catalytic performance of PtIn/Mg(Al)O catalysts for the propane dehydrogenation reaction: Effects of pH value in preparing Mg(Al)O supports by the co-precipitation method. *J. Catal.* **2016**, *338*, 104–114. [CrossRef]
22. Li, J.; Zhang, M.; Song, Z.; Liu, S.; Wang, J.; Zhang, L. Hierarchical PtIn/Mg(Al)O Derived from Reconstructed PtIn-hydrotalcite-like Compounds for Highly Efficient Propane Dehydrogenation. *Catalysts* **2019**, *9*, 767. [CrossRef]
23. Gao, Z.; Sasaki, K.; Qiu, X. Structural Memory Effect of Mg–Al and Zn–Al layered Double Hydroxides in the Presence of Different Natural Humic Acids: Process and Mechanism. *Langmuir* **2018**, *34*, 5386–5395. [CrossRef] [PubMed]
24. Ping, J.; Wang, Y.; Lu, Q.; Chen, B.; Chen, J.; Huang, Y.; Ma, Q.; Tan, C.; Yang, J.; Cao, X.; et al. Self-Assembly of Single-Layer CoAl-Layered Double Hydroxide Nanosheets on 3D Graphene Network Used as Highly Efficient Electrocatalyst for Oxygen Evolution Reaction. *Adv. Mater.* **2016**, *28*, 7640–7645. [CrossRef]
25. Yang, S.; Zhang, Z.; Zhou, J.; Sui, Z.; Zhou, X. Hierarchical NiCo LDH-rGO/Ni Foam Composite as Electrode Material for High-Performance Supercapacitors. *Trans. Tianjin Univ.* **2019**, *25*, 266–275. [CrossRef]
26. Jiang, J.; Zhu, J.; Ding, R.; Li, Y.; Wu, F.; Liu, J.; Huang, X. Co-Fe layered double hydroxide nanowall array grown from an alloy substrate and its calcined product as a composite anode for lithium-ion batteries. *J. Mater. Chem.* **2011**, *21*, 15969. [CrossRef]
27. Zhu, Y.; An, Z.; He, J. Single-atom and small-cluster Pt induced by Sn (IV) sites confined in an LDH lattice for catalytic reforming. *J. Catal.* **2016**, *341*, 44–54. [CrossRef]
28. Chen, X.; Chen, X.; Wang, L.; Wang, L.; Qin, H.; Qin, H.; Yang, Z.; Yang, Z. Fabrication and electrochemical performance of flower-like ZnAl LDH/SnO₂ composites for zinc-nickel secondary batteries. *Ionics* **2019**, *25*, 1715–1724. [CrossRef]

29. Wang, F.; Liu, M.; Zhang, X.; Lv, G.; Sun, M. In Situ Growth of 3D Hierarchical ZnO@Ni_xCo_{1-x}(OH)_y Core/Shell Nanowire/Nanosheet Arrays on Ni Foam for High-Performance Aqueous Hybrid Supercapacitors. *Trans. Tianjin Univ.* **2018**, *24*, 201–211. [CrossRef]
30. Shen, L.; Xia, K.; Lang, W.; Chu, L.; Yan, X.; Guo, Y. The effects of calcination temperature of support on PtIn/Mg(Al)O catalysts for propane dehydrogenation reaction. *Chem. Eng. J.* **2017**, *324*, 336–346. [CrossRef]
31. Yang, Y.; Fan, G.; Li, F. Synthesis of novel marigold-like carbonate-type Mg-Al layered double hydroxide micro-nanostructures via a two-step intercalation route. *Mater. Lett.* **2014**, *116*, 203–205. [CrossRef]
32. Filez, M.; Redekop, E.A.; Poelman, H.; Galvita, V.V.; Meledina, M.; Turner, S.; Van Tendeloo, G.; Detavernier, C.; Marin, G.B. One-pot synthesis of Pt catalysts based on layered double hydroxides: An application in propane dehydrogenation. *Catal. Sci. Technol.* **2016**, *6*, 1863–1869. [CrossRef]
33. Stepanova, L.N.; Belskaya, O.B.; Likholobov, V.A. Effect of the Nature of the Active-Component Precursor on the Properties of Pt/MgAlO_x Catalysts in Propane and *n*-Decane Dehydrogenation. *Kinet. Catal.* **2017**, *4*, 400–409. [CrossRef]
34. Wu, J.; Peng, Z.; Sun, P.; Bell, A.T. *n*-Butane dehydrogenation over Pt/Mg(In)(Al)O. *Appl. Catal. A* **2014**, *470*, 208–214. [CrossRef]
35. Larsson, M.; Hultén, M.; Blekkan, E.A.; Andersson, B. The Effect of Reaction Conditions and Time on Stream on the Coke Formed during Propane Dehydrogenation. *J. Catal.* **1996**, *164*, 44–53. [CrossRef]
36. Airaksinen, S.M.K.; Krause, A.O.I.; Sainio, J.; Lahtinen, J.; Chao, K.; Ares, M.O.G.R. Reduction of chromia/alumina catalyst monitored by DRIFTS-mass spectrometry and TPR-Raman spectroscopy. *Phys. Chem. Chem. Phys.* **2003**, *20*, 4371–4377. [CrossRef]
37. Hakuli, A.; Kytokivi, A.; Krause, A.O.I.; Suntola, T. Initial Activity of Reduced Chromia/Alumina Catalyst in *n*-Butane Dehydrogenation Monitored by On-Line FT-IR Gas Analysis. *J. Catal.* **1996**, *161*, 393–400. [CrossRef]
38. Galvita, V.; Siddiqi, G.; Sun, P.; Bell, A.T. Ethane dehydrogenation on Pt/Mg(Al)O and PtSn/Mg(Al)O catalysts. *J. Catal.* **2010**, *271*, 209–219. [CrossRef]
39. Santhosh Kumar, M.; Chen, D.; Walmsley, J.C.; Holmen, A. Dehydrogenation of propane over Pt-SBA-15: Effect of Pt particle size. *Catal. Commun.* **2008**, *9*, 747–750. [CrossRef]
40. Chen, X.; Ge, M.; Li, Y.; Liu, Y.; Wang, J.; Zhang, L. Fabrication of highly dispersed Pt-based catalysts on γ -Al₂O₃ supported perovskite Nano islands: High durability and tolerance to coke deposition in propane dehydrogenation. *Appl. Surf. Sci.* **2019**, *490*, 611–621. [CrossRef]
41. Xia, K.; Lang, W.; Li, P.; Yan, X.; Guo, Y. Analysis of the catalytic activity induction and deactivation of PtIn/Mg(Al)O catalysts for propane dehydrogenation reaction. *Rsc Adv.* **2015**, *5*, 64689–64695. [CrossRef]
42. Wang, T.; Jiang, F.; Liu, G.; Zeng, L.; Zhao, Z.J.; Gong, J. Effects of Ga doping on Pt/CeO₂-Al₂O₃ catalysts for propane dehydrogenation. *Aiche J.* **2016**, *62*, 4365–4376. [CrossRef]
43. Yu, J.; Wang, R.; Ren, S.; Sun, X.; Chen, C.; Ge, Q.; Fang, W.; Zhang, J.; Xu, H.; Su, D.S. The Unique Role of CaO in Stabilizing the Pt/Al₂O₃ Catalyst for the Dehydrogenation of Cyclohexane. *Chemcatchem* **2012**, *4*, 1376–1381. [CrossRef]
44. Mitchell, P.C.H.; Wass, S.A. Propane dehydrogenation over molybdenum hydrotalcite catalysts. *Appl. Catal. A* **2002**, *225*, 153–165. [CrossRef]
45. Mokhtar, M.; Inayat, A.; Ofili, J.; Schwieger, W. Thermal decomposition, gas phase hydration and liquid phase reconstruction in the system Mg/Al hydrotalcite/mixed oxide: A comparative study. *Appl. Clay Sci.* **2010**, *50*, 176–181. [CrossRef]
46. Pérez-Ramírez, J.; Abelló, S.; van der Pers, N.M. Memory Effect of Activated Mg-Al Hydrotalcite: In Situ XRD Studies during Decomposition and Gas-Phase Reconstruction. *Chem.-Eur. J.* **2007**, *13*, 870–878. [CrossRef]
47. Airaksinen, S.M.K.; Harlin, M.E.; Krause, A.O.I. Kinetic Modeling of Dehydrogenation of Isobutane on Chromia/Alumina Catalyst. *Ind. Eng. Chem. Res.* **2002**, *41*, 5619–5626. [CrossRef]
48. Derossi, S.; Ferraris, G.; Fremiotti, S.; Garrone, E.; Ghiotti, G.; Campa, M.C.; Indovina, V. Propane Dehydrogenation on Chromia/Silica and Chromia/Alumina catalysts. *J. Catal.* **1994**, *148*, 36–46. [CrossRef]
49. Prinetto, F.; Ghiotti, G.; Durand, R.; Tichit, D. Investigation of Acid–Base Properties of Catalysts Obtained from Layered Double Hydroxides. *J. Phys. Chem. B* **2000**, *104*, 11117–11126. [CrossRef]
50. Mounfield, W.P.; Claire, M.T.; Agrawal, P.K.; Jones, C.W.; Walton, K.S. Synergistic Effect of Mixed Oxide on the Adsorption of Ammonia with Metal-Organic Frameworks. *Ind. Eng. Chem. Res.* **2016**, *22*, 6492–6500. [CrossRef]

51. Rao, K.K.; Gravelle, M.; Valente, J.S.; Figueras, F. Activation of Mg-Al Hydrotalcite Catalysts for Aldol Condensation Reactions. *J. Catal.* **1998**, *173*, 115–121. [CrossRef]
52. Liu, G.; Zhao, Z.; Wu, T.; Zeng, L.; Gong, J. Nature of the Active Sites of VO_x/Al₂O₃ Catalysts for Propane Dehydrogenation. *Acs Catal.* **2016**, *6*, 5207–5214. [CrossRef]
53. Han, Z.; Li, S.; Jiang, F.; Wang, T.; Ma, X.; Gong, J. Propane dehydrogenation over Pt-Cu bimetallic catalysts: The nature of coke deposition and the role of copper. *Nanoscale* **2014**, *6*, 1–18. [CrossRef] [PubMed]



© 2020 by the authors. Licensee MDPI, Basel, Switzerland. This article is an open access article distributed under the terms and conditions of the Creative Commons Attribution (CC BY) license (<http://creativecommons.org/licenses/by/4.0/>).

Article

Gas-Phase Hydrogenation of Furfural to Furfuryl Alcohol over Cu-ZnO-Al₂O₃ Catalysts Prepared from Layered Double Hydroxides

Guillermo R. Bertolini¹, Carmen P. Jiménez-Gómez^{2,*}, Juan Antonio Cecilia^{2,*} 
and Pedro Maireles-Torres² 

¹ Centro de Investigación y Desarrollo en Ciencias Aplicadas Dr. J. Ronco CINDECA-CCT La Plata-CONICET-UNLP, Calle 47 N° 257, La Plata 1900, Argentina; bertolg@quimica.unlp.edu.ar

² Departamento de Química Inorgánica, Universidad de Málaga, Cristalografía y Mineralogía (Unidad Asociada al ICP-CSIC), Facultad de Ciencias, Campus de Teatinos, 29071 Málaga, Spain; maireles@uma.es

* Correspondence: carmenpjm@uma.es (C.P.J.-G.); jacecilia@uma.es (J.A.C.); Tel.: +34-952132373

Received: 15 April 2020; Accepted: 27 April 2020; Published: 29 April 2020

Abstract: Several layered double hydroxides (LDHs) with general chemical composition $(\text{Cu,Zn})_{1-x}\text{Al}_x(\text{OH})_2(\text{CO}_3)_{x/2}\cdot m\text{H}_2\text{O}$ have been synthesized by the co-precipitation method, maintaining a $(\text{M}^{2+}/\text{M}^{3+})$ molar ratio of 3, and varying the $\text{Cu}^{2+}/\text{Zn}^{2+}$ molar ratio between 0.2 and 6.0. After calcination and reduction steps, Cu/ZnO/Al₂O₃ catalysts were synthesized. These catalysts were characterized by X-ray diffraction (XRD), transmission electron microscopy (TEM), H₂ thermoprogrammed reduction (H₂-TPR), N₂ adsorption-desorption at −196 °C, N₂O titration, X-ray photoelectron microscopy (XPS), NH₃-thermoprogrammed desorption (NH₃-TPD) and CO₂-thermoprogrammed desorption (CO₂-TPD). The characterization data revealed that these catalysts are mainly meso- and macroporous, where Cu, ZnO and Al₂O₃ are well dispersed. The catalytic results show that these catalysts are active in the gas-phase hydrogenation of furfural, being highly selective to furfuryl alcohol (FOL) and reaching the highest FOL yield for the catalyst with a $\text{Cu}^{2+}/\text{Zn}^{2+}$ molar ratio of 1. In an additional study, the influence of the aging time on the synthesis of the LDHs was also evaluated. The catalytic data revealed that the use of shorter aging time in the formation of the LDH has a beneficial effect on the catalytic behavior, since more disordered structures with a higher amount of available Cu sites is obtained, leading to a higher yield towards FOL (71% after 5 h of time-on-stream at 210 °C).

Keywords: layered double hydroxides; Cu-based catalysts; Cu/ZnO/Al₂O₃; furfural; furfuryl alcohol

1. Introduction

Layered double hydroxides (LDHs), also known as anionic-clays or hydrotalcites, are a group of inorganic lamellar compounds of basic nature. In the last decades, much attention is being paid to the study of these inorganic materials due to their chemical and structural properties, which make them useful in interesting applications, such as adsorbents, catalysts, anion exchangers or flame retardants, among others [1–3]. These materials exhibit high chemical stability, good biocompatibility and pH-dependent solubility [4]. The first LDH reported in the literature, discovered in 1842, was the mineral hydrotalcite $[\text{Mg}_6\text{Al}_2(\text{OH})_{16}]\text{CO}_3\cdot 4\text{H}_2\text{O}$. This inorganic structure results from stacked brucite layers, $\text{Mg}(\text{OH})_2$, where some Mg^{2+} ions can be replaced by Al^{3+} ions, thus generating an excess of positive charge in layers, which must be counterbalanced by the presence of anions, mainly carbonates (CO_3^{2-}), in the interlayer spacing [1–3].

The general formula of LDH is $[M(II)_{1-x}M(III)_x(OH)_2]_x + [A_{n-x/n}]_{x-} \cdot mH_2O$, where M(II) are divalent cations (Mg^{2+} , Zn^{2+} , Cu^{2+} , Ni^{2+}) and M(III) are trivalent cations (Al^{3+} , Fe^{3+} , Cr^{3+}). A^{n-} is an anion of charge n , and m is the stoichiometric value of co-intercalated water [1].

LDHs can be synthesized through several synthesis methods, such as co-precipitation, sol-gel, hydrothermal or urea hydrolysis, although the most usual method is co-precipitation, which can be performed at variable or constant pH [3].

Focusing only on the catalytic properties of LDHs themselves, these inorganic compounds can display both acid and basic sites [5,6]. However, the amount and strength of these acid/basic sites can be modified by thermal treatment, where dehydroxylation and decarbonation processes cause the collapse of the layered structure, leading to the formation of their respective metal oxides [6]. In addition, if any of M(II) or M(III) cations is easily reducible, it is feasible to obtain catalysts with metallic, acid and basic sites, in such a way that they can find a large spectrum of catalytic applications.

Among the great variety of catalytic processes that have emerged in the last century, the biomass valorization to produce high value-added chemicals is attracting the interest of many research groups, as a sustainable alternative to the use of fossil-based raw materials. This great interest has been prompted by the depletion of fossil fuels, which has led to the search and development of alternative sources that can satisfy both chemical and energy demands [7,8]. Biomass is the only feedstock that can replace fossil fuels, but many efforts are still required for the implementation and integration of these processes in the forthcoming biorefineries. However, the selection of a biomass source must be carried out with care and responsibility, since this biomass could interfere with the food chain, causing serious speculation problems and social imbalances. Taking into account these premises, lignocellulosic biomass, coming from agricultural waste, has emerged as an abundant, sustainable and non-edible source of energy, biofuels and chemicals [9]. Lignocellulose is composed by cellulose (40–50%), hemicellulose (20–35%) and lignin (15–25%), which can be extracted selectively by using several thermal, physical and chemical treatments [10].

Focusing only on the hemicellulose fraction, this can be isolated under mild hydrolysis treatment, leading, after depolymerization and hydrolysis, to the respective monosaccharides, mainly xylose [11,12]. Xylose, in turn, can also be dehydrated through homogeneous and/or heterogeneous catalysts to obtain furfural (FUR) as the main product [12,13]. After bioethanol, furfural is the second most produced compound in the sugar platform. The great interest in this organic compound lies in its chemical structure (an aldehyde group and a furan ring with α,β -unsaturations), which confer it a high reactivity [12]. Thus, furfural can be used as feedstock to give rise to a wide range of products with applications in fields, such as polymers, pharmacy, cosmetics, among others, through hydrogenation, oxidation, dehydration, decarbonylation or condensation reactions [12,14,15]. Thus, for instance, different environmentally friendly processes have been reported aimed at the furfural derivatization for the synthesis of valuable chemicals in aqueous media [16,17], as well as in eco-sustainable removable media as deep eutectic solvents, by using homogeneous [18] or heterogeneous catalysts [19,20].

Among the products that can be derived from FUR, furfuryl alcohol (FOL) is the most important. It has been estimated that about 62% of FUR production is employed for the synthesis of FOL due to its importance in resin manufacture for the foundry industry and for chemicals [15]. Industrially, FOL has been synthesized through furfural hydrogenation using a copper chromite catalyst [21–24]. Another product obtained in high proportions during FUR hydrogenation is 2-methylfuran (MF) [12], which is also considered a valuable product as a biofuel additive and for the synthesis of heterocycles [15].

Despite the good performance of the commercial copper chromite catalyst, in the last decade, environmental awareness has led to the search for chromium-free catalysts, which can be more sustainable. As alternative, transition metal-based catalysts, e.g., Cu [25–35], Ni [28,35–41] or Pd [28,42,43] have been proposed to replace copper chromite. Generally, these metals have been dispersed on different supports. Both the hydrogenating character of the metal and the acid/base/redox properties of the support play a determining role in the activity and the product pattern, mainly for those processes where FUR hydrogenation takes place in the gas phase.

In this context, the design of LDHs as catalyst precursors, where some of their cations can be easily reducible, is a suitable approach for the development of active catalysts for FUR hydrogenation to obtain high value-added chemicals. Several authors have reported the synthesis of Ni-based hydrotalcites as efficient catalysts for this reaction, although the high hydrogenating nature of Ni sites [28] leads to a wide range of products, including a high proportion of carbonaceous deposits in many cases [35,36]. A suitable alternative could be the use of Cu-based hydrotalcites, since Cu active centers display a lower hydrogenating capacity, in such a way that the selectivity pattern can be easily controlled. In this sense, previous research has evaluated the role of Al source in the synthesis of Cu/ZnO/Al₂O₃ from their respective hydroxides, after calcination and reduction [44]. These authors achieved well dispersed Cu centers, which were selective towards FOL [44]. In the present work, a series of [CuZn_{1-x}Al_x(OH)₂]_x + [A_{n-x}/n]_x · mH₂O hydrotalcites have been synthesized by coprecipitation method, with different Cu/Zn molar ratio, although the M(II)/M(III) molar ratio (M(II) is Cu(II) + Zn(II)) was 3 in all cases, since this value favors the formation of ordered LDH structures [1–3]. Moreover, the effect of other parameters, like aging time, was also evaluated for the synthesis of LDHs. Precursors were calcined and reduced, and then characterized and tested in the FUR hydrogenation, with special emphasis on the correlation between the amount of available metal sites and their catalytic behavior.

2. Characterization of the Catalysts

The identification of crystalline phases was carried out by powder X-ray diffraction. In all cases, the XRD patterns of LHDs synthesized (Figure 1) are similar to those reported in the literature [1,45]. The most intense peaks correspond to the typical basal (00*l*) planes, thereby, those located at 2θ (°) ≈ 12, 24 and 34 are attributed to the (003), (006) and (009) planes. These can be indexed in a rhombohedral symmetry, which is assigned to a (Cu,Zn)_{1-x}Al_x(OH)₂ (CO₃)_{x/2} m H₂O layered double hydroxide (Powder Diffraction File: PDF: 00-37-0629). In addition, less intense peaks ascribed to non-basal planes of hydrotalcites are also observed, together with other low intense peaks, mainly in those LDHs whose Cu²⁺ or Zn²⁺ content is higher. Thus, in the case of Cu-rich LDH, diffraction peaks attributed to copper(II) hydroxide are presented, while Zn-rich LDH also exhibits broad and poorly defined diffraction peaks attributed to zinc hydroxycarbonate.

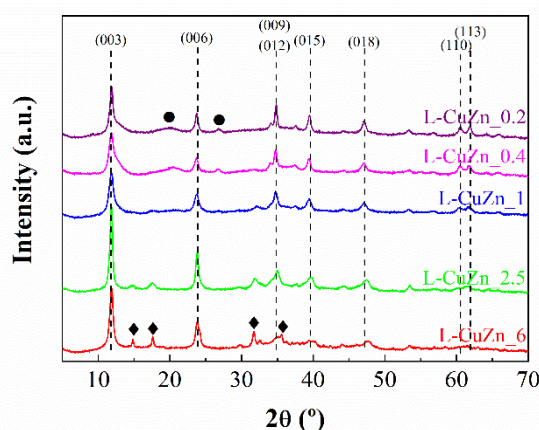


Figure 1. XRD patterns of the layered double CuZnAl hydroxides. (Circles: zinc hydroxycarbonate), (diamonds: copper(II) hydroxide).

CuZnAl-based hydrotalcites have been previously studied by FTIR and Raman spectroscopies, demonstrating that the Cu/Zn molar ratio influences their microstructure. Thus, higher Cu/Zn ratios lead to more homogeneous CuZnAl hydrotalcites, while lower values give rise to less homogeneous structures due to its composition is closer to pure ZnAl and CuAl hydrotalcites [46]. This latter could provoke the asymmetric broadening of Bragg peak profiles of LDH for lower Cu/Zn molar ratio, also characteristic of the stacking disorder for Zn-rich compounds (Figure 1). Moreover, this Raman study

also confirmed the presence of carbonate species, not only as counterion in the interlayer region of LDH, but also in partial segregated malachite for high Cu/Zn molar ratios, which is in agreement with XRD data [46]. Following the procedure described by Santos et al. for $(\text{Cu,Zn})_{1-x}\text{Al}_x(\text{OH})_2(\text{CO}_3)_{x/2}\cdot m\text{H}_2\text{O}$ LDHs [46], these layered materials were thermally treated at 300 °C for 4 h. In their XRD patterns (Figure 2), a broadening of the diffraction peak in comparison to their respective LDHs is noticeable, as a consequence of the stacking disorder of the layered structure due to decarbonation and dehydroxylation of the LDH, leading to the typical diffraction peaks of their mixed metal oxides [1]. Thus, XRD profiles reveal an evolution from the calcined Cu-rich (P-CuZn_6) to the Zn-rich (P-CuZn_0.2) sample. In this sense, the XRD pattern of calcined P-CuZn_6 displays defined bands located at 2θ (°) = 32.5, 35.5, 38.7, 48.8, 53.5, 58.3, 61.6, 66.2 and 68.1 assigned to CuO (PDF: 00-048-1548). The progressive increase in Zn content gives rise to a much more amorphous XRD pattern, being only a broad band observed at 2θ (°) \approx 33. These data suggest that calcined P-CuZn_2.5, P-CuZn_1 and P-CuZn_0.4 display a more amorphous structure, or are formed by smaller particles than that the calcined P-CuZn_6. For the calcined LDH with the highest Zn content (P-CuZn_0.2), broad bands at 2θ (°) = 31.8, 34.4, 36.2, 48.3, 56.5, 63.1 and 68.2, start to emerge. These peaks are assigned to hexagonal ZnO (PDF: 00-36-1451). On the other hand, no diffraction peaks could be ascribed to the presence of crystalline Al species, in such a way that these species must be amorphous, or dispersed in the other phases.

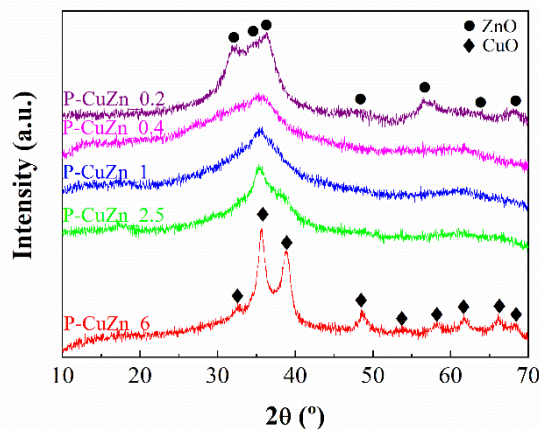


Figure 2. XRD profiles of the mixed oxides obtained after the calcination of LDHs at 300 °C.

Once the catalyst precursors were synthesized after subsequently calcined, H_2 -TPR analysis was carried out to determine the appropriate reduction temperature to obtain the Cu^0 -based catalysts (Figure 3). It has been previously reported that usually it is not possible to discern the different stages of Cu reduction ($\text{Cu}^{2+} \rightarrow \text{Cu}^+ \rightarrow \text{Cu}^0$), so the different contributions observed are ascribed to Cu particles with different size and/or with different interaction with the support ($\text{ZnO}/\text{Al}_2\text{O}_3$) [26,30,34]. From the H_2 -TPR profiles, it can be inferred that the sample with the highest Cu content (CuZn_6) is more easily reducible than the rest of catalysts. Its reduction curve shows two well-defined reduction steps located at 185 and 240 °C, which can be explained by the co-existence of CuO particles with different interaction with the support, or particles with different size. As the Cu content decreases and the Zn content concomitantly increases, the H_2 -TPR profile progressively changes. Thus, it seems clear that the hydrogen consumption at low temperature progressively decreased, as observed for CuZn_2.5 and CuZn_1. In the case of CuZn_0.4, this low temperature band disappears, being only noticeable the presence of a single band whose maximum is located about 245 °C. Those catalysts with a lower proportion of Zn seem to be more reducible than the richer ones, thus indicating that the presence of ZnO would modify the electronic environment around CuO particles, as previously pointed out by other authors [47,48]. Previous research has reported that the reduction of Cu species in CuO/ZnO takes place about 210 °C [30], so Al species could exert an additional electronic promoter effect on the interaction between ZnO and CuO particles, in such a way that the reduction of Cu^{2+} species occurs at

higher temperature, as was indicated in the literature [49]. On the other hand, as the catalyst with a lower Zn content is easily reducible, it is expected that Al species possess a less pronounced promoter effect than ZnO.

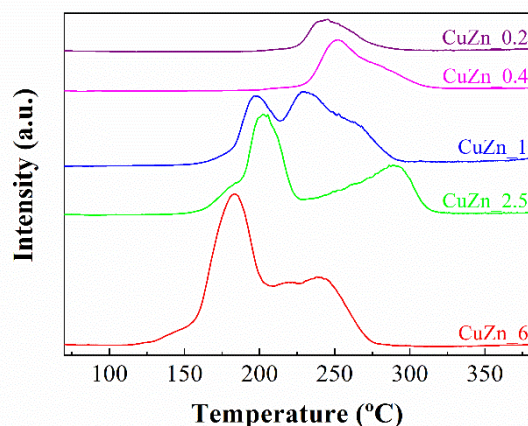


Figure 3. H₂-TPR profiles of the mixed metal oxides obtained after calcination of LDHs.

H₂ consumption data of calcined P-CuZn_X materials are always lower than theoretical values, so a fraction of Cu²⁺ species could not be reduced (Table 1). In this sense, several authors have reported that the reduction of segregated metal carbonates can take place at high temperature, about 550 °C [46]. However, other authors have noted that Cu²⁺ ions could also be embedded in the octahedral sites of Al₂O₃, ZnO, or even ZnAl₂O₄, whose reduction should require a higher temperature [50,51].

Table 1. Chemical composition and H₂ consumption of mixed metal oxides obtained by calcination of LDHs.

Catalyst	Content (wt.%)			Deconvolution H ₂ -TPR (%)		H ₂ Consumption (μmol g ⁻¹)	
	Cu	ZnO	Al ₂ O ₃	Peak 1	Peak 2	Experimental	Theoretical
CuZn_0.2	11.1	71.1	17.8	68	32	1516	1696
CuZn_0.4	19.4	62.3	18.2	59	41	2763	2921
CuZn_1	35.6	45.5	19.0	38	62	4868	5131
CuZn_2.5	53.0	27.2	19.9	5	95	6823	7356
CuZn_6	65.6	14.0	20.5	2	98	8376	8857

Taking into account the H₂-TPR profiles, the precursors were reduced at 300 °C, maintaining this temperature for 1 h to ensure the complete reduction of Cu²⁺ species.

XRD profiles of the CuZn_X catalysts show the typical diffraction peaks of the metallic Cu⁰ at 2θ (°) = 43.3 and 50.4 (PDF: 00-85-1326) (Figure 4). The presence of Cu₂O should be discarded since, despite the main peak at 2θ (°) = 38.3 overlaps with a diffraction peak of ZnO, the secondary peaks of Cu₂O do not appear, so partially reduced copper oxide (Cu₂O) crystallites are not detected, or these are too small to be detected by XRD.

These signals are more defined than those corresponding to the hexagonal ZnO, which does not evolve to reduced Zn species. In the case of Al species, diffractograms do not reveal any characteristic peaks, so these Al species must be highly dispersed in the catalysts. The determination of the crystallite size for Cu⁰ was carried out from the Williamson-Hall equation [52], using the main diffraction peak at 2θ (°) = 43.3. The analysis of this (111) crystallographic plane reveals that the crystallinity of the Cu⁰ particles increases directly with the Cu content, from 5.0 nm for the lowest content (CuZn_0.2) to 28.8 nm for the highest (CuZn_6). These values are slightly lower than those observed for Cu/ZnO or Cu/MgO synthesized by the co-precipitation method [26,30], so Al species, in addition of exerting an electronic promoter effect, seem to favor the dispersion of Cu nanoparticles [49,53].

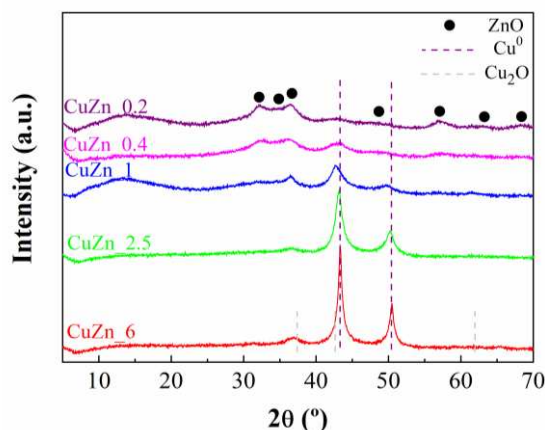


Figure 4. XRD patterns of the CuZn_X catalysts.

In order to elucidate the catalyst morphology, CuZn_X catalysts were analyzed by TEM (Figure 5). In all cases, the micrographs allow to distinguish different morphologies, including layered structures probably due to the hydroxalcite structure that did not fully collapse after the thermal treatment. These data are in agreement with the literature, where a proportion of the layered structure was reported to be maintained after the thermal treatment [54]. In addition, it is noticeable the presence of pseudospherical and well-dispersed nanoparticles, mainly in the samples with a higher Cu content. In both cases, these particles are very small, below 15 nm.

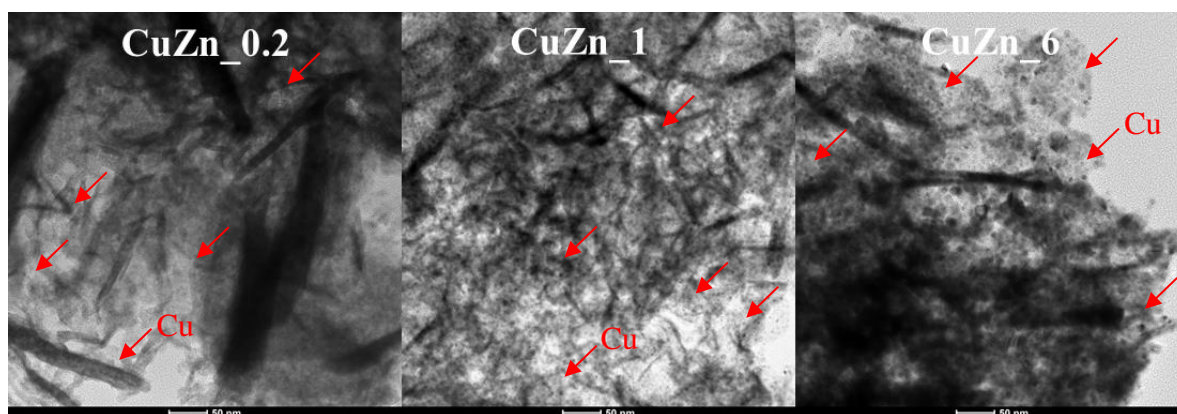


Figure 5. TEM micrographs for CuZn_0.2, CuZn_1 and CuZn_6. (Scale bar: 50 nm).

The analysis of these samples was also performed by Energy Dispersive X-Ray (EDX) (Figure 6). The images show that all elements (Cu, Zn, Al and O) are well dispersed in both lamellar and pseudospherical structures. In Figures 5 and 6, it can be seen the existence of interparticle voids between adjacent nanoparticles.

The textural properties of CuZn_X catalysts were evaluated from their N₂ adsorption-desorption isotherms at −196 °C (Figure 7A). According to the International Union of Pure and Applied Chemistry (IUPAC) classification [55], these isotherms can be considered as Type II, which are typical of macroporous solids, as suggests the great growing of N₂ adsorbed at high relative pressure. The shape is similar for all CuZn_X catalysts, and, consequently, the modification of the Cu/Zn molar ratio does not seem to affect the textural properties of catalysts (Table 2). Thus, S_{BET} values hardly vary, being between 70 and 85 m² g^{−1}, while *t*-plot data indicate that the surface ascribed to the microporosity can be considered as negligible, since values are below 10 m² g^{−1} in all cases. In the same way, the pore volume is very similar for all catalysts, being in the range 0.474–0.679 cm³ g^{−1}, while the micropore volume is very low in comparison to the total volume.

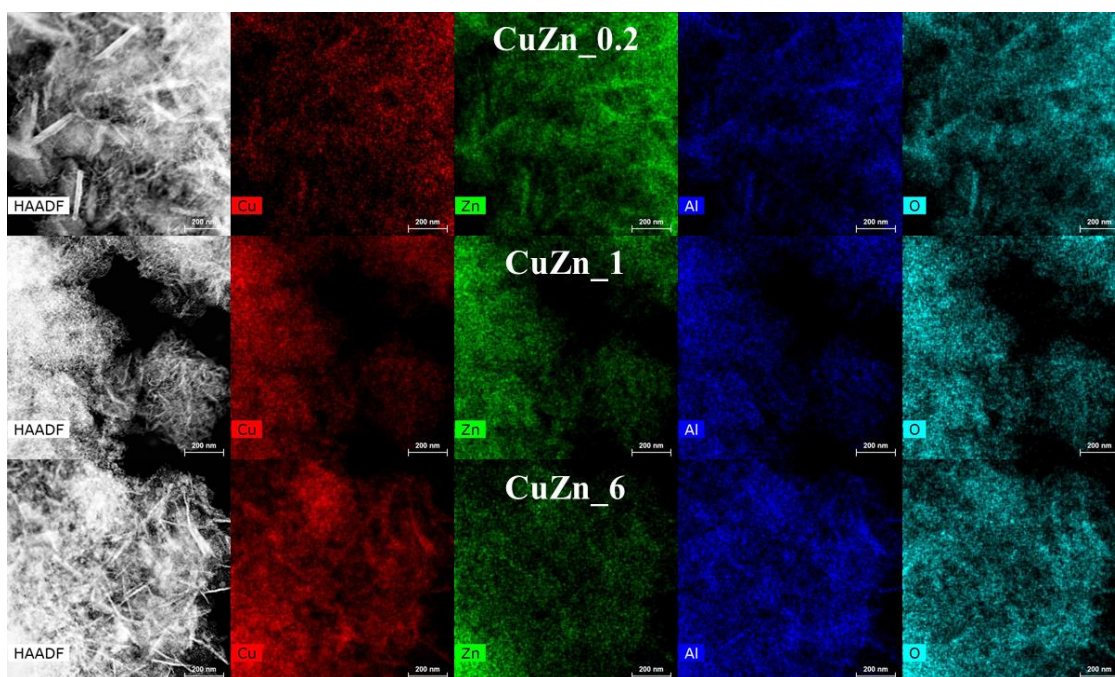


Figure 6. EDX images of CuZn_0.2, CuZn_1 and CuZn_6. (Scale bar: 200 nm).

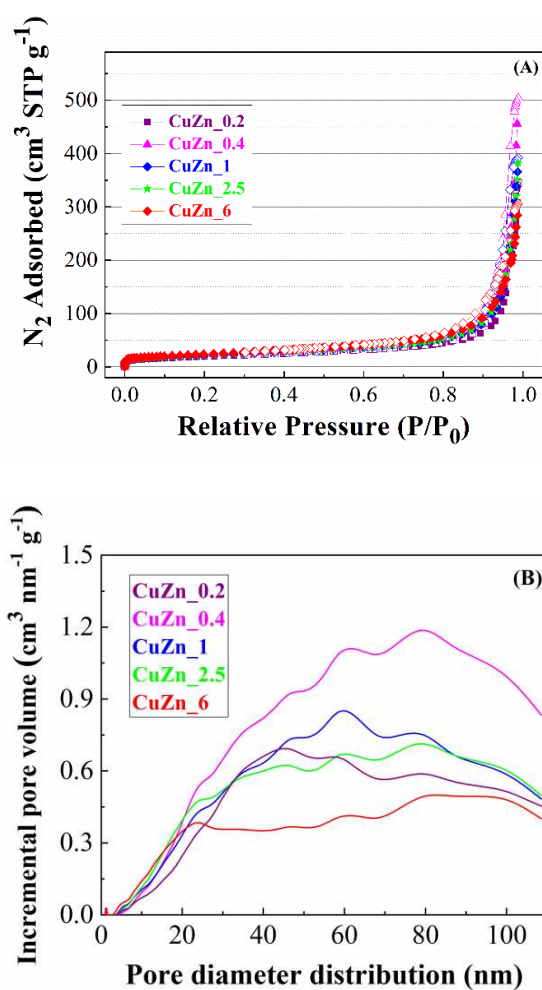


Figure 7. N₂ adsorption-desorption isotherms at −196 °C (A) and pore size distribution estimated by DFT method (B) for CuZn_X catalysts.

Table 2. Textural properties of the CuZn_X catalysts.

Catalyst	S _{BET} (m ² g ⁻¹)	t-Plot (m ² g ⁻¹)	Pore Volume (cm ³ g ⁻¹)	Micropore Volume ¹ (cm ³ g ⁻¹)	Amount Acid Sites ² (μmol g ⁻¹)	Amount Basic Sites ³ (μmol g ⁻¹)
CuZn_0.2	85	5	0.474	0.002	78	39
CuZn_0.4	79	6	0.590	0.003	76	31
CuZn_1	79	1	0.607	0.001	69	22
CuZn_2.5	84	9	0.679	0.005	59	17
CuZn_6	70	8	0.533	0.003	60	15

¹ Micropore volume estimated from alpha-s-plot. ² Quantification of acid sites by NH₃-TPD. ³ Quantification of acid sites by CO₂-TPD.

With regard to the pore size distribution, estimated by Density Functional Theory (DFT) [56] (Figure 7B), all CuZn_X catalysts follow the same pattern. The microporosity is barely appreciated, and only a small contribution appears at 1.2 nm. However, these samples exhibit a wide pore size distribution, extending from 3 to 150 nm, in such a way that these catalysts can be labeled as meso- and mainly macroporous. This porosity is ascribed to the voids between adjacent particles, as was suggested previously from the TEM micrographs (Figures 5 and 6).

The quantification of surface Cu⁰ species of CuZn_X catalysts was carried out by N₂O titration at 60 °C [57] (Table 3). The data indicate that dispersion decreases with the Cu content, going from 21% for CuZn_0.2 to 7% for CuZn_6. In the same way, the metallic surface area (m²_{Cu} g_{Cu}⁻¹) follows a similar trend, and the catalyst with the lowest Cu content (CuZn_0.2) displays the highest value. This study also reveals that the metal particle size increases directly with the Cu loading, from 5 nm for CuZn_0.2 to 19 nm for CuZn_6, being these data slightly lower than those obtained from XRD by using the Williamson-Hall method [52].

Table 3. Metallic properties of CuZn_X catalysts, as determined from N₂O titration.

Catalyst	Superficial	Metallic Surface		Dispersion (%)	Particle Size (nm)	Crystallite Size ¹ (nm)
	H ₂ Uptake (μmol g ⁻¹)	(m ² _{Cu} g _{Cu} ⁻¹)	(m ² _{Cu} g _{cat} ⁻¹)			
CuZn_0.2	317	118	13	21	5	5
CuZn_0.4	385	82	16	14	8	6
CuZn_1	475	55	19	10	12	15
CuZn_2.5	563	44	23	8	15	21
CuZn_6	555	35	23	7	19	29

¹ By applying the Williamson-Hall equation to XRD data [52].

In order to determine the surface chemical composition of catalysts, X-ray photoelectron spectroscopy (XPS) analysis was carried out. Cu 2p core level spectra (Figure 8A) show that Cu 2p_{3/2} consists of a single contribution located at 932.0 eV, ascribed to reduced Cu species [30,32], since the absence of the typical shake-up satellite of divalent metals about 942–943 eV would exclude the existence of Cu(II) [58].

However, from this contribution, it is not possible to discern between Cu⁺ and Cu⁰ species, so the Auger Cu_{LMM} signal is used to identify these oxidation states [30,32]. The broad Auger Cu_{LMM} band (Figure 8B) can be deconvoluted in two main contributions: 918.5 eV, which is ascribed to Cu⁰, and 917.0 eV due to Cu⁺ [30]. The proportion of Cu⁰ increases directly with the Cu content, being about 65–70% of the total reduced Cu species. The analysis of the Zn 2p region (Table 4) evidences a single band between 1021.6–1022.1 eV, which is assigned to ZnO. Some studies of Cu/ZnO catalysts have demonstrated that ZnO can be partially reduced, arising a new contribution located at lower binding energy. This new band is not observed in the Zn 2p core level spectra; however, the Auger Zn_{LMM} line (Figure 8C) shows an asymmetric band that would confirm the existence of a small proportion of Zn partially reduced (Zn^{δ+}), or even a synergistic effect between Cu⁰ and ZnO [59,60]. With regard to

the Al 2p core level spectra, all CuZn_X catalysts display a contribution about 74.3 eV, which can be attributed to Al₂O₃ [61]. In the case of O 1s, all catalysts display a main contribution located about 531.0 eV, assigned to oxide species, and another less intense at 532.6 eV, that is assigned to hydroxyl and/or carbonate [61]. The existence of carbonates could be confirmed by the signal at a binding energy of 288–289 eV in the C 1s core level spectra [61], which could result from a low proportion of LDH, or a possible carbonation of the catalyst surface.

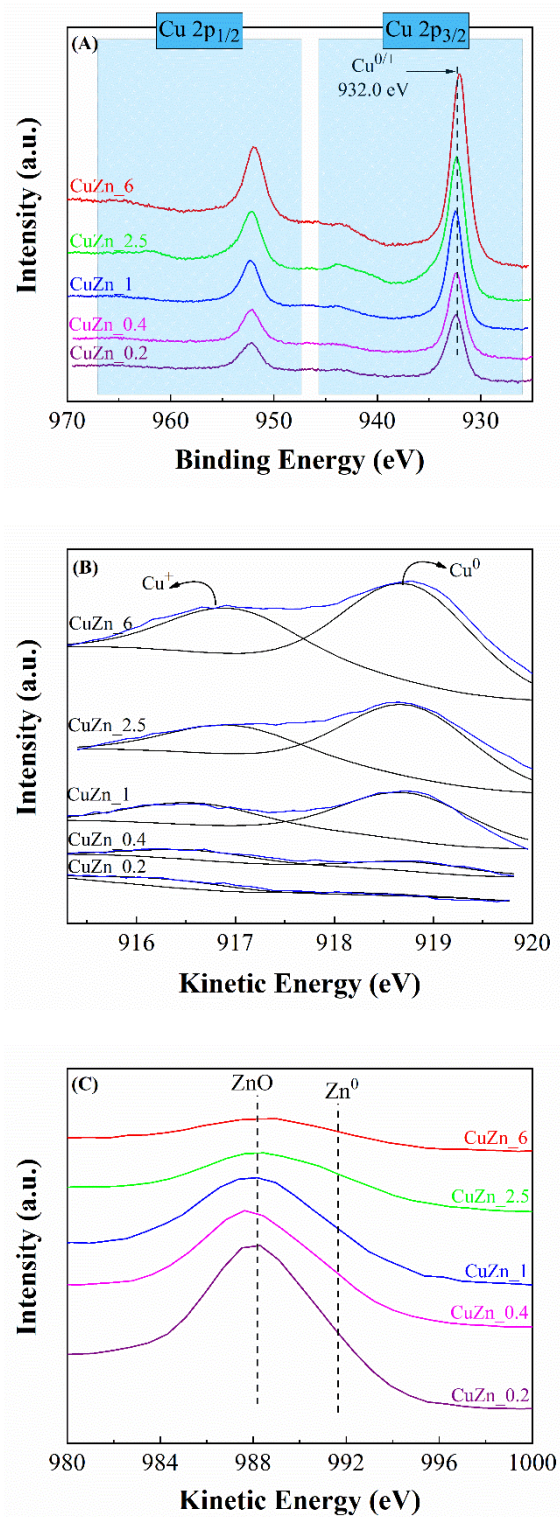


Figure 8. Cu 2p core level (A), Auger Cu_{LMM} (B) and Auger Zn_{LMM} (C) spectra of CuZn_X catalysts.

Table 4. XPS data of CuZn_X catalysts.

Catalyst	Binding Energy, eV (Atomic Concentration, %)						Surface Molar Ratio		
	C 1s		O 1s		Al 2p	Cu 2p	Zn 2p	Cu/Zn	(Cu + Zn)/Al
CuZn_0.2	284.8 (9.6)	288.7 (1.6)	531.1 (46.2)	532.7 (5.8)	74.4 (10.9)	932.0 (3.7)	1022.1 (22.1)	0.15	2.37
CuZn_0.4	284.8 (16.6)	288.8 (0.9)	530.8 (40.7)	532.5 (13.0)	74.3 (9.1)	932.1 (4.5)	1021.9 (15.2)	0.29	2.16
CuZn_1	284.8 (10.1)	288.6 (1.0)	531.0 (38.6)	532.6 (14.1)	74.4 (12.2)	932.1 (8.1)	1022.1 (16.0)	0.51	1.97
CuZn_2.5	284.8 (14.1)	288.4 (0.7)	531.0 (36.7)	532.7 (15.3)	74.5 (11.5)	932.0 (9.8)	1022.1 (11.8)	0.83	1.88
CuZn_6	284.8 (17.4)	288.4 (1.1)	531.0 (37.9)	532.5 (8.7)	74.5 (9.6)	932.0 (11.0)	1021.7 (6.0)	1.83	1.77

The atomic concentration data show that the surface Cu content progressive increases with the Cu loading, as expected (Table 4), although surface molar ratios seem to be lower than the theoretical values. This fact could be ascribed to both ZnO and Al₂O₃ exhibit a smaller crystallite size than Cu⁰, in such a way that both metal oxides should be better dispersed in catalysts. This fact can lead to lower than expected surface Cu concentrations.

As both acid and basic sites could also influence on the gas-phase FUR hydrogenation reaction, NH₃-TPD and CO₂-TPD studies were performed (Table 2). The NH₃-TPD data show a relatively low amount of acid sites, decreasing from 78 μmol g⁻¹ for CuZn_0.2 to 60 μmol g⁻¹ for CuZn_6. The presence of these acid sites is ascribed to Al₂O₃ and Cu⁺, which provide Lewis acid sites, and even to ZnO due to its amphoteric character, similar to alumina. Several authors have reported that the modulation of the acidity plays a key role in FUR conversion, since a high number of acid sites can cause the polymerization of FUR, mainly in gas-phase, leading to the formation of a high proportion of carbonaceous deposits [29,37,62]. These polymerized FUR species interact strongly with the active sites, in such a way that catalysts tend to be deactivated relatively fast. However, the presence of weak acid sites could exert a beneficial effect on the catalytic behavior, since the interaction between FUR, or reaction products, and the catalyst is weakened in comparison with catalyst with higher acidity, thus favoring the desorption of products adsorbed on the catalyst surface. In this sense, several supports, such as SiO₂ or clay minerals, with similar amount of acid sites [29,37], have provided good catalytic activity in FUR hydrogenation, under similar experimental conditions.

Similarly, a basic support (MgO, CaO, ZnO or CeO₂) [25,26,30,63,64] also seems to have a positive effect in this catalytic process. CuZn_X catalysts display a small concentration of basic sites, between 15 and 39 μmol g⁻¹, raising as the Cu content decreases. The presence of these basic sites is ascribed to the amphoteric character of both ZnO and Al₂O₃, as previously mentioned [65,66].

3. Catalytic Results

CuZn_X catalysts were tested in the gas-phase FUR hydrogenation, using FUR dissolved in cyclopentyl methyl ether (CPME). This solvent was selected due to its interesting physico-chemical properties, such as low solubility in H₂O in comparison to other ethereal solvents, low formation of peroxides, low boiling point (106 °C) or relative high stability under acid or basic conditions [67]. Considering these premises, the first study was to evaluate the stability of the solvent under similar experimental conditions to those used for the catalytic evaluation of CuZn_X catalysts. At a reaction temperature of 190 °C, CPME was recovered without any modification, such as the cleavage of the –C–O–C– bond or isomerization.

3.1. Influence of Cu Content

Thereafter, CuZn_X catalysts were studied in the FUR hydrogenation at 190 °C (Figure 9). All the catalysts are prone to suffer a progressive deactivation, which could be a consequence of the strong interaction of FUR, or FOL molecules, with Cu active sites [68]. The catalyst with the lowest Cu content (CuZn_0.2) is also the least active catalyst, reaching a FUR conversion of 40% after 1 h of time-on-stream (TOS), which decreases until 26% after 5 h. By increasing the Cu content, the catalytic performance is clearly improved, since CuZn_0.4 attains a FUR conversion of 43% after 5 h of TOS, while CuZn_1 seems to be the most stable catalyst with a FUR conversion of 59%. However, this trend is not followed when the Cu content raises further, since both CuZn_2.5 and CuZn_6 catalysts exhibit a similar pattern, reaching a FUR conversion close to 50% after 5 h of TOS.

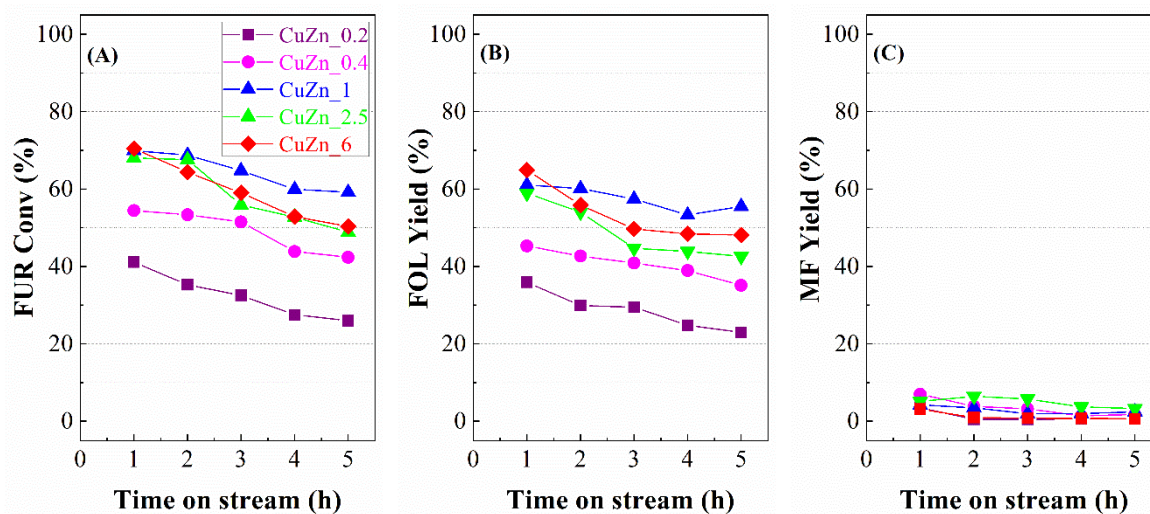


Figure 9. FUR conversion (A), FOL yield (B), and MF yield (C) in the FUR hydrogenation over CuZn_X catalysts (Experimental conditions: Mass of catalyst = 0.15 g, Reaction temperature = 190 °C, Pressure = 0.1 MPa, H₂ flow = 10 mL min⁻¹, Fed flow = 2.3 mmol FUR h⁻¹).

With regards to the selectivity pattern (Figure 9B,C), the modification of the Cu/Zn molar ratio hardly varies the ratio of the obtained products, since FOL always is the main compound, with a maximum yield of 55% for CuZn_1, after 5 h of TOS. In all cases, MF was also detected, although this can be considered a minority because MF yield did not exceed 6% after 5 h of TOS. The catalytic data can be compared with other catalysts reported in the literature. Thus, Cu/ZnO and Cu/CeO₂ catalysts exhibited a high activity in the FUR hydrogenation, but the selectivity pattern is slightly different, since the amount of MF was higher in both cases [30,63]. Other authors have reported that the incorporation of Al₂O₃ exerts a promoter effect in the catalytic behavior due to Al species weaken the Cu-ZnO interaction [44]. This data could be in agreement with those obtained in the H₂-TPR analysis, where the catalyst with a lower ZnO content (CuZn_6) is easily reducible. In earlier studies, Nagajara et al. established that co-precipitation is the most appropriate method to obtain a high dispersion of Cu species on a basic support like MgO [25]. These authors also reached a high activity in FUR conversion, with a high selectivity mainly towards FOL. In the same way, Dong et al. carried out a comparative study with Cu/ZnO, Cu/Al₂O₃ and Cu/SiO₂ [29]. They concluded that the modification of the electronic density in the catalyst due to the Cu-support interaction has a determining role in the catalytic behavior, pointing out that the existence of weak acid sites favors MF formation, mainly in the case of Cu/SiO₂, as a consequence of consecutive reactions (FUR → FOL → MF) [29]. These weak acid sites, associated to both the support and Cu⁺ sites, could be involved in the hydrogenolysis of FOL to MF due to their electron-deficiency [29,69]. Similar results were obtained by Jiménez-Gomez et al., who synthesized Cu/SiO₂ catalyst by a complexation method to disperse Cu species [32]. They observed that, besides the presence of weak acid sites, it is necessary the existence of well-dispersed Cu nanoparticles, since the

electron-deficiency of the catalyst enhanced [29,32]. In the present work, in spite of CuZn_X catalysts have acid sites, the amount of MF can be considered negligible in comparison to data reported in the literature [29,32]. In this sense, the catalysts highly selective towards MF display higher S_{BET} values. This fact supposes a higher FUR-support interaction and consequently a longer residence time, which can favor consecutive reactions. CuZn_X catalysts showed lower S_{BET} values and reduced porosity (Table 2 and Figure 7), mainly ascribed to their meso-macroporous nature. As the pore size is not modulated to the dimensions of the FUR molecule, the interaction FUR-active sites should be weaker, although this fact also has some advantage related to the presence of more labile sites that favor an easier desorption of FUR and products. This trend was also observed for other catalysts synthesized by co-precipitation method, such as Cu/MgO, Cu/ZnO or Cu/CeO₂ [25,30,63]. The existence of Cu⁺ sites, as determined by XPS, does not favor the hydrogenolysis process to form MF, so it could be inferred that textural properties have a more determining role in the hydrogenolysis reaction than the amount of acid sites. However, the hydrogenation FUR → FOL takes place on the metallic sites [28,29] and it does not seem to be affected by the textural properties of catalysts. This fact was confirmed in Cu-based catalysts supported on clay minerals [33,37,70]. Thus, those catalysts with very poor textural properties, like bentonite, or whose pore dimensions hinder the incorporation of Cu nanoparticles, like sepiolite, only dispersed metal nanoparticles on the catalyst surface [33]. In both cases, the catalysts were selective towards FOL. However, the use of a clay mineral with less crystallinity as support led to higher S_{BET} values due to an increase in the micro- and mesoporosity, thus favoring a higher interaction between FUR and the catalyst and longer residence time, in such a way that the reaction can evolve toward consecutive reaction steps [70]. In this sense, the formation of MF is favored by the existence of weak acid sites associated to the aluminosilicate, used as support, (kerolite) and the presence of a small fraction of Cu⁺ species. In these studies, the incorporation of promoters, such as ZnO, MgO or CeO₂, modified the selectivity pattern, with an increase in the FOL yield due to milder interaction between support and Cu species, as indicated their H₂-TPR data [29,37,70], which is in agreement with data reported in the present work.

3.2. Turnover Frequency (TOF)

In order to evaluate the activity of Cu sites, turnover frequency (TOF) data of catalysts were determined. It must be considered that most of catalysts are prone to suffer deactivation by the formation of carbonaceous deposits on the catalyst surface, and consequently the evaluation of the activity of these Cu sites only makes sense at zero time (t_0), as long as these catalysts do not reach a total conversion at t_0 . In this sense, the linearization of the Figure 9A reveals that FUR conversion values vary between 43% for CuZn_0.2 and 76% for CuZn_2.5, at t_0 .

From the extrapolation to t_0 (Figure 10A), it is feasible to determine the corresponding TOF values. The obtained data reveal that CuZn_0.2 displays the lowest TOF (28 h⁻¹), whereas an increase in the Cu content improves TOF, and CuZn_0.4 and CuZn_1 show TOF values of 43 and 44 h⁻¹ respectively. However, the use of larger Cu loadings worsens the efficiency of Cu active sites, since CuZn_2.5 and CuZn_6 reach TOF values of 36 and 37 h⁻¹, respectively. In the same way, from the linearization of the data obtained in Figure 9A, it is possible to evaluate the amount of FUR converted per time unit and mass of catalyst at t_0 (Figure 10B). These data reveal that the highest FUR rate was $1.113 \cdot 10^{-2}$ mmol FUR g⁻¹ h⁻¹ for CuZn_1, while the poorest value was obtained for CuZn_0.2, with a rate of $0.678 \cdot 10^{-2}$ mmol FUR g⁻¹ h⁻¹. In addition, from Figure 10B, an estimation of the catalyst lifetime can be made by extrapolation. These data reveal that the catalyst with longer life is CuZn_1, which could be active for 15.15 h. In this time, the catalyst could convert 0.1537 mmol FUR g⁻¹ before exhaustion.

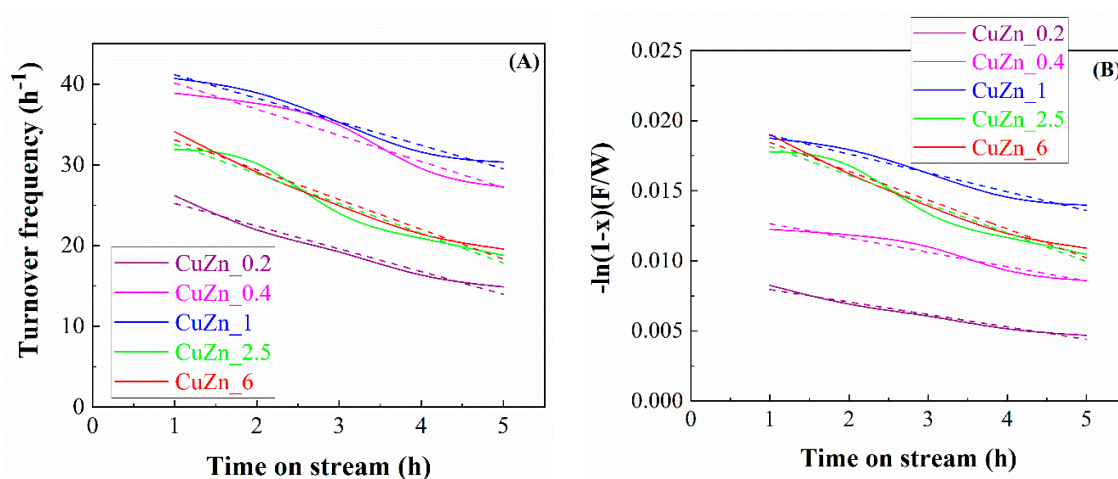


Figure 10. Linearization of TOF values (A) and FUR consumption rate (B) with time-on-stream for CuZn_X catalysts.

3.3. Influence of Reaction Temperature

Considering that CuZn_1 showed the longest lifetime, as well as the most efficient Cu active sites (Table 5), this catalyst was selected to evaluate the influence of the reaction temperature on the catalytic performance (Figure 11). FUR conversion clearly increases with the reaction temperature (Figure 11A), from 34% to 79% after raising the temperature from 170 to 230 °C, after 5 h of TOS. Several authors have reported that FUR hydrogenation is thermodynamically favored; however, the FUR conversion often displays a volcano shape with the reaction temperature, reaching a maximum conversion at 190–210 °C [27,62]. The worsening of the conversion at higher reaction temperature was attributed to FUR polymerization, due to its strong adsorption on the active sites involved in the hydrogenation process. This trend was not observed in the present work, which could be explained by the meso- and macroporosity of catalysts and the relatively low concentration of acid sites, in such a way that the FUR-active site interaction is weaker, so the desorption of FUR and reaction products should be easier [29,37,70]. With regard to the hydrogenation products (Figure 11B,C), in all cases, the main product was FOL, reaching a maximum yield of 65% after 5 h of TOS at 210 °C. MF yield values always were very low, although they increase slightly with the reaction temperature, attaining a maximum MF yield of 7% after 5 h of TOS at 230 °C [62]. Several authors have pointed out that the formation of MF is favored at higher reaction temperature ($T > 190$ °C) [25,30,62]. However, CuZn_1 hardly modifies its selectivity pattern when the reaction temperature increases, probably due to the weaker interaction between the active sites and FUR molecules. Thus, this catalyst seems to be highly stable and selective toward FOL, along the TOS, in a wide range of reaction temperatures [15].

Table 5. Turnover frequency and lifetime analysis of CuZn_X catalysts, obtained from linearization of Figure 10.

Catalyst	TOF ₀ ¹ (h ⁻¹)	C ₀ ² (%)	r ₀ ³ (mmol _{FUR} h ⁻¹ g ⁻¹)	Exhaustion Time ⁴ (h)	Total FUR Converted ⁵ (mmol _{FUR} g ⁻¹)	FUR Converted (1–5 h) ⁶ (mmol _{FUR} g ⁻¹)
CuZn_0.2	28	43	0.6748·10 ⁻²	10.0	0.0440	0.0201
CuZn_0.4	43	58	0.9105·10 ⁻²	13.4	0.0916	0.0307
CuZn_1	44	72	1.1352·10 ⁻²	15.2	0.1537	0.0402
CuZn_2.5	36	76	1.1897·10 ⁻²	9.9	0.0996	0.0366
CuZn_6	37	73	1.1410·10 ⁻²	10.0	0.1021	0.0369

¹ Turnover frequency determined at t₀ (metallic surface data were obtained from Table 3). ² Conversion of FUR at t₀. ³ FUR rates at t₀. ⁴ Total exhaustion time of catalysts. ⁵ Total FUR converted until catalyst exhaustion. ⁶ FUR converted between 1 and 5 h of TOS.

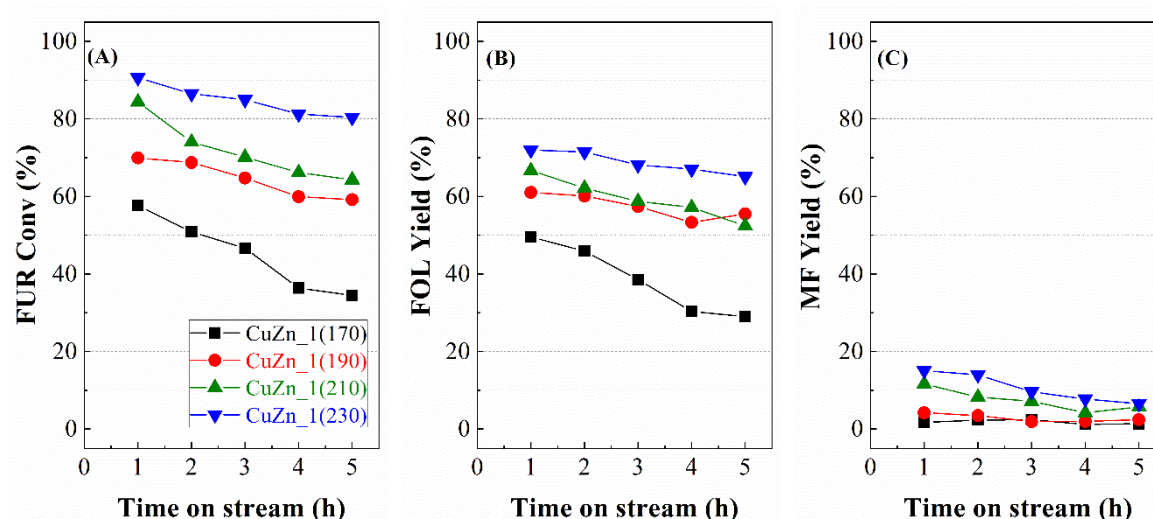


Figure 11. FUR conversion (A), FOL yield (B), and MF yield (C) in the FUR hydrogenation with CuZn₆ (Experimental conditions: Mass of catalyst = 0.15 g, Pressure = 0.1 MPa, H₂ flow = 10 mL min⁻¹, Fed flow = 2.3 mmol FUR h⁻¹).

3.4. Influence of Aging Time in the Synthesis

In the next study, the aging time of the LDHs was modified to evaluate its influence on the catalytic behavior. Thus, three CuZn₁ catalysts with different aging time (1, 48 and 168 h) were compared. The catalytic data show that longer aging time in the synthesis of LDHs has an adverse effect on the catalytic activity (Figure 12A). Thus, that LDH whose aging time was only 1 h gave rise to a catalyst that hardly undergoes deactivation, since it maintains a FUR conversion of 84% after 5 h of TOS at 210 °C. However, a more prolonged aging treatment (168 h) worsens the catalytic activity, achieving a FUR conversion of only 37%, under similar experimental conditions. The selectivity (Figure 12B,C) follows the same trend than that observed previously for CuZn_X catalysts, since FOL was the main product in all cases, attaining a maximum yield of 71%, after 5 h of TOS at 210 °C, with CuZn₁ aged for 1 h. The amount of MF was very low in all cases, although a decrease in MF yield took place as aging time was increased.

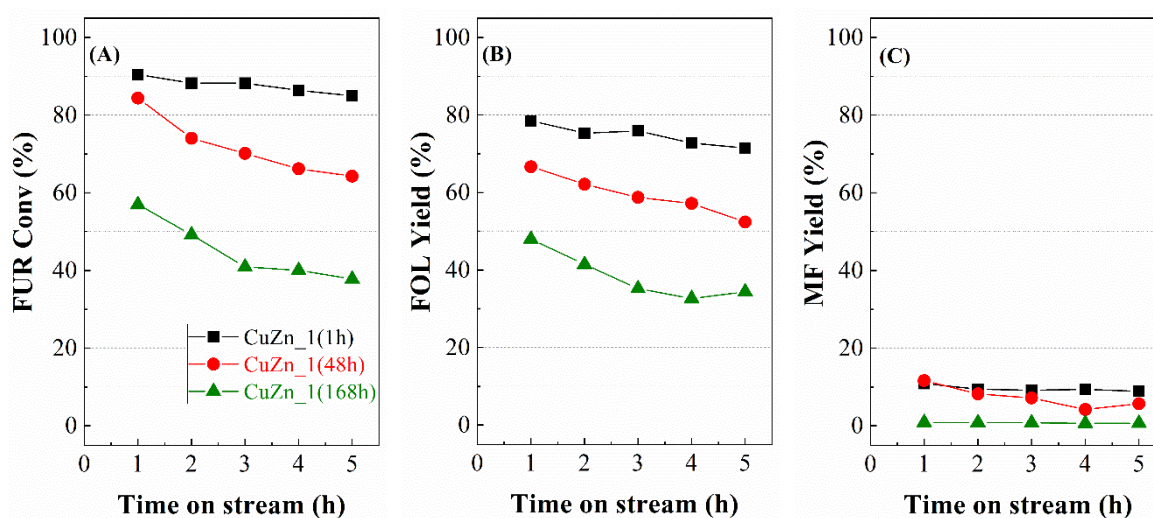


Figure 12. FUR conversion (A), FOL yield (B), and MF yield (C) in the FUR hydrogenation over CuZn₁ catalysts synthesized with different aging time (1–168 h) (Experimental conditions: Mass of catalyst = 0.15 g, Pressure = 0.1 MPa, H₂ flow = 10 mL min⁻¹, Fed flow = 2.3 mmol FUR h⁻¹).

In order to understand the changes of the catalytic behavior for the CuZn_1 catalysts synthesized with different aging times, these catalysts were characterized. Their XRD patterns show clear differences in crystallinity (Figure 13A). Thus, the diffractogram of sample prepared with the shortest aging time (CuZn_1(1h)) does not display any diffraction peak, which are clearly visible for catalysts obtained by increasing the aging time. Thus, CuZn_1(168h) catalyst shows Cu crystallites of 33 nm. These data are in agreement with the literature, since the use of higher temperature and longer aging time favor the growing and better crystallization of layered double hydroxides [3,71]. This fact implies the formation of catalysts where nanoparticles of support and active phase are larger.

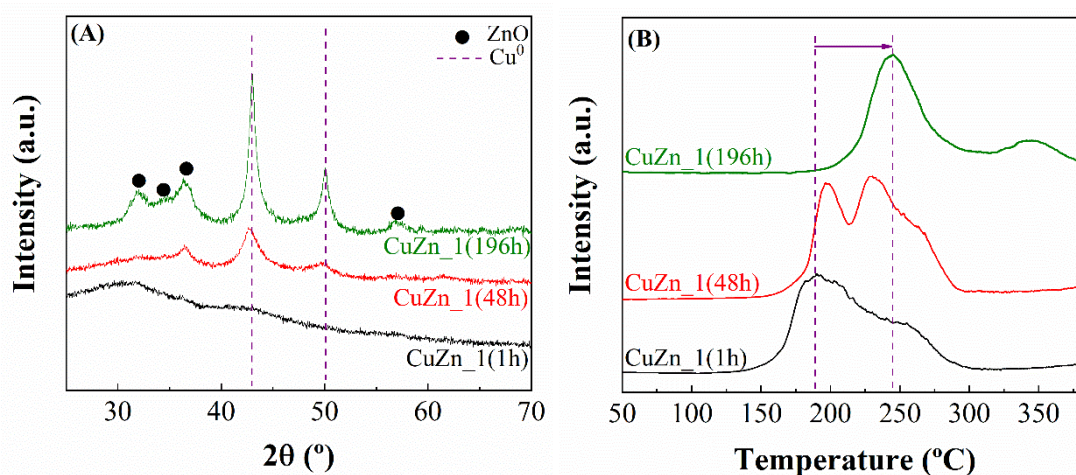


Figure 13. XRD (A) and H₂-TPR (B) profiles of CuZn₁ catalysts synthesized with different aging time.

The analysis of the H₂-TPR profiles also reveals clear modifications depending on the aging time (Figure 13B). Considering that the three catalysts display the same chemical composition, it is expected that the profile differences should be attributable to differences in the size of their Cu nanoparticles. In this sense, a catalyst whose Cu crystallite sizes are smaller (CuZn_1(1h)) is more easily reducible than those catalysts with bigger sizes, as a consequence of the weaker interaction between small CuO nanoparticles and the ZnO/Al₂O₃ support.

In addition, it is also noticeable that both CuZn_1(1h) and CuZn_1(48 h) catalysts display two defined peaks, which could point out the formation of Cu nanoparticles with two different sizes. However, CuZn_1(196h) only shows a peak at higher temperature. This fact could be ascribed to the use of longer aging time, which favors the formation of more homogenous structures. N₂O titration data (Table 6) follow the trend observed by XRD and H₂-TPR, since the catalyst with the lowest aging time (CuZn_1(1h)) is also the catalyst with a higher amount of available surface Cu sites. This would confirm the formation of smaller particles and consequently a higher metallic surface area is obtained, which is in agreement with its better catalytic performance.

Table 6. Metallic characteristic of CuZn₁ catalysts synthesized with different aging time. determined from N₂O titration.

Catalyst	Superficial H ₂ -Uptake ($\mu\text{mol g}^{-1}$)	Metallic Surface		D ¹ (%)	Particle Size (nm)	Crystal Size ² (nm)
		($\text{m}^2_{\text{Cu}} \text{g}_{\text{Cu}}^{-1}$)	($\text{m}^2_{\text{Cu}} \text{g}_{\text{cat}}^{-1}$)			
CuZn_1(1h)	595	69	24	12	9	-
CuZn_1(48h)	475	55	19	10	12	15
CuZn_1(168h)	307	36	12	6	19	33

¹ Copper dispersion. ² Crystal size estimated by Williamson-Hall equation from XRD data [52].

Finally, the superficial analysis of these catalysts by XPS (Table 7) does not reveal any variation in core level spectra in comparison to CuZn_X catalysts. It is only noteworthy a decrease in the surface

Cu content with the aging time, which can be explained by the formation of larger Cu nanoparticles, thus limiting the amount of Cu detected by XPS due to this technique only allows to analyze 2–3 nm of depth (Table 6). With regard to the oxidation state of Cu species, Cu⁰ is the main oxidation state, about a 70–75% of the total Cu, while the Cu⁺ is about 25–30%.

Table 7. Surface atomic concentration of CuZn_1 catalysts synthesized with different aging time.

Catalyst	Atomic Concentration (%)				
	C 1s	O 1s	Al 2p	Cu 2p	Zn 2p
CuZn_1(1h)	11.01	52.83	11.95	8.35	15.86
CuZn_1(48h)	11.06	52.71	12.21	8.07	15.99
CuZn_1(196h)	15.46	50.70	10.87	6.71	16.26

4. Materials and Methods

4.1. Preparation of Catalysts

A series of Cu/ZnO/Al₂O₃ catalysts has been synthesized by co-precipitation method, according to the methodology described by Santos et al. [46]. The LDH precursors were synthesized from aqueous solutions of Cu(NO₃)₂·2H₂O (99%, Aldrich, Saint Louis, MI, USA), Zn(NO₃)₂·6H₂O (99%, Aldrich) and Al(NO₃)₃·9H₂O (99%, Aldrich) with a total metal concentration of 0.3 M. In all cases, (Cu²⁺+Zn²⁺)/Al³⁺ molar ratio was 3, whereas the Cu²⁺/Zn²⁺ molar ratio was varied between 0.2 and 6. In the next step, an aqueous solution of Na₂CO₃ (1.0 M) was slowly added to precipitate metal hydroxides and form the LDH structure. Later, the obtained gel was aged at room temperature for 48 h (in two different synthesis, the gel was aged 1 and 168 h). The obtained solid was filtered and washed with distilled water until reach a neutral pH to ensure the total removal of Na⁺ ions. Finally, the solid was dried overnight at 90 °C and calcined at 300 °C for 4 h, using a ramp of 10 °C min⁻¹.

4.2. Characterization of Catalysts

An X'Pert Pro automated diffractometer (PANanalytical, Bruker, Rheinstetten, Germany) was used to obtain powder X-ray diffraction patterns, this equipment are composed of a Ge (111) primary monochromator (Cu Kα1) and a X'Celerator detector with a step size of 0.017° (2θ), between 2θ = 10° and 70° with an equivalent counting time of 712 s per step. Williamson-Hall Equation (1) [52] was applied to calculate the crystallite size (D):

$$B \cos \theta = (K\lambda/D) + (2 \varepsilon \sin \theta) \quad (1)$$

where B is the full width at half maximum (FWHM) of the XRD peaks, θ the Bragg angle, B is, K is the Scherrer constant, λ is the wavelength of the X ray and ε is the lattice strain.

A FEI Talos F200X (Thermo Fisher Scientific, Waltham, MA, USA) system was used to study the catalyst morphology by transmission electron microscopy (TEM). The images obtained with this technique show a high resolution; moreover, this equipment allows the combination of STEM and TEM imaging and, therefore, a 3D characterization with chemical composition mapping. The samples were dispersed in isopropyl alcohol and each one of them was put on a carbon grid.

The temperature of catalysts reduction was evaluated by H₂-TPR (hydrogen temperature-programmed reduction). To carry out the experiments, 0.080 g of sample has been used. First, the catalyst precursor is treated under a He flow (35 mL min⁻¹) at 100 °C for 30 min, after this, it is cooling to room temperature to start the analysis, where the H₂ consumption is monitored between 50 and 800 °C, by using an Ar/H₂ flow (48 mL min⁻¹, 10 vol.% H₂) with a heating rate of 10 °C min⁻¹. An on-line thermal conductivity detector (TCD) (Shimadzu, Kyoto, Japan) was used to carry out the H₂ quantification. It is necessary to trap the water formed in the process to avoid equipment contamination,

so the outcoming flow is passed through a cold finger immersed in a liquid N₂/isopropanol bath (−80 °C).

In previous research [30,37], N₂O titration has been employed to determine the metallic surface area and the dispersion of Cu⁰ species, where the superficial oxidation of Cu⁰ under a N₂O flow takes place according to the Equation (2):



Prior to the analysis, the catalyst precursor was treated under a He flow (35 mL min^{−1}) at 100 °C for 30 min, followed by a reduction step under a 10 vol.% H₂/Ar-flow (48 mL min^{−1}) at 300 °C for 1 h, with a heating rate of 5 °C min^{−1}, being monitored the H₂ consumption by TCD. When the catalyst was reduced, it was cooled until 60 °C under a He flow to carry out the Cu⁰ oxidation to Cu⁺ performed by titration N₂O (5 vol.% N₂O/He), at 60 °C for 1 h. At last, a second sample reduction was carried out by heating from room temperature to 300 °C with a heating rate of 5 °C min^{−1}, being also monitored its H₂ consumption by TCD.

The textural parameters were determined from the N₂ adsorption-desorption isotherms at −196 °C by using an automatic ASAP 2020 Micromeritics apparatus (Micromeritics, Norcross, GA, USA). The sample was previously outgassed at 200 °C and 10^{−4} mbar for 12 h. The Brunauer-Emmet-Teller (BET) equation [72] was utilized to determine surface area taking a N₂ cross section of 16.2 Å². Micropore volume was determined from alpha-s- method. Pore size distribution was determined using the density functional theory (DFT) [56].

X-ray photoelectron spectra were obtained using a Physical Electronic PHI 5700 spectrometer (Physical Electronics, Eden Prairie, MN, USA), equipped with an Electronics 80-365B multichannel hemispherical electron analyzer and an Mg Kα X-ray excitation source (300 W, 15 kV, hv = 1253.6 eV). High-resolution spectra were recorded by a concentric hemispherical analyzer in a 29.35 eV constant energy mode, using a 720 μm diameter analysis area, and the pressure in the analysis chamber was kept below 5 × 10^{−6} Pa. Binding energies (BE) were determined to an accuracy of ± 0.1 eV, using the adventitious carbon C 1s signal at 284.8 eV as reference. PHI ACCESS ESCA-F V6 software (Eden Prairie, Minnesota, USA) was used for data acquisition and analysis. A Shirley-type background was subtracted from the signals. The recorded spectra were always analyzed with Gauss-Lorentz curves, in order to determine more precisely the binding energy of the atomic levels of the different elements. To avoid sample oxidation after reduction, they were stored in sealed vials with an inert solvent; moreover, samples were prepared in a dry box under a N₂ flow, where the solvent was evaporated prior to its introduction into the analysis chamber, and directly analyzed without previous treatment.

To calculate the total acid sites present in the samples, thermo-programmed desorption of ammonia (NH₃-TPD) was carried out. In a typical procedure, 0.08 g of catalyst is placed in a U-shape quartz reactor and cleaned flowing He (40 mL·min^{−1}) up to 400 °C with a heating rate of 10 °C·min^{−1}. Then, the sample is cooled until 100 °C under the same He flow, and once the temperature is stabilized at 100 °C, the sample is saturated with ammonia for 5 minutes and then physisorbed NH₃ was removed under He. Ammonia desorption is performed by heating the sample from 100 to 400 °C, with a rate of 10 °C·min^{−1}, registering the signal using a GC-14B instrument (Shimadzu, Kyoto, Japan) equipped with a thermal conductivity detector (TCD), previously calibrated with Ni(NH₃)₆Cl₂ (Aldrich) in order to quantify total acid sites.

Thermo-programmed desorption of CO₂ (CO₂-TPD) was employed for the quantification of basic sites. In a typical procedure, 0.03 g of catalyst is pretreated under a He flow (40 mL min^{−1}) at 400 °C for 15 min (10 °C·min^{−1}). Later, the sample was cooled to 100 °C and a pure CO₂ stream (60 mL min^{−1}) was subsequently introduced into the reactor for 30 min. Finally, the amount of CO₂ evolved was analyzed using a TCD detector between 100 and 600 °C and a helium flow (10 °C min^{−1}).

4.3. Catalytic Tests

The furfural hydrogenation was carried out at atmospheric pressure in a tubular quartz reactor with an internal diameter of 6.35 mm. For this, 150 mg of pelletized catalyst (325–400 μm) were placed inside the reactor between two layers of quartz wool, which is placed inside a programmable temperature tubular furnace, controlled with a thermocouple. Before starting the reaction, catalysts were reduced in-situ with a hydrogen flow (99.99%, Airgas, Paris, France) of 60 mL min^{-1} for 1 h at the reduction temperature deduced from their corresponding H_2 -TPR profiles (350 $^\circ\text{C}$). Subsequently, the desired reaction temperature is set and once the system is stable, the reaction is carried out under a flow of H_2 that ranges between 10 and 60 ml min^{-1} and a feed flow of 3.87 mL h^{-1} of a furfural solution in cyclopentyl methyl ether (CPME, 5 vol.%), which is introduced with the help of an HPLC piston pump, model 307 SC-10 (Gilson, Middleton, WI, USA).

To avoid problems, such as blockage of the lines in the equipment, furfural was dissolved in cyclopentyl methyl ether (CPME). This solvent is environmentally friendly and has been used in different organic reactions [30]. Reaction samples were collected every hour, dissolved with a chloroform and o-xylene solution (internal standard), stored in sealed vials to be subsequently analyzed by gas chromatography, using a Shimadzu GB-14A chromatograph equipped with a flame ionization detector and a CP-Wax 52 CB capillary column.

In a preliminary test, the CuZn_1 catalyst was chosen to evaluate the stability of this solvent at 190 $^\circ\text{C}$, after 5 h of time-on-stream (TOS), but in the absence of furfural. The analysis of the collected samples confirmed the full recovery of CPME; without any products different from this ether, thus demonstrating its stability. The conversion, selectivity and yield values were determined using the following expressions:

$$\text{Conversion (\%)} = \frac{\text{mol of furfural converted}}{\text{mol of furfural fed}} \times 100 \quad (3)$$

$$\text{Selectivity (\%)} = \frac{\text{mol of the product}}{\text{mol of furfural converted}} \times 100 \quad (4)$$

$$\text{Yield (\%)} = \frac{\text{mol of the product}}{\text{mol of furfural fed}} \times 100 \quad (5)$$

The turnover frequency was calculated as follows (6):

$$\text{TOF} = -\frac{\ln(1-X)}{\left(\frac{W}{F}\right) \times M} \quad (6)$$

where F is the molar rate of furfural (mol h^{-1}), W is the catalyst weight (g), X is the conversion and M is the mole of sites loaded (mol g^{-1}). This equation, in which $-\ln(1-X)$ substitutes for X assumes a pseudo first-order reaction which may be justified by the excess of hydrogen [63].

5. Conclusions

Several LDHs with chemical composition $(\text{Cu,Zn})_{1-x}\text{Al}_x(\text{OH})_2(\text{CO}_3)_{x/2} \cdot n\text{H}_2\text{O}$ have been synthesized by the co-precipitation method, maintaining a $(\text{Cu}^{2+} + \text{Zn}^{2+})/\text{Al}^{3+}$ molar ratio of 3, and varying the $\text{Cu}^{2+}/\text{Zn}^{2+}$ molar ratio between 0.2 and 6.0. After calcination and reduction steps, Cu/ZnO/Al₂O₃ catalysts were obtained. The physico-chemical characterization has revealed the formation of small Cu nanoparticles highly dispersed in the ZnO-Al₂O₃ structure.

All the catalysts were active in the gas-phase hydrogenation of furfural, with a high selectivity toward furfuryl alcohol, which is considered a valuable product due to its use for manufacturing resins. The presence of a low proportion of acid sites seems to disfavor consecutive reactions, being the formation of MF very limited in all cases. In addition, the textural properties of catalysts are typical of meso- and mainly macroporous solids, and the weaker Cu⁰-FUR interaction, in comparison to other

supports with stronger acidity, favors the lability of adsorbed reaction products and consequently shorter residence times, minimizing the deactivation by the formation of carbonaceous deposits.

In additional studies, the influence of the aging time in the synthesis of LDHs was also evaluated. The catalytic results have demonstrated that a shorter aging time leads to the formation of catalyst with a lower crystallinity, which favors the formation of Cu⁰-rich surfaces. This provides more active and stable catalysts, highly selective to FOL, obtaining a maximum FOL yield of 71% after 5 h of TOS at 210 °C for the CuZn_1 catalyst that was aged for 1 h.

Author Contributions: Conceptualization: J.A.C. and P.M.-T.; methodology: C.P.J.-G. and J.A.C.; validation: C.P.J.-G., J.A.C. and P.M.-T.; formal analysis: G.R.B. and C.P.J.-G.; investigation: G.R.B. and C.P.J.-G.; resources: P.M.-T.; data curation: C.P.J.-G. and J.A.C.; writing—original draft preparation: J.A.C.; writing—review and editing: C.P.J.-G., J.A.C. and P.M.-T.; visualization: C.P.J.-G. and J.A.C.; supervision: J.A.C. and P.M.-T.; project administration: P.M.-T.; funding acquisition: P.M.-T. All authors have read and agreed to the published version of the manuscript.

Funding: The authors are grateful to financial support from the Spanish Ministry of Innovation, Science and Universities (Project RTI2018- 094918-B-C44) and FEDER (European Union) funds.

Acknowledgments: J.A.C. and C.P.J.-G. thank University of Malaga for contracts of PhD incorporation.

Conflicts of Interest: The authors declare that they have no known competing financial interests or personal relationships that could have appeared to influence the work reported in this paper.

References

1. Cavanni, F.; Trifiró, F.; Vaccari, A. Hydrotalcite-type anionic clays: Preparation, properties and applications. *Catal. Today* **1991**, *11*, 173–301. [CrossRef]
2. Mishra, G.; Dash, B.; Pandey, S. Layered double hydroxides: A brief review from fundamentals to application as evolving biomaterials. *Appl. Clay Sci.* **2018**, *153*, 172–186. [CrossRef]
3. Bukhtiyarova, M.V. A review on effect of synthesis conditions on the formation of layered double hydroxides. *J. Solid State Chem.* **2019**, *269*, 494–506. [CrossRef]
4. Kuthati, Y.; Kankala, R.K.; Lee, C.H. Layered double hydroxide nanoparticles for biomedical applications: Current status and recent prospects. *Appl. Clay Sci.* **2015**, *112*, 100–116. [CrossRef]
5. Constantino, V.R.L.; Pinnavaia, T.J. Structure-reactivity relationships for basic catalysts derived from a Mg²⁺/Al³⁺/CO³⁻ layered double hydroxide. *Catal. Lett.* **1994**, *23*, 361–367. [CrossRef]
6. Prinetto, F.; Ghiotti, G.; Durand, R.; Tichit, D. Investigation of acid-base properties of catalysts obtained from layered double hydroxides. *J. Phys. Chem. B* **2000**, *104*, 11117–11126. [CrossRef]
7. Corma Canos, A.; Iborra, S.; Velty, A. Chemical routes for the transformation of biomass into chemicals. *Chem. Rev.* **2007**, *107*, 2411–2502. [CrossRef]
8. Climent, M.J.; Corma, A.; Iborra, S. Conversion of biomass platform molecules into fuel additives and liquid hydrocarbon fuels. *Green Chem.* **2014**, *16*, 516–547. [CrossRef]
9. Binder, J.B.; Raines, R.T. Simple chemical transformation of lignocellulosic biomass into furans for fuels and chemicals. *J. Am. Chem. Soc.* **2009**, *131*, 1979–1985. [CrossRef]
10. Alonso, D.M.; Wettstein, S.G.; Mellmer, M.A.; Gurbuz, E.I.; Dumesic, J.A. Integrated conversion of hemicellulose and cellulose from lignocellulosic biomass. *Energy Environ. Sci.* **2013**, *6*, 76–80. [CrossRef]
11. Delbecq, F.; Wang, Y.; Muralidhara, A.; El Ouardi, K.E.; Marlair, G.; Len, C. Hydrolysis of hemicellulose and derivatives—a review of recent advances in the production of furfural. *Front. Chem.* **2018**, *6*, 146–175. [CrossRef]
12. Mariscal, R.; Maireles-Torres, P.; Ojeda, M.; Sádaba, I.; López Granados, M. Furfural: A renewable and versatile platform molecule for the synthesis of chemicals and fuels. *Energy Environ. Sci.* **2016**, *9*, 1144–1189. [CrossRef]
13. Fúnez-Núñez, I.; García-Sancho, C.; Cecilia, J.A.; Moreno-Tost, R.; Pérez-Inestrosa, E.; Serrano-Cantador, L.; Maireles-Torres, P. Synergistic effect between CaCl₂ and γ-Al₂O₃ for furfural production by dehydration of hemicellulosic carbohydrates. *Appl. Catal. A Gen.* **2019**, *585*, 117188. [CrossRef]
14. Zeitsch, K.J. *The Chemistry and Technology of Furfural and Its Many By-Products*; Elsevier Science: New York, NY, USA, 2000.

15. Yan, K.; Wu, G.; Lafleur, T.; Jarvis, C. Production, properties and catalytic hydrogenation of furfural to fuel additives and value-added chemicals. *Renew. Sustain. Energy Rev.* **2014**, *38*, 663–676. [CrossRef]
16. Ramesh, D.; Reddy, T.S.; Narasimhulu, M.; Rajaram, S.; Suryakiran, N.; Mahesh, K.C.; Venkateswarlu, Y. Efficient and rapid stereoselective synthesis of trans-4,5-diaminocyclopent-2-enones by acidic ionic liquid under solvent-free conditions. *Chem. Lett* **2009**, *38*, 586–587. [CrossRef]
17. Nardi, M.; Costanzo, P.; de Nino, A.; di Gioia, M.L.; Olivito, F.; Sindona, G.; Procopio, A. Water excellent solvent for the synthesis of bifunctionalized cyclopentenones from furfural. *Green Chem.* **2017**, *19*, 5403–5411. [CrossRef]
18. Guo, J.; Xu, G.; Han, Z.; Zhang, Y.; Fu, Y.; Guo, Q. Selective conversion of furfural to cyclopentanone with CuZnAl catalysts. *ACS Sustain. Chem. Eng.* **2014**, *2*, 2259–2266. [CrossRef]
19. Li, S.W.; Batey, R.A. Mild lanthanide(III) catalyzed formation of 4,5-diaminocyclopent-2-enones from 2-furaldehyde and secondary amines: A domino condensation/ring-opening/electrocyclization process. *Chem. Commun.* **2007**, 3759–3761. [CrossRef]
20. Procopio, A.; Costanzo, P.; Curini, M.; Nardi, M.; Oliveira, M.; Sindona, G. Erbium(III) Chloride in ethyl lactate as a smart ecofriendly system for efficient and rapid stereoselective synthesis of trans-4,5-diaminocyclopent-2-enones. *ACS Sustain. Chem. Eng.* **2013**, *1*, 541–544. [CrossRef]
21. Burnett, L.W.; Johns, I.B.; Holdren, R.F.; Hixon, R.M. Production of 2-Methylfuran by Vapor-Phase Hydrogenation of Furfural. *Ind. Eng. Chem.* **1948**, *40*, 502–505. [CrossRef]
22. Manly, D.; Dunlop, A.P. Catalytic Hydrogenation. I. Kinetics and catalyst composition in the preparation of 2-methylfuran. *J. Org. Chem.* **1958**, *23*, 1093–1095. [CrossRef]
23. Seo, G.; Chon, H. Hydrogenation of furfural over copper-containing catalysts. *J. Catal.* **1981**, *67*, 424–429. [CrossRef]
24. Rao, R.; Dandekar, A.; Baker, R.T.K.; Vannice, M.A. Properties of Copper Chromite Catalysts in Hydrogenation Reactions. *J. Catal.* **1997**, *171*, 406–419. [CrossRef]
25. Nagaraja, B.M.; Siva Kumar, V.; Shasikala, V.; Padmasri, A.H.; Sreedhar, B.; David Raju, B.; Rama Rao, K.S. A highly efficient Cu/MgO catalyst for vapour phase hydrogenation of furfural to furfuryl alcohol. *Catal. Commun.* **2003**, *4*, 287–293. [CrossRef]
26. Nagaraja, B.M.; Padmasri, A.H.; David Raju, B.; Rama Rao, K.S. Vapor phase selective hydrogenation of furfural to furfuryl alcohol over Cu-MgO coprecipitated catalysts. *J. Mol. Catal. A Chem.* **2007**, *265*, 90–97. [CrossRef]
27. Sitthisa, S.; Sooknoi, T.; Ma, Y.; Balbuena, P.B.; Resasco, D.E. Kinetics and mechanism of hydrogenation of furfural on Cu/SiO₂ catalysts. *J. Catal.* **2011**, *277*, 1–13. [CrossRef]
28. Sitthisa, S.; Resasco, D.E. Hydrodeoxygenation of Furfural Over Supported Metal Catalysts: A Comparative Study of Cu, Pd and Ni. *Catal. Lett.* **2011**, *141*, 784–791. [CrossRef]
29. Dong, F.; Zhu, Y.; Zheng, H.; Zhu, Y.; Li, X.; Li, Y. Cr-free Cu-catalysts for the selective hydrogenation of biomass-derived furfural to 2-methylfuran: The synergistic effect of metal and acid sites. *J. Mol. Catal. A Chem.* **2015**, *398*, 140–148. [CrossRef]
30. Jiménez-Gómez, C.P.; Cecilia, J.A.; Durán-Martín, D.; Moreno-Tost, R.; Santamaría-González, J.; Mérida-Robles, J.; Mariscal, R.; Maireles-Torres, P. Gas-phase hydrogenation of furfural to furfuryl alcohol over Cu/ZnO catalysts. *J. Catal.* **2016**, *336*, 107–115. [CrossRef]
31. Ghashghae, M.; Sadjadi, S.; Shirvani, S.; Farzaneh, V. A Novel Consecutive Approach for the Preparation of Cu–MgO Catalysts with High Activity for Hydrogenation of Furfural to Furfuryl Alcohol. *Catal. Lett.* **2017**, *147*, 318–327. [CrossRef]
32. Jiménez-Gómez, C.P.; Cecilia, J.A.; Moreno-Tost, R.; Maireles-Torres, P. Selective Production of 2-Methylfuran by Gas-Phase Hydrogenation of Furfural on Copper Incorporated by Complexation in Mesoporous Silica Catalysts. *ChemSusChem* **2017**, *10*, 1448–1459. [CrossRef] [PubMed]
33. Jiménez-Gómez, C.P.; Cecilia, J.A.; Moreno-Tost, R.; Maireles-Torres, P. Selective Furfural Hydrogenation to Furfuryl Alcohol Using Cu-Based Catalysts Supported on Clay Minerals. *Top. Catal.* **2017**, *60*, 1040–1053. [CrossRef]
34. Yang, X.; Chen, H.; Meng, Q.; Zheng, H.; Zhu, Y.; Li, Y.W. Insights into influence of nanoparticle size and metal-support interactions of Cu/ZnO catalysts on activity for furfural hydrogenation. *Catal. Sci. Technol.* **2017**, *7*, 5625–5634. [CrossRef]

35. Sulmonetti, T.P.; Pang, S.H.; Claire, M.T.; Lee, S.; Cullen, D.A.; Agrawal, P.K.; Jones, C.W. Vapor phase hydrogenation of furfural over nickel mixed metal oxide catalysts derived from layered double hydroxides. *Appl. Catal. A Gen.* **2016**, *517*, 187–195. [CrossRef]
36. Manikandan, M.; Venugopal, A.K.; Prabu, K.; Jha, R.K.; Thirumalaiswamy, R. Role of surface synergistic effect on the performance of Ni-based hydrotalcite catalyst for highly efficient hydrogenation of furfural. *J. Mol. Catal. A Chem.* **2016**, *417*, 153–162. [CrossRef]
37. Guerrero-Torres, A.; Jiménez-Gómez, C.P.; Cecilia, J.A.; García-Sancho, C.; Quirante-Sánchez, J.J.; Mérida-Robles, J.M.; Maireles-Torres, P. Influence of the incorporation of basic or amphoteric oxides on the performance of Cu-based catalysts supported on sepiolite in furfural hydrogenation. *Catalysts* **2019**, *9*, 315. [CrossRef]
38. Nakagawa, Y.; Nakazawa, H.; Watanabe, H.; Tomishige, K. Total Hydrogenation of Furfural over a Silica-Supported Nickel Catalyst Prepared by the Reduction of a Nickel Nitrate Precursor. *ChemCatChem* **2012**, *4*, 1791–1797. [CrossRef]
39. Jiménez-Gómez, C.P.; Cecilia, J.A.; Moreno-Tost, R.; Maireles-Torres, P. Nickel Phosphide/Silica Catalysts for the Gas-Phase Hydrogenation of Furfural to High-Added-Value Chemicals. *ChemCatChem* **2017**, *9*, 2881–2889. [CrossRef]
40. Jiménez-Gómez, C.P.; Cecilia, J.A.; García-Sancho, C.; Moreno-Tost, R.; Maireles-Torres, P. Selective Production of Furan from Gas-Phase Furfural Decarbonylation on Ni-MgO Catalysts. *ACS Sustain. Chem. Eng.* **2019**, *7*, 7676–7685. [CrossRef]
41. Guerrero-Torres, A.; Jiménez-Gómez, C.P.; Cecilia, J.A.; García-Sancho, C.; Franco, F.; Quirante-Sánchez, J.J.; Maireles-Torres, P. Ni supported on sepiolite catalysts for the hydrogenation of furfural to value-added chemicals: Influence of the synthesis method on the catalytic performance. *Top. Catal.* **2019**, *62*, 535–550. [CrossRef]
42. Sitthisa, S.; Pham, T.; Prasomsri, T.; Sooknoi, T.; Mallinson, R.G.; Resasco, D.E. Conversion of furfural and 2-methylpentanal on Pd/SiO₂ and Pd-Cu/SiO₂ catalysts. *J. Catal.* **2011**, *280*, 17–27. [CrossRef]
43. Pino, N.; Sitthisa, S.; Tan, Q.; Souza, T.; López, D.; Resasco, D.E. Structure, activity, and selectivity of bimetallic Pd-Fe/SiO₂ and Pd-Fe/ γ -Al₂O₃ catalysts for the conversion of furfural. *J. Catal.* **2017**, *350*, 30–40. [CrossRef]
44. Yang, X.; Meng, Q.; Ding, G.; Wang, Y.; Chen, H.; Zhu, Y.L.; Li, Y.W. Construction of novel Cu/ZnO-Al₂O₃ composites for furfural hydrogenation: The role of Al components. *Appl. Catal. A Gen.* **2018**, *561*, 78–86. [CrossRef]
45. Nogueira, K.A.B.; Cecilia, J.A.; Santos, S.O.; Aguiar, J.E.; Vilarrasa-García, E.; Rodríguez-Castellón, E.; Azevedo, D.C.S.; Silva, I.J. Adsorption behavior of bovine serum albumin on Zn-Al and Mg-Al layered double hydroxides. *J. Sol-Gel Sci. Technol.* **2016**, *80*, 748–758. [CrossRef]
46. Santos, J.L.; Reina, T.R.; Ivanova, S.; Centeno, M.A.; Odriozola, J.A. Gold promoted Cu/ZnO/Al₂O₃ catalysts prepared from hydrotalcite precursors: Advanced materials for the WGS reaction. *Appl. Catal. B Environ.* **2017**, *201*, 310–317. [CrossRef]
47. He, L.; Cheng, H.; Liang, G.; Yu, Y.; Zhao, F. Effect of structure of CuO/ZnO/Al₂O₃ composites on catalytic performance for hydrogenation of fatty acid ester. *Appl. Catal. A Gen.* **2013**, *452*, 88–93. [CrossRef]
48. Fierro, J.L.G.; Melián-Cabrera, I.; López Granados, M. Reverse topotactic transformation of a Cu-Zn-Al catalyst during wet Pd impregnation: Relevance for the performance in methanol synthesis from CO₂/H₂ mixtures. *J. Catal.* **2002**, *210*, 273–284.
49. Chinchén, G.C.; Waugh, K.C.; Whan, D.A. The activity and state of the copper surface in methanol synthesis catalysts. *Appl. Catal.* **1986**, *25*, 101–107. [CrossRef]
50. Gervasini, A.; Bennici, S. Dispersion and surface states of copper catalysts by temperature-programmed-reduction of oxidized surfaces (s-TPR). *Appl. Catal. A Gen.* **2005**, *281*, 199–205. [CrossRef]
51. Yahiro, H.; Nakaya, K.; Yamamoto, T.; Saiki, K.; Yamaura, H. Effect of calcination temperature on the catalytic activity of copper supported on γ -alumina for the water-gas-shift reaction. *Catal. Commun.* **2006**, *7*, 228–231. [CrossRef]
52. Williamson, G.K.; Hall, W.H. X-ray line broadening line from filed aluminium and wolfram. *Acta Metall.* **1953**, *1*, 22–31. [CrossRef]
53. Studt, F.; Abild-Pedersen, F.; Varley, J.B.; Nørskov, J.K. CO and CO₂ hydrogenation to methanol calculated using the BEEF-vdW functional. *Catal. Lett.* **2013**, *143*, 71–73. [CrossRef]

54. Maderuelo-Solera, R.; López-Asensio, R.; Cecilia, J.A.; Jiménez-Gómez, C.P.; García-Sancho, C.; Moreno-Tost, R.; Maireles-Torres, P. Catalytic transfer hydrogenation of furfural to furfuryl alcohol over calcined MgFe hydrotalcites. *Appl. Clay Sci.* **2019**, *183*, 105351–105363. [CrossRef]
55. Thommes, M.; Kaneko, K.; Neimark, A.V.; Olivier, J.P.; Rodriguez-Reinoso, F.; Rouquerol, J.; Sing, K.S.W. Physisorption of gases, with special reference to the evaluation of surface area and pore size distribution (IUPAC Technical Report). *Pure Appl. Chem.* **2015**, *87*, 1051–1069. [CrossRef]
56. Landers, J.; Gor, G.Y.; Neimark, A.V. Density functional theory methods for characterization of porous materials. *Colloids Surfaces A Physicochem. Eng. Asp.* **2013**, *437*, 3–32.
57. Pakharukova, V.P.; Moroz, E.M.; Zyuzin, D.A.; Ishchenko, A.V.; Dolgikh, L.Y.; Strizhak, P.E. Structure of Copper Oxide Species Supported on Monoclinic Zirconia. *J. Phys. Chem. C* **2015**, *119*, 28828–28835.
58. Arango-Díaz, A.; Cecilia, J.A.; Dos Santos-Gómez, L.; Marrero-López, D.; Losilla, E.R.; Jiménez-Jiménez, J.; Rodríguez-Castellón, E. Characterization and performance in preferential oxidation of CO of CuO-CeO₂ catalysts synthesized using polymethyl metacrylate (PMMA) as template. *Int. J. Hydrog. Energy* **2015**, *40*, 11254–11260.
59. Kattel, S.; Ramírez, P.J.; Chen, J.G.; Rodriguez, J.A.; Liu, P. Active sites for CO₂ hydrogenation to methanol on Cu/ZnO catalysts. *Science (80-)* **2017**, *355*, 1296–1299. [CrossRef]
60. Peplinski, B.; Unger, W.E.S.; Grohmann, I. Characterization of CuZnAl oxide catalysts in the precipitated, calcined and reduced state by means of XPS with the help of a finger-print data base. *Appl. Surf. Sci.* **1992**, *62*, 115–129. [CrossRef]
61. Moulder, J.F.; Stickle, W.F.; Sool, P.E.; Bombardieri, K.D. *Handbook of X-ray Photoelectron Spectroscopy*; Perkin-Elmer: Eden Prairie, NM, USA, 1992.
62. Liu, D.; Zemlyanov, D.; Wu, T.; Lobo-Lapidus, R.J.; Dumesic, J.A.; Miller, J.T.; Marshall, C.L. Deactivation mechanistic studies of copper chromite catalyst for selective hydrogenation of 2-furfuraldehyde. *J. Catal.* **2013**, *299*, 336–345. [CrossRef]
63. Jiménez-Gómez, C.P.; Cecilia, J.A.; Márquez-Rodríguez, I.; Moreno-Tost, R.; Santamaría-González, J.; Mérida-Robles, J.; Maireles-Torres, P. Gas-phase hydrogenation of furfural over Cu/CeO₂ catalysts. *Catal. Today* **2017**, *279*, 327–338. [CrossRef]
64. Wu, J.; Shen, Y.; Liu, C.; Wang, H.; Geng, C.; Zhang, Z. Vapor phase hydrogenation of furfural to furfuryl alcohol over environmentally friendly Cu-Ca/SiO₂ catalyst. *Catal. Commun.* **2005**, *6*, 633–637. [CrossRef]
65. Solinas, V.; Ferino, I. Microcalorimetric characterisation of acid-basic catalysts. *Catal. Today* **1998**, *41*, 179–189. [CrossRef]
66. Gervasini, A.; Auroux, A. Microcalorimetric investigation of the acidity and basicity of metal oxides. *J. Therm. Anal.* **1991**, *37*, 1737–1744. [CrossRef]
67. Watanabe, K.; Yamagiwa, N.; Torisawa, Y. Cyclopentyl methyl ether as a new and alternative process solvent. *Org. Process Res. Dev.* **2007**, *11*, 251–258. [CrossRef]
68. Shi, Y.; Zhu, Y.; Yang, Y.; Li, Y.W.; Jiao, H. Exploring Furfural Catalytic Conversion on Cu(111) from Computation. *ACS Catal.* **2015**, *5*, 4020–4032. [CrossRef]
69. Pillai, U.R.; Deevi, S. Copper-zinc oxide and ceria promoted copper-zinc oxide as highly active catalysts for low temperature oxidation of carbon monoxide. *Appl. Catal. B Environ.* **2006**, *65*, 110–117. [CrossRef]
70. Jiménez-Gómez, C.P.; Cecilia, J.A.; Franco-Duro, F.I.; Pozo, M.; Moreno-Tost, R.; Maireles-Torres, P. Promotion effect of Ce or Zn oxides for improving furfuryl alcohol yield in the furfural hydrogenation using inexpensive Cu-based catalysts. *Mol. Catal.* **2018**, *455*, 121–131. [CrossRef]
71. Abderrazek, K.; Frini Srasra, N.; Srasra, E. Synthesis and Characterization of [Zn-Al] Layered Double Hydroxides: Effect of the Operating Parameters. *J. Chin. Chem. Soc.* **2017**, *64*, 346–353. [CrossRef]
72. Brunauer, S.; Emmett, P.H.; Teller, E. Adsorption of Gases in Multimolecular Layers. *J. Am. Chem. Soc.* **1938**, *60*, 309–319. [CrossRef]



Article

Hierarchical PtIn/Mg(Al)O Derived from Reconstructed PtIn-hydrotalcite-like Compounds for Highly Efficient Propane Dehydrogenation

Jiaxin Li, Ming Zhang, Zhen Song, Shuo Liu, Jiameng Wang and Lihong Zhang * 

Department of Catalysis Science and Technology and Tianjin Key Laboratory of Applied Catalysis Science & Technology, School of Chemical Engineering and Technology, Tianjin University, Tianjin 300350, China; xgclone@163.com (J.L.); minne_zhang@hotmail.com (M.Z.); songzhens12345@163.com (Z.S.); shuoecho@outlook.com (S.L.); wangjiameng0216@163.com (J.W.)

* Correspondence: zlh_224@163.com or zlh_224@tju.edu.cn

Received: 8 August 2019; Accepted: 9 September 2019; Published: 12 September 2019

Abstract: The challenges facing propane dehydrogenation are to solve the Pt sintering and carbon deposition. This paper provides a new way to disperse and stabilize Pt species and resist carbon deposition. Highly dispersed Pt species were topologically transformed from reconstructed PtIn-hydrotalcite-like precursors in a flower-like hierarchical microstructure. The lattice confinement of reconstructed hydrotalcite-like precursor is in favor of stabilizing the highly dispersed Pt species, and the hierarchical microstructure is an important factor to prolong its lifetime by enhancing tolerance to carbon deposition. In propane dehydrogenation, the propene selectivity decreases in the sequences of catalyst in flower-like > single-plate > block mass with small, flakes. A propene selectivity of >97% with a conversion of 48% at 600 °C has been achieved over a flower-like PtIn/Mg(Al)O catalyst. Additionally, no visible Pt sintering can even be observed on this catalyst after a reaction time of 190 h. This strategy provides an effective and feasible alternative for the facile preparation of highly dispersed metal catalysts.

Keywords: propane dehydrogenation; hierarchical microstructure; reconstruction; high selectivity; excellent durability

1. Introduction

Industrially, propene is a vital chemical material with a huge demand [1,2]. Catalytic propane dehydrogenation (PDH) is considered an efficient technique to obtain propene [3,4]. In this process, catalyst Pt/Al₂O₃ is widely used [5,6].

However, there are several open issues for this Pt-based catalyst under reaction conditions [3,7,8], such as Pt sintering, carbon deposition and propane cracking. Extensive research efforts have been made to inhibit deactivation and improve propene selectivity of Pt-based catalysts by doping promoters of Sn [9,10], In [11,12], Ga [13,14] and Cu [15] to form bimetallic catalysts. For example, Pt–In [16] and Pt–Ga [17,18] bimetallic nanoparticles (NPs) supported on calcined hydrotalcites (HT) show higher activity and selectivity in PDH, which has been attributed to the increased Pt dispersion and electron transfer from In or Ga to Pt [11,18]. Besides promoters, another method is to modify Al₂O₃ support with ZnO [19], La₂O₃ [20] or TiO₂ [21] or replace Al₂O₃ support with ZnAl₂O₄ [22], ZSM-5 [23] or Mg(Al)O oxide [8,24]. Additionally, it has been verified that the single Pt atom sites on Pt–Sn/γ–Al₂O₃ with a “sandwich structure” are more favorable for PDH reaction than Pt ensembles [25,26]. Gong et al. [15] also reported that the PtCu single atom alloys can enhance the propane conversion and propene selectivity simultaneously in PDH.

Whether as promoters or supports, an important aim of using them is to obtain highly and stably dispersed Pt-based catalysts so that improving PDH performance. However, it is still difficult to

break through these challenges for PDH reactions [27], and the exact Pt-M-support relationship is still unclear. Therefore, it is extremely necessary to find more efficient methods to solve the problems mentioned above.

In fact, the hierarchical morphology and porous structure play important roles in many heterogeneous catalytic reactions. However, the effect of hierarchical microstructure is seldom reported.

Additionally, calcined HT-like compounds are regarded as a good way to obtain supported metal catalysts with high surface area and atomic-scale uniform distribution of metal species due to the topotactic transformation [28]. These features, the changeable composition and the acid-base property make it possible to improve PDH performance by optimizing Pt-based catalysts [8,24,29].

However, the most of HT-like compounds are prepared by co-precipitation method; as a result, the morphologies of as-synthesized products are usually low crystalline NPs consisting of a great number of small and thick plates [3,8]. That must be detrimental to fully utilizing the active metal species in bulk. Fortunately, the calcined HT can be reconstructed due to the memory effect of HT. During the process, some metal ions have the chance to be introduced into the layer of reconstructed HT [30,31]. The lattice-confined metal species can be converted into highly dispersed metal NPs and even single metal atom sites.

Given that the small Pt NPs and hierarchical microstructure may provide more stable and easily accessible active sites for PDH reaction, a promising design for obtaining the desired size of active Pt and hierarchical pore morphology was proposed. In this paper, PtIn/Mg(Al)O catalyst in a flower-like nanosheet array (PtInHT-FR) was fabricated by reduction—followed by calcination of the flower-like PtIn-HT precursor (PtInHT-F) with a hierarchical microstructure, which produced from a sodium dodecyl sulfate-assisted hydrothermal synthesis, followed by thermal decomposition and structural reconstruction. Although there is no additional support for this catalyst with low specific surface area, a stable and excellent propene selectivity of >97% and a high conversion of 48% still can be achieved at 600 °C. As contrasting samples, the single-plate (PtInHT-PR) and block mass (PtInHT-MR) PtIn/Mg(Al)O catalysts were derived from the corresponding high crystalline single-plate HT (PtInHT-P) and low crystalline block mass HT (PtInHT-M) with small, flake-like structures, which were synthesized by the hydrothermal synthesis and co-precipitation methods, respectively. The corresponding calcined samples were marked as PtInHT-XC (X represents morphology of F—flower-like, P—single-plate and M—block mass). After PDH reaction, the catalysts used were labeled as PtInHT-XU. During the preparation process, the HT-X, HT-XC, InHT-X and InHT-XC samples were also prepared. The structure and physico-chemical properties of catalysts and precursors were studied. The promoted effects of HT reconstruction on the microstructure and morphology of the 3D oxide nanosheet array catalyst, and the subsequently superior PDH performance, were profoundly discussed.

2. Results and Discussion

2.1. Phase Structure and Reconstruction Study

In order to ascertain the crystal phase structure of all samples in details, the XRD patterns of precursors, calcined and reduced samples are shown together in Figure 1, and the analyzing results of XRD patterns of all samples before calcination are given in Table 1.

It can be seen that the XRD patterns of HT-F, HT-P and HT-M exhibit strong characteristic diffraction peaks in the HT phase [32], although their preparation processes are different. After calcination, followed by the impregnation of HT-FC, HT-PC and HT-MC with In³⁺ ions, the characteristic diffraction peaks of the HT phase appear again in the XRD patterns of InHT-F, InHT-P and InHT-M, without other diffraction peaks. That suggests that the impregnation condition is beneficial to reconstructing the HT phase. A similar HT recrystallization phenomenon happened again after the impregnation of In-based metal oxides with Pt⁴⁺ ions. For HT-M, the broad and well-defined diffraction peaks indicate that the obtained single HT phase was poorly crystallized. With the introduction of In³⁺ ions and further Pt⁴⁺ ions, the relative intensity of diffraction peaks of HT phase gives a decreasing tendency. From HT-F

to InHT-F and HT-P to InHT-P, the shrinkage of peak intensities is more considerable than that from HT-M to InHT-M. This should be related to the decrease of HT crystallinity. At the same time, the average crystallite size in the *c* direction (*L_c*) also decreases with reconstruction and even drops from PtInHT-M to PtInHT-P and to PtInHT-F (see Table 1), which can be estimated by means of the Scherrer equation [33]. This indicates that the HT layer becomes thinner and thinner.

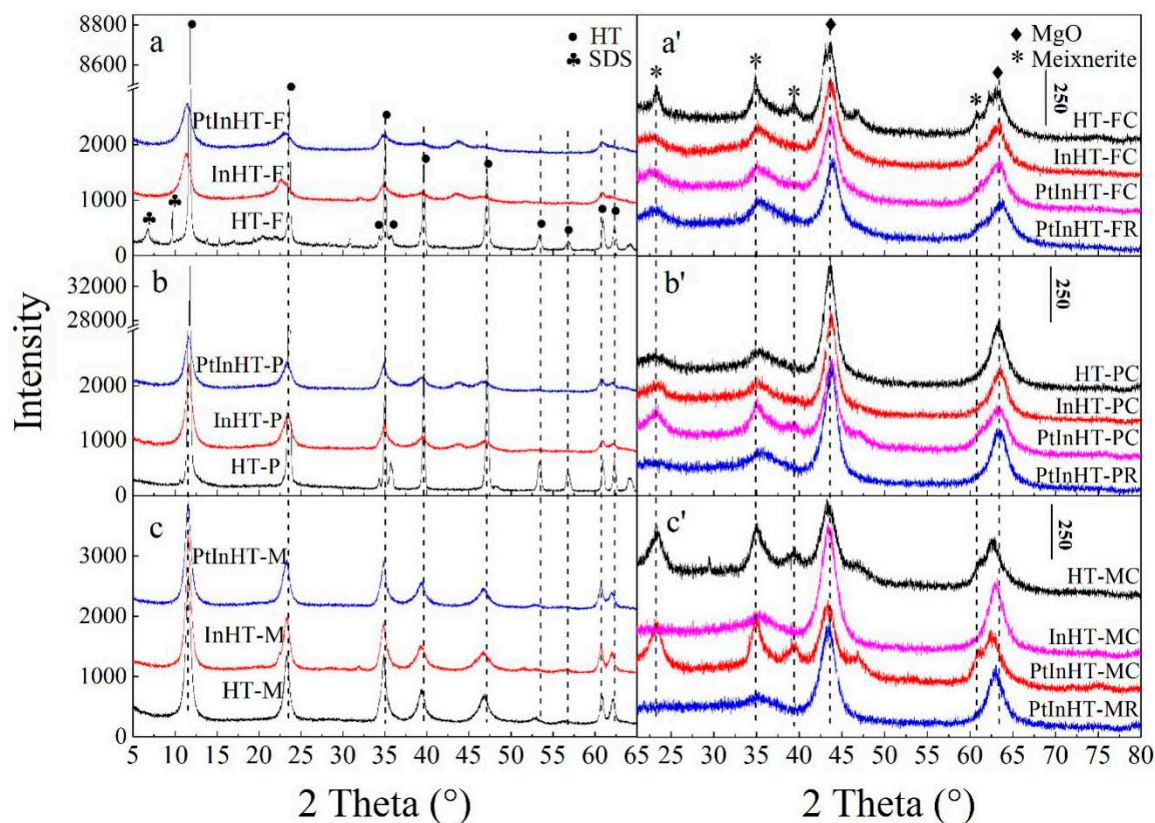


Figure 1. XRD patterns of HT precursors and derived samples in different morphology.

Table 1. Lattice parameters of HT phase in all dried samples.

Sample	Lattice Parameter <i>a</i> (nm) ^a	Lattice Parameter <i>c</i> (nm) ^b	<i>L_c</i> (nm) ^c	
HT	-F	0.3037	2.2551	233.5
	-P	0.3039	2.2588	235.7
	-M	0.3045	2.2847	64.1
InHT	-F	0.3051	2.3246	34.2
	-P	0.3041	2.2673	48.4
PtInHT	-M	0.3049	2.2858	60.1
	-F	0.3052	2.3027	42.6
	-P	0.3049	2.2764	44.2
	-M	0.3050	2.2936	51.3

^a $a = 2d_{110}$. ^b Average value calculated from (003), (006), and (009) reflections. ^c Average crystallite size in *c* direction calculated from the Scherrer equation using the FWHM (Full Width at Half Maximum) of (003) and (006) reflections [33].

Additionally, the decreasing $M^{2+}/(M^{3+} + M^{4+})$ ratio can cause the increase of positive charge density in the layers, while the big radii of In^{3+} (0.080 nm, the Shannon ionic radius [34]) and Pt^{4+} (0.063 nm, Shannon ionic radius [34]) ions can broaden the distance of metal ions in the layers. These can make the octahedral cell shrink or expand and then influence the value of the lattice parameter *a* and *c* of HT phase, as shown in Table 1. The change of lattice parameters *a* and *c* of the HT phase (Table 1) demonstrates that In^{3+} and Pt^{4+} ions have been introduced into the HT layer. It signifies that

the Pt and In species could be highly dispersed on the final metal oxides with close contact among them, and support [10].

After calcination and reduction, the HT phase disappears along with the occurrence of MgO (JCPDS file number 45-0946) and meixnerite ($\text{Mg}_4\text{Al}_2(\text{OH})_{14}\cdot 3\text{H}_2\text{O}$, JCPDS file number 35-0964) diffraction peaks in Figure 1. At the same time, there are not any metal phase diffraction peaks can be found in the XRD patterns, which means that Pt and/or In metal phases are exactly evenly-dispersed on the surface of HT-derived catalysts.

From TEM images of PtInHT-FR, PtInHT-PR and PtInHT-MR in Figure 2, it is difficult to find metal particles except thin nanosheets. That indicates that the metal particles are so small that the TEM cannot identify them. Therefore, it is reasonable to infer that metal atom clusters or single metal atoms are possibly formed on the surface of metal oxide nanosheets due to the low metal loading amount and the HT lattice confinement effect [10]. The EDS element-mapping images of PtInHT-FR further demonstrate the uniform distribution of Pt and In elements without aggregation, and support the probability of metal atoms or atom clusters type distributions [35].

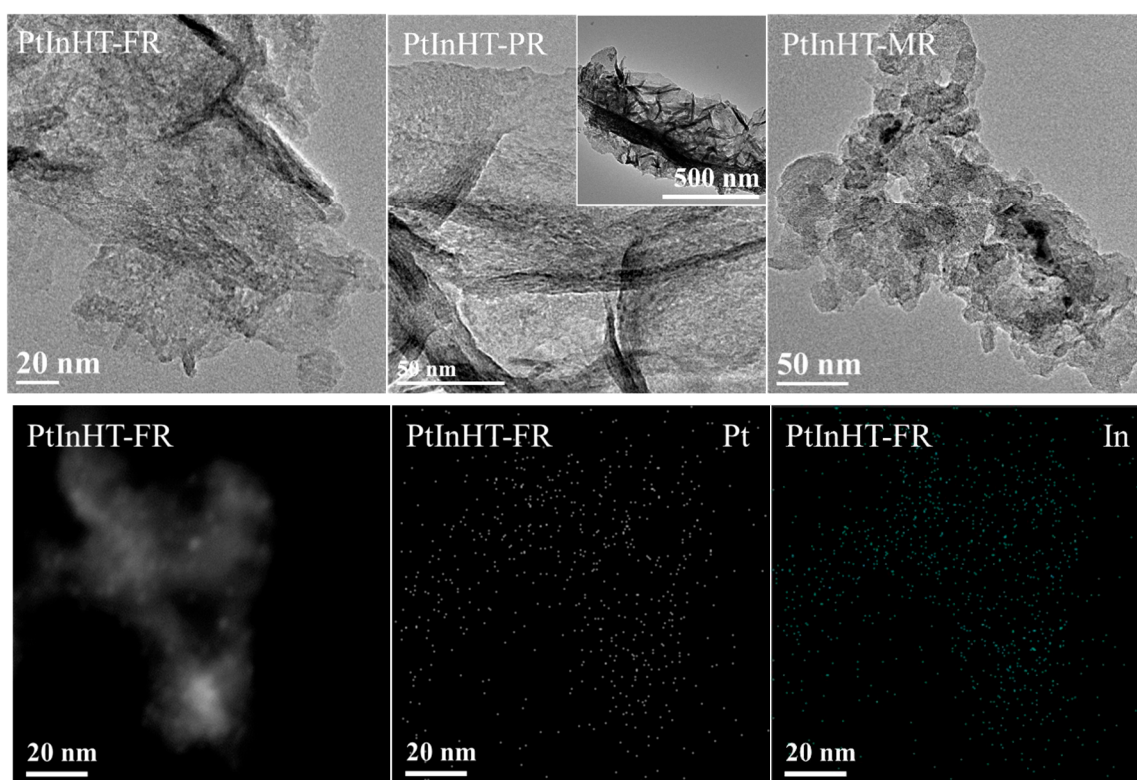


Figure 2. TEM images of reduced samples: PtInHT-FR, PtInHT-PR, PtInHT-MR and EDS element-mapping analysis of PtInHT-FR. In the abbreviations: F—flower-like, P—single-plate, and M—block mass and R—reduced sample.

2.2. Morphology, Texture and Pt–In Interaction Analysis

Figure 3 shows SEM images of three series of samples. It clearly depicts that the HT-F and corresponding derivative samples are constructed by huge ball-flower-like microstructure. For fresh HT-P and its derivative samples, perfect single-plate NPs are displayed in the SEM images. On the contrary, small, flakes are disorderly stacked into big block masses for HT-M and its derivative products. The calcination makes the nanosheets become rough and the impregnation-induced reconstruction makes them become smooth again. The loose surface for the calcined samples is related to the newly formed pores, which is the result of the decomposition and removal of interlayer anions and hydroxyl groups. It is clear that a large amount of small and ultrathin nanosheets grow in an orderly manner with *ab*-planes interdigitated perpendicular to the two lateral surfaces of recrystallizing original HT

nanosheets for InHT-F and InHT-P. According to the XRD results in Figure 1, the reconstruction should also take place in InHT-M, although it is difficult to distinguish the small new nanosheets from the original flakes. In other words, this microstructure is indistinctive in the reconstructed HT-M series and instead severely aggregated nanoplates without any regular shape leave over. This microstructure should be the result of abundant hydroxyl groups on the edge sites and the basal plane of calcined HT plates [36]. The similar morphology can be seen in the SEM images of corresponding PtIn-based samples. In any case, there must be a strong interaction between the newly formed nanoplates and the initial huge templates, originating from the shared Al and other elements [36]. The strong interaction is beneficial to stabilize and disperse metal active species. The formation of ultrathin nanosheets is bound to decrease the average crystallite size in the *c* direction (Table 1) and weaken the diffraction peaks of HT phase in initial huge HT-F and HT-P template, which is consistent with the XRD results in Figure 1. As for the reduced samples, the basic morphology feature still can be maintained, but some broken particles can be found on the surface of single-plate PtInHT-PR sample. That indicates that the fully opening surface is detrimental to protect the newly formed nanosheets from destruction by an external force.

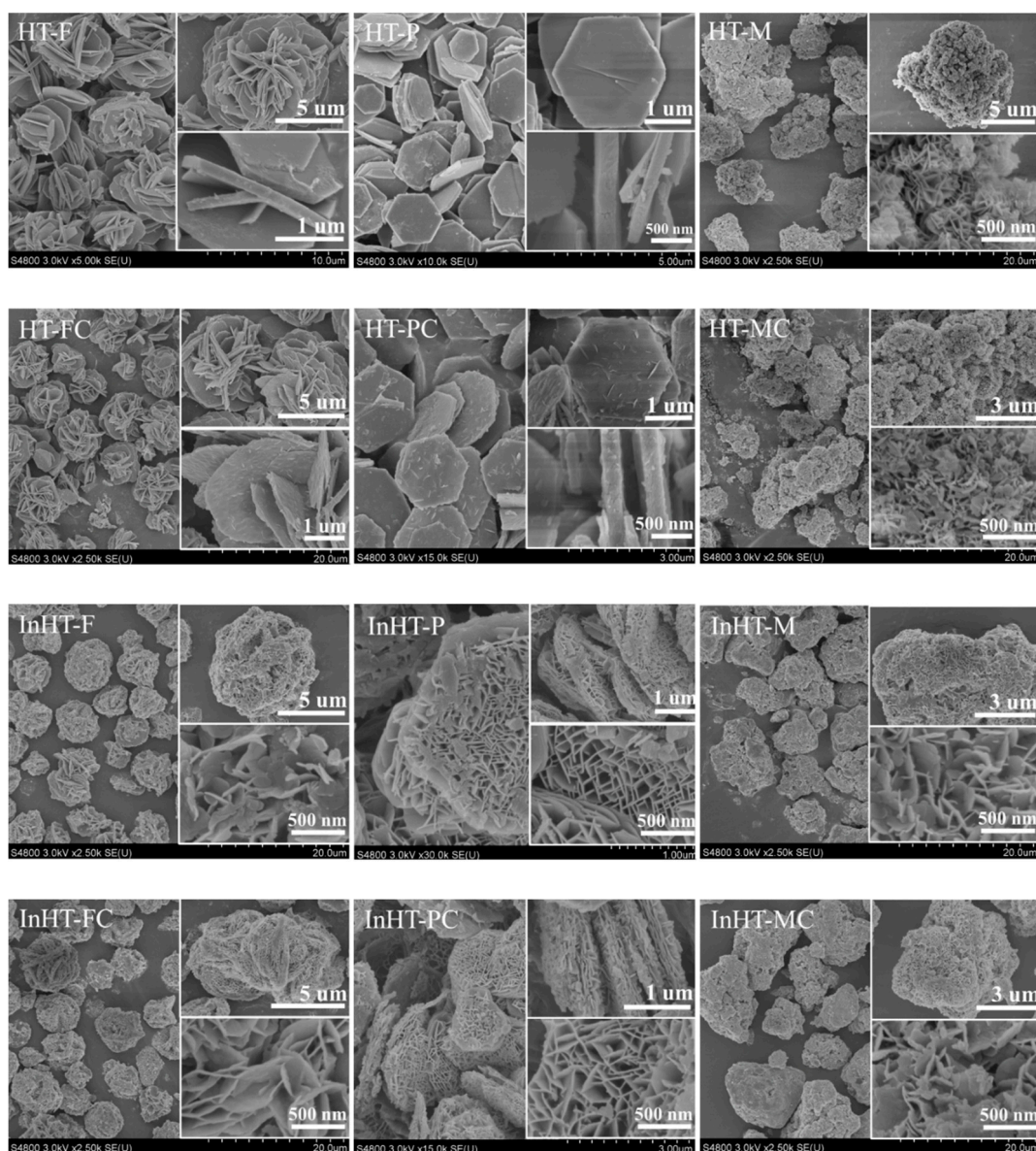


Figure 3. Cont.

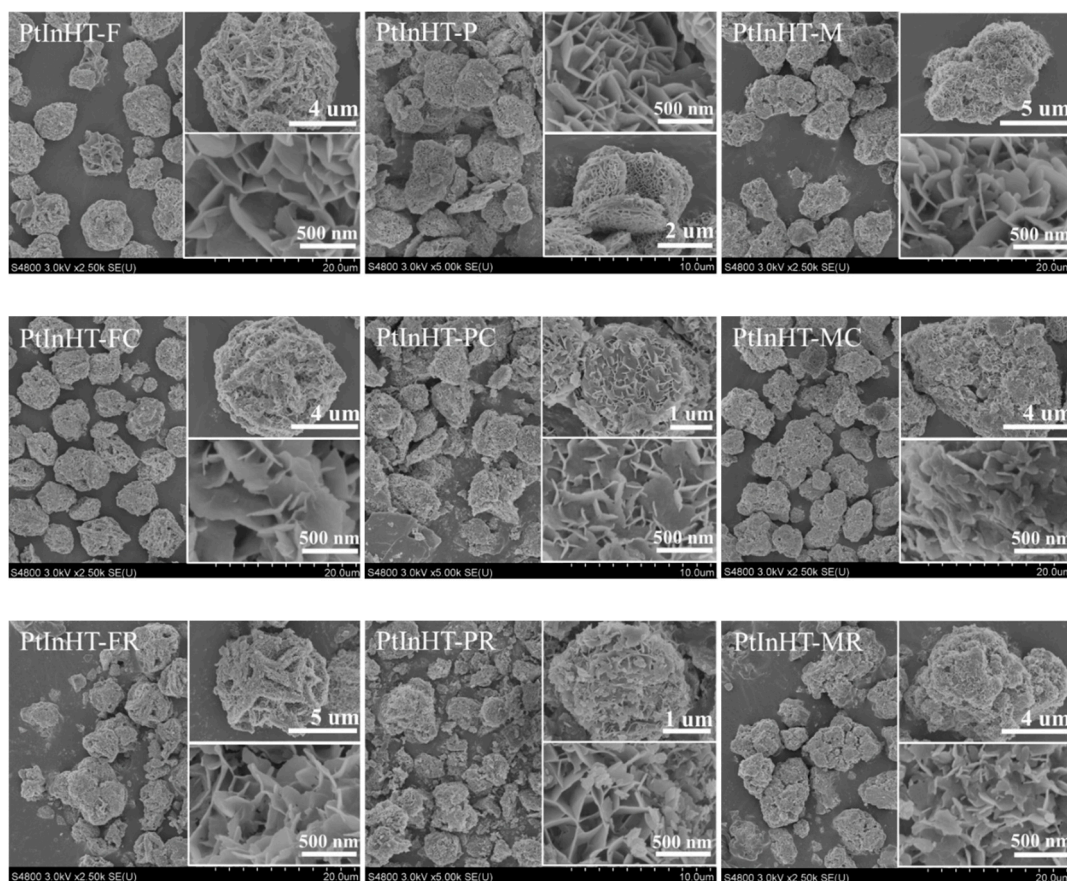


Figure 3. SEM images of HT precursor, calcined, reconstructed and reduced samples with different morphologies.

It can be seen that the slit-shaped mesopores are the common features of all samples. As for the recrystallizing single-plate samples, including InHT-P, PtInHT-P and corresponding calcined and reduced products, the reconstruction not only results in the formation of narrow slit-like pores due to the nanoplates' delaminating, but also leads to the appearance of honeycomb-like pores arising from the growth of ultrathin nanosheets perpendicular to the surface of the primary large single-plate nanoplates. Especially in the InHT-F and PtInHT-F series, the big wedge-shaped pore channels appear in the huge ball-flower-like microstructure, except the honeycomb-like pores. However, the similar size between the original flakes and newly formed nanosheets make the pore structures of the HT-M and reconstructed samples no different. Therefore, the obvious hierarchical pore feature can be assigned to recrystallizing flower-like and single-plate samples; and the pore shape and size of recrystallizing flower-like samples are more complicated than those of single-plate samples.

Low-temperature N_2 adsorption-desorption isotherms and pore-size distribution (PSD) curves were conducted to evaluate the textural properties of PtInHT-FC, PtInHT-PC and PtInHT-MC. Their plots are shown in Figure 4 and the corresponding S_{BET} , V_p and d_p are given in Table 2. According to the isotherm classification, all samples exhibit a type IV isotherm with H3 hysteresis loops, implying the presence of typical slit-shaped mesopores [8,24]. The PSD curves and d_p values show that the pore size increases in the following order, PtInHT-FC < PtInHT-PC < PtInHT-MC, and the same trend can be found for their S_{BET} values.

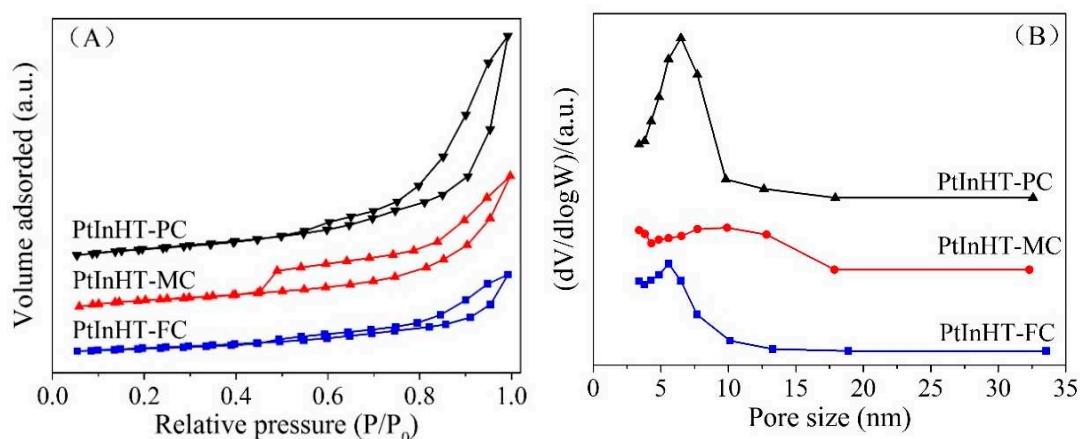


Figure 4. (A) Low temperature N_2 adsorption-desorption isotherms and (B) PSD curves of different catalysts.

Table 2. Textural properties and the dispersion degree of Pt (D_{Pt}) for PtInHT-XC catalysts.

Sample	S_{BET}^a ($m^2 \cdot g^{-1}$)	V_p^b ($cm^3 \cdot g^{-1}$)	d_p^c (nm)	D_{Pt}^d (%)
PtInHT-FC	57.9	0.17	5.58	33.6
PtInHT-PC	131.6	0.48	6.48	21.1
PtInHT-MC	144.4	0.31	9.91	27.3

^a BET specific surface area. ^b Total pore volume. ^c The most probable pore size determined by the BJH method. ^d Pt dispersion of PtInHT-XR determined by the pulse chemisorption of CO.

The broad PSD was in the mesopore range; big d_p and S_{BET} values of PtInHT-MC are related to unordered aggregation of small, flakey-like particles. As expected, the big, ordered nanosheets make PtInHT-FC and PtInHT-PC present the narrow PSD feature, and small d_p and S_{BET} values. The V_p , d_p and S_{BET} values of PtInHT-FC are far lower than that of PtInHT-PC especially, which is attributed to the fully open surface of PtInHT-PC relative to that of PtInHT-FC.

XPS analysis was applied to investigate the surface chemical state and relative concentration of In element on the reduced samples. The broad $In3d_{5/2}$ and $In3d_{3/2}$ peaks of catalysts can be deconvoluted into two peaks, respectively, in Figure 5. The deconvolution results of the corresponding spectra are listed in Table 3. The low bind energy (BE) contribution is assigned to metallic state In (In^0), and the high one is related to oxidation state In (In^{3+}). A slightly decreasing BE value of In^0 from PtInHT-FR to PtInHT-PR and to PtInHT-MR reflects the weakening electrons' transfer from metallic In to Pt species and the Pt–In interaction. Additionally, a slightly increased ratio of In^{3+}/In^0 can be seen in Table 3, in accordance with the order of PtInHT-MR, PtInHT-PR and PtInHT-FR. This indicates that the flower-like hierarchical structure with porous channels is in favor of maintaining the In element in In^{3+} ions rather than In^0 states, while the In^{3+} ions in PtInHT-MR, with small, flakey NPs, can easily be reduced.

It is worth mentioning that PtInHT-FC exhibits a higher surface Pt density than that of PtInHT-PC and PtInHT-MC, due to its low S_{BET} and high D_{Pt} , as listed in Table 2. In addition, the relative content of surface, metallic-state In increases in the order of PtInHT-FR, PtInHT-PR and PtInHT-MR (see Figure 5 and Table 3). Therefore, it can be inferred that the most of the surface In species have a chance to make close contact with Pt species and form plenty of strongly interacting Pt–In centers over PtInHT-FR. Accordingly, the Pt–In interaction over PtInHT-PR and PtInHT-MR should be decreased and weakened due to their low D_{Pt} and high S_{BET} . Additionally, too much In over PtInHT-MR could block Pt sites, thus cause a disadvantageous influence to the PDH reaction [8,24].

On the basis of the aforementioned results and preparation conditions, the formation of a ball-flower-like and single-plate hierarchical microstructure is tentatively proposed in Scheme 1.

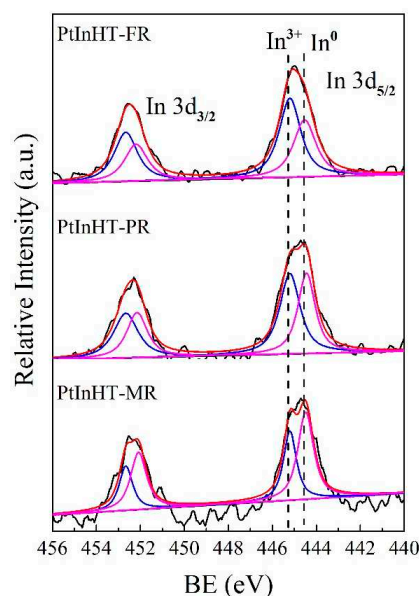
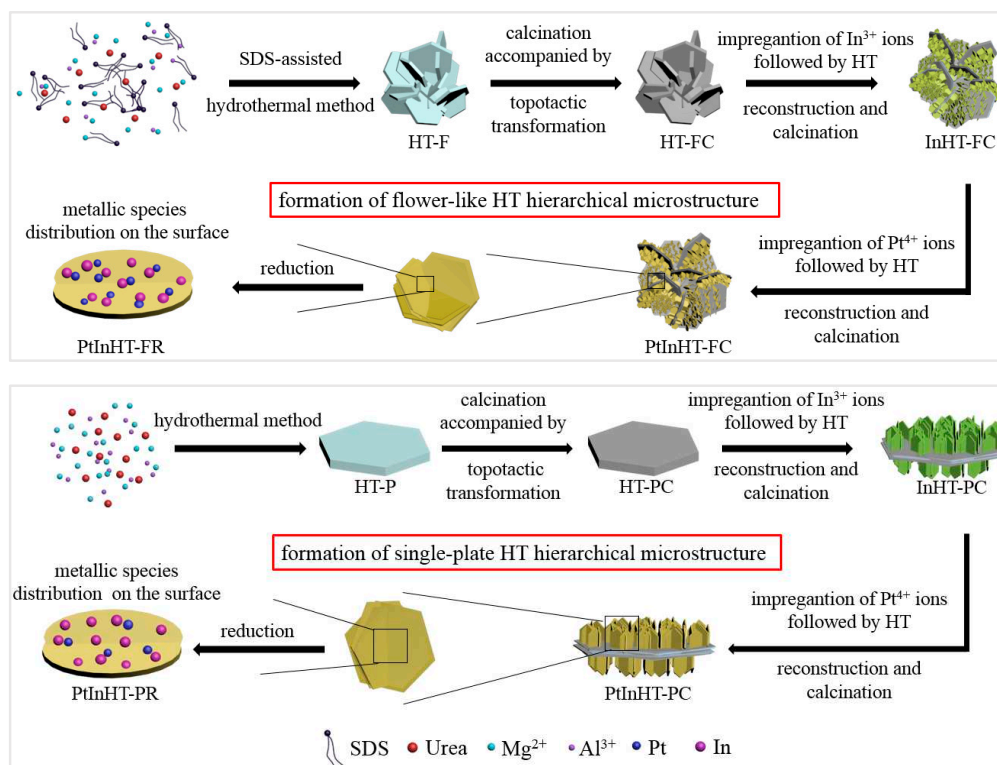


Figure 5. XPS spectra of the In 3D region of reduced catalysts.

Table 3. XPS results of reduced catalysts.

Catalyst	BE (eV)				$\text{In}^{3+}/\text{In}^0$ ^a
	In3d _{5/2}		In3d _{3/2}		
	In ³⁺	In ⁰	In ³⁺	In ⁰	
PtInHT-FR	445.2	444.5	452.7	452.2	1.34
PtInHT-PR	445.2	444.4	452.7	452.1	1.17
PtInHT-MR	445.2	444.4	452.7	452.0	0.66

^a Peak area ratio of the oxidation state In to metallic state In.



Scheme 1. Schematic illustrations of the formation of the ball-flower-like and single-plate hierarchical microstructure.

2.3. Catalytic Performance and Structure–Activity Relationship Discussion

To investigate the performance, three catalysts were evaluated in the PDH reaction. Figure 6 presents the propane conversion and propene selectivity against time for these catalysts. The homogeneous reaction is also tested in the blank tube and the propane conversion and propene selectivity as functions of time are shown in Figure S1. It was found that the conversion of propane is only around 1%, with a propene selectivity of around 65%. This indicates that the contribution of homogeneous reaction can be ignored. As shown in Figure S2, the selectivities to by-products (methane, ethane and ethene) are very low and can be ignored. In the PDH reaction, the initial propane conversions for PtInHT-FR, PtInHT-PR and PtInHT-MR are 6%, 44% and 28%, respectively. After a long induction period of 20 h, the propane conversion and propene selectivity of PtInHT-FR can be stabilized at above 40% and 97% with a maximum conversion of 48%. Until upon 190 h of time on stream, the conversion of PtInHT-FR only decreases to 36%. Despite a high initial conversion with a short induction period of around 5 h, a smooth stable period for around 50 h can be achieved by PtInHT-PR. A decreased propene selectivity cannot be ignored during the whole reaction process. As for PtInHT-MR, the reaction only can run for 20 h with moderate initial conversion; in the same period, the propene selectivity decreases severely with the rising propane conversion.

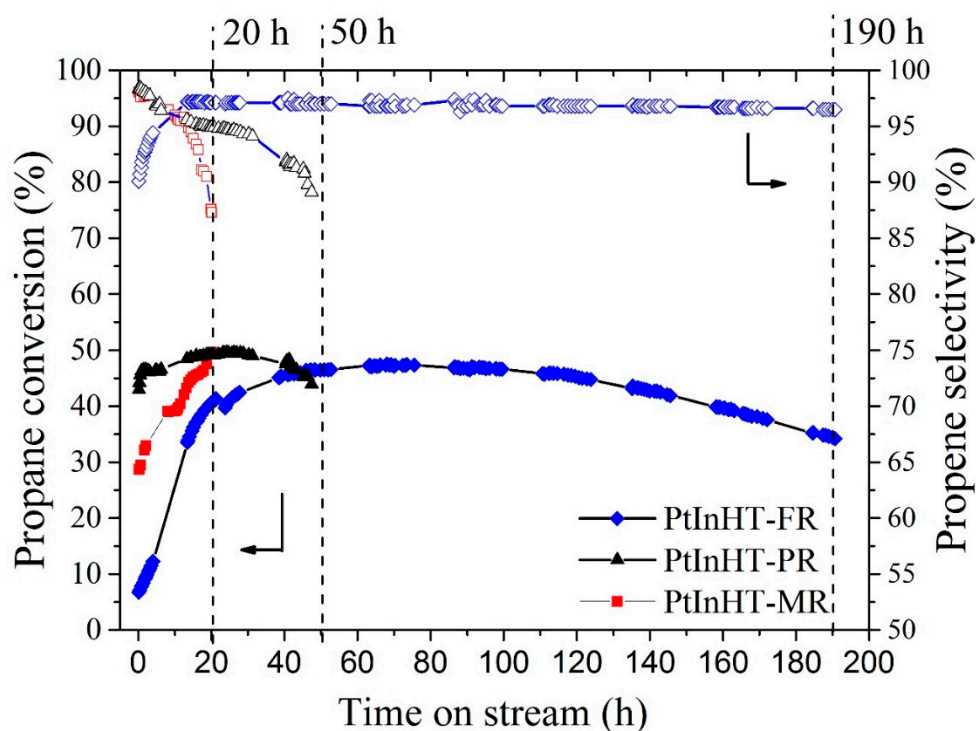


Figure 6. Propane conversion and propene selectivity as functions of time for different catalysts (reaction conditions: $T = 600\text{ }^{\circ}\text{C}$, $\text{H}_2:\text{C}_3\text{H}_8:\text{N}_2 = 7:8:35$ (molar ratio), weight hourly space velocity (WHSV) = 3 h^{-1} , $m_{\text{cat}} = 0.4\text{ g}$).

After the reaction, the XRD patterns of used samples are shown in Figure 7. It can be found that the meixnerite phase is still retained in the used PtInHT-FU, which is supposed to be favorable for the PDH reaction [7]. Additionally, the change occurs from fresh PtInHT-FR having more MgO phase (see Figures 1 and 7) while the used one has more meixnerite phase. This phase transfer of support could be the one cause of induction of performance during reaction. In addition, a new diffraction peak appears at around 26.0° in all the used samples, which belongs to the carbon deposits (JCPD file number 44-1644). The diffraction peak intensity of carbon deposits increases following the order: PtInHT-PU > PtInHT-MU > PtInHT-FU, which must be consistent with the amount of deposited carbon.

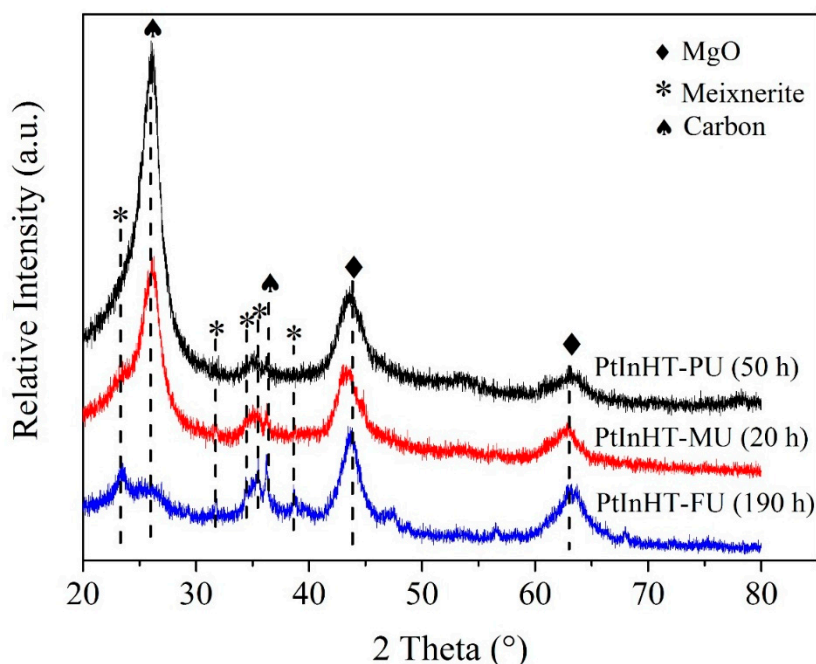


Figure 7. XRD patterns of used catalysts with different reaction time.

As shown in Figure 8, a large amount of carbon deposits with different sizes and morphologies, including granule, stick, loop and so on, are formed on the surface of used catalysts after reactions. Moreover, even the morphology features of PtInHT-PU and PtInHT-MU disappear, due to the surface coverage and pore blockage by carbon deposits. However, the flower-like particles of PtInHT-FU are still well dispersed and recognizable after a long reaction time, reflecting the fact that the amount of carbon deposits on PtInHT-FU number fewer than those on PtInHT-PU and PtInHT-MU. The most important thing is that the carbon is only deposited on the partial pore channel mouth of PtInHT-FU, meaning the active sites in the pore channels have no chance to be covered by the deposited carbon.

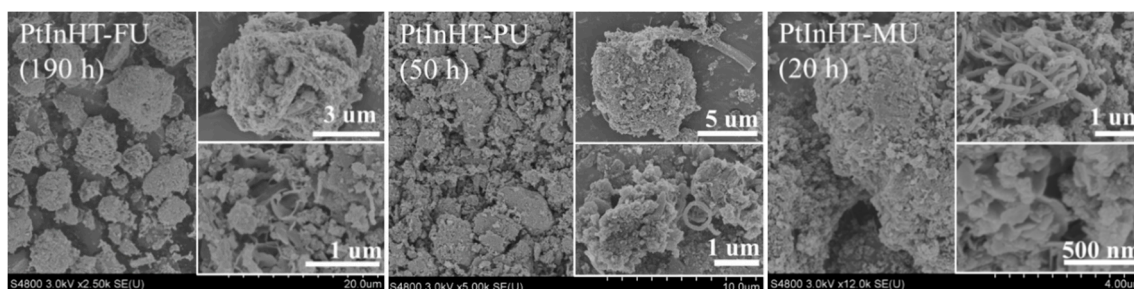


Figure 8. SEM images of used catalysts with different reaction time.

In order to determine the degree of carbon deposition during PDH reaction, TG experiments were conducted over the used catalysts. As shown in Figure 9, the mass loss of all samples must be related to the removal of deposited carbon. The amount of deposited carbon on the catalysts used increases following the order of PtInHT-FU, to PtInHT-MU and finally to PtInHT-PU. The low carbon amount is the most important factor to extend the lifetime of the flower-like PtInHT-FU.

After 190 h of reaction, it is still difficult to pick out metallic particles from the TEM images of PtInHT-FU in Figure 10. However, the Pt particles can be found on the surface of PtInHT-PU and PtInHT-MU. According to the particle size distribution of PtInHT-MU, the average particle size is higher for PtInHT-MU (5.5 nm) than that for PtInHT-PU (3.2 nm). That implies that the metallic particles on PtInHT-FU are more stable than those on PtInHT-PU and PtInHT-MU under a high

temperature reaction, which has a vital influence for the performance of PDH. Certainly, the carbon deposits also can be easily found on the surface of all samples.

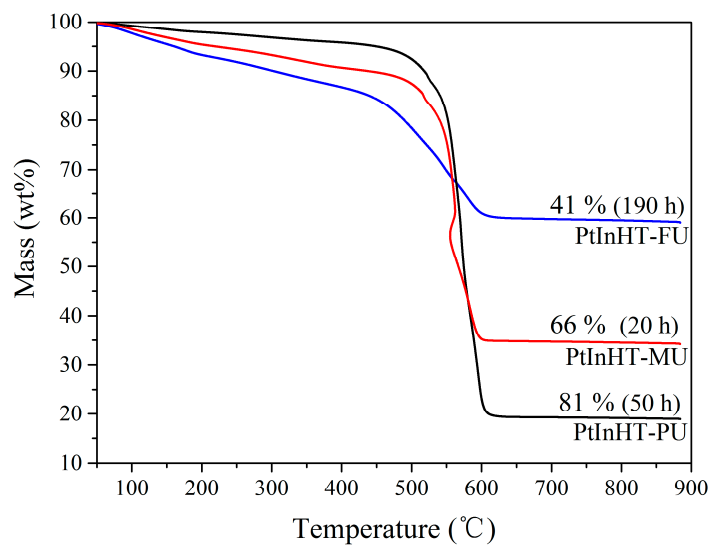
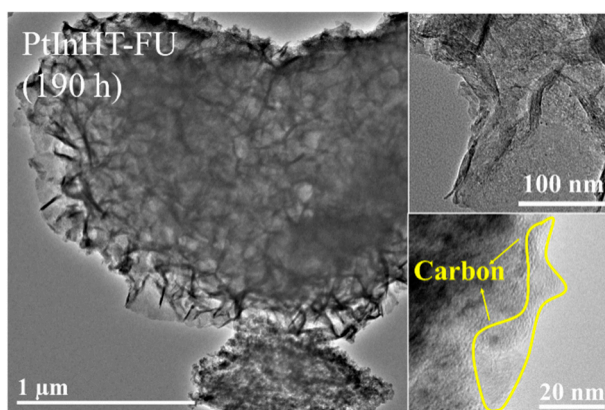
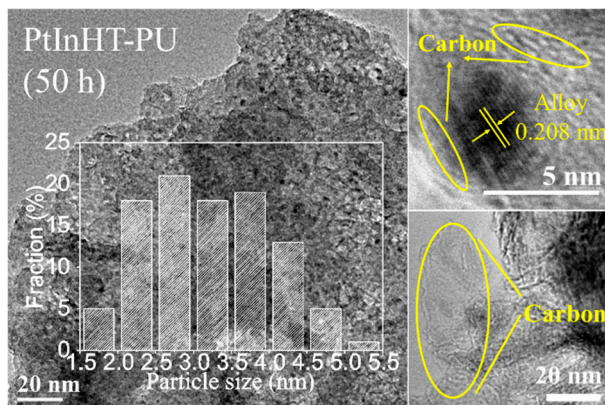


Figure 9. TG profiles of used catalysts with different reaction times.

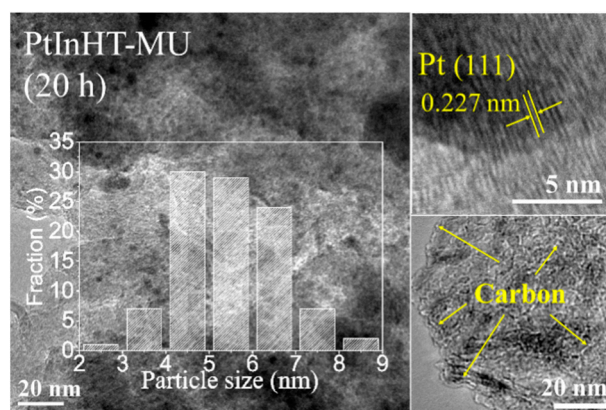


(A)



(B)

Figure 10. Cont.



(C)

Figure 10. TEM images, HR-TEM and the statistics of particle size distributions in the insets of the used catalysts with different reaction times. (A) 190 h, (B) 50 h and (C) 20 h.

The activity induction should be closely related with the partial coverage of the active metal surface by In_2O_3 species [7]. We propose that the covered, active Pt particles tend to slowly migrate from the support onto In_2O_3 particles to build highly dispersed “sandwich structure” of the Pt– In_2O_3 –support under the reaction atmosphere [25,26]. Therefore the duration of induction should be determined by the coverage degree of In_2O_3 species.

Although the maximum conversion is up to 50%, the PDH reaction cannot be carried out after 50 h for PtInHT-PR and 20 h for PtInHT-MR due to the reactor blockage by a large amount of deposited carbon (see Figures 7–10), and the deposited carbon particles fully block the honeycomb-like pores of PtInHT-PR and cover the block mass particles of PtInHT-MR. Fortunately, the deposited carbon over PtInHT-FR after reacting for 190 h is much less than that over others. It is interesting to note that the carbon is mainly deposited on the pore mouth of ball-flower-like PtInHT-FR, which protects the metallic sites on the interior honeycomb-like surface of wedge-shaped pores.

Obviously, the deposited carbon amount is inversely correlated to the corresponding propene selectivity. The ball-flower-like multi-level hierarchical microstructure with abundant wedge-shaped pores, and short-channel honeycomb-like pores, but not the slit-like pores, is in favor of propane and propene diffusion. Furthermore, the low S_{BET} of PtInHT-FR facilitates the propene desorption and then decreases the likelihood of deep dehydrogenation and hydrogenolysis on metal sites. These can be used to explain the high selectivity and low carbon deposits of PtInHT-FR. On the contrary, plenty of carbon deposits and the sharply reduced selectivities of PtInHT-PR and PtInHT-MR arise from the propene concentrating on the surface with a high S_{BET} value, which triggers carbon formation and accumulation.

Except for the influences of texture and morphology, the propene selectivity and catalytic stability can be improved, by partially transferring electrons from IN to Pt [11]. PtInHT-FR presents a high surface $\text{In}^{3+}/\text{In}^0$ ratio and BE value of In^0 , indicating that a high electron density of Pt and strong Pt–In interaction can be obtained (see Figure 5 and Table 3), which facilitates the desorption of propene and the migration of carbon precursors from the metal surface to the support [7,11]. Moreover, the suitable In^0 species can strengthen the Pt–In-support interaction, improve dispersion and prevent sintering of Pt particles (see Figures 2 and 10), stabilizing the catalytic performance of PtInHT-FR. Meanwhile, the overabundant In^0 species could bring about a disadvantageous influence to the PDH reaction. The high content In^0 species in PtInHT-PR and PtInHT-MR can not only block Pt active sites [8], but also weaken Pt–In interactions and lead to the Pt sintering (see Figures 2, 8 and 10). This is associated with the fact that the carbon deposits can easily form on the large-size Pt sites over PtInHT-PR and PtInHT-MR [37].

The regeneration and activation test for PtInHT-FU is shown in Figure 11. After each regeneration, the activity can be restored up to the level before regeneration, but decreases rapidly; almost no change in the selectivity can be observed. Although, the deposited carbon can be removed by a simple oxidation process (not the industrial condition), but the regeneration conditions can cause Pt sintering and decrease the Pt dispersion to a certain extent, which can result in the decrease of initial activity with cycles of regeneration [38,39].

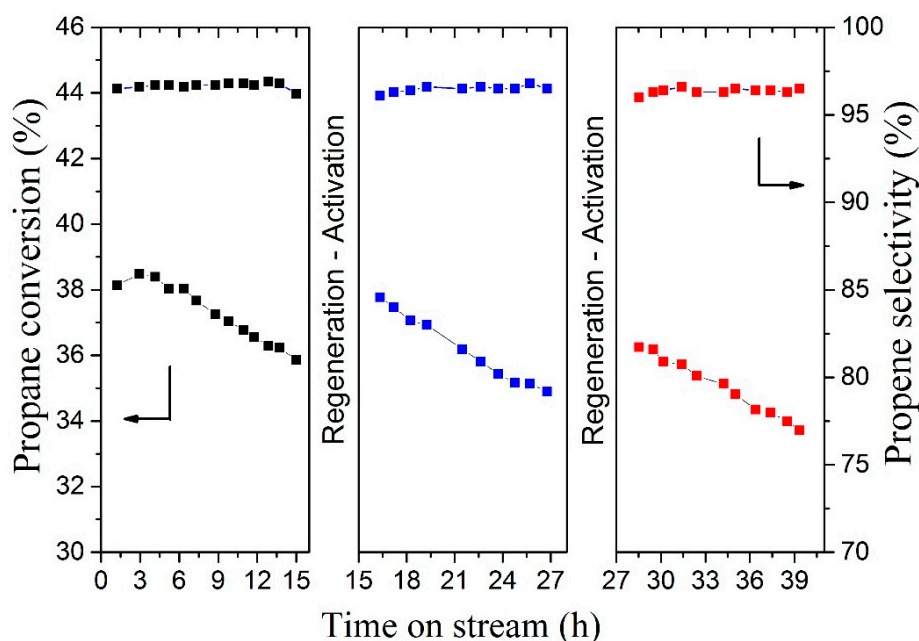


Figure 11. Propane conversion and propene selectivity as function of time for PtInHT-FU after regeneration and activation (regeneration conditions: $T = 600\text{ }^{\circ}\text{C}$, oxidation in air for 2 h, sequencing purge with N_2 for 30 min and then reduction in 5 vol% H_2/N_2 for 2 h; reaction conditions: $T = 600\text{ }^{\circ}\text{C}$, $\text{H}_2:\text{C}_3\text{H}_8:\text{N}_2 = 7:8:35$ (molar ratio) and $\text{WHSV} = 3\text{ h}^{-1}$ and $m_{\text{cat}} = 0.4\text{ g}$).

3. Materials and Methods

3.1. Materials

$\text{Mg}(\text{NO}_3)_2 \cdot 6\text{H}_2\text{O}$, $\text{Al}(\text{NO}_3)_3 \cdot 9\text{H}_2\text{O}$, urea and sodium dodecyl sulfate (SDS) were all of analytical purity. $\text{H}_2\text{PtCl}_6 \cdot 6\text{H}_2\text{O}$ powder was at 99.6% purity. All the chemicals were purchased from Fuchen (Tianjin) chemical reagent co. LTD (Tianjin, China).

3.2. Preparation

The flower-like precursor (HT-F) was prepared by a hydrothermal method. 0.82 g $\text{Mg}(\text{NO}_3)_2 \cdot 6\text{H}_2\text{O}$, 0.6 g $\text{Al}(\text{NO}_3)_3 \cdot 9\text{H}_2\text{O}$, 0.2 g SDS and 6 g urea were dissolved in 65 mL deionized water, then moved into a 100 mL Teflon autoclave. After aging at $100\text{ }^{\circ}\text{C}$ for 20 h, the sample was filtered, washed with deionized water to neutrality and dried in air at $100\text{ }^{\circ}\text{C}$ overnight.

Single-plate precursor (HT-P) was prepared using the same method as HT-F, except with no addition of SDS.

Block mass precursor (HT-M) was prepared by coprecipitation method. First, 17.09 g $\text{Mg}(\text{NO}_3)_2 \cdot 6\text{H}_2\text{O}$ and 12.50 g $\text{Al}(\text{NO}_3)_3 \cdot 9\text{H}_2\text{O}$ were dissolved in 100 mL deionized water. Another solution was prepared with 8 g NaOH and 10.6 g Na_2CO_3 dissolved in 100 mL deionized water. Then, two solutions were mixed drop-wise, with strong stirring at room temperature for 2 h. The pH value was controlled at about 10. Subsequently, the mixed solution was aged at $65\text{ }^{\circ}\text{C}$ for 12 h. The resulting suspension was filtered, washed with deionized water to neutrality and dried in air at $100\text{ }^{\circ}\text{C}$ overnight.

All the precursors were calcined for 4 h at 600 °C to obtain the corresponding calcined samples, named HT-XC (X represents morphology, either F, P or M).

The corresponding In-based precursors, InHT-X, were acquired by incipient wetness impregnation method for calcined samples HT-XC with $\text{In}(\text{NO}_3)_3 \cdot x\text{H}_2\text{O}$ aqueous solution at room temperature for 6 h. Next, PtInHT-XC catalysts were prepared by successive incipient impregnation method. Firstly, HT-XC was impregnated with an $\text{In}(\text{NO}_3)_3 \cdot x\text{H}_2\text{O}$ aqueous solution at room temperature for 6 h and later dried at 120 °C for 12 h to obtain In-based precursors InHT-X, and then these solids were calcined at 550 °C for 4 h; corresponding products were labeled InHT-XC. Finally, the same procedures and conditions were performed on InHT-XC impregnated with $\text{H}_2\text{PtCl}_6 \cdot 6\text{H}_2\text{O}$, except that the time of impregnation was 2 h. After drying and calcination, the resulting solids were defined as PtInHT-X and PtInHT-XC, respectively. The loadings of Pt and In were 0.48 wt% and 1.38 wt%, respectively. After the reduction treatment under 5 vol% H_2/N_2 at 600 °C for 2.5 h, these samples were labeled PtInHT-XR. And the used catalysts were marked as PtInHT-XU.

3.3. Characterizations

X-ray diffraction (XRD) characterization was carried on a Bruker D8-Focus X-ray diffractometer (BRUKER AXS GMBH, Karlsruhe, Germany) by Ni-filtered $\text{Cu K}\alpha$ radiation ($\lambda = 0.15406$ nm) with a scan speed of $2\theta = 8^\circ \cdot \text{min}^{-1}$.

Low-temperature N_2 adsorption-desorption was performed at 77 K on a TriStar 3000 micromeritics apparatus (Micromeritics, Norcross, GA, USA) to collect the textural properties. Prior to measurements, the samples were outgassed under vacuum at 300 °C for 4 h, and then the specific surface area of samples was calculated by the Brunauer–Emmett–Teller (BET) method; the pore size distribution (PSD) was determined by the Barrett–Joyner–Halenda (BJH) method, used upon the adsorption branch of the isotherms.

Field emission scanning electron microscopy (FESEM) was carried out on a Hitachi S-4800 instrument (Tokyo, Japan) using a 3.0 kV electron beam.

Transmission electron microscopy and energy dispersive spectroscopy (TEM-EDS) were performed on a JEM-2100F field-emission transmission electron microscope (JEOL, Tokyo, Japan) with an accelerating voltage of 200 kV.

The X-ray photoelectron spectra (XPS) of catalysts were recorded on a Thermo Scientific Escalab 250Xi X-ray photoelectron spectrometer (Thermo Fisher Scientific, Waltham, MA, USA) using $\text{Al K}\alpha$ ($h\nu = 1253.6$ eV) radiation. The BE was calibrated using the C1s level at 284.8 as an internal standard.

The dispersion degree of Pt (D_{Pt}) was calculated by CO chemisorption. CO chemisorption was conducted on AutoChem II 2920 analyzer (Micromeritics, Norcross, USA). A total of 100 mg of the samples were reduced under 10 vol% H_2/Ar atmosphere at 600 °C for 2 h with a heating rate of $10^\circ\text{C} \cdot \text{min}^{-1}$. After reduction, the catalysts were swept with He, at 600 °C for 30 min, to remove H_2 , and then cooled down to 50 °C. Subsequently, the CO pulse chemisorption was carried out at 50 °C by injecting pulses of 5 vol% CO/He until CO was adsorbed to saturation.

Thermogravimetric analysis (TG) was carried on a DTG-50/50H thermal analyzer (PerkinElmer, Waltham, MA, USA) to determine the carbon amount over the used catalysts with a heating rate of $10^\circ\text{C} \cdot \text{min}^{-1}$ from room temperature to 800 °C in air.

3.4. Catalytic Tests

Propane dehydrogenation (PDH) reaction was carried out in a fixed-bed reactor. The calcined sample (0.4 g) was placed into the stainless-steel tube and reduced to a flow of 5 vol% H_2/N_2 at 600 °C for 2.5 h with a rising rate of $5^\circ\text{C} \cdot \text{min}^{-1}$. Afterwards, the PDH reaction was performed in a mixture of H_2 , N_2 and C_3H_8 ($\text{H}_2:\text{C}_3\text{H}_8:\text{N}_2 = 7:8:35$ (molar ratio) and $\text{WHSV} = 3 \text{ h}^{-1}$) at 600 °C. The regeneration test was performed at 600 °C, including oxidation in air for 2 h, sequencing purge with N_2 for 30 min and then reduction in 5 vol% H_2/N_2 for 2 h. The propane and gas products were analyzed by an online

gas chromatograph equipped with a FID detector and an Al₂O₃ column. The propane conversion and propene selectivity were calculated as follows:

$$\text{Propane conversion(\%)} = \frac{\text{propane, in} - \text{propane, out}}{\text{propane, in}} \times 100\% \quad (1)$$

$$\text{Propene selectivity(\%)} = \frac{\text{propene, out}}{\text{propane, in} - \text{propane, out}} \times 100\% \quad (2)$$

4. Conclusions

In conclusion, the ball-flower-like, single-plate and block mass PtIn/Mg(Al)O catalysts were obtained by topological transformation and the reconstruction of HT precursors. The diversified morphology of catalysts was dependent on the conditions of synthesis. The metal ions of Pt⁴⁺ and In³⁺ can be introduced into the HT layer during the reconstruction process and the metallic species can be highly dispersed on the surface of Mg(Al)O. The ball-flower-like PtIn/Mg(Al)O catalyst exhibited high activity, excellent propene selectivity and superior durability as well as excellent resistance to the carbon deposition and Pt-sintering in the propane dehydrogenation to propene, which were mainly arising from its multi-level hierarchical microstructure with low specific surface area, and a large amount of strong and stable Pt–In interactions. It will be of great importance to revisit these catalysts and research the essential reasons for different catalytic performance in the PDH reaction by using more methods.

Supplementary Materials: The following are available online at <http://www.mdpi.com/2073-4344/9/9/767/s1>, Figure S1: Propane conversion and propene selectivity as function of time for blank tube, Figure S2: The selectivity of methane, ethane and ethene as function of time for different catalysts.

Author Contributions: J.L. wrote the manuscript, performed the experiments and analyzed data; M.Z. and Z.S. collected references and characterized the physico-chemical properties of materials; S.L. and J.W. made the figures and tables, collected and checked data; L.Z. provided research ideas, analyzed data and revised the manuscript.

Funding: This research was funded by the National Natural Science Foundation of China (21776214).

Acknowledgments: This work was supported by the National Natural Science Foundation of China (21776214) and State Key Laboratory of Chemical Resource Engineering.

Conflicts of Interest: The authors declare no conflict of interest.

References

- Zhu, J.; Yang, M.L.; Yu, Y.; Zhu, Y.A.; Sui, Z.J.; Zhou, X.G.; Holmen, A.; Chen, D. Size-Dependent Reaction Mechanism and Kinetics for Propane Dehydrogenation over Pt Catalysts. *ACS Catal.* **2015**, *5*, 6310–6319. [CrossRef]
- Xiong, H.; Lin, S.; Goetze, J.; Pletcher, P.; Guo, H.; Kovarik, L.; Artyushkova, K.; Weckhuysen, B.M.; Datye, A.K. Thermally Stable and Regenerable Platinum–Tin Clusters for Propane Dehydrogenation Prepared by Atom Trapping on Ceria. *Angew. Chem. Int. Ed.* **2017**, *56*, 8986–8991. [CrossRef] [PubMed]
- Xia, K.; Lang, W.Z.; Li, P.P.; Yan, X.; Guo, Y.J. The properties and catalytic performance of PtIn/Mg(Al)O catalysts for the propane dehydrogenation reaction: Effects of pH value in preparing Mg(Al)O supports by the co-precipitation method. *J. Catal.* **2016**, *338*, 104–114. [CrossRef]
- Cai, W.; Mu, R.; Zha, S.; Sun, G.; Chen, S.; Zhao, Z.J.; Li, H.; Tian, H.; Tang, Y.; Tao, F.; et al. Subsurface catalysis-mediated selectivity of dehydrogenation reaction. *Sci. Adv.* **2018**, *4*, eaar5418. [CrossRef] [PubMed]
- Yu, C.; Ge, Q.; Xu, H.; Li, W. Effects of Ce addition on the Pt-Sn/gamma-Al₂O₃ catalyst for propane dehydrogenation to propylene. *Appl. Catal. A* **2006**, *315*, 58–67. [CrossRef]
- Jung, J.W.; Kim, W.I.; Kim, J.R.; Oh, K.; Koh, H.L. Effect of Direct Reduction Treatment on Pt–Sn/Al₂O₃ Catalyst for Propane Dehydrogenation. *Catalysts* **2019**, *9*, 446. [CrossRef]
- Xia, K.; Lang, W.Z.; Li, P.P.; Yan, X.; Guo, Y.J. Analysis of the catalytic activity induction and deactivation of PtIn/Mg(Al)O catalysts for propane dehydrogenation reaction. *RSC Adv.* **2015**, *5*, 64689–64695. [CrossRef]

8. Xia, K.; Lang, W.Z.; Li, P.P.; Long, L.L.; Yan, X.; Guo, Y.J. The influences of Mg/Al molar ratio on the properties of PtIn/Mg(Al)O-x catalysts for propane dehydrogenation reaction. *Chem. Eng. J.* **2016**, *284*, 1068–1079. [CrossRef]
9. Pham, H.N.; Sattler, J.J.H.B.; Weckhuysen, B.M.; Datye, A.K. Role of Sn in the Regeneration of Pt/ γ -Al₂O₃ Light Alkane Dehydrogenation Catalysts. *ACS Catal.* **2016**, *6*, 2257–2264. [CrossRef]
10. Zhu, Y.; An, Z.; Song, H.; Xiang, X.; Yan, W.; He, J. Lattice-Confined Sn (IV/II) Stabilizing Raft-Like Pt Clusters: High Selectivity and Durability in Propane Dehydrogenation. *ACS Catal.* **2017**, *7*, 6973–6978. [CrossRef]
11. Sun, P.; Siddiqi, G.; Vining, W.C.; Chi, M.; Bell, A.T. Novel Pt/Mg(In)(Al)O catalysts for ethane and propane dehydrogenation. *J. Catal.* **2011**, *282*, 165–174. [CrossRef]
12. Chen, M.; Xu, J.; Cao, Y.; He, H.Y.; Fan, K.N.; Zhuang, J.H. Dehydrogenation of propane over In₂O₃-Al₂O₃ mixed oxide in the presence of carbon dioxide. *J. Catal.* **2010**, *272*, 101–108. [CrossRef]
13. Redekop, E.A.; Galvita, V.V.; Poelman, H.; Bliznuk, V.; Detavernier, C.; Marin, G.B. Delivering a Modifying Element to Metal Nanoparticles via Support: Pt–Ga Alloying during the Reduction of Pt/Mg(Al,Ga)O_x Catalysts and Its Effects on Propane Dehydrogenation. *ACS Catal.* **2014**, *4*, 1812–1824. [CrossRef]
14. Fang, S.; Zhang, K.; Wang, C.; Ma, L.; Zhang, Q.; Liu, Q.; Chen, L.; Chen, L.; Zhang, Q.; Tian, Z. The properties and catalytic performance of PtSn/Mg(x-Ga)AlO catalysts for ethane dehydrogenation. *RSC Adv.* **2017**, *7*, 22836–22844. [CrossRef]
15. Sun, G.; Zhao, Z.J.; Mu, R.; Zha, S.; Li, L.; Chen, S.; Zang, K.; Luo, J.; Li, Z.; Purdy, S.C.; et al. Breaking the scaling relationship via thermally stable Pt/Cu single atom alloys for catalytic dehydrogenation. *Nat. Commun.* **2018**, *9*, 4454. [CrossRef] [PubMed]
16. Wegener, E.C.; Wu, Z.; Tseng, H.T.; Gallagher, J.R.; Ren, Y.; Diaz, R.E.; Ribeiro, F.H.; Miller, J.T. Structure and reactivity of Pt–In intermetallic alloy nanoparticles: Highly selective catalysts for ethane dehydrogenation. *Catal. Today.* **2018**, *299*, 146–153. [CrossRef]
17. Wang, T.; Jiang, F.; Liu, G.; Zeng, L.; Zhao, Z.J.; Gong, J.L. Effects of Ga doping on Pt/CeO₂-Al₂O₃ catalysts for propane dehydrogenation. *AIChE J.* **2016**, *62*, 4365–4376. [CrossRef]
18. Siddiqi, G.; Sun, P.; Galvita, V.; Bell, A.T. Catalyst performance of novel Pt/Mg(Ga)(Al)O catalysts for alkane dehydrogenation. *J. Catal.* **2010**, *274*, 200–206. [CrossRef]
19. Liu, G.; Zeng, L.; Zhao, Z.J.; Tian, H.; Wu, T.; Gong, J.L. Platinum-Modified ZnO/Al₂O₃ for Propane Dehydrogenation: Minimized Platinum Usage and Improved Catalytic Stability. *ACS Catal.* **2016**, *6*, 2158–2162. [CrossRef]
20. Del Angel, G.; Bonilla, A.; Peña, Y.; Navarrete, J.; Fierro, J.L.G.; Acosta, D.R. Effect of lanthanum on the catalytic properties of PtSn/ γ -Al₂O₃ bimetallic catalysts prepared by successive impregnation and controlled surface reaction. *J. Catal.* **2003**, *219*, 63–73. [CrossRef]
21. Jiang, F.; Zeng, L.; Li, S.; Liu, G.; Wang, S.; Gong, J.L. Propane Dehydrogenation over Pt/TiO₂-Al₂O₃ Catalysts. *ACS Catal.* **2015**, *5*, 438–447. [CrossRef]
22. De Miguel, S.R.; Jablonski, E.L.; Castro, A.A.; Scelza, O.A. Highly selective and stable multimetallic catalysts for propane dehydrogenation. *J. Chem. Technol. Biotechnol.* **2000**, *75*, 596–600. [CrossRef]
23. Zhang, Y.; Zhou, Y.; Qiu, A.; Wang, Y.; Xu, Y.; Wu, P. Propane dehydrogenation on PtSn/ZSM-5 catalyst: Effect of tin as a promoter. *Catal. Commun.* **2006**, *7*, 860–866. [CrossRef]
24. Shen, L.L.; Xia, K.; Lang, W.Z.; Chu, L.F.; Yan, X.; Guo, Y.J. The effects of calcination temperature of support on PtIn/Mg(Al)O catalysts for propane dehydrogenation reaction. *Chem. Eng. J.* **2017**, *324*, 336–346. [CrossRef]
25. Nawaz, Z.; Tang, X.; Wang, Y.; Wei, F. Parametric Characterization and Influence of Tin on the Performance of Pt–Sn/SAPO-34 Catalyst for Selective Propane Dehydrogenation to Propylene. *Ind. Eng. Chem. Res.* **2010**, *49*, 1274–1280. [CrossRef]
26. Lin, L.; Yang, W.; Jia, J.; Xu, Z.; Zhang, T.; Fan, Y.; Kou, Y.; Shen, J. Surface structure and reaction performances of highly dispersed and supported bimetallic catalysts. *Sci. China Ser. B Chem.* **1999**, *42*, 571. [CrossRef]
27. Takehira, K.; Shishido, T. Preparation of supported metal catalysts starting from hydrotalcites as the precursors and their improvements by adopting “memory effect”. *Catal. Surv. Asia.* **2007**, *11*, 1–30. [CrossRef]
28. Oladipo, A.A.; Ifebajo, A.O.; Gazi, M. Magnetic LDH-based CoO–NiFe₂O₄ catalyst with enhanced performance and recyclability for efficient decolorization of azo dye via Fenton-like reactions. *Appl. Catal. B* **2019**, *243*, 243–252. [CrossRef]

29. Belskaya, O.B.; Stepanova, L.N.; Gulyaeva, T.I.; Erenburg, S.B.; Trubina, S.V.; Kvashnina, K.; Nizovskii, A.I.; Kalinkin, A.V.; Zaikovskii, V.I.; Bukhtiyarov, V.I.; et al. Zinc influence on the formation and properties of Pt/Mg(Zn)AlO_x catalysts synthesized from layered hydroxides. *J. Catal.* **2016**, *341*, 13–23. [CrossRef]
30. Hibino, T.; Tsunashima, A. Characterization of Repeatedly Reconstructed Mg–Al Hydrotalcite-like Compounds: Gradual Segregation of Aluminum from the Structure. *Chem. Mater.* **1998**, *10*, 4055–4061. [CrossRef]
31. Wu, M.; Zhang, J.; Peng, Y.; Zhou, J.; Ruan, X.; Liu, J.; Liu, Q.; Xi, Y.; Frost, R.; Qian, G. An investigation into mechanism of cation adsorption by reconstruction of calcined layered double hydroxide. *Microporous Mesoporous Mater.* **2017**, *242*, 182–189. [CrossRef]
32. Yu, J.; Fan, G.; Yang, Y.; Li, F. Multi-level three-dimensional Mg–Al layered double hydroxide hierarchical microstructures with enhanced basic catalytic property. *J. Colloid Interface Sci.* **2014**, *432*, 1–9. [CrossRef] [PubMed]
33. Cavani, F.; Trifirò, F.; Vaccari, A. Hydrotalcite-type anionic clays: Preparation, properties and applications. *Catal. Today* **1991**, *11*, 173–301. [CrossRef]
34. Shannon, R.D. Revised effective ionic radii and systematic studies of interatomic distances in halides and chalcogenides. *Acta Crystallogr. Sect. A* **1976**, *32*, 751–767. [CrossRef]
35. Ma, X.; An, Z.; Zhu, Y.; Wang, W.; He, J. Pseudo-single-atom Platinum Induced by the Promoter Confined in Brucite-like Lattice for Catalytic Reforming. *ChemCatChem* **2016**, *8*, 1773–1777. [CrossRef]
36. Gao, Z.; Sasaki, K.; Qiu, X. Structural Memory Effect of Mg–Al and Zn–Al layered Double Hydroxides in the Presence of Different Natural Humic Acids: Process and Mechanism. *Langmuir* **2018**, *34*, 5386–5395. [CrossRef] [PubMed]
37. Zhang, Y.; Zhou, Y.; Wan, L.; Xue, M.; Duan, Y.; Liu, X. Synergistic effect between Sn and K promoters on supported platinum catalyst for isobutane dehydrogenation. *J. Nat. Gas Chem.* **2011**, *20*, 639–646. [CrossRef]
38. Im, J.; Choi, M. Physicochemical Stabilization of Pt against Sintering for a Dehydrogenation Catalyst with High Activity, Selectivity, and Durability. *ACS Catal.* **2016**, *6*, 2819–2826. [CrossRef]
39. Nagai, Y.; Hirabayashi, T.; Dohmae, K.; Takagi, N.; Minami, T.; Shinjoh, H.; Matsumoto, S.I. Sintering inhibition mechanism of platinum supported on ceria-based oxide and Pt-oxide–support interaction. *J. Catal.* **2006**, *242*, 103–109. [CrossRef]



© 2019 by the authors. Licensee MDPI, Basel, Switzerland. This article is an open access article distributed under the terms and conditions of the Creative Commons Attribution (CC BY) license (<http://creativecommons.org/licenses/by/4.0/>).

MDPI
St. Alban-Anlage 66
4052 Basel
Switzerland
Tel. +41 61 683 77 34
Fax +41 61 302 89 18
www.mdpi.com

Catalysts Editorial Office
E-mail: catalysts@mdpi.com
www.mdpi.com/journal/catalysts



MDPI
St. Alban-Anlage 66
4052 Basel
Switzerland

Tel: +41 61 683 77 34
Fax: +41 61 302 89 18

www.mdpi.com



ISBN 978-3-0365-3551-7